DTU

Rasmus Walter

Cement-Based Overlay
for Orthotropic Steel Bridge Decks

A Multi-Scale Modeling Approach

PHD THESIS

BYG·DTU

Cement-Based Overlay for Orthotropic Steel Bridge Decks

A Multi-Scale Modeling Approach

Rasmus Walter

Ph.D. Thesis

Department of Civil Engineering
Technical University of Denmark

2005

Preface

This thesis is submitted as a partial fulfilment of the requirements for the Danish Ph.d. degree. The thesis is divided into two parts. The first part introduces the motivation and highlights the major conclusions and findings. The second part is a collection of seven papers, presenting the research in greater details.

Acknowledgements

Abstract

The success of the traditional orthotropic steel bridge deck may be due to its high strength to weight ratio. However, fatigue damage has been experienced within heavily trafficked routes due to the low stiffness of this deck in combination with increasing traffic intensity and wheel pressure. This thesis investigates a system to stiffen an orthotropic steel bridge deck, using a cement-based overlay. The investigation is based on nonlinear fracture mechanics and aims to determine the performance of the bridge deck in terms of cracking behavior. The main goal of applying a cement-based overlay to an orthotropic steel bridge deck, is to increase the deck stiffness and thereby reduce the stresses in fatigue sensitive steel parts. Cracking of the cement-based overlay will have considerable influence on the composite action and durability of the system. The system has to be economically beneficial and show a good performance with regards to cracking behavior. Since cracking plays a major role on the performance, cracking behavior of the overlay is the main focus of the present thesis.

The strategy utilized in the present thesis is based on multi scale modeling, which spans from modeling and experiments on the steel-concrete interface scale, to modeling of a real size structure. The multi scale concept is utilized by identifying mechanical behavior on the steel-concrete interface scale and later applying the mechanical behavior on the structural scale. On the steel-concrete interface scale, normal cracking (Mode I) and combined normal and shear cracking (mixed mode cracking) are analyzed through experiments and modeling. The aim and outcome of the study on the interface scale, is a set of constitutive parameters which later are applied on the structural scale. The composite action between an overlay and steel plate is analyzed experimentally through small beam and plate elements with spans in the range of 0.8 to 1.0 meter. Through these tests, the numerical tools applied are verified by comparing experimental results to numerical results. Cracking between the overlay and steel plate (debonding) is also analyzed through small scale experiments and further investigated numerically. The investigation shows that debonding is initiated from a defect in the overlay, e.g. an overlay crack. Debonding initiation is observed for a certain crack width of the overlay. Significant findings on the composite elements, such as the overlay crack width which initiates debonding, are also observed when modeling a full size structure.

A set of theoretical tools have been established to analyze the performance of an orthotropic steel bridge deck stiffened with a cement-based overlay, with respect to cracking behavior. For a given design situation, it might be possible to give an estimate on the crack pattern and maximum crack width when applying a given cement-based overlay.

This thesis demonstrates a nonlinear investigation of a real size structure, with emphasis on the performance of the overlay system, using different cement-based materials. Effects, such as traffic load, early age shrinkage, and temperature gradients are taken into account, and it is showed that all these effects might have a significant influence on the cracking behavior. The overlay performance, e.g. the relation between the magnitude of axle load and maximum crack width, is dependent on the constitutive parameters of the overlay material. Temperature gradients and early age shrinkage, have a considerable influence on the relationship between axle load and maximum crack width. The analysis shows that cracking of the overlay, for the given structure and design regulations, might be unavoidable. Therefore, the challenge in certain design situations, might be to minimize the maximum crack width of the overlay.

Resumé

De traditionelle orthotrope stålbrodæks succes kan tilskrives deres høje styrke-til-vægt forhold. Der er dog, indenfor de senere år, observeret udmattelsesskader på de traditionelle orthotrope stålbrodæk. Udmattelsesskaderne er især observeret på orthotrope stålbrodæk der er placeret på højt trafikerede strækninger og skyldes den lave stivhed af et orthotropt stålbrodæk i kombination med stigende trafikintensitet og højere hjultryk Denne afhandling undersøger et system til at forstærke orthotrope stålbrodæk ved anvendelsen af et cementbaseret dæklag. Undersøgelsen baserer sig på ikke-lineær brudmekanik med det mål, at bestemme stålbrodækkets mekaniske opførelse med fokus på revnedannelse. Hovedformålet med at anvende et cementbaseret dæklag er at forøge stivheden af stålpladen i det orthotrope stålbrodæk. Ved at forøge stivheden, sænkes spændingerne i de kritiske stålsamlinger og levetiden af brodækket forøges. Holdbarhed og samvirke mellem det cementbaseret dæklag og stålpladen, er begge forhold der er styret af revnedannelse. Anvendelsen af systemet er afhængigt af om det er økonomisk fordelagtigt, samtidig med at det udviser en stor modstandsdygtighed overfor revnedannelse. Idet revnedannelsen har en markant indflydelse på levetiden af systemet, er revnedannelse centralt i nærværende afhandling.

Strategien i afhandlingen baserer sig på multi-skala modellering, der spænder fra modellering og eksperimenter af en skilleflade mellem beton og stål, til modelleringen af et brodæk på konstruktionsniveau. Den betydningsfulde mekaniske opførelse på skillefladeniveau er identificeret, der senere hen er medtaget i analysen af et brodæk på konstruktionsniveau. På skillefladeniveau er revnedannelse i normalretningen (Mode I) og kombineret revnedannelse i normal- og forskydningsretningen, analyseret gennem eksperimenter og modellering. Målet og resultatet af analysen på skillefladeniveau, er et sæt af konstitutive parametre til senere anvendelse på konstruktionsniveau. Samvirke mellem stål og det cementbaseret dæklag er analyseret gennem en række eksperimenter bestående af et antal plade- og bjælkeforsøg, med spænd i størrelsesordenen 0.8 til 1.0 m. Ved at modellere plade- og bjælkeforsøgene kan de, i afhandlingen anvendte, numeriske Finite Element (FE) metoder verificeres ved at sammenligne numeriske og eksperimentelle resultater. Revnedannelse mellem det cementbaseret dæklag og stålpladen er ligeledes analyseret gennem forsøg og FE. Undersøgelsen viser at delaminering mellem dæklaget og stålpladen initieres pga. en defekt i dæklaget, til eksempel revnedannelse i dæklaget. Delamineringen initieres oftest, for en bestemt revnevidde i dæklaget, hvilket også er observeret ved FE modellering af et brodæk på konstruktionsniveau.

Igennem Ph.D. arbejdet er der etableret et sæt teoretiske værktøjer til at analysere et or-

thotropt stålbrodæk med vægt på revnedannelse. I en given design situation, er det evt. muligt at give et bud på revnemønster og maksimum revnevidde. Afhandlingen demonstrer en ikke-lineær FE analyse af et orthotropt stålbrodæk forstærket med forskellige cementbaseret materialer. Forhold som trafiklast, svind i tidlig alder, og temperaturgradienter er medtaget i analysen, der viser at alle disse forhold har betydning for revnedannelse. Relationen mellem aksellast og maksimum revnevidde afhænger af dæklagets konstitutive parametre. Temperaturgradienter og svind i tidlig alder påvirker ligeledes relationen mellem aksellast og maksimum revnevidde. Analysen viser, for den givne konstruktion og norm, at revnedannelse i overlaget er uundgåeligt. Udfordringen vil, i et givent tilfælde, være at minimere den maksimale revnevidde af det cementbaseret dæklag.

Table of Contents

Paper I *Cohesive Mixed Mode Fracture Modelling and Experiments*, submitted to: Journal of Engineering Fracture Mechanics

Paper II *Wedge Splitting Test for a Steel-Concrete Interface*, Journal of Engineering Fracture Mechanics 72(17), pp. 2565-2583, 2005.

Paper III *Cement-Based Overlay in Negative Bending - Experimental and FEM Studies*, submitted for publication

Paper IV *Experimental Investigation of Fatigue in a Steel-Concrete Interface* in: 5th International Conference on Fracture Mechanics of Concrete and Concrete Structures, Vail Colorado, USA, pp. 839-845, 2004.

Paper V *Debonding of FRC Composite Bridge Deck Overlay*, in the proceedings of: 7th International Symposium on brittle matrix composites - BMC 7, Warsaw, Poland, pp. 191-200, 2003.

Paper VI *Method for Determination of Tensile Properties of ECC*, in the proceedings of: ConMat'05, Vancouver, Canada, 2005.

Paper VII *Analysis of Steel Bridge Deck Stiffened with Cement-Based Overlay*, submitted to: ASCE - Journal of Bridge Engineering

Additional reading (not included in thesis)

[1] Walter R., Olesen J. F. & Stang H.:*Interface Mixed Mode Model*,
    in: 11th International Conference on Fracture - ICF11, Turin, Italy, 2005.

[2] Walter R., Stang H., Gimsing N.J. & Olesen J.F.:*High Performance Composite
    Bridge Decks Using SCSFRC*, in: High Performance Fiber Reinforced Cement
    Composites - HPFRCC 4, RILEM Workshop, June, Ann Arbor, Michigan, USA,
    pp. 495-504, 2003.

[3] Walter R., Li V.C. & Stang H.:*Comparison of FRC and ECC in a Composite*,
    Bridge Deck in: 5th International PhD Symposium in Civil Engineering,
    June 16-19, Delft, The Netherlands, pp. 477-484, 2004.

[4] Walter R., Gimsing N.J. & Stang H.:*Composite steel-concrete orthotropic bridge*,
    deck in: 10th Nordic Steel Construction Conference, June 7-9, Copenhagen,
    Denmark, pp. 519-530, 2004.

Part I

Introduction and Summary

Chapter 1

Introduction

1.1 Orthotropic Steel Bridge Decks

The development of orthotropic steel bridge decks can be traced back to the 1930s and 1940s, when German and American engineers used the principles of ship decks in bridge engineering. After World War II, rebuilding of the long span bridges in Germany, being short on steel supply, lead German engineers to the closed rib stiffener design as we know the decks today, (Dowling 1968), (Wolchuk 1963). The typical orthotropic steel bridge deck consists of a top steel plate with a number of closed rib stiffeners welded to the bottom face. Typically, each 4 meters in the longitudinal direction, a transverse beam is installed to distribute load to other parts of the bridge, cf. Figure 1.1.
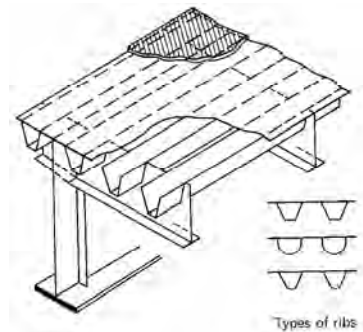
Figure 1.1 *Orthotropic steel bridge deck (AISC 1962).*

The primary task of a highway bridge is to provide a flat surface that is capable of carrying large numbers of heavy concentrated wheel loads. Lightness is very important since it affects the cost-effectiveness of a long span structure. Whole life cost is also important since bridges are designed for a long service life. Orthotropic steel bridge decks provide lightness, but their record of durability on routes with heavy traffic is not satisfactory. Repairs on highway bridges have been necessary on important bridges within 20 years

or less, cf. Smith & Bright (2003). There are three primary reasons for the durability problems on orthotropic steel bridge decks. These are increasing traffic volume, increasing axle loads, and tire designers' development of higher pressure tires with more concentrated loads (Jong et al. 2004).

1.2   Fatigue in Orthotropic Steel Bridge Decks

Fatigue is a critical factor in the design of orthotropic steel bridge decks. Compared to a concrete deck, the thin plate weld is relatively flexible, and high stresses are induced due to highly concentrated wheel loads. Passing of a truck causes a transverse bending moment over the stiffening web, and fatigue damage due to the transverse bending moment in the asphalt pavement and steel plate, have been observed in many bridges, cf. (Flint & Smith 1992). The transverse moment induces high stresses in the joint, where the top steel plate is welded to the bottom rib. This joint has in many cases been characterized as the most common fatigue sensitive detail in orthotropic steel bridge decks, see e.g. (Jong et al. 2004). Furthermore, the splice joint between the ribs, and the joint between the rib and transverse beam, have also experienced fatigue damage in orthotropic steel bridge decks. The problem of fatigue in orthotropic steel bridge decks has achieved international attention and numerous research projects are carried out to find a solution to stiffening the orthotropic steel bridge deck.

1.3   Stiffening of Orthotropic Steel Bridge Decks

A well-known fatigue example is the bascule part of the Van Brienenoord bridge in Rotterdam, (Kolstein & Wardenier 1998),(Kolstein & Wardenier 1999). Since the discovery of fatigue cracks in this bridge, research in the area of retrofitting and alternative systems to stiffening orthotropic steel bridge decks has been investigated.

1.3.1   Conventional Surfacing

Studies by Kolstein & Wardenier (1997) and later by Wolchuk (2002), show the stiffness contribution of surfacing due to its composite behavior with the steel deck plate. Assuming a rigid bond between the surfacing and underlying steel plate, surfacing may well contribute to the strain and stress distribution using the elementary bending theory. When using the surfacing as an integral part of the deck system, a considerable amount of stress reduction is observed. However, surfacing materials are generally visco-elastic to plastic and behaves elastically at low temperatures only. The elastic moduli of a general surfacing material depends highly on the temperature. Experimental recordings by Kolstein & Wardenier (1997) and Smith & Cullimore (1987), show, when using a thick polyurethane surfacing layer, that a stress reduction factor of 6 may be expected at -20^0C and about 4 at $+30^0$C. However, polyurethane materials are distinctly different than conventional asphalt materials. It is relatively soft throughout a wide temperature range. For the mastic asphalt pavements used on European and Japanese orthotropic steel bridge decks, the elastic moduli ranges from close to that of Portland cement concrete at -20^0C to 2GPa at a temperature of $+30^0$C. A new approach has been proposed by Smith &

Bright (2003), combining lightweight asphalt, conventional asphalt and a layer of glass fiber mesh embedded just beneath the chip-sealed surface, cf. Figure 1.2. Applying this system was found to increase the durability by a factor 10.
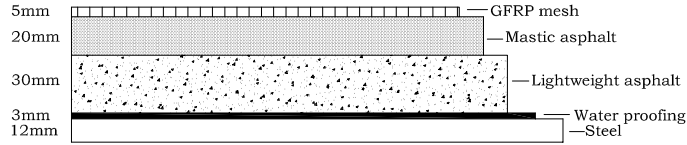
Figure 1.2 *Lightweight layered surfacing system, after Smith & Bright (2003).*

1.3.2   Steel Plate Reinforcements and Concrete Filled Ribs

Several kinds of retrofit applications to improve the fatigue performance of orthotropic steel bridge decks have been studied by Machida et al. (2004). Two methods are summarized here. One approach is to bolt an overlaid steel plate with a thickness of 12 mm to the underlying steel plate, cf. Figure 1.3(a). By this, they achieve a stress reduction of about 40 %. A second approach is to fill the ribs with a lightweight self-compacting concrete, cf. Figure 1.3(b). This method performs rather poor compared to the steel reinforcement case and reduces the critical stresses with 10 % to 20 %. They recommend combining this method with other alternative stiffening solutions to achieve a satisfactory result, e.g. to combine a cement-based overlay with concrete filled ribs.
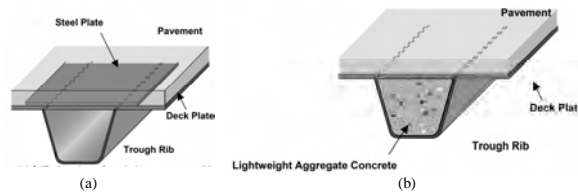
Figure 1.3 *Retrofit approaches by Machida et al. (2004), (a) steel plate reinforcement, (b) concrete filled ribs.*

1.3.3   Synthetic Overlays

The use of synthetic layers to reduce the stress range in orthotropic steel bridge decks has been investigated by De Backer et al. (2004). They have carried out investigations on orthotropic railroad bridge decks to reduce the stresses at the sensitive fatigue details. Their approach is to install a synthetic layer on top of the steel plate to improve the load dispersion. This system has been investigated for different synthetic layers both as an

independent layer, a glued on layer, and as a sandwich structure with a steel plate on top. The synthetic layers investigated were of different types, such as neopren mats, rubber mats, and polyurethane panels. The investigations showed a general trend, a glued on layer with high elastic moduli achieved a remarkable stress reduction in the steel plate. In one example, a 40 mm thick neoprene layer simply placed on top of the steel plate allows only for a 20 % reduction in stresses, whereas in the case of a rigid connection between the neoprene layer and steel plate a stress reduction by 50 % is achieved. One of the possible problems, using rubber like dispersion layers with a considerable thickness, is the high Poisson ratio of the material. A local vertical compression will result in a considerable transversal compression and consequently deformation of the synthetic layer.

1.3.4   Cement-Based Overlays

An alternative, less temperature dependent, and with relatively high elastic moduli, is to use a cement-based overlay to reduce the stress range in the fatigue sensitive details. This idea has been investigated by several authors, see e.g. (Battista & Pfeil 2000), (Braam et al. 2003) and (Jong & Kolstein 2004).

The application of a cement-based overlay for retrofitting an orthotropic steel bridge deck has already been carried out, as a pilot test, in practice. An area of the bascule part of the Van Brienenoord bridge in Rotterdam, The Netherlands has been chosen as a test area and reinforced by a 50 mm cement-based overlay using a fiber reinforced concrete with a fiber concentration of 5 kg/m^2 (Buitelaar 2002). The test area has the size of 60 m^2 and the overlay was placed in October 2000. A traditional steel reinforcement was also applied, using 24 kg/m^2. The steel reinforcement consisted of a special welded mesh of three layers with a spacing of 50x50 mm with a steel bar diameter of 8 mm. Initial conclusions show that the stresses in fatigue sensitive details, compared to a traditional orthotropic steel bridge deck are reduced from approximately 128 MPa to 28 MPa. The economical investment for placing the overlay is equal to the cost of a traditional bituminous wearing course of melted asphalt.

1.4   Proposed Cement-Based Overlay System

The main subject of this thesis is an investigation of cement-based overlays for orthotropic steel bridge decks. In the proposed system, a typical deck consist of a 40-60 mm thick cement-based overlay bonded to the steel plate. It is suggested, in this system, to achieve composite action through adhesion between the overlay and underlying steel deck. The current system leaves out mechanical shear connectors as used in traditional concrete-steel structures. Adhesion between the cement-based overlay and steel plate is ensured by sand blasting of the steel plate prior to casting of the overlay. The proposed overlay system is shown in Figure 1.4 along with a traditional steel deck.

The motivation for leaving out mechanical shear connectors is mainly based on two reasons: (i) using shear connectors creates undesirable stress concentrations, and (ii) a system with small shear connectors in large numbers will be costly with regards to labor. Since
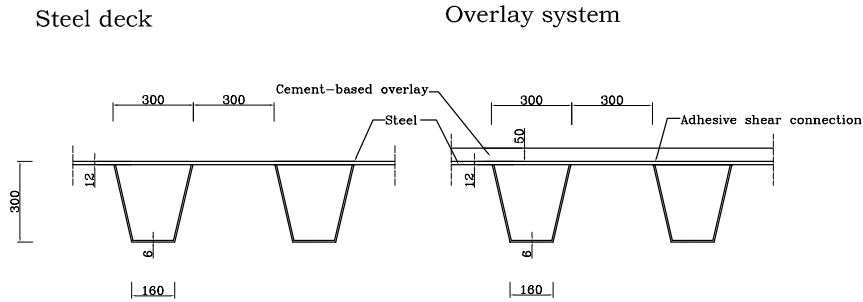
Steel deck   Overlay system

Figure 1.4 *(a) Typical steel system, with a center span of 300 mm between the supporting ribs and a 12 mm steel plate. (b) Cement-based overlay system with a 50 mm thick cement-based overlay.*

adhesion between the overlay and steel deck plays a central role on the composite action, interface fracture is of main focus in the present thesis.

The thesis concerns numerical and experimental work on different length scales. In example, when considering the interface between the cement-based overlay and steel deck, crack openings are several orders of magnitudes smaller than an actual piece of bridge deck. The results presented in this thesis are based on numerical and experimental studies on the length scale of a steel-concrete interface, which later are implemented on the structural scale. The method illustrates how to link the gap between the important features on the small length scale and modeling on structural scale.

1.5 Overview of the Thesis

The thesis can be divided into two main parts. The first part introduces the motivation and background of this study and highlights the major conclusions and findings. The second part is a collection of seven papers, explaining the research in greater details.

This first part, introduces the motivation and the problem at hand. Additionally, strategy and scope are included, along with an overview of the papers appended. The next three chapters highlight the major conclusions and findings, on three different length scales, from micro mechanical studies to numerical simulations on the structural scale. Finally in Chapter 5, an overall conclusion is drawn together with recommendations for further work.

The order, in which the papers are presented, does not follow a chronical time line in the thesis work as a whole, but in an order making it easy to relate the individual results from each paper to each other. Moreover, the order in which the papers are presented is also discussed in relation to the strategy employed in the PhD study.

1.5.1   Aim and Motivation

The present study investigates the application of casting a cement-based overlay to stiffen the steel plate in an orthotropic steel bridge deck. The motivation for doing so is the well-known fatigue problems associated with orthotropic steel bridge decks as described in the present chapter. The goal is to integrate detailed materials modeling with the structural modeling. The overall aim is, with emphasis on cracking behavior, to model the structural response of an orthotropic steel bridge deck reinforced with a cement-based overlay.

1.5.2   Strategy and Method

The strategy and the method of modeling a bridge deck using an integrated material-structural approach is explained. The strategy used in the present study can be characterized as a multi scale approach. This study takes into account various lengths scales and shows how these can be linked together. In order to get an overview of the study, all the work carried out can roughly be dived into three length scales, from: (i) interface characterization, to (ii) material-interface interaction, to (iii) structural design. The length scales are shown in Figure 1.5.

The smallest length scale, fundamental interface behavior, includes fracture mechanical studies of a steel-concrete interface. Here, the aim is to model steel-concrete interface fracture utilizing finite elements. Constitutive parameters are obtained through testing, and the results on the small length scale are then later used in analysis at larger length scales. The intermediate length scale, material-interface interaction, concerns studies on the composite behavior between a concrete overlay and a steel plate. Studies on this length scale are based on numerical simulations and experiments. One of the main goals on this length scale is to analyze the effects of debonding (delamination between the overlay and steel plate). The significance of the overlay material and steel-concrete interface in relation to debonding behavior is analyzed. A sound connection between the overlay and steel plate is of vital importance in regards to the composite action between the two materials. The third and final length scale, the structural scale, is analyzed using numerical simulations only. The aim on this length scale is to study the performance of the orthotropic steel bridge deck on a large length scale. This is carried out by applying experience from from smaller length scales.

1.5.3   Scope and Original Features

The study can be regarded as a collection of seven papers from *I* to *VII*. The aim of each individual part is given in each individual paper, and will not be repeated in great details here. The paper order from *I* to *VII* is organized according to the length scales as sketched in Figure 1.5. So that *Paper I* is characterized by the smallest length scale to *Paper VII* dealing with the largest length scale.

Paper I concerns numerical mixed mode modeling of a steel-concrete interface. It describes and presents a nonlinear fracture mechanical model, which can be applied to
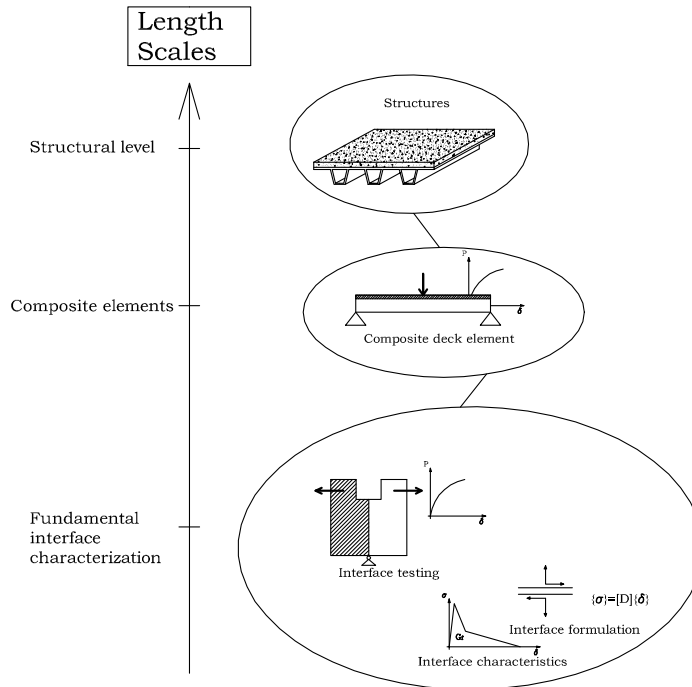
Figure 1.5 *The length scales in the study can be organized as 1. steel-concrete interface behavior, 2. material-interface behaviour, and 3. structural design.*

model the connection between steel and concrete. Additionally, it introduces an experimental set-up to measure the fracture properties of a steel-concrete interface in order to feed the model with constitutive parameters. As this paper is placed on the smallest length scale, the model is the backbone of the study, since this model is used throughout most of the papers at larger length scales.

Paper II is also placed at the smallest length scale and deals with experimental testing of a steel-concrete interface. The paper introduces a modification of the well-known Wedge Splitting Test (WST) for concrete to test the fracture mechanical Mode I behavior of a steel-concrete interface. Additionally, an inverse analysis, in order to obtain the Mode I fracture parameters, are introduced and applied on composite steel-concrete specimens.

Paper III is based on the intermediate length scale and deals with a composite deck element. The aim of the study is to analyze the debonding behavior between a cement-based overlay and a steel plate. It especially investigates the composite beam subjected to negative bending (the overlay is subject to tension). The paper investigates a macro crack propagating through the overlay, which subsequently causes debonding. By using a fairly simple deck element (can be viewed as a part of the orthotropic steel deck), both

experimental and numerical studies are carried out. Furthermore, the correlation between numerical and experimental results is studied, and can be viewed as the first link between two length scales.

Paper IV is also placed in the intermediate length scale. This paper deals with an experimental set-up to determine the fatigue properties of a steel-concrete interface. The specimen is also a composite deck element, which has been analyzed numerically and experimentally. A four point bending configuration is applied, with and without a pre-notch, exposed to cyclic loading. Different kinds of steel plates were applied in order to investigate the influence of surface roughness.

Paper V is a pure numerical paper dealing with debonding between the cement-based overlay and steel plate. The paper discusses modeling of the overlay and discrete interfacial cracking. It solely concerns the situation when a crack propagates through the overlay and how this affects debonding between the overlay and steel plate. Through a parametric investigation, the parameters which affect the debonding process are analyzed. The paper aims to analyze the parameters which might be important with regards to debonding, e.g. the fracture energy of the steel-concrete interface, the fracture energy of the overlay, etc.

Paper VI proposes a test and inverse analysis to determine the fracture properties of strain hardening materials, in this case Engineered Cementitious Composites (ECC). In order to analyze the bridge deck based on fracture mechanics, constitutive parameters of the overlay material are of great importance. Fibre reinforced cement-based materials can be categorized into two main groups, either tension softening or strain hardening materials. A large amount of research has been carried out in the field of experimental determination of fracture properties for tension softening materials. In the case of strain hardening materials as ECC, little research on testing methods to determine fracture properties has been carried out. This paper contributes to research in standard fracture mechanical test methods for strain hardening materials.

Paper VII can be classified on the largest length scale dealing with structural design. This paper looks at a part of an orthotropic steel bridge deck reinforced with a cement-based overlay. The study investigates the performance of the reinforced bridge deck, and takes into account temperature loads, traffic load, and shrinkage at early age. The study is based on numerical analysis and takes into account results from papers on smaller length scales. In particular *Paper I*, which is very important since it describes how the interface between the cement-based overlay and orthotropic steel bridge deck is modeled. Furthermore, some of the phenomena described in *Paper III* and *Paper V* are important and can directly be related to what is observed on the structural length scale.

Additional work has been carried out which is not included in the thesis. Paper (Walter et al. 2005) deals with interfacial mixed mode modeling. Most of this paper is reported in appended *Paper I*, however some FE implementation and mixed mode debonding is discussed. Both papers (Walter et al. 2003) and (Walter, Gimsing & Stang 2004) include results, which are not presented in the appended papers. Both papers include experimental studies on three dimensional composite plates. However, the results observed do

not differ significantly from what can be observed in experiments on the two dimensional composite beams which have been analyzed experimentally in *Paper III* and numerically in *Paper V*. Another published paper (Walter, Li & Stang 2004) has been extended and published in the form of *Paper III*.

Chapter 2

Interface Characterization

The aim of the interface investigations has been to describe steel-concrete interface fracture using nonlinear fracture mechanics. In context to the cement-based overlay system, cracking between concrete and steel makes this topic of special interest. An overview and some of the major results and conclusions on the interface level are summarized in this chapter. For a more complete review, the reader is referred to the individual appended papers.

The studies on steel-concrete interface behavior can be subdivided into an experimental and numerical section. The overall goal is to establish a numerical model for use in finite elements, which is capable of modeling cracking between a steel and concrete interface. A number of test methods have been established to obtain parameters for later use in numerical models.

In the past, experimental studies have been carried out by several researchers to obtain the fracture properties of a cement-based interface. This has mainly been carried out on concrete-rock interfaces to analyze the bond between the matrix and aggregates within concrete. A technical committee (RILEM TC-108 1996) has carried out studies on the so-called Interfacial Tranzition Zone (ITZ). Experimental studies on a larger scale has been carried out on mortar-rock interfaces by Wang & Maji (1995) and later by Chandra Kishen & Saouma (2004). The significance of the results on steel-concrete fracture presented in this thesis, compared to studies in the past, is an inverse analysis to obtain constitutive Mode I parameters. An inverse method has been established to characterize the Mode I fracture parameters of a concrete-steel interface to use in the Fictitious Crack Model (FCM) by Hillerborg et al. (1976). A steel-concrete interface has been investigated applying the well-known Wedge Splitting Test (WST) set-up. Using a modification of the cracked hinge model (Olesen 2001) an inverse analysis has been established to translate experimental data into constitutive parameters. Furthermore, the influence of shear forces (Mode II) on Mode I cracking is studied utilizing a mixed mode model developed by Wernersson (1994). A rather simple test set-up has been developed to feed the model with constitutive parameters.

2.1   Studies on Interface Fracture in Mode I

The difference between interfacial steel-concrete fracture and concrete fracture can be explained by the so-called *wall effect*, cf. Figure 2.1. As a crack propagates along a steel-concrete interface, the crack path is dominated by the presence of cement paste and lack of large aggregates which makes an interface fracture different from cracking observed in concrete.
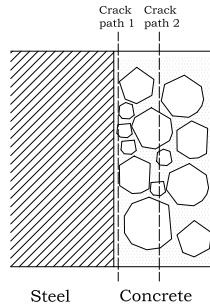

Figure 2.1 *Schematic illustration of the wall-effect. A crack path (path 1) close to a steel wall might be dominated by matrix crack propagation where as in the case of crack propagation in the concrete material (path 2) crack propagation takes place in combination of aggregates and matrix.*

The difference in concrete and steel-concrete interface fracture has been analyzed in *Paper II*. The test set-up applied is similar to the well-known Wedge Splitting Test (WST), originally proposed by Linsbauer & Tschegg (1986). The size and shape of the wedge splitting specimen is the same as described by Brühwiler & Wittmann (1990). The idea is to replace half of the specimen with a steel block, cf. Figure 2.2.

The specimen is placed on a linear support and two loading devices equipped with roller bearings are placed on top of the specimen. A steel profile shaped as a wedge is placed between the bearings. Moving the actuator of the testing machine results in a splitting force between the two bearings. The experimental results obtained in the test are load versus the splitting force. As the goal of the study is to achieve a stress-crack opening relationship, an inverse analysis is needed. This has been carried out utilizing the cracked hinge model originally proposed by Ulfkjær et al. (1995) and further developed by Olesen (2001). The advantage of this model is that it yields closed form analytical solutions, which can be implemented in an inverse analysis program. This was achieved by modifying an already established inverse analysis program by Østergaard (2003). The model and inverse analysis has been calibrated and verified using finite elements. It can be concluded that the inverse analysis to obtain the stress-crack opening relationship for a steel-concrete interface using the wedge splitting test, is acceptable. The optimization strategy employed is always able to find the global minimum.

The proposed test and inverse analysis has been employed to investigate the fracture
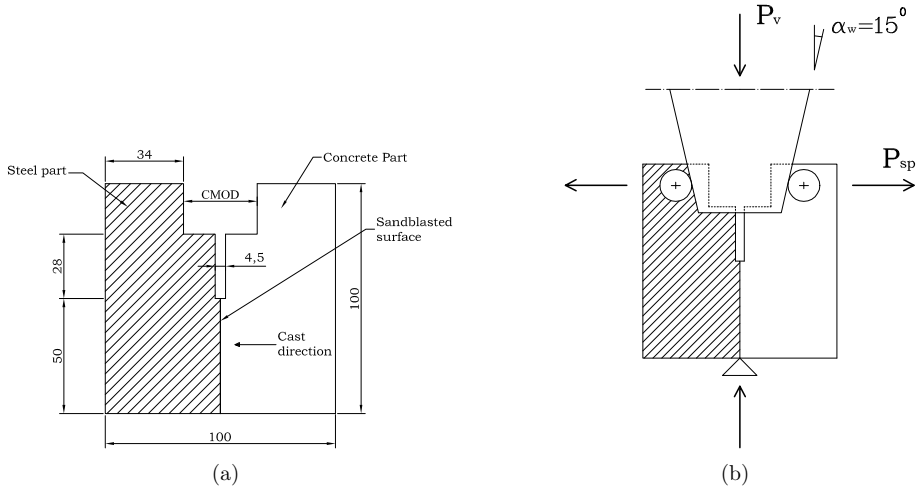
Figure 2.2 *(a) Geometry of the tested bimaterial WST specimen. The hatched part represents a steel block. (b) Load configuration.*

properties of a steel-concrete interface. For comparison with concrete fracture, full concrete specimens were also tested and analyzed. Two batches were cast, in each batch, three composite and three full concrete specimens were cast. The steel surface was sandblasted prior to casting. A self-compacting concrete was used, since it is believed that a self-compacting feature enhances the steel-concrete bond. Vibration of the concrete might cause water to separate from the mix and create a weak interface. Comparison between steel-concrete and concrete fracture can be viewed by comparing bilinear stress-crack opening relationships. The bilinear stress-crack opening relationships have been obtained utilizing the cracked hinge model and are displayed in Figure 2.3.
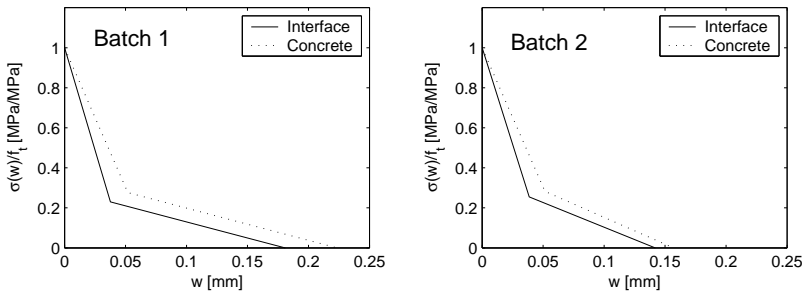
Figure 2.3 *Stress-crack opening relationship for (a) batch no. 1 and (b) batch no. 2 determined using the inverse analysis.*

It is observed from Figure 2.3 that a higher drop in the beginning of the $\sigma - w$ curve is present for the interface tests compared to the full concrete specimens. This is due to the

wall effect, since the shape of the $\sigma - w$ curve is influenced by the fracture strength of aggregates and matrix. Crack propagation in the composite specimen takes place in the matrix, whereas in the full concrete specimens cracking takes place in a combination of aggregates/matrix. The higher stress drop in the beginning of the stress-crack opening relationship might be due to the fact that the matrix is more brittle compared to the aggregates.

2.2   Studies on Mixed Mode Interface Fracture

Cracking between the overlay and underlying steel bridge deck would in many cases be characterized by fracture in a combination of normal and shear stresses. This type of fracture is offend referred to as mixed mode fracture. Hence, pure Mode I cracking as studied in the previous section might not be sufficient to describe the behavior. Together with a brief summary of a mixed mode model applied in *Paper I*, experimental work on mixed mode testing for steel-concrete interfaces is presented. This has not, as far as the author is informed, been carried out on steel-concrete interfaces in the past.

Pure Mode I cracking can be modeled using the FCM. In order to compensate for the influence of shear on interface fracture, a mixed mode model based on the FCM, has been studied and applied. Previous modeling on discrete mixed mode fracture in cement-based materials has been carried out by Loureno & Rots (1997) and later by Cervenka et al. (1998). These models have a limitation on the shape of the stress-crack opening relationship, and require the pure Mode II fracture energy as input, which is complex to measure experimentally. The aim of the mixed mode studies is to have a model, which can be implemented into a commercial finite element program. Another demand is the possibility to suply the model with constitutive parameters obtained in experiments. Therefore, the model used in this thesis, based on a model first presented by Wernersson (1994), is easy to correlate with data obtained in experiments. The finite element implementation of the model is described in (Walter et al. 2005), whereas *Paper I* gives a review of the model along with experimental studies. The implementation of the model in a commercial FE code DIANA (2003) has been carried out, and is aimed at fracture mechanical studies on the structural level.

2.2.1   Mixed Mode Model

When discussing mixed mode cracking in Linear Elastic Fracture Mechanics (LEFM), a common parameter is the so-called phase angle ψ_k, as a function of Mode I and II stress intensity factors K_I and K_{II}

$$\psi_k = arctan\left(\frac{K_{II}}{K_I}\right) \tag{2.1}$$

which is directly related to the stress state at the vicinity of the crack tip. Materials have been classified by He et al. (1990) using the phase angle. He related the phase angle to the total critical energy release rate, G_c, which shows two typical behaviors, which can define the difference between ductile and brittle materials. It is stated that for brittle materials

the energy release rate increases significantly for increasing phase angle ψ_k, which means that it is weaker in Mode I than II. Concrete may be considered as a quasi-brittle material compared to e.g. steel. The ratio between the critical energy release rates in Mode I and II, G_{IIc}/G_{Ic}, has for concrete been measured larger than 1 and in some cases around 5, see e.g. Carpenteri & Swartz (1991).

A stress intensity based failure criterion, was suggested by Wu (1967) in the form:

$$\left(\frac{K_I}{K_{Ic}}\right)^m + \left(\frac{K_{II}}{K_{IIc}}\right)^n \leq 1.0 \tag{2.2}$$

where the exponents m and n are material constants. By using the present failure criterion it is possible to define a failure criterion based on the state of stress, e.g. the combination of normal and shear stress. Carpenteri & Swartz (1991) utilized studies using the present failure criterion on concrete. However, a theory based on LEFM is not applicable in the case of concrete due to its large fracture process zone, cf. Peterson (1981).

The aim of the mixed mode studies in the present thesis is to obtain experimental data and implement them into a numerical model. Fracture behavior of a steel-concrete interface can be characterized as a discrete process, and the following model is targeted at a standard FE interface element. Configuration of a standard two-dimensional interface element is shown in Figure 2.4.
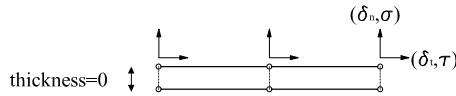
Figure 2.4 A three node interface element and node stresses and displacements.

where σ and τ, are the normal and shear stresses, respectively, acting across the interface. The crack opening in normal and tangential direction are expressed by δ_n and δ_t, respectively. The 2-D relationship between the gradients of stress and crack opening in the normal and tangential direction is given by:

$$\begin{bmatrix} \dot{\sigma} \\ \dot{\tau} \end{bmatrix} = \begin{bmatrix} D_{11} & D_{12} \\ D_{21} & D_{22} \end{bmatrix} \begin{bmatrix} \dot{\delta_n} \\ \dot{\delta_t} \end{bmatrix} \tag{2.3}$$

The D_{ij} components describe the relation between gradients of stress and crack displacements. In pure elastic mode, no coupling is assumed between normal and shear mode and the off-diagonal terms are set to zero, $D_{12} = D_{21} = 0$. Furthermore, the diagonal elements D_{11} and D_{22}, are assigned large values in the elastic state to model continuous geometry. After peak stress, it is important to couple the two crack modes, Mode I and II. The situation where the off-diagonal terms are set to zero is equal to a situation with two independent springs.

The coupling, after peak stress, is based on two given curves in pure Mode I and II, cf. Figure 2.5.

Figure 2.5 *Curves in pure Mode I and II. Until peak stress linear elasticity is assumed.*

The coupling between the pure Mode I and II curves, the current stresses (σ, τ), and crack deformations (δ_n, δ_t), can be found assuming the following criteria:

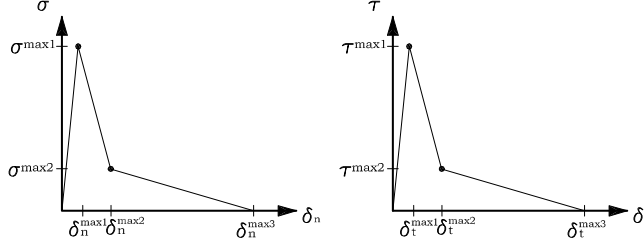$$\left(\frac{\delta_n^k}{\delta_n^{max\ k}}\right)^m + \left(\frac{\delta_t^k}{\delta_t^{max\ k}}\right)^n = 1.0 \tag{2.4}$$

$$\sigma^k = \delta_n^k \frac{\sigma^{max\ k}}{\delta_n^{max\ k}} \tag{2.5}$$

$$\tau^k = \delta_t^k \frac{\tau^{max\ k}}{\delta_t^{max\ k}} \tag{2.6}$$

where n and m are material constants. The kink points on the pure Mode I and II curves (e.g. (σ^{max1}, δ_n^{max1}) with (τ^{max1}, δ_t^{max1})) are linked using Equations (2.4)-(2.6). Thus, for any given mixed mode combination, the current stresses can be found using linear interpolation. Equation (2.4) can be plotted in a $\delta_n - \delta_t$ space, cf. Figure 2.6(a). An example on how the coupling affects the σ-δ_n curve, is shown in Figure 2.6(b). As observed, two crack paths are considered, which can be defined by their mixed mode angle ψ. The crack path with a mixed mode angle ψ_1, is Mode I dominated compared to the crack path defined by mixed mode angle ψ_2. As a result, the σ-δ_n curve diminish for increased mixed mode angle, whereas the τ-δ_t curve (not shown) expands for increasing mixed mode angle. From Figure 2.6, it is furthermore observed, that a mixed mode angle of 90^0 results in a situation where the Mode I contribution is equal to zero and a the Mode II contribution is equal to the pure Mode II curve. Decreasing the mixed mode angle results in a situation where the Mode II contribution diminishes and the Mode I contribution increases. When the mixed mode angle reaches 0^0 the Mode II contribution is zero and the Mode I contribution is equal to the pure Mode I curve. From the constructed surfaces $\sigma(\delta_n, \delta_t)$ and $\tau(\delta_n, \delta_t)$, it is now possible, via differentiation, to determine the D_{ij} elements in Equation 2.3.

Dilation effects are not considered in the present mixed mode formulation. In the present application it is assumed that the effect of dilation is negligible, since interface cracks are characterized by low surface roughness and Mode I dominated crack growth.
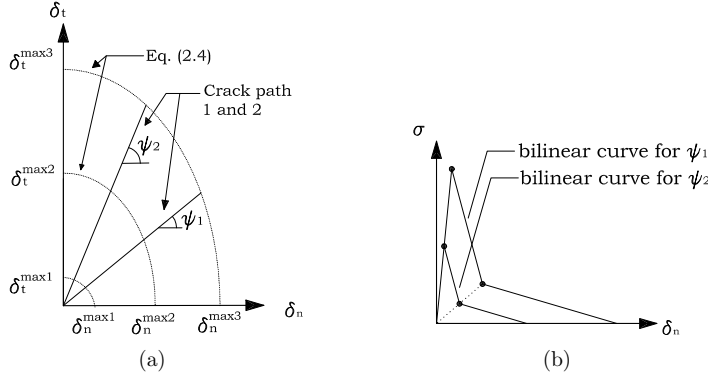
Figure 2.6 *(a) Consider two crack paths in the δ_t-δ_n space, their (b) corresponding bilinear curve, e.g. the $\sigma - \delta_n$ curve, changes as a function of the mixed mode angle ψ.*
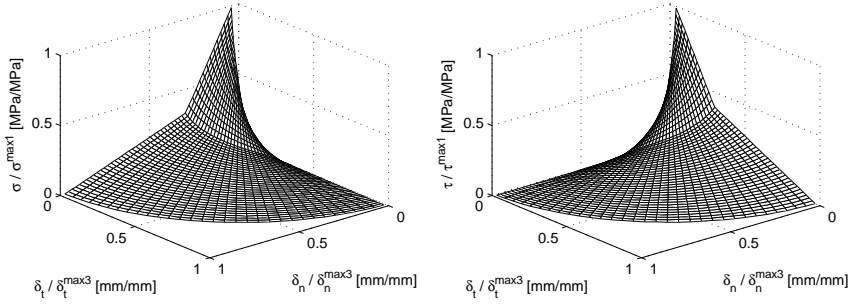
Figure 2.7 *Model visualization, for the case m=n=2 using bilinear softening relationships in pure Mode I and II. (a) Variation of the normal stress σ with respect to the normal and tangential displacements across the crack. (b) Variation of the shear stress τ with respect to the normal and tangential displacements across the crack.*

The interface response can also be visualized in a 3D surface. The visualization is carried out in terms of a stress surface in a displacement space e.g. σ versus the normal and tangential crack openings, cf. Figure 2.7(a). Two curves, in pure Mode I and II, are given as input along with a value of the material constants, $m = n = 2$. The surface plot shows the amount of normalized normal stress σ, the z-axis, for various values of normal crack-opening δ_n and tangential crack opening δ_t. As observed in the figure, in pure Mode I deformation, when $\delta_t = 0$, a full bilinear response $\sigma - \delta_n$ is observed, which

is equivalent to the pure Mode I curve given as input. As the tangential crack opening is increased, the response on the normal stress diminishes to a minimum. Along with the normal stress response, a diagram in Figure 2.7(b) displays the response of the shear stress τ. It is clearly seen that the shear stress response is affected oppositely of the case of normal stress.

2.2.2   Mixed Mode Experiments

In order to obtain experimental data for the mixed mode model, a set-up has been developed. Full stress displacement curves from different mixed mode angles have to be collected and combined in accordance with the criterion in Equation (2.4). A simple test set-up, developed for a uniaxial testing machine, is presented here. The idea is to have a steel block with a plane rotated with a certain angle α, cf. Figure 2.8.
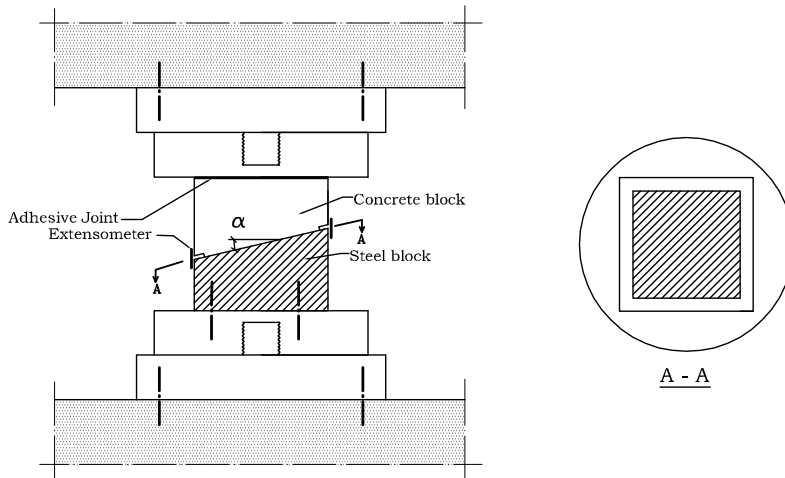
Figure 2.8 *Schematic representation of the set-up to test an interface exposed to mixed mode loading. Only Mode I loading and displacement are recorded during the experiment.*

As observed in the figure, by varying the inclination angle α, it is possible to test the steel-concrete interface exposed to different mixed mode combinations of normal and shear stress. The experiment is carried out by gluing the concrete part to the top part of the loading device using a fast curing polymer. An important parameter, in order to carry out a stable test, is the stiffness of the system. Insufficient stiffness causes the two parts, the steel and concrete part, to rotate with respect to each other, producing non-physical experimental data. This phenomenon was first described by Hillerborg (1989). As the rotational stiffness of the set-up is of crucial importance the proposed set-up is not capable of testing steel-concrete interfaces for large mixed mode angles. As the inclination angle α of the specimen increases, the specimen becomes long and slender and consequently

very flexible, and hence unsuitable for testing. In the present study, the stiffness has been measured for the specific set-up and the maximum testing angle α was found to be 30 degrees.

A test program to obtain constitutive parameters for the mixed mode model was performed. A total number of nine specimens, three for each of the mixed mode angles 0^0, 15^0, and 30^0, were tested. A two step inverse analysis to couple the experiments in the $\delta_n - \delta_t$ space, was established. First step is to translate each experiment into a bilinear stress-crack opening relationship (for Mode I) and a bilinear stress-crack tangential opening (for Mode II). This is shown for an experiment on a test with $\alpha=30^0$, in Figure 2.9.
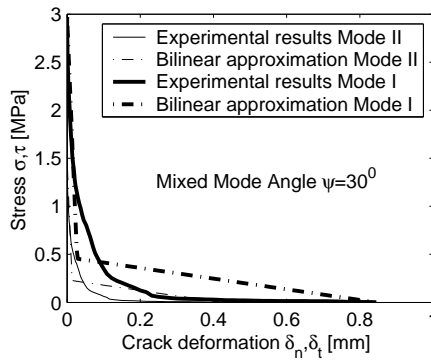
Figure 2.9 *Example on experimental data from a test with $\alpha = 30^0$ and the approximation of two bilinear curves in Mode I and II.*

As displayed in Figure 2.9, an experiment on a specimen with an inclination angle of 30^0 produces a larger Mode I response compared to the Mode II response. The translation of the experimental data into a bilinear shape makes later numerical interpretation simple. The final step in the inverse analysis is to couple the bilinear curves obtained in the $\delta_n - \delta_t$ and $\sigma - \tau$ space. The kink points in the bilinear curves are coupled according to Equation (2.4). When applying a bilinear shape, a total number of 4 kink points need to be coupled. Two stress kink points need to be coupled in the $\sigma - \tau$ space, and two crack deformation kink points need to be coupled in the $\delta_n - \delta_t$ space. Coupling of the stress kink points are shown in Figure 2.10(a)-(b), and coupling of the deformation kink points are shown in Figure 2.11(a)-(b).

As observed in the figures, coupling of the experimental data is possible and acceptable. However, a large amount of scatter is present for the kink points in the deformation measurements, Figure 2.11(a), though the scale of the deformations has to be considered when comparing to the deformations in Figure 2.11(b).

It should be noted that only reliable results are obtained from experiments on low mixed

mode angles, and via extrapolation of these, it is possible to derive the pure Mode II curve. The final results, which can be given as input in the constitutive model are: (i) a pure Mode I and II curve, and (ii) exponents m and n for use in the failure criterion (Equation (2.4)). The values of the pure Mode I and II curves are shown in Table 2.1.

Mode I n-direction	σ^{max1} [MPa]	σ^{max2} [MPa]	δ_n^{max2} [mm]	δ_n^{max3} [mm]	G_f [n/mm]
Mode I n-direction	3.0	0.4	0.02	0.5	0.12
Mode II t-direction	τ^{max1} [MPa]	τ^{max2} [MPa]	δ_t^{max2} [mm]	δ_t^{max3} [mm]	G_f [n/mm]
Mode II t-direction	3.5	0.5	0.02	0.77	0.23

Table 2.1 *Pure Mode I and II parameters (Figure 2.5), obtained in the inverse analysis.*

The results in Table 2.1 are found for the exponents $m = n = 2$. Optimization of the exponents can not be justified on the small amount of data available and has not been utilized in the present study. The two curves are found as two bilinear curves where a_1 and a_2 are the slopes of the two line segments and b_2 is the cross point of the second line segment and the normalized stress axis (y-axis).

Since data has solely been collected for low mixed mode angles, extrapolated data for high mixed mode angles is less reliable. The ideal case, and a major improvement of the data collected, is to carry out tests using a biaxial testing machine capable of changing the ratio of shear and normal deformation. Then by testing different mixed mode angles a full set of stress deformation curves in a mixed mode angle range from 0^0 to 90^0 could be collected.
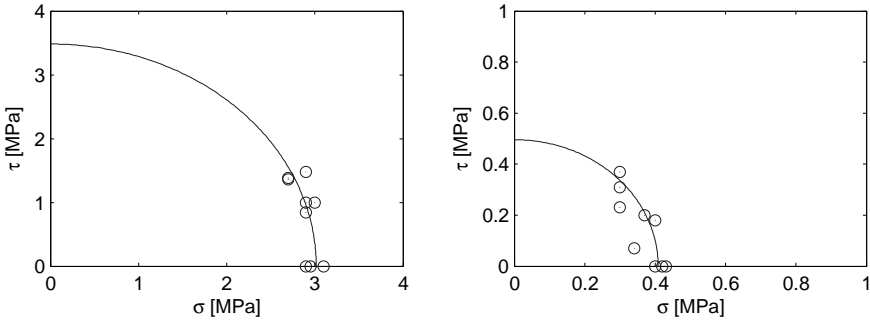

Figure 2.10 *(a) Plot of coupling stress kink points, $(\sigma^{max1}, \tau^{max1})$ (b) Plot of coupling stress kink points, $(\sigma^{max2}, \tau^{max2})$.*
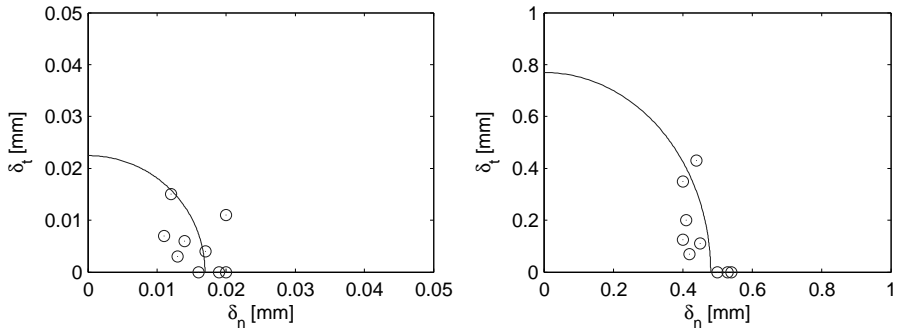
Figure 2.11 *(a) Plot of coupling crack deformation kink points, $(\delta_n^{max2}, \delta_t^{max2})$ (b) Plot of coupling crack deformation kink points, $(\delta_n^{max3}, \delta_t^{max3})$.*

Chapter 3

Composite Elements

An important issue in the cement-based overlay system for stiffening orthotropic steel bridge decks, is cracking of the overlay. The composite strength of the system is closely related to cracking of the overlay, and subsequently cracking of the steel-concrete interface (debonding). Penetration of a vertical crack in the overlay, might for a certain crack width, initiate large stresses at the interface. Increased interfacial stresses will consequently lead to debonding. Using numerical tools can help identifying important parameters, which influence the performance, with regards to cracking of a steel deck stiffened with a cement-based overlay. Through testing and numerical simulations it might be possible to identify the significance of overlay and interface cracking in relation to the composite behavior. The major outcome of *Paper V* is a number of numerical parametric studies on different constitutive parameters of the overlay and interface with regards to the composite behavior between a cement-based overlay and steel plate. Both *Paper III* and *Paper IV* contains numerical and experimental studies of overlay fracture. In the present chapter, a short overview is given on numerical and experimental studies on small composite elements. The reader is referred to the appended papers for a review in greater details.

3.1 Numerical Studies on Composite Beams

The composite behavior between the overlay and a the steel plate can be analyzed using a simple three point bending test. Consider a composite beam exposed to negative bending as shown in Figure 3.1. The composite beam is viewed as the very top part of the bridge deck, turned up-side down for convenience. Cracking and debonding can be analyzed as discrete processes, vertical cracking in the overlay and horizontal cracking at the interface, respectively.

Loading of the composite beam will at some point cause cracking of the overlay as the overlay reaches its tensile strength. As the vertical crack propagates through the overlay, its crack front will at some stage be opposed by the steel plate. The opposition of the steel plate will lead to an increase of normal stress in the plane perpendicular to the vertical crack tip, i.e. in the plane of the steel concrete interface. The increase in horizontal stresses is likely to introduce cracking of the steel-concrete interface. This situation can be analyzed using finite elements. Consider a close up look of the part where the overlay
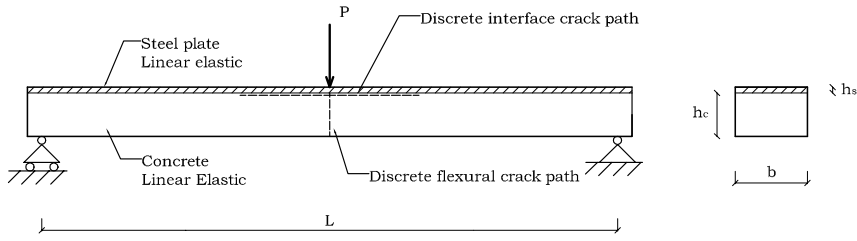
Figure 3.1 *Three point bending set-up: simulating a negative bending moment in a bridge deck.*

crack initiates as sketched in Figure 3.2(a). Two situations are analyzed: (i) an overlay Crack Mouth Opening Displacement (CMOD) of 0 mm, and (ii) an overlay crack opening of 0.03 mm. The shear and normal stress can be plotted along the interface to analyze the problem, cf. Figure 3.2(b).

(a)   (b)
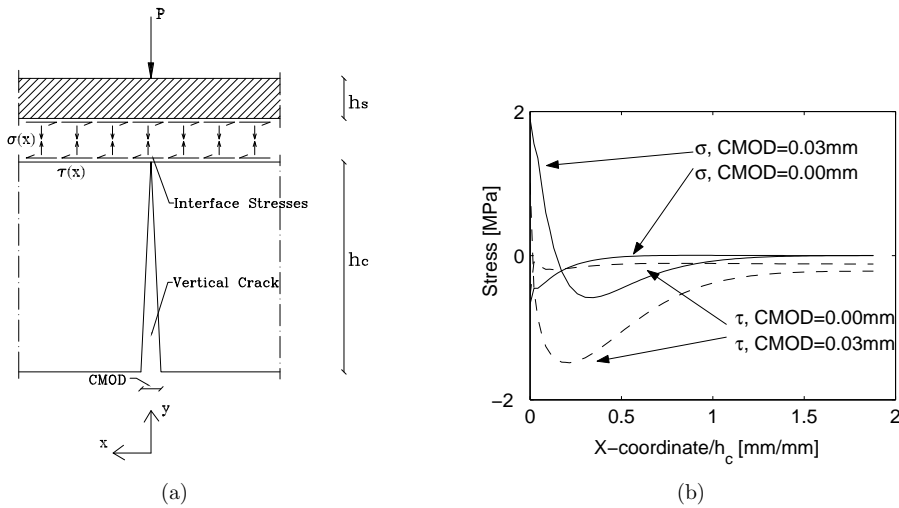
Figure 3.2 *Stress distribution along the interface for a CMOD value of zero and 0.03 mm. (a) Interfacial forces and configuration. (b) Stress distribution along the interface versus the x-coordinate normalized with the concrete height h_c. Dashed lines represent shear stress τ and solid line represent the normal stress σ.*

The first situation corresponds to a sound overlay with no cracking, whereas the second situation corresponds to the initiation of a small overlay crack. The interfacial stresses (normal, σ, and shear, τ) can be plotted in a stress vs. x-coordinate diagram ($x = 0$ is the location of the vertical overlay crack). It is observed from Figure 3.2(b), that the interfacial stresses change dramatically for an increase of crack opening from 0 to 0.03 mm. The normal stresses change from compression to tension, which in many cases are

critical for a concrete-steel interface.

The debonding behavior can also be studied in terms of the overlay fracture energy. Increasing the toughness of the overlay does not necessarily eliminate the effects of debonding. This is shown in a FE study on a composite beam with three different overlay materials (denoted A1, A2 and A3). Each of the materials considered posses a different fracture energy, G_f. The global behavior in terms of load versus crack mouth opening, is displayed, cf. Figure 3.3(a).
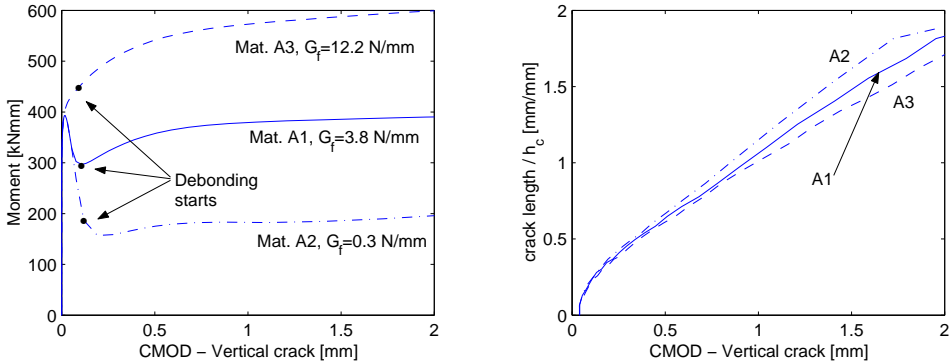
Figure 3.3 *Graphical representation of three hypothetical cases: —A1, -.-. A2, - - - A3. (a) The bending moment $M = PL/4$ versus the crack opening of the vertical crack - CMOD. (b) The interface crack length normalized with respect to the overlay height h_c versus CMOD.*

Debonding starts approximately for the same vertical crack opening (CMOD) for each of the materials A1-A3. However, for the material with the largest amount of fracture energy A3, debonding initiates for a higher load level. Additionally, the debonding crack length can be plotted as a function of the crack opening of the vertical crack (CMOD). This is illustrated in Figure 3.3(b). This clearly illustrates that the fracture energy of the overlay hardly influences the relation between CMOD and the length of the interfacial crack.

3.2   Test Methods to Obtain Constitutive Parameters of Overlay

An important issue in the investigation of the cement-based overlay as a stiffening system to steel bridge decks are constitutive parameters. Standard test methods can be used, if available, to characterize materials used in experimental investigations on composite elements.

The well-known advantage of fiber reinforced concrete is its ability to sustain larger deformation after the first crack is formed. The fibers will typically stay unbroken after crack initiation and the fibers that cross a crack will resist further opening. Depending on the so-called *crack bridging effect*, fiber reinforced composites can show different failure

modes. If the fiber bridging effect is increasing during crack initiation and propagation, multiple cracks can form. This behavior is also known as strain hardening behavior. On the other hand, if the fibers cannot carry more load after the formation of the first crack, then further deformation is characterized by opening of a single crack. This behavior is in terms called tension softening. Experimental tests to obtain constitutive parameters for both strain hardening and tension softening materials is an important issue with regards to fracture mechanical modeling. To model cracking in the overlay, constitutive parameters are important, and should reflect the material behavior observed in experiments. In this study, tension softening and strain hardening materials are analyzed as overlay material. In the case of tension softening materials, well established test methods are at hand, see e.g. (RILEM 2000) or (RILEM 2001). Furthermore, Østergaard (2003) made a full review and has compared standard test methods for tension softening materials. In the case of strain hardening materials, little or no work has been performed so far to establish a standard test method. *Paper VI* contributes to the work in the field of a test method to achieve the constitutive strain hardening parameters, using a four-point bending set-up.

3.3   Verification of Numerical Modeling Tools

Experimental tests on composite beams using both tension softening and strain hardening materials have been performed. Numerical tools applied in this thesis are verified experimentally in *Paper III*, by comparing the modeling work to experimental data. Previous experimental studies have been carried out on beams reinforced with concrete overlays. Early studies by Silfwerbrand (1984), show results from tests on concrete beams with concrete overlays. More recently, studies by Granju (1996), investigate the influence of fibers in cement-based overlays. *Paper III* contributes to these studies, and the major outcome of this paper is the treatment of the significant influence of overlay defects and their relationship to debonding.

Three different fiber reinforced composites have been tested as overlay material. Two tension softening materials: Fibre Reinforced Concrete (FRC), and Fibre Reinforced Densit®(FRD), as well as one strain hardening material, known as Engineered Cementitious Composites (ECC). The significant findings in this study are the experimental and numerical investigations of macro crack formation in the overlay and its influence on debonding. Furthermore, the verification of the numerical modeling work is carried out by comparing FE results with experimental data. Two experimental set-ups, one for FRC and FRD beams, cf. Figure 3.4, and one for ECC beams, cf. Figure 3.5, have been proposed. The experimental set-ups applied, have been utilized as the primary set-up to test tension softening and strain hardening materials in composite with steel.

The general experimental results of a test program is displayed in Figure 3.6. In the figure, tests on FRC, FRD, and ECC composite beams are shown in a load vs. displacement diagram. As observed, the composite beam with the ECC material exhibits a larger load bearing capacity compared to FRC and FRD. Additionally, a second y-axis shows the measured debonding signal. This shows clearly the significance of macro cracks and their
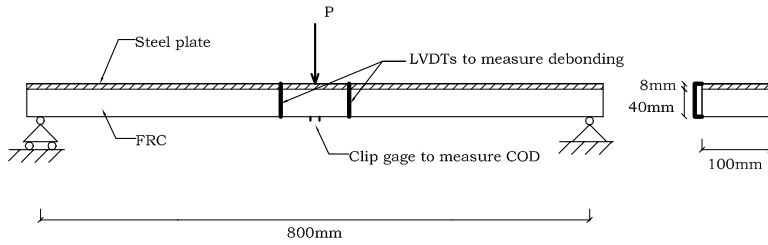
Figure 3.4 *Experimental set-up for FRD and FRC composite beams. Since a single crack is formed at midspan a clip gauge is placed to measure the crack opening displacement (COD). The test set-up simulates a part of a stiffening overlay cast on a steel bridge deck loaded in negative bending.*
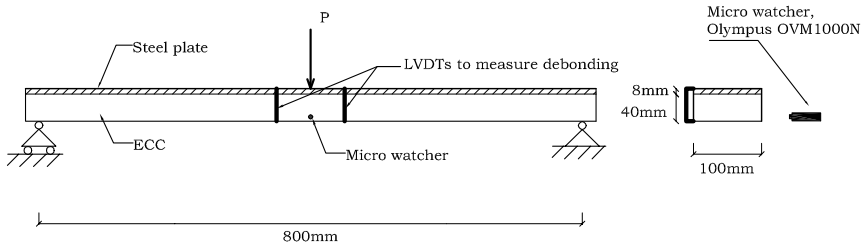
Figure 3.5 *Experimental set-up for ECC composite beams, the crack width of the overlay cracks are monitored and debonding is measured. The test set-up simulates a part of a stiffening overlay cast on a steel bridge deck loaded in negative bending.*
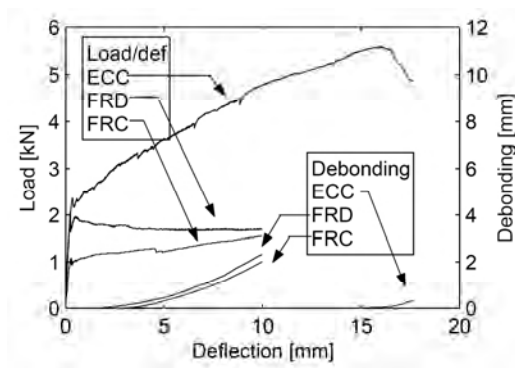
Figure 3.6 *Results from three representative tests of composite beams with FRD, FRC and ECC overlay materials. Result are plotted in a load versus displacement diagram with a second y-axis showing the corresponding debonding.*

initiation of debonding. The two tension softening materials, FRC and FRD, form one single crack and for deflection values of 2-3 mm, debonding is observed. The FRD material, which has a much stronger matrix than FRC, initiates debonding for approximately for the same deflection value as for the FRC material. This concludes, that the governing mechanism for debonding is the magnitude of the crack width, also evident by numerical studies as showed in the previous section. Furthermore, observing the experimental data of the ECC composite beam, debonding initiates for a large beam deflection value compared to FRC and FRD. This is due to the fact that the ECC composite beam behavior is characterized by multiple cracking. The largest crack width, before localization in the ECC beam, was measured using a micro camera in the range of 100 micron. In comparison, crack openings of the discrete crack in the FRD and FRC tests, had a value in the range of 0.1 to 0.2 mm at debond initiation. It should be noted that when comparing these crack openings to the numerical crack opening in the previous section, debonding was measured 50 mm from the point where the vertical crack propagates. For a more complete and detailed review of the experimental set-up, and how debonding is measured, the reader is referred to *Paper III*.

The numerical tools applied using the finite element method has been verified comparing numerical results with experimental results. The comparisons are shown in Figures 3.7(a)-(b) and 3.8. As observed in the figures, the numerical results correlate well with the experimental data. It should be noted that for the FRC and FRD beams, the comparisons are shown in a load vs. Crack Opening Displacement (COD). When using numerical tools, it is possible to extract more information on the composite beam behavior than might be possible in the experiments. In the present case, it is possible via the numerical calculation to extract information on the deformation state in the steel plate. As very large deformations are achieved, yielding of the steel plate starts (marked in Figure 3.8), before a macro crack localizes in the ECC composite beam.

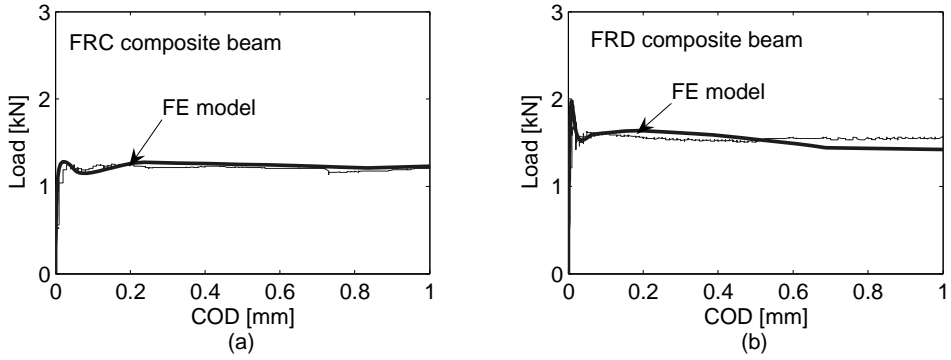Figure 3.7 *Comparison between experimental and numerical results. (a), and (b) show comparison between numerical and experimental results for a FRC, and FRD composite beam test, respectively.*
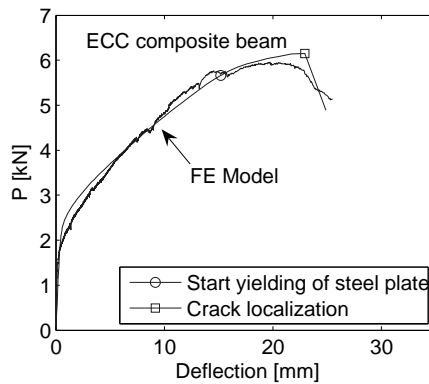

Figure 3.8 *Comparison between experimental and numerical results for an ECC composite beam test.*

3.4   Testing of Composite Plates

In addition to the two-dimensional composite beam tests in negative bending, testing of full three-dimensional composite plates have been performed. The primary set-up is a double-cantilever plate subjected to negative bending. The plate had the dimensions 1 m x 2 m and an overlay thickness of 50 mm and a steel plate thickness of 8 mm. To ensure an interfacial bond between the overlay and steel plate, the steel surface was sand blasted prior to casting of the overlay. A test program of three composite plates were carried out, each cast in separate batches. A self-compacting steel fiber reinforced concrete comprised of 1 % by volume hooked-end steel fibers was used. Fibres were placed in random orientation along with standard matrix components, cement, fly ash, micro silica, water and aggregates with a maximum diameter of 16 mm. To improve the fresh properties of the mixture super-plasticizer was added. Mechanical properties of the material were determined using the RILEM standard three-point bending test (RILEM 2000). The average ultimate tensile strength was determined to be 4.6 MPa. Furthermore, the ultimate average compressive strength, determined using cylindrical specimens, was 47 MPa.

To test the composite plate in negative bending, a set-up is used where the middle part of the plate is placed on a fixed line support allowing rotation. Figure 3.9 shows the idea of having a fixed and a free edge and a single load point P.

In order to test for different negative moment distribution, the set-up allows changing the eccentricity of the load, denoted ξ. Furthermore, the set-up also allows testing for different combinations between interfacial shear stresses and a negative bending moment. The actual set-up is depicted in Figure 3.9(b). The middle part of the specimen with the dimensions 1 m x 2 m is placed on a line support. A stiff crossbeam was used to apply a force P on each side of the line support. To ensure a stable set-up, the crossbeam is supported using a spring on each side. To check the applicability of equal load on each side of the composite plate, the elongation of the springs were monitored throughout each experiment.

The experiment is conducted with a 200 kN hydraulic testing actuator placed on the crossbeam. The crossbeam distributes the total load $2P$ from the hydraulic actuator into two load points P, acting on approximately 0.1 m x 0.1 m area on the concrete side of the plate. To obtain an even reaction force on the line support, a soft material was laid between the specimen and line support. The test was manually force-controlled, i.e. open-loop controlled. During the experiment, the deflection was recorded at the free edge in the line of the point load, using LVDTs.

Applying a point load P creates a bending moment along the clamped edge of the composite plate. The magnitude and distribution of the negative bending moment can be calculated in an elastic manner, using an analytical solution by Gere & Timoshenko (1999). The distribution of the elastic bending moment along the clamped edge is illustrated in Figure 3.10. The magnitude of the bending moment is given as a ratio between the moment and the point load. The maximum bending moment along the clamped edge
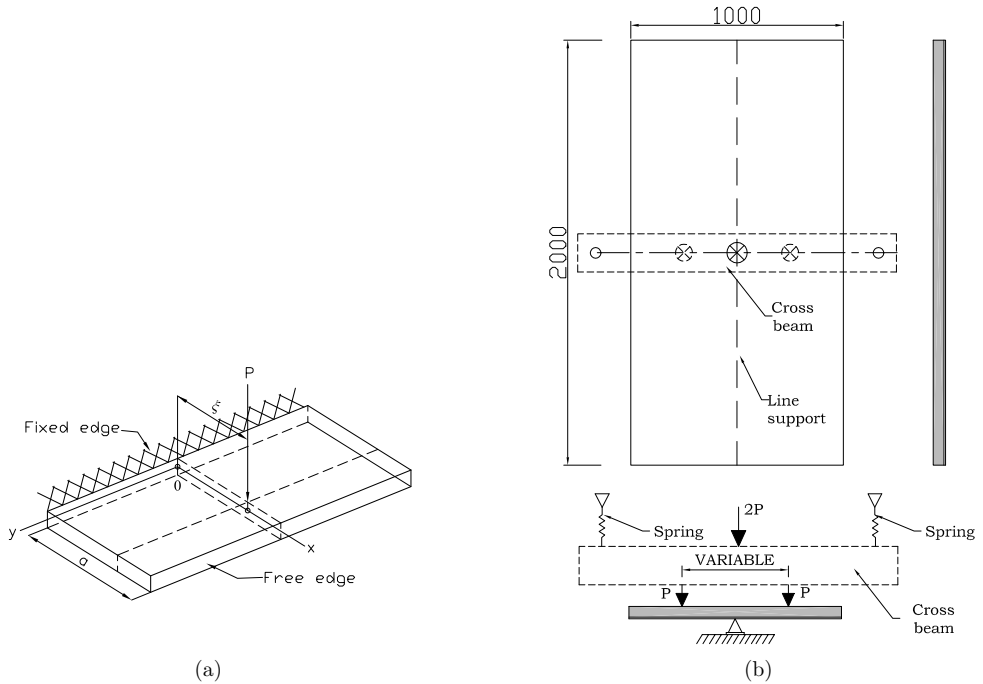
Figure 3.9 *Experimental set-up. (a) Concept of experimental set-up, half composite plate is subjected to a load point P with an eccentricity of ξ. (b) Experimental set-up in details, the composite plate is loaded using a double cantilever plate, the cross beam applies the two load points on each half of the composite plate.*

(i.e. $y/a=0$) can be obtained for different ratios between the load eccentricity ξ and length a.

The three composite plates used in the test program, each had a different eccentricity as summarized in Table 3.1. For each test the maximum elastic bending moment has been calculated as a function of the point load P according to the concept in Figure 3.10.

The results are presented graphically in two ways, cf. Figure 3.11. The magnitude of the point load P is plotted versus the maximum deflection, measured at the free edge on the load line, Figure 3.11(a). Furthermore, each test is also presented in a maximum elastic bending moment versus deflection diagram, cf. Figure 3.11(b).

All the tests showed a good and acceptable load bearing capacity and good ductility in the nonlinear deformation range. For the eccentricities tested, the composite plate did not have any problems sustaining the interfacial shear stresses between the overlay and steel plate. Visible cracks, along the clamped support, were observed during testing. Cracks formed, in all test series, for a load magnitude close to the threshold part of the load deflection diagram. Total failure of the composite plates are characterized by
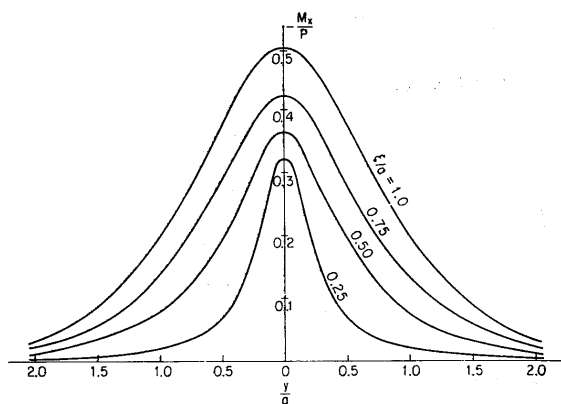
Figure 3.10 *The distribution of elastic bending moments along the clamped edge for various ratios of the plate width a and load eccentricity ξ, after Timoshenko (1999).*

Test No.	Eccentricity ξ [mm]	ξ/a [mm/mm]	M [Nmm/mm]
1	300	0.300	$0.33P$
2	250	0.250	$0.32P$
3	200	0.200	$0.30P$

Table 3.1 *The eccentricity and maximum elastic bending moment M for each test.*

the formation of a major crack along the clamped support, which eventually leads to debonding between the fiber reinforced overlay and underlying steel plate. Formation of a macro crack along the clamped support initiates normal tensile stresses at the interface between the steel plate and overlay. Tensile stresses are in many cases severe for interfacial bond, but in the elastic state, the normal stresses at the interface are compressive.

Numerical simulation of the set-up and comparison to tests results are found in (Sigurdsson 2003). The conclusion upon the numerical investigations is a good agreement between experimental and numerical results. Similar modeling concepts were applied as described in appended papers and in previous section for composite beam elements.
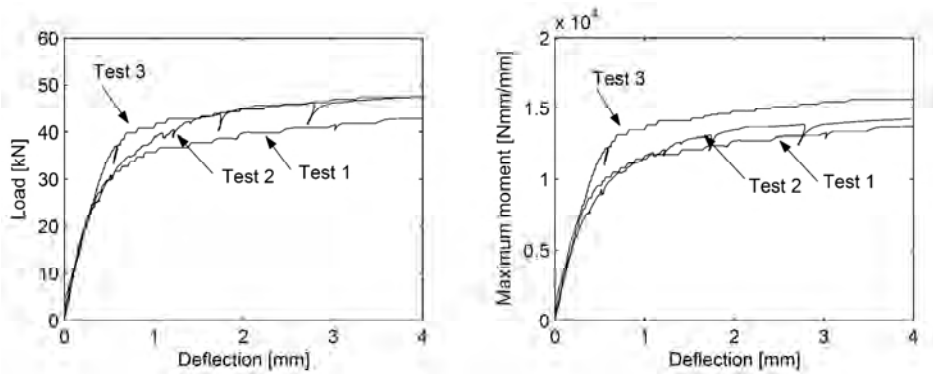
Figure 3.11 *Experimental results from each of the three tests. (a) Graphical representation of the three tests in a load-deflection diagram. (b) The same results plotted as maximum elastic bending moment vs. deflection. The maximum elastic bending moments is calculated using the concepts by Timoshenko (1999).*

Chapter 4

Structural Behavior

The main purpose of the cement-based overlay is to stiffen the underlying orthotropic steel bridge deck. The durability of the cement-based overlay is influenced by cracking of the overlay and cracking between the overlay and steel deck (debonding). Both cracking of the overlay and debonding can reduce the composite action between the steel deck and overlay. In a design situation numerous effects, which can cause overlay cracking, have to be taken into account. Apart from mechanical loading such as traffic, environmental loading can have considerable influence on the overlay and its composite behavior with the steel deck. Especially, shrinkage and temperature gradients have to be taken into account. *Paper VII* is a purely numerical paper looking at a part of an orthotropic steel bridge deck, using results from papers I-IV. The overlay system is investigated, for realistic purposes, on an existing bridge. The Farø Bridges, located in southern Denmark linking Copenhagen to the European Continent, are analyzed. The Farø Bridges were build between 1980 and 1985, and their orthotropic steel bridge decks are a part of a steel box girder, which span 80 m, cf. Figure 4.1 for a cross-sectional view of the girder.
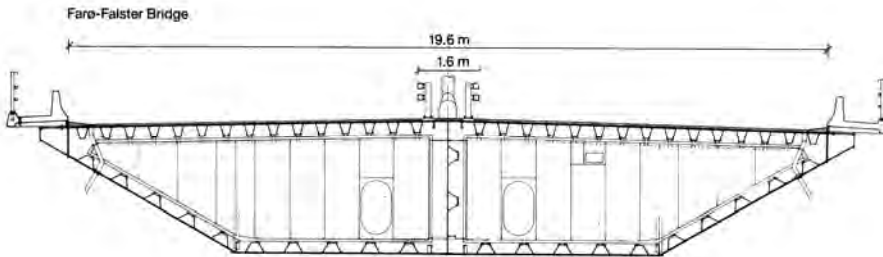
Figure 4.1 *Cross-sectional view of steel girder on the Farø Bridges.*

The bridge deck is designed with a 12 mm deck plate with trapezoidal ribs with a thickness of 6 mm. The ribs are 300 mm high and placed with a center distance of 620 mm. The main goal of the study is to analyze the performance of the overlay system in a real size structure. In the steel box girder design, a number of bulkheads are placed every 4

meters, cf. Figure 4.2. The bridge deck section close to the transverse bulkheads is of special concern since the overlay is subject to tension due to a negative bending moment.
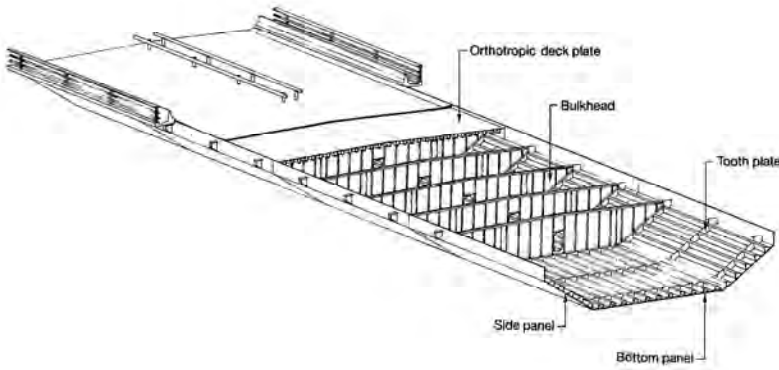
Figure 4.2 *Box girder, structural principle. Bulkheads every 4 m.*

Studies on the performance of the overlay system are based on nonlinear fracture mechanics utilized using finite elements. Global effects, such as traffic and dead load, are taken into account. Emphasis is put on the situation where the cement-based overlay is exposed to maximum negative bending, which is considered to be the most critical situation. A local model of 3.9 times 8 meters, has been modeled in three dimensions using the software package DIANA (2003). The applied mesh is shown in Figure 4.3.

As illustrated, in addition to the orthotropic steel deck plate, a part of the bulkhead is modeled as well. The steel and overlay parts have been modeled using standard 20-node solid elements. The connection between the overlay and underlying steel deck has been modeled using an 8-node interface element. The constitutive formulation of the interface is based on the mixed mode model as described in Chapter 2. The model presented in Chapter 2 was presented in a two-dimensional configuration, however in the present case a three-dimensional formulation is needed. The applied three dimensional formulation is presented in details in *Paper VII*. Furthermore, global bending moments and shear forces are found by using simple two-dimensional beam models. The exterior effects from traffic and dead load is then applied as boundary conditions. The magnitude of traffic load has been chosen according to ENV 1991-3 (1991).

4.1 Linear Elastic Studies

Lack of transverse bending stiffness is one of the main problems causing fatigue in traditional orthotropic steel bridge decks. Concentrated wheel loads induce considerable transverse bending moments, which are critical to the connection between the steel plate and rib. Consider a load system of a double-axle tandem with an axle load of 260 kN
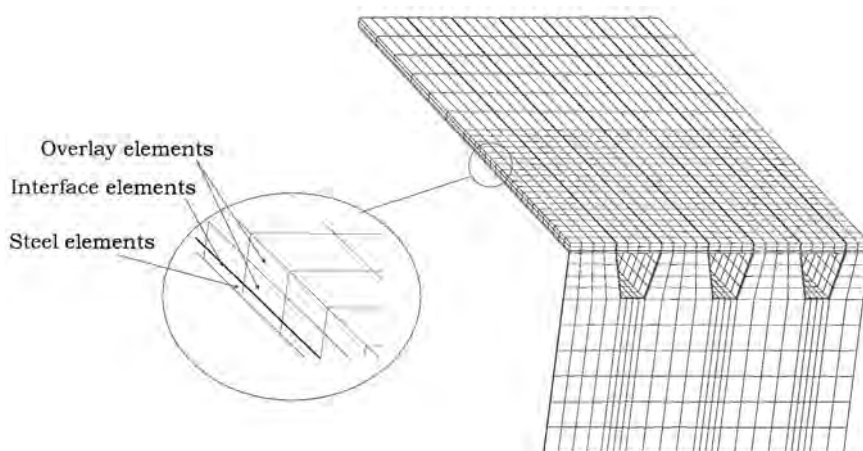
Figure 4.3 *Applied finite element mesh of the deck part. To model steel and overlay a solid 20-node element is used. The connection between the overlay and steel plate is modeled using an 8-node interface element.*

together with global traffic and dead load. Figure 4.4, shows a deformation plot of a steel bridge deck (no overlay) exposed to the given loading system.

(a)   (b)
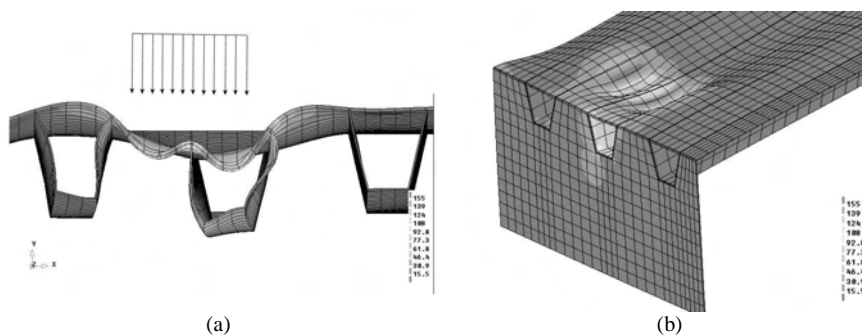
Figure 4.4 *Result from linear elastic FE calculations. (a) Wheel load causing transverse bending. (b) Three dimensional view of deformation caused by wheel load.*

The figure illustrates the transverse deformations induced by a concentrated wheel load, which gives rise to high stresses in the intersection between the steel plate and rib. The benefits of the overlay system contra upgrading the steel deck by increasing the steel plate thickness, can be shown through a parametric study. The parametric study investigates the influence of: (i) different steel plate heights, and (ii) different overlay height for a steel deck thickness of 12 mm. In the study, full composite action is considered, thus no

cracking of the overlay is modeled. The focus in the study is the maximum von Mises stress in the intersection between the steel plate and rib. The results from the linear elastic study is presented in Figure 4.5.
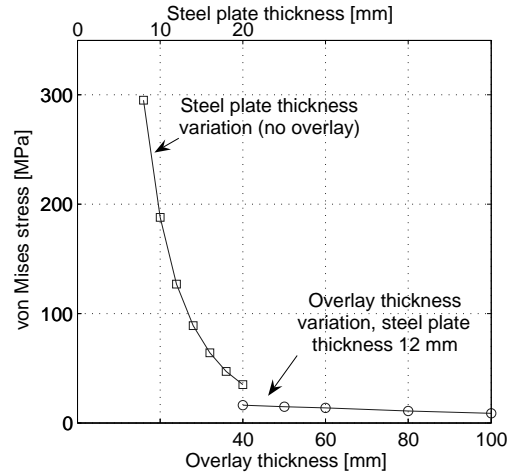
Figure 4.5 *Result of linear elastic studies for traffic and an axle load of 260 kN. The left most line represents the von Mises stress of different steel plate thicknesses without an overlay. The other line represents results from a steel plate of 12 mm and different overlay thicknesses.*

The graph shows the maximum von Mises stress in the intersection between the steel plate and rib for different orthotropic deck geometries. The first parametric study investigates a steel deck without any overlay. In this study, the geometry of the Farø Bridge is applied, and the only modification to the original design is changing of the steel plate thickness. As observed in Figure 4.5, the von Mises stress has been calculated for steel plate thicknesses of 8, 12, 14, 18, and 20 mm. In the second parametric study, von Mises stresses have been calculated in the similar connection, where the only modification to the original design is different overlay thicknesses. The results show a reduction of the von Mises stresses for increasing steel plate thickness. For an 8 mm plate the von Mises stress is around 200 MPa, while for a 20 mm plate, it is reduced to around 25 MPa. However, comparing the stress level to that of the overlay system, it is observed that even applying a thin overlay cause a significant reduction in the von Mises stresses.

Stress reductions in the intersection of the rib and steel plate through linear elastic studies and experiments have also been investigated by other authors. Numerical simulations on an orthotropic steel bridge deck have been reported by Buitelaar et al. (2004). This study shows a stress reduction factor of 21 in the steel plate near the rib. A paper by Jong & Kolstein (2004), reports strain measurements on the Caland Bridge in Rotterdam, The Netherlands, prior to and after upgrading the deck with a cement-based overlay. Four weeks prior to the repair work, strain gauges at various locations collected data. After

casting of a 50 mm thick overlay, the strain gauges collected additional data for five weeks. For strain signals caused by heavy vehicles, at the steel plate close to the rib, stress reduction factors were measured in the range of 5.9 to 7.7.

4.2 Nonlinear Studies

In addition to the linear elastic studies, cracking and debonding have been included in a nonlinear fracture mechanical study. The aim of the nonlinear study is to investigate the factors that play a role on overlay cracking, and to give an estimate on the crack width and initiation of debonding. Some of the main goals in a design situation might be to minimize crack widths and to keep the solution economically beneficial.

Four different overlay materials have been analyzed. The investigated overlay materials have all been analyzed in the composite beam configuration as described in Chapter 3. The materials are: FRC, FRD, concrete, and ECC. Their constitutive behaviors are given in tables 4.1 and 4.2.

Material	f_t [MPa]	a_1 [mm^{-1}]	a_2 [mm^{-1}]	b_2 [-]	G_f [N/mm]
FRC	2.3	27	0.50	0.35	0.30
FRD	4.8	64	0.57	0.46	0.90
Concrete	2.0	50	1.0	0.1	0.03

Table 4.1 *Constitutive parameters of three tension softening materials analyzed as overlay material. Parameters are based on values from Paper III.*

Material	f_t [MPa]	f_u [MPa]	ϵ_u [%]	w_u [mm]
ECC	4.2	5.3	1.9	4*

Table 4.2 *Constitutive parameters of a strain hardening material ECC (*Note this value is an assumption). Parameters are based on values from Paper III.*

The constitutive parameters in Table 4.1 are given as a normalized bilinear stress-crack opening relationship, where a_1 and a_2 are the negative slopes of the two line segments and b_2 is the intersection between the second line segments and the y-axis. The tensile stress f_t and the fracture energy G_f are shown as well. In the case of a strain hardening material, as ECC, the constitutive parameters from Table 4.2, are given as the tensile strength f_t, ultimate tensile strength f_u, and ultimate strain ϵ_u. The softening part is normally not measured and is in the study assumed to behave with an ultimate crack opening w_u for zero stress.

The nonlinear analysis concerns cracking pattern and crack widths with regards to mechanical loading. The development of cracks in the overlay for fixed traffic load and increasing axle load can be investigated utilizing finite elements. The present investigation on crack pattern is carried out considering concrete as overlay material, cf. Table

4.1. The development of cracks for various stages of axle loads is illustrated in Figure 4.6(a)-(d).
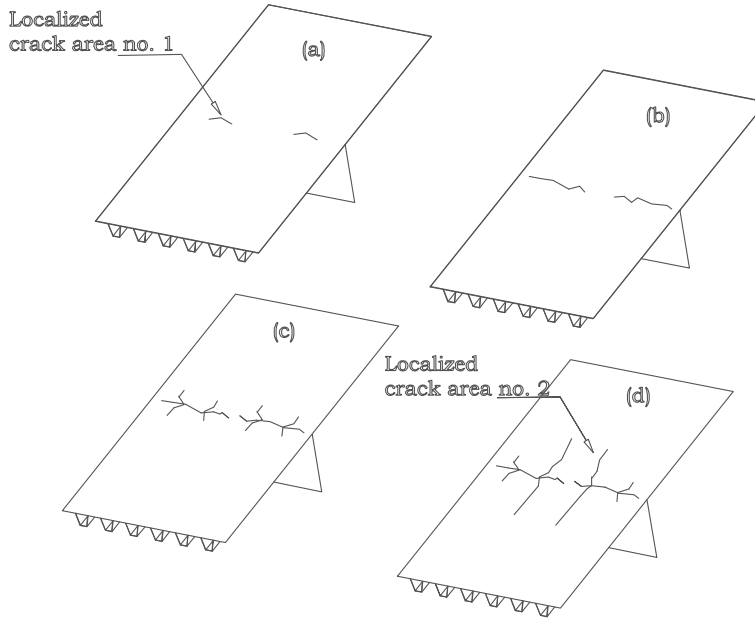
Figure 4.6 *Crack patterns of the overlay (concrete) for traffic and an axle load of: (a) 50 kN, (b) 180 kN, (c) 260 kN, and (d) 290 kN.*

As observed in the figure, the first cracks develop in the area on top of the bulkhead, denoted localized crack area no. 1, cf. Figure 4.6(a). Even for a small axle load of approximately 50 kN, the concrete overlay reaches a tensile value of 2 MPa. When further loading is applied, the maximum crack width is increased and more cracks develop. At some point, in this case for an axle load of approximately 290 kN, cracks develop in the direction of the bridge axis. Cracking of the overlay in the direction of the bridge axis is denoted crack area no. 2, cf. Figure 4.6(d).

The maximum crack width can for fixed traffic load, and variable tandem load, be viewed in a load vs. crack width diagram, cf. Figure 4.7.

The figure displays the axle load as a function of the maximum crack width for the four materials considered: Concrete, FRC, FRD, and ECC. In the case of ECC, the results are presented as load vs. strain. In the load range considered, the maximum crack width is always located in crack area no. 1 as defined in Figure 4.6(a). In addition to the crack width, initiation of cracking in crack area no. 2, as defined in Figure 4.6(d), is marked. In the load range considered, only concrete and FRC initiates cracking in crack area no.
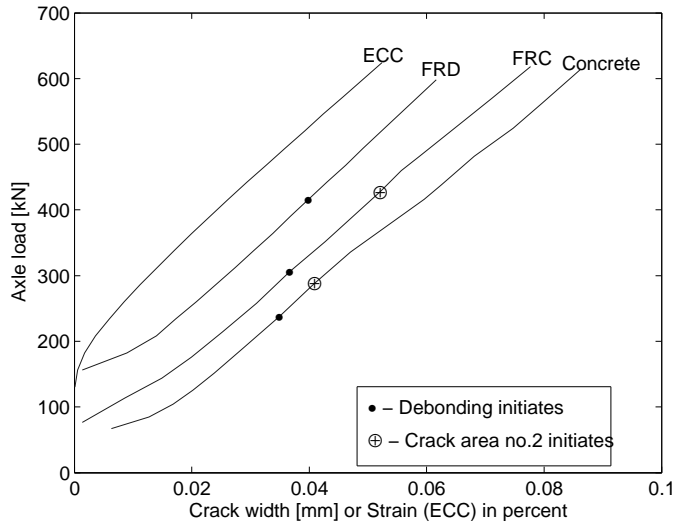
Figure 4.7 *Numerical results of three overlay materials for fixed traffic load and variable axle loading. The results are presented in a load vs. crack width diagram for concrete, FRC, and FRD. In the case of ECC material the result are presented as load vs. strain in percent.*

2. In the case of tension softening materials, increasing crack width will at some point lead to debonding. Debonding is initiated for a certain crack width and is also marked in Figure 4.7. It is noted that debonding is initiated for approximately the same crack width for: Concrete, FRC, and FRD.

Apart from traffic loading and dead load, effects such as shrinkage and temperature gradients might also have a significant influence on the overlay performance. These effects have also been analyzed utilizing finite elements, and are included in *Paper IV*. These two effects have a considerable influence on the cracking behavior and the stress state of the overlay material.

In the case of temperature loading, cooling of the overlay (bottom warmer than top) is of special concern. Since the overlay is restrained from moving due to its bond with the steel deck, cooling of the overlay results in a situation with tensile stresses. This, in combination with traffic load will consequently lower the load level where cracking and debonding are initiated.

When using high performance concretes as overlay material, early age shrinkage can have considerable influence on the cracking behavior. After casting of the overlay, the cement starts to hydrate and the material will experience a macroscopic volume change, hence

internal stresses will develop in the overlay. This can, in worst case, lead to cracking of the overlay and needs to be controlled. Another aspect is the level of internal stresses, due to shrinkage of the overlay material, when the bridge is opened for traffic. *Paper IV* shows modeling of shrinkage and creep in the overlay which aims to give a stress history at early age.

Chapter 5

Conclusions

Fatigue damage of orthotropic steel bridge decks has achieved international attention in the past years. The work within this thesis contributes to the ongoing research. Various systems to stiffening an orthotropic steel bridge deck have been proposed by several authors. A promising system is to use a cement-based overlay as investigated in this thesis. The strategy of the present study is to investigate the cement-based overlay system using multi scale modeling based on fracture mechanics. The study as a whole, can be divided into three length scales: (i) interface behavior, (ii) material interface interaction, and (iii) structural design.

On the steel-concrete interface length scale, a robust test method and inverse analysis to obtain Mode I fracture parameters for a steel-concrete interface has been established. A modification of the well known Wedge Splitting Test (WST) has proven to be a good and reliable test method to investigate a steel-concrete interface. However, with regards to the cement-based overlay system, cracking might not always occur in pure Mode I. Mixed mode cracking has been investigated theoretically as well as experimentally. A mixed mode model by Wernersson (1994), which is easy to implement into finite elements codes, showed good correlation between experiments and theory. However, the set-up developed in the present study is limited to tests on low mixed mode angles. Results on interface fracture under high mixed mode angles have been extrapolated.

Studies on composite beams show that when a crack propagates through the overlay, the interface stresses, at some point, change dramatically from compression to tension. Since tension is critical to the interface, the change in interface stresses might at some point lead to debonding. In the case of a composite beam with an overlay material such as ECC subjected to negative bending, debonding is prevented as long as the material is in its hardening state. This is due to the fact that a material like ECC forms multiple cracks, and one single crack never evolves to a stage where the risk of debonding becomes critical. Experimental tests on small composite elements also served a good purpose in verifying the numerical tools applied in the thesis.

Linear elastic studies on a real size structure, utilizing the overlay system, show a considerable stress reduction in fatigue sensitive steel parts. Upgrading an orthotropic steel bridge deck by adding an overlay might be more cost-effective than increasing the steel

plate thickness. A nonlinear method to give an estimate on the performance, with regards to cracking behavior, of an orthotropic steel bridge deck stiffened with a cement-based overlay, is demonstrated on a real size structure. The numerical investigation has been carried out on the orthotropic steel bridge deck of the Farø Bridges located in Denmark. Effects such as traffic load, early age shrinkage and temperature gradients, have been taken into account. Cooling of the bridge deck (bottom warmer than top), has a considerable influence on the cracking behavior. Since the overlay is restrained from moving due to its bond with the steel plate, the cooling situation initiates internal stresses in the overlay.

The current system with an adhesive connection between the overlay and steel deck depends highly on the interface and debonding would be unacceptable. However, the nonlinear analysis shows, that cracking of the overlay might be unavoidable for the axle loads found in codes. However, the solution might be durable by minimizing the maximum crack width, and thereby avoiding debonding. Minimizing the crack width might be a central issue when applying a cement-based overlay that exhibits localized cracking behavior (a tension softening material). Since, a certain crack width, will at some point, lead to debonding. A more promising solution is to use a cement-based overlay that exhibits multiple cracking behavior (a strain hardening material). Since the study shows, that the overlay, in the load range considered, never reaches a crack width that initiates debonding.

5.1   Recommendations for Future Work

The outcome of the present study has contributed to the work within stiffening of an orthotropic steel bridge deck using a cement-based overlay. Looking at the thesis as a whole, the author feels that a theoretical background, to model a steel deck reinforced with a cement-based overlay has been established. However, one important aspect is full scale testing. With all the important parameters pointed out in this study, it would be of importance to see whether it is possible to reproduce the full scale behavior using the numerical tools and concepts described in this thesis. However, contributions are still needed for every part of this study. Numerical testing of interfacial mixed mode fracture, presented in *Paper I* could well be improved. In the present study, a uniaxial testing machine has been applied. It is not possible to test high mixed mode angle using the uniaxial set-up presented in this thesis. An improvement would be to use a biaxial testing machine to test a steel-concrete interface exposed to different mixed mode angles. By using a biaxial testing machine, it would be possible to vary the amount of normal and shear stress, and thereby test the interface for higher mixed mode angles than possible in the current uniaxial test set-up.

As shown in *Paper IIV*, temperature gradients and shrinkage can have major influence on the composite behavior on the structural scale. In this thesis, no experimental work has been carried out on shrinkage and temperature gradients and its influence on the composite behavior.

Another important issue, which has not been analyzed in greater details in the present thesis is fatigue. In order to give a full recommendation on the cement-based overlay system the effect of cyclic loading and its influence on the overlay crack width has to be considered. Somehow, the influence of cyclic loading should be implemented in the constitutive models to analyze the effect of fatigue. Cyclic loading will consequently increase the maximum overlay crack width and thereby increase the risk of debonding.

Bibliography

AISC (1962), *Design Manual for Orthotropic Steel Plate Deck Bridges*, American Institute of Steel Construction, Inc.

Battista, R. & Pfeil, M. (2000), Stranghening fatigue cracked orthotropic decks with composite layers, *in* 'Annual Technical Sesseion, and Meetin, Structural Stability Research Council', pp. 376–389.

Brühwiler, E. & Wittmann, F. H. (1990), 'The wedge splitting test, a method of performing stable fracture mechanics tests', *Engineering Fracture Mechanics* **35**, 117–126.

Buitelaar, P. (2002), Ultra thin heavy reinforced high performance concrete overlays, *in* '6th International Symposium on Utilization of High Strength / High Performance Concrete, Leipzig, Germany', pp. 1577–1590.

Buitelaar, P., Braam, C. R. & Kaptaijn, N. (2003), Reinforced high performance concrete overlay system for steel bridges, *in* 'In the 5th International CROW-Workshop on Fundamental Modelling of the Design and Performance of Concrete Pavements, Istanbul, Turkey'.

Buitelaar, P., Braam, R. & Kaptijn, N. (2004), Reinforced hig performance concrete overlay system for rehabilitation and strengthening of orthotropic steel bridge decks, *in* 'Orthotropic Bridge Conference, Sacremento, USA', ASCE, pp. 384–401.

Carpenteri, A. & Swartz, S. (1991), *Fracture Mechanics Test Methods for Concrete, Chapmann and Hall*, Chapmann and Hall, chapter 3, pp. 129–197.

Cervenka, J., Kishen, J. M. C. & Saouma, A. E. (1998), 'Mixed mode fracture of cemetitous bimaterial interfaces; part ii: Numerical simulation', *Engineering Fracture Mechanics* **60**(1), 95–107.

Chandra Kishen, J. M. & Saouma, V. E. (2004), 'Fracture of rock-concrete interfaces: Laboratory tests and applications', *ACI Structural Journal* **101**(3), 325–331.

De Backer, H., De Corte, W., De Pauw, B. & Van Bogaert, P. (2004), The use of dispersion layers to reduce the fatigue damage in orthotropic steel bridge decks, *in* 'Proc. of 10th Nordic Steel Construction Conference, Copenhagen', pp. 413–424.

DIANA (2003), *DIANA User's Manual – Release 8.1*, june edn, TNO Building and Construction Research, P.O. Box 49, 2600 AA Delft, The Netherlands.

Bibliography

Dowling, P. J. (1968), The Behaviour of Stiffened Plate Bridge Deck under Wheel Loading, PhD thesis, Imperial College London.

ENV 1991-3 (1991), *Eurocode 1 - Basis of Design and Actions on Structures, Part 3: Traffic Loads on Bridges*, European Commitee for Standardisation.

Flint, A. R. & Smith, B. W. (1992), Strengthening and refubishment of servern crossing part5: Other background research and development, *in* 'Proc. Inst. Civil Engr.', Vol. 94, pp. 51–60.

Gere, J. & Timoshenko, S. (1999), *Mechanics of Materials*, Stanley Thomes, Fourth SI edition.

Granju, J. L. (1996), 'Thin bonded overlays: About the role of fiber reinforcement on the limitation of their debonding', *Adv. Cement Based Mat* **4**(1), 21–27.

He, M., Cao, H. & Evans, A. (1990), 'Mixed-mode fracture: The four point shear specimen', *Acta Metal. Mater.* **38**, 839–846.

Hillerborg, A. (1989), 'Stability problems in fracture mechanics testing', *Fracture of concrete and rock: recent developments* pp. 369–378.

Hillerborg, A., Moder, M. & Petersson, P. (1976), 'Analysis of crack formation and crack growth in concrete by means of fracture mechanics and finite elements', *Cem. Concr. Res.* **6**(6), 773–782.

Jong, F. B. P. & Kolstein, M. H. (2004), Strenghening a bridge deck with high performance concrete, *in* 'Orthotropic Bridge Conference, Sacremento, USA', ASCE, pp. 328–347.

Jong, F. B. P., Kolstein, M. H. & Bijlaard, F. S. K. (2004), Strain measurement tests at orthotropic steel bridge decks with a heavy vehicle simulator, *in* 'Prooceddings of the 10th Nordic Steel Construction Conference, Copenhagen, Denmark', pp. 401–412.

Kolstein, M. H. & Wardenier, J. (1997), 'Stress reduction due to surfacing on orthotropic steel decks', *IABSE Workshop, IABSE Reports, Vol. 76, Zurich, Lausanne* .

Kolstein, M. H. & Wardenier, J. (1998), A new type of fatigue failures in steel orthotropic bridge decks, *in* 'Proceedings of the fifth Pacific Structural Conference, Korea', pp. 483–488.

Kolstein, M. H. & Wardenier, J. (1999), Laboratory tests of the deckplate weld at the intersection of the through and the crossbeam of steel orthotropic bridge decks, *in* 'Proceedings of the Eurosteel', pp. 411–414.

Linsbauer, H. N. & Tschegg, E. K. (1986), 'Fracture energy determination of concrete with cube shaped specimens (in german)', *Zement und Beton* **31**, 38–40.

Loureno, P. B. & Rots, J. G. (1997), 'Multisurface interface model for analysis of masonry structures', *Journal of Engineering Mechanics* **123**(7), 660–668.

Machida, F., Wakabayashi, N., Shimozato, T., Masui, T., Ono, S. & Miki, C. (2004), 'Orthotropic steel bridge decks study on fatigue improvement of weld connection to trough stiffeners in orthotropic steel bridge decks.', *International Institute of Welding, Document XII-2024-04* .

Olesen, J. F. (2001), 'Fictitious crack propagation in fiber-reinforced concrete beams', *Journal of Engineering Mechanics* **127**(3), 272–280.

Østergaard, L. (2003), Early-Age Fracture Mechanics and Cracking of Concrete. Experiments and Modelling, PhD thesis, Department of Civil Engineering, Technical University of Denmark, Lyngby, Denmark.

Peterson, P. (1981), Crack growth and development of fracture zones in plain concrete and similar materials, Technical report, Report TVBM-1006, Division of Building Materials, Lund Institute of Technology.

RILEM (2000), 'Test and design methods for steel fiber reinforced concrete. recommendations for the three point bending test', *Materials and Structures* **33**, 3–5. Prepared by RILEM-Committee-TDF-162, Chairlady L. Vandewalle.

RILEM (2001), 'Test and design methods for steel fiber reinforced concrete. recommendations for uniaxial tension test', *Materials and Structures* **34**(3–6). Prepared by RILEM-Committee-TDF-162, Chairlady L. Vandewalle.

RILEM TC-108 (1996), *Interfacial Transition Zone in Concrete*, RILEM Report 11, Chapman and Hall.

Sigurdsson, S. (2003), Composite bridge decks of sfrc/steel, Master's thesis, Department of Civil Engineering, Technical University of Denmark, Lyngby.

Silfwerbrand, J. (1984), 'Composite action between partially chipped concrete bridge deck and overlay', *Bulletin No. 142, Dept. of Structural Mechanics and Engineering, Royal Institute of Technology, Stockholm, Sweden (in swedish)* p. 149.

Smith, J. W. & Bright, S. (2003), Upgrading orthotropic bridge decks with fiber reinforced composites, *in* 'High Performance Materials in Bridges', pp. 463–472.

Smith, J. W. & Cullimore, M. S. G. (1987), Stress reduction due to surfacing on a steel bridge deck, *in* 'Int. Conf. Steel and Aluminimum Structures, Cardiff', pp. 806–816.

Ulfkjær, J., Krenk, S. & Brincker, R. (1995), 'Analytical model for fictitious crack propagation in concrete beams', *Journal of Engineering Mechanics* **121**(1), 7–15.

Walter, R., Gimsing, N. & Stang, H. (2004), 'Composite steel-concrete orthotropic bridge deck', *10th Nordic Steel Construction Conference, Copenhagen, Denmark, pp.519-530* .

Walter, R., Li, V. C. & Stang, H. (2004), 'Comparison of frc and ecc in a composite bridge deck', *5th International PhD Symposium, Delft, The Netherlands, pp. 477-484* .

Walter, R., Olesen, J. F. & Stang, H. (2005), 'Interfacial mixed mode model', *In: The 11th International Conference on Fracture, Turin, Italy* .

Walter, R., Stang, H., Gimsing, N. J. & Olesen, J. F. (2003), 'High performance composite bridge decks using scsfrc', *The Fourth International Workshop on High Performance Fiber Reinforced Cement Composites, Ann Arbor, Michigan* pp. 495–504.

Wang, J. & Maji, A. K. (1995), Experimental studies and modeling of the concrete/rock interface, *in* B. O. & W. M., eds, 'Interface Fracture and Bond', ACI SP-156, pp. 45–68.

Wernersson, H. (1994), 'Fracture characterization of wood adhesive joints', *Report TVSM-1006, Lund University, Division of Structural Mechanics* .

Wolchuk, R. (1963), *Design Manual for Ortotropic Steel Plate Deck Bridges*, American Institue of Steel Construction.

Wolchuk, R. (2002), 'Structural behaviour of surfacing on steel orthotropic decks and considerations for practical design', *Structural Engineering International* **2**, 124–129.

Wu, E. (1967), 'Application of fracture mechanics to anisotropic plates', *ASME Journal of Applied Mechanics* **34**, 967–974.

Part II

Appended Papers
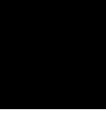
Paper I

Cohesive Mixed Mode Fracture Modelling and Experiments

Cohesive Mixed Mode Fracture Modelling and Experiments

Rasmus Walter* & John F. Olesen

Department of Civil Engineering Technical University of Denmark DK-2800 Kgs. Lyngby, Denmark, *e-mail: rw@byg.dtu.dk

Abstract

A nonlinear mixed mode model originally developed by Wernersson (1994), based on nonlinear fracture mechanics, is discussed and applied to model interfacial cracking in a steel-concrete interface. The model is based on the principles of Hillerborgs fictitious crack model, however, the Mode I softening description is modified taking into account the influence of shear. The model couples normal and shear stresses for a given combination of Mode I and II fracture. An experimental set-up for the assessment of mixed mode interfacial fracture properties is presented, applying a bi-material specimen, half steel and half concrete, with an inclined interface and under uniaxial load. Loading the inclined steel-concrete interface under different angles produces load-crack opening curves, which may be interpreted using the nonlinear mixed mode model. The interpretation of test results is carried out in a two step inverse analysis applying numerical optimization tools. It is demonstrated how to perform the inverse analysis, which couples the assumed individual experimental load-crack opening curves. The individual load-crack opening curves are obtained under different combinations of normal and shear stresses. Reliable results are obtained in pure Mode I, whereas experimental data for small mixed mode angles are used to extrapolate the pure Mode II curve.

Keywords Nonlinear fracture mechanics, mixed mode fracture, steel-concrete interface.

1 Introduction

Since Hillerborg et al. (1976) introduced the fictitious crack model, discrete Mode I cracking in concrete has been the subject of intensified research, which has demonstrated the usefulness of the concepts of this cohesive crack model. The focus of this study is the influence of shear on the process of discrete cracking, which in the terminology of fracture mechanics is called mixed mode cracking. Mixed mode cracking will be treated both theoretically and experimentally. In the present study the mixed mode interfacial cracking of a steel-concrete interface is in focus, where the interface is defined as a region of concrete mortar near the boundary between the two materials. Experimental experience shows that interfacial cracking of a steel-concrete interface usually occurs at a certain distance

from the physical boundary between the two materials, cf. (RILEM TC-108 1996). Physically, the interfacial transition zone between concrete and steel has a finite thickness on the micro scale, which is related to the penetration of the cement paste into the rough steel surface. In the present study interfacial cracking is defined as taking place close to or inside the interfacial transition zone.

Recordings of Mode I behavior of steel-concrete interfaces have already been made, see e.g. (Walter et al. 2005). Less experimental research has been carried out on mixed mode cracking of cement-based interfaces, however, serval numerical models to describe interfacial mixed mode cracking based on nonlinear fracture mechanics have been proposed, see e.g. Lourenço & Rots (1997) or Cervenka et al. (1998). In the present study mixed mode modelling is based on a model originally presented by Wernersson (1994). To introduce the concepts and ideas of this mixed mode model, a brief summary of the concepts of coupling stress intensity factors in linear elastic fracture mechanics (LEFM) for mixed mode loading is given. These concepts are well understood and the summary explains how some of these concepts can be adopted to nonlinear cohesive crack modelling. When describing mixed mode cracking in linear elastic fracture mechanics the phase angle ψ_k is introduced, which is a function of the Mode I and II stress intensity factors K_I and K_{II}.

$$\psi_k = arctan\left(\frac{K_{II}}{K_I}\right) \tag{1}$$

Thus, the phase angle is directly related to the stress state in the vicinity of the crack tip. Relating the phase angle to the total critical energy release rate shows two typical behaviours, which can explain the difference between ductile and brittle materials. Materials have been classified by He et al. (1990) using the phase angle. There it is stated, that for brittle materials the energy release rate increases significantly when increasing the phase angle ψ_k, thus the material is weaker in Mode I than in Mode II. The critical energy release rate ratio between Mode II and I, G_{IIc}/G_{Ic}, for concrete is larger than 1 and in some cases it has been measured in the range of 5, see, e.g. Carpenteri & Swartz (1991). So in this respect concrete may be considered as a brittle material, and consequently also the steel-concrete interface, since interfacial fracture is related to the behaviour of the concrete.

A stress intensity based failure criterion, has been suggested by Wu (1967) in the form

$$\left(\frac{K_I}{K_{Ic}}\right)^m + \left(\frac{K_{II}}{K_{IIc}}\right)^n \leq 1.0 \tag{2}$$

where m, n are material exponents. Using this criterion it is possible to define a failure criterion based on the state of stress, i.e. the combination of normal and shear stress, see for instance (Carpenteri & Swartz 1991). However, LEFM is not applicable in the case of concrete fracture due to its large fracture process zone, cf. Peterson (1981). Therefore, the present study adopts some of the concepts by applying the same form of interaction as given in Equation (2). The present analysis is carried out using cohesive crack modelling and is nonlinear in the sense that softening after crack initiation is included. As the

interface has reached its peak load, e.g. in uniaxial tension, the interface degradation is not necessarily abrupt as it may involve an amount of energy dissipation before complete separation.

In the general theory of elasticity, materials can be classified in two main groups: hyper- and Cauchy elastic materials. The strain energy function of a hyper-elastic material, $w_s = \int \sigma_{ij} d\epsilon_{ij}$, is equal to a potential. Hence the strain energy function is not dependent on the strain path. Contrary to this every state of stress for a Cauchy material is unique and defined by the strain path. Cracking in both hyper- and Cauchy materials have been modelled by serval authors using nonlinear fracture mechanics. Needleman (1987) formulated a cohesive crack model to study interfacial debonding with hyper-elastic material properties. He derived normal and shear stresses from an elastic potential which only depended on the normal and tangential displacements.

A nonlinear interfacial mixed mode model with path dependency has been defined by (Wernersson 1994), based on cohesive crack modelling. In this case, contrary to the case of a potential, the total fracture energy, G_f, is defined by

$$G_f = \int_\Gamma (\sigma d\delta_n + \tau d\delta_t) \tag{3}$$

where Γ is the deformation path that results in complete failure of the considered crack. As reported by serval authors, see e.g. (Cervenka et al. 1998), a cementitious interface can be described as a path dependent media, and different amounts of fracture energy are consumed in the cases of pure Mode I and II failures. These observations support a model taking into account path dependency and cohesive crack modelling with softening.

2   Mixed Mode Model

The mixed mode model by Wernersson (1994) is briefly presented here. For a full review on the mixed mode model the reader is referred to the original work by Wernersson (1994). The reason and motivation for using the present mixed mode model is the possibility of including the fracture behaviour which is expected when modelling a steel-concrete interface. The main features governing the mixed mode behaviour of a steel-concrete interface are as listed:

- Discrete cracking (cracking along an interface)

- Stress softening (include tension and shear softening)

- Mixed mode cracking (coupling of normal and tangential crack opening)

- Path dependency (the amount of fracture energy consumed depends on the fracture mode and path, i.e. how Mode I and II are combined during cracking)

A limitation to the present study is that only monotonic loading is considered, thus no effects from cyclic loading are taken into account. In the case of unloading, the model

will follow the same path as followed during loading, however, this is a violation of the expected material behavior, but accepted as a limitation in the present study since only monotonic crack growth is considered. Finally, it is assumed that no compression failure occurs, the mixed mode model only applies to tensile load under the influence of shear.

2.1 General Interface Description

The final goal for the mixed mode modelling is the implementation of a constitutive model for discrete cracks in a finite element code. For instance the mixed mode model may be applied in an interface element. Usually, to model a continuous geometry, a FE interface is modelled with a thickness of zero, and every node is associated with a normal and a tangential displacement and associated normal and shear stresses, corresponding to the crack opening. This is illustrated in Figure 1 showing a three node interface element.
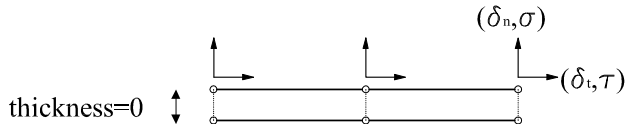
Figure 1: A three node interface element with node stresses and displacements indicated

The relationship between stresses and crack opening in plane strain is given by the following expression

$$\begin{bmatrix} \sigma \\ \tau \end{bmatrix} = \begin{bmatrix} D_{11} & D_{12} \\ D_{21} & D_{22} \end{bmatrix} \begin{bmatrix} \delta_n \\ \delta_t \end{bmatrix} \tag{4}$$

where σ and τ are the normal and shear stress, respectively. The displacements δ_n and δ_s are the normal and tangential displacement, respectively. The D_{ij} components relate the stresses to the normal and tangential displacement, δ_n and δ_t, respectively. In pure elastic mode no coupling is assumed between normal and shear mode and as a consequence, the off diagonal terms are set to zero, $D_{12} = D_{21} = 0$. After peak stress it is important to couple the two crack modes, Mode I and II. A situation with the off diagonal terms set to zero is equal to having two independent springs. The model derived here allows for the implementation of a constitutive relationship to represent a general interface behaviour.

2.2 Coupling of Mode I and II

Consider two stress-crack opening relationships, one for the normal opening and another for the tangential displacement of the crack: $\sigma(\delta_n)$ and $\tau(\delta_t)$, visualized in Figure 2. The curves are described in two parts, an elastic and a nonlinear part. The elastic part is described as the initial ascending part from zero stress to peak stress and is characterized by a very large stiffness, D_n and D_t, to model initial continuous geometry of the interfacial zone. This part has no physical meaning but is purely modelled having a slope in order for

the numerical solver applied to be able to converge. In this, non-physical elastic stage, the two modes are uncoupled. The post peak behavior is described by a descending, softening part, which relates the normal and shear stresses acting across the crack to the normal (δ_n) or tangential (δ_t) openings, respectively.
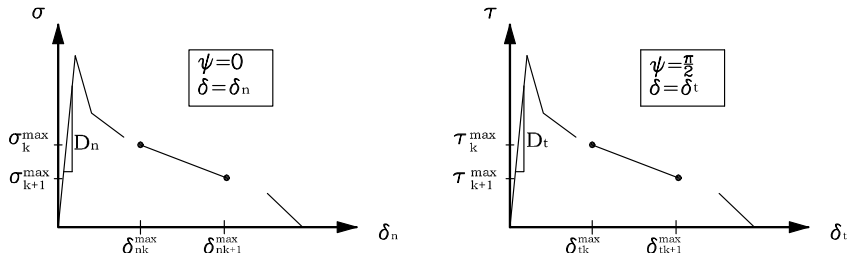
Figure 2: Uniaxial stress-crack opening relationships in (a) pure Mode I and (b) pure Mode II. The curves are described by a stiff, linear ascending part until peak stress and a multi linear post peak softening part.

Each linear segment of the complete stress-crack deformation relationship is treated individually. The indices (k) and (k+1) refer to two successive kink points, which define a linear segment on the uniaxial softening curve. The subscript 'max' is applied as notation when referring to the pure Mode I and II uniaxial curves. Maximum is used, since it is assumed that the maximum Mode I and II fracture energy consumption only can be obtain under pure Mode I and II uniaxial conditions, respectively. The coupling of the two Mode I and II uniaxial softening curves is carried out by expanding the uniaxial curves in the ($\delta_n - \delta_t$)-plane. This results in a situation where the normal and shear stresses depend, not only on their corresponding displacement, but also on both shear and normal opening, according to the following equations:

$$\sigma(\delta_n, \delta_t) \tag{5}$$

$$\tau(\delta_n, \delta_t) \tag{6}$$

In order to describe how the stresses depend on the relative displacement δ_n and δ_t, it is convenient to introduce a polar coordinate system. The mixed mode angle ψ and displacement δ are given by

$$\psi = arctan\left(\frac{\delta_t}{\delta_n}\right) \tag{7}$$

$$\delta = \sqrt{\delta_n^2 + \delta_t^2} \tag{8}$$

5

From Equations (7)-(8) δ_n and δ_t may be expressed in terms of the mixed mode displacement and angle, δ and ψ. This allows (5) and (6) to be written in terms of δ and ψ:

$$\sigma(\delta, \psi) \tag{9}$$

$$\tau(\delta, \psi) \tag{10}$$

A failure in pure Mode I corresponds to $\delta_t = 0 \Rightarrow \psi = 0^0$ and pure Mode II corresponds to $\delta_n = 0 \Rightarrow \psi = 90^0$. The normal stress-crack opening and shear stress-crack tangential displacement curves maintain their stepwise linear shape for constant mixed mode angle ψ. The curves vary smoothly as a function of ψ, accordingly, for increasing value of ψ, the normal stress-crack opening curve will diminish from a maximum at $\psi = 0^0$, while the shear stress-crack sliding curve will expand towards a maximum for $\psi = 90^0$.

Let δ_n^{max} and δ_t^{max} be two specific values corresponding to pure Mode I and II, and denoted by 'max' since it is assumed that they attain maximum value in uniaxial response. In order to find the crack displacements δ_n and δ_t for any given mixed mode angle the following criterion is assumed:

$$\left(\frac{\delta_n}{\delta_n^{max}}\right)^m + \left(\frac{\delta_t}{\delta_t^{max}}\right)^n = 1.0 \tag{11}$$

where m and n are material properties. The function in equation (11) can be plotted over the $\delta_n - \delta_t$ area. This is carried out for the values of the coefficients $m = n = 2.0$ and for two uniaxial kink points denoted k and $k + 1$, cf. Figure 3
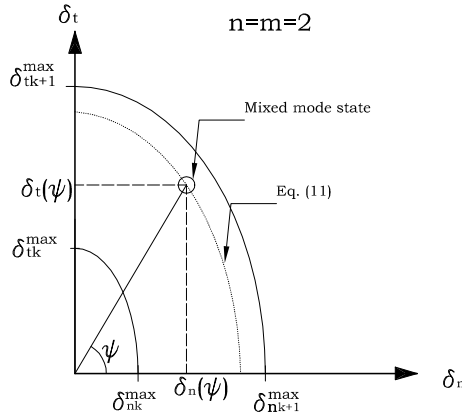
Figure 3: For a given mixed mode state the crack openings δ_n and δ_t can be found as a function of the mixed mode angle ψ

6

As seen from Figure 3 the crack displacements δ_n and δ_t can be related to the displacement δ, as defined in Equation (8) by $\delta_n = \delta cos(\psi)$ and $\delta_t = \delta sin(\psi)$.

In order to define a proper function for δ, the function $\delta(\psi)$ is introduced for the case where $n = m$:

$$\delta(\psi) = \left[\left(\frac{cos\psi}{\delta_n^{max}} \right)^m + \left(\frac{sin\psi}{\delta_t^{max}} \right)^m \right]^{-\frac{1}{m}} \tag{12}$$

An expression for $\delta(\psi)$ is extracted for two cases, m equal to 1 and 2.

$$\delta(\psi) = \frac{\delta_t^{max}}{ccos\psi + sin\psi} \quad for \quad m = n = 1 \tag{13}$$

$$\delta(\psi) = \frac{\delta_t^{max}}{\sqrt{c^2cos^2\psi + sin^2\psi}} \quad for \quad m = n = 2 \tag{14}$$

where $c = \delta_t/\delta_n$. The stresses σ and τ, for a given mixed mode angle, are related to the uniaxial stress by the relation

$$\sigma = \sigma^{max} \frac{\delta(\psi)cos(\psi)}{\delta_n^{max}} \tag{15}$$

$$\tau = \tau_k^{max} \frac{\delta(\psi)sin(\psi)}{\delta_t^{max}} \tag{16}$$

2.3 Bilinear Mode I and II Curves

As shown in serval cases, e.g. (Olesen 2001), using the fictitious crack model applying a bilinear stress-crack opening relationship gives a good correlation between numerical/analytical and experimental results. As this model requires pure Mode I and II softening relations a convention as shown in Figure 4 is used. The stress-crack displacement curves for pure Mode I and II are represented in a bilinear form.

2.3.1 Model Visualization

Applying the proposed convention, the interface response can be visualized as a 3D surface. A case study is shown using the following parameters in pure Mode I and II:

	σ_f, τ_f [MPa]	a_{n1}, a_{t1} [mm^{-1}]	a_{n2}, a_{t2} [mm^{-1}]	b_{n2}, b_{t2}	G_f^I, G_f^{II} [n/mm]
Mode I	3.0	25	0.3	0.1	0.10
Mode II	4.0	25	0.1	0.1	0.27

Table 1: Parameters for modelling pure Mode I and II softening curves used in case study

The visualization is carried out in terms of a stress surface over a displacement area, i.e. σ versus the normal and tangential crack displacement, cf. Figure 5(a). The surface plot
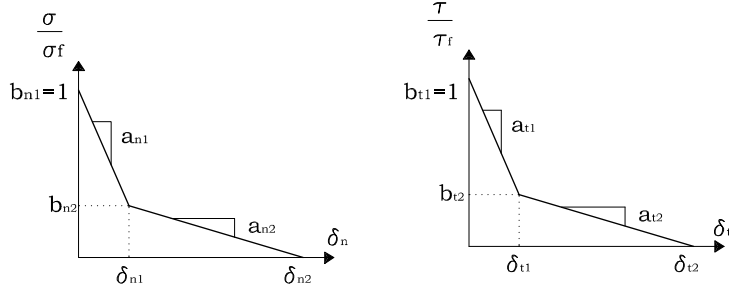
Figure 4: Convention for bilinear description of Mode I and II softening relationships (a) stress-crack opening relationship and (b) stress-crack tangential opening relationship

shows the amount of normal stress σ on the z-axis for various values of normal crack-opening δ_n and tangential crack sliding δ_t. As observed in the figure, in pure Mode I deformation, when $\delta_t = 0$, a full bilinear response $\sigma - \delta_n$ is retrieved. As the amount of tangential crack displacement is increased, the normal stress diminishes to a minimum. Along with the normal stress response, a diagram in Figure 5(b) displays the response of the shear stress τ. It is seen that the shear stress response is affected in an opposite manner of the normal stress, i.e. the shear stress diminishes as the normal crack opening increases.
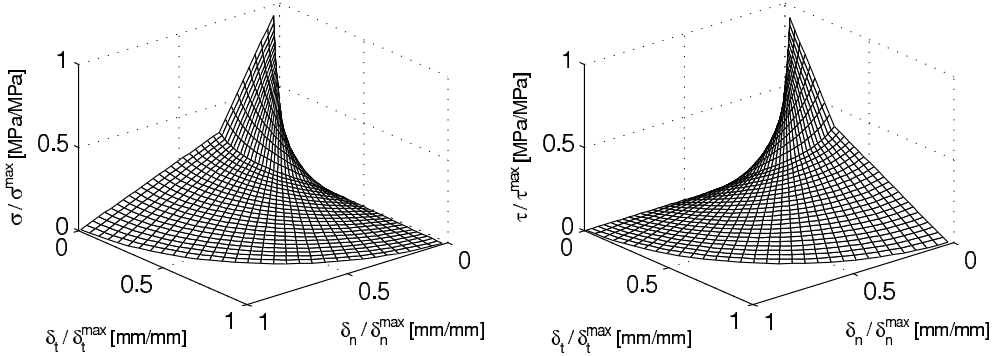
Figure 5: Model visualization, for the case m=n=2 using a uniaxial bilinear softening relations in pure Mode I and II given in Table 1. (a) Variation of the normal stress σ with respect to the normal and tangential displacements across the crack. (b) Variation of the shear stress τ with respect to the normal and tangential displacements across the crack.

2.3.2 Path Dependency

As already mentioned in the introduction the model takes into account path dependency according to Equation (3). The amount of fracture energy required to separate the interface to get a stress free crack surface is dependent on the path, i.e. the amount of normal crack opening and tangential crack displacement experienced along the path to a stress free crack surface. Starting from a fully bonded interface ending up with a fully separated interface, can be achieved in various ways. To separate the fracture surface in pure Mode I cracking may consume less fracture energy than separation through pure Mode II cracking. For a cementitious interface a path dependency may exist. In order to illustrate path dependency, pure Mode I and II parameters are chosen according to Table 1. The pure Mode I fracture energy is taken to be smaller than pure Mode II fracture energy.

In order to visualize the path dependency an academic example of three different paths ending at the same point, with a fully separated, stress free interface, are compared in terms of fracture energy consumed. The three paths are denoted A, B and C, cf. Figure (6). Path A is a radial path, which opens in a mixed mode, and is characterized by a constant mixed mode angle ψ. From the starting point to the end point, path B follows a path with a mixed mode angle of 90^0 (pure Mode II) until it reaches the amount of tangential crack displacement of the end point. Then it changes its opening mode to pure Mode I until it ends up with the same amount of normal and tangential crack opening as path A. The final path C, leads to interfacial separation in a sequence opposite that of path B, starting in pure Mode I and ending with propagation in pure Mode II. For each path A, B and C, the amount of fracture energy consumed is calculated. This is carried out for various end points, changing the mixed mode angle ψ, such that $\psi \in [0; \frac{\pi}{2}]$.

In case A, for each mixed mode angle calculated, the total amount of fracture energy consumed consists of a Mode I and Mode II contribution. In Figure 7(a) the amount of Mode I and Mode II energy consumed, G_f^I and G_f^{II}, respectively, is shown along with the total fracture energy as a function of the mixed mode angle ψ. As expected, for a low mixed mode angle the total fracture energy consumed is dominated by Mode I energy. The opposite is the case for a large mixed mode angle, when the fracture energy is dominated by Mode II fracture energy. Furthermore, as the mixed mode angle increases the total amount of energy consumed increases, which is a consequence of the parameters given in Table 1, when the pure Mode I energy is smaller than the pure Mode II fracture energy. The three different paths A, B and C, and their total amount of fracture energy consumed are compared as a function of the mixed mode angle, cf. Figure 7(b). In general path B consumes the least amount of energy and path C the largest, whereas path A is intermediate. This can again be explained by the parameters given in Table 1, since path C is dominated by Mode II crack propagation it consumes more fracture energy than the two other paths.
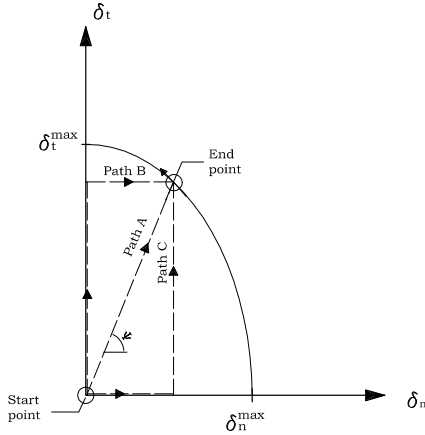
Figure 6: Three paths A,B and C to study the path dependency of the model. Path A is the radial part leading to full separation in a mixed mode opening, whereas the B and C paths opens in pure Mode I and II, all ending up in the same end point. This is carried out for each ending point, i.e. for $\psi \in [0; \frac{\pi}{2}]$

3   Experimental Set-up

A test set-up is developed with the aim of obtaining the constitutive parameters for the interfacial mixed mode model as described in the previous sections. The set-up was designed for a steel-concrete interface. In order to have a general model covering a range of mode mixity it is necessary to measure the stress-separation curve for an interface loaded under various mixed mode angles. The experimentally measured curves may then be interpreted according to the nonlinear mixed mode model.

Much work has been carried out on pure Mode I cracks in full concrete specimens recording the complete stress-crack opening relationship using different set-ups, see e.g. (Østergaard 2003) for a comparison of standard test methods. The aim in the present study is to develop a simple uniaxial test method to determine the mixed mode behavior of a steel-concrete interface. To capture the whole stress-deformation curve of brittle materials, the stiffness of the material that surrounds the fracture zone is of crucial importance. Peterson (1981) suggest the following criterion to be met in order to produce a stable test.

$$K_s > -A_s \frac{d\sigma(w)}{dw} \tag{17}$$

where $\frac{d\sigma(w)}{dw}$ is the slope of the $\sigma - w$ curve, w denotes Mode I crack opening, and A_s is the cross-sectional area of the fracture zone. The stiffness K_s holds a contribution from the specimen outside the fracture zone and the stiffness of the testing machine itself. As
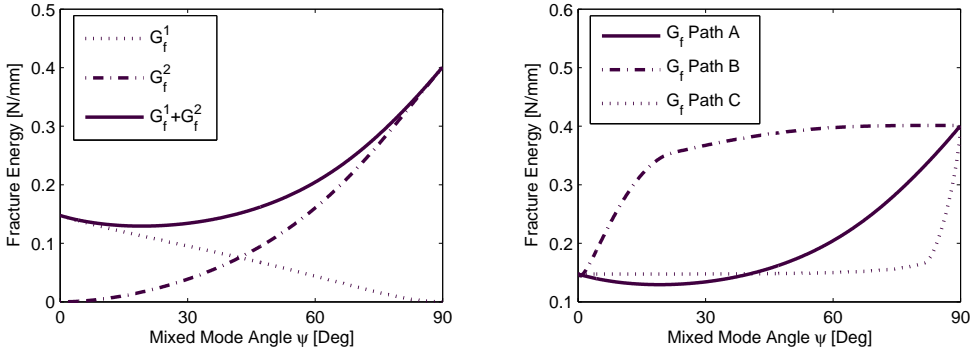
Figure 7: (a) Fracture energy of path A consumed for different mixed mode angles (b) Total fracture energy consumed compared for three different paths A, B and C as a function of the mixed mode angle.

the criterion suggests a small specimen, e.g. low height and small area, tested in a very stiff machine is needed to perform a stable test on brittle materials. However, to obtain representative results for the specific material a lower bound on the specimen size exist, see e.g. Gustafsson (1985) for further discussions on specimen size.

Furthermore, when performing a uniaxial test, the rotational stiffness of the machine and specimen must meet a minimum requirement. Insufficient rotational stiffness of the system causes the two parts of the specimen to rotate with respect to each other. This behavior results in an uneven stress distribution of the fracture process zone. This phenomenon has been analyzed by Hillerborg (1989) and he concludes that insufficient rotational stiffness causes a non-physical plateau on the stress-deformation curve. This plateau is caused by increasing eccentricity of the system as the specimen starts to bend. Similar studies supported by FE calculations have been carried out by Østergaard (2003). According to the studies by Hillerborg (1989) rotational instability can by avoided if the stiffness outside the fracture zone K_s fulfills the criterion in equation (18).

$$K_s > I \frac{d\sigma(w)}{dw} \tag{18}$$

Here I is the moment of inertia of the cross-section of the fracture process zone. Based on the before mentioned considerations a set-up to determine the complete stress-crack normal/tangntial opening relationship for an interface has been developed. The set-up is presented in Figure 8, which shows the interface specimen, and how it is mounted in the testing machine.

The interface specimen is characterized by the inclination angle α. By varying the angle α it is possible to test the interface exposed to different mixed mode combinations of normal and shear stress. The experiment is carried out by gluing the concrete part of the specimen to the top part of the loading device using a fast curing polymeric adhesive.

11

Adhesive Joint

Extensometer

Concrete block

α

Steel block

A

A

A - A
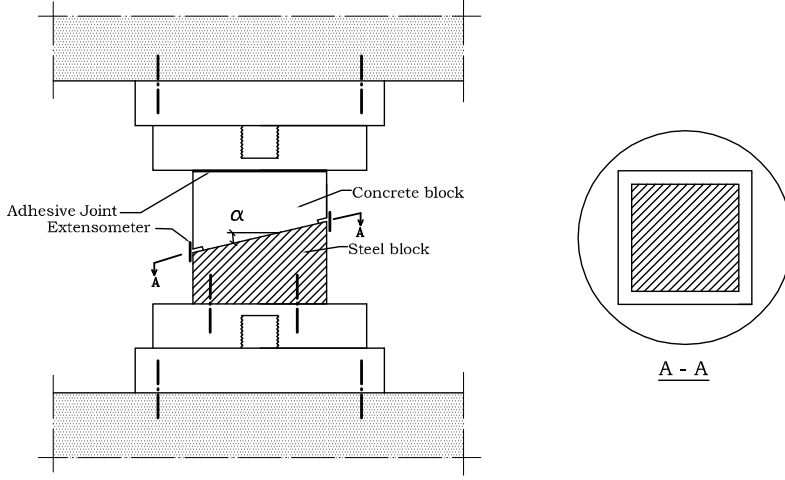
Figure 8: Schematic representation of the set-up to test an interface exposed to mixed mode loading. Only Mode I loading and displacement are recorded during the experiment.

The loading device consist of two interchangeable steel blocks rigidly connected to the machine.

The specimen size is chosen in accordance with the criterions discussed above. The specimen, including steel and concrete parts, is cubed and measures 75x75 mm^2 with a notch depth of 12.5 mm, leaving a fracture area of 50x50 mm^2. The notch are established by preventing the concrete from bonding to the steel part. This is ensured by a strip of plastic tape prior to casting. The material tested is a self-compacting concrete with a maximum aggregate size of 16 mm. According to (ASTM C192-96 1996) the area tested is greater than three time the aggregate size and is thereby a representative area. The preparation of the specimens are carried out by first sand blasting the steel part, thus minimizing the risk of defects, and then pouring the self-compacting concrete.

The tests are conducted in a 100 kN electro-mechanical 6025 Instron testing machine equipped for closed-loop control. The displacement across the fracture process zone is measured using two standard Instron clip gauges with a maximum travel length of 4 mm. The stiffness of the machine including the set-up and the specimen outside the fracture zone has been measured to 0.64 kN/m. In order to ensure necessary stiffness throughout the whole experiment special attention has to be paid to the fastening of bolts in the set-up. The bolts have to be prestressed, as a minimum, with a value higher than corresponding to the peak load in the specific experiment. To ensure stable testing with sufficient rotational stiffness, as specified in equations (17), (18) a notch depth of 12.5 mm has proven sufficient.

4   Test Program

A test program has been carried out consisting of specimens with different inclinations of the interface. The angle of inclination is measured with respect to a plane normal to the axis of loading, and three different values of the inclination angle were tested: $\alpha = 0^0$, 15^0, and 30^0. For each inclination or mixed mode angle, α, a total number of three specimens were tested. All specimens were cast according to the mix design shown in Table 2.

Table 2: Mix design

Mix	kg/m^3
Cement (Portland, CEM I 52.5)	245
Fly ash	94.5
Silica fume	10.5
Water	142.9
Air entraining agent	0.4
Plasticizer	4.2
Sand, 00-04 mm	752.6
Aggregates, 04-08 mm	450.6
Aggregates, 08-16 mm	594.0

The specimens were de-molded after 24 Hours, curing of the specimens was completed in 100% humidity and testing was carried out after 28 days of curing.

5   Test Results and Inverse Analysis

The recordings during an experiment consist of the deformation signal $\delta_{measured}$ and the load signal P. The deformation measurement can be transformed into the crack-opening value δ and further into Mode I and II components as sketched in Figure 9(a).

The measured deformation signal $\delta_{measured}$ consist of two contributions, one due to elastic deformations and one due to the crack opening. Only recordings in the cracked state of the experiment are of interest. The crack-opening value δ are found by subtracting the elastic response found from the overall response measured. This may, according to Østergaard (2003), be done in the following way.

$$\delta = \delta_{measured}(\sigma) - \delta_{measured}(\sigma_{max}) + \frac{\sigma_{max} - \sigma}{K_i} \tag{19}$$

Here K_i is the initial flexibility of the specimen, inside the measured length, $\delta_{measured}$ is the measured deformation at the stress σ and $\delta_{measured}(\sigma_{max})$ is the measured deformation at peak stress σ_{max}, cf. Figure 9(b). The crack-opening value δ may then be split into a Mode I and II contribution.

There may exist numerous solutions to the present constitutive model for a single stress-crack normal/tangential opening curve. An inverse analysis is needed to obtain reliable
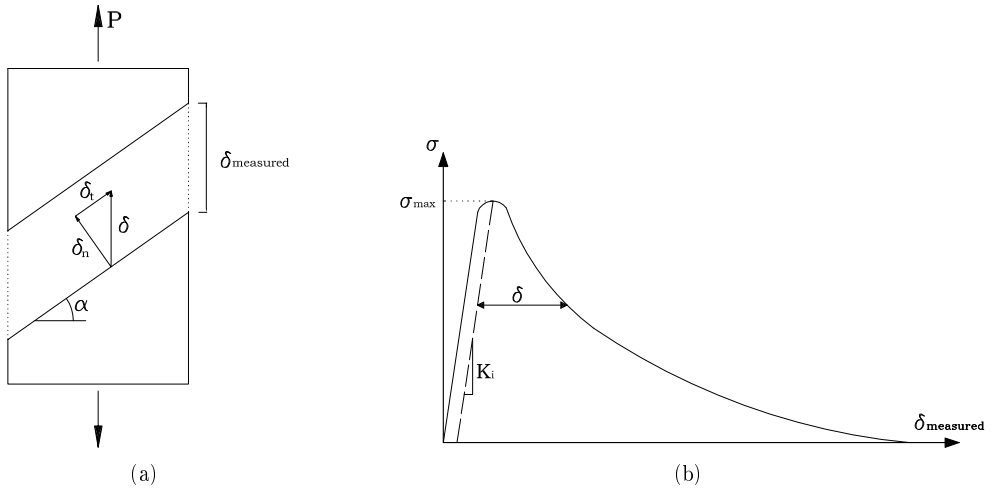
Figure 9: (a) Transforming $\delta_{measured}$ to Mode I and II components (b) Transformation of the deformation $\delta_{measured}$ measured in the experiment to the crack-opening measurement δ.

results. Ideally the model assumes the existence of a pure Mode I and Mode II stress-crack normal/tangential opening relationship along with a failure criterion in the shear normal stress plane. Since its very difficult to perform a pure Mode II experiment it is demonstrated how data from different mixed mode angles may be used to extrapolate the pure Mode II curve.

The strategy for obtaining the necessary parameters for the constitutive mixed mode model can be subdivided into two steps. An amount of experiments performed under specific mixed mode angles are only a fraction of the whole failure surface for $\psi \in [0; \frac{\pi}{2}]$. First step is to approximate a bilinear stress-crack deformation curve from each experiment. Finally, all the approximated bilinear curves are combined, in the $\delta_n - \delta_t$-space, according to the failure criterion given in Equation (11). The inverse analysis process is shown schematically in Figure 10.

For each step an inverse analysis is run, correlating the experimental data to the model in order to optimize the sought parameters. As shown in the figure, first step is to approximate each experiment with two bilinear stress-crack opening curves, one as normal stress vs. normal opening and a second as shear stress vs. tangential opening. Using this information, kink points for each curve are used in step 2 in order to define a failure criterion in the $\delta_n - \delta_t$ space. Both steps are explained in the following.

14
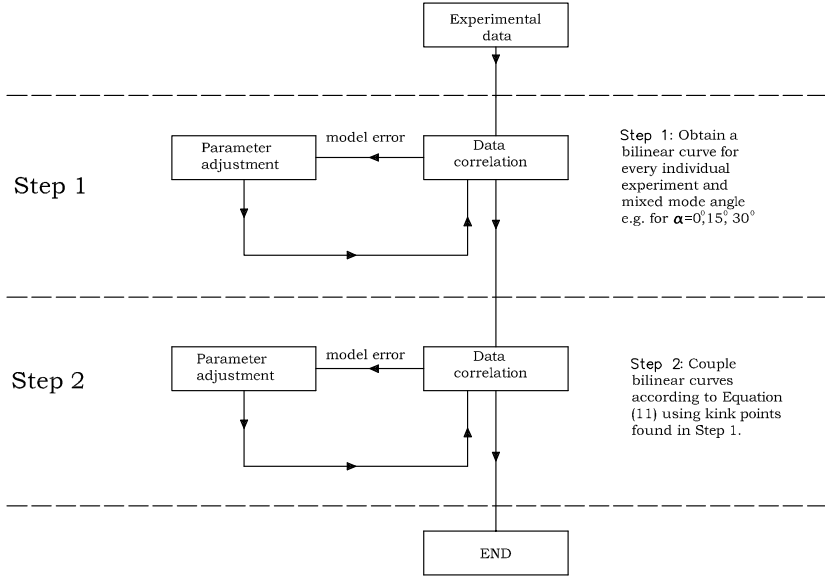
Figure 10: Schematic representation of the two step inverse analysis procedure

5.1 Inverse Analysis Step 1

First step in the inverse analysis is to approximate each individual experiment to two bilinear stress-crack opening curves. It is assumed that after peak load the mixed mode angle in the fracture process zone ψ is constant along the cracking plane and equal to the angle α as shown in Figure 8. In this case three experiments have been performed for each mixed mode angle e.g. $\alpha \in [0^0, 15^0, 30^0]$. A total number of 15 bilinear curves are then found, since an experiment with $\alpha = 0^0$ only produces one bilinear curve.

The bilinear approximations in Mode I and II are obtained in three steps, first δ, as explained earlier, is decomposed into δ_n and δ_t according to the angle α. The maximum stress and maximum crack deformation measurement δ_n or δ_t is then fixed in the further analysis. They represent the starting and ending points of the two line segments sought. The two unknowns in the fitting procedures are hence the slopes of the two line segments, $a_{n1}; a_{t1}$ and $a_{n2}; a_{t2}$, as shown in Figure 4. These slopes are calculated by minimizing the difference between experimental and model data. The two slopes in the bilinear relationship can be estimated by optimizing each of the following expressions:

$$\min_{(a_{n1},a_{n2})} \Sigma(Q_n - \hat{Q}_n)^2 \tag{20}$$

$$\min_{(a_{t1},a_{t2})} \Sigma(Q_t - \hat{Q}_t)^2 \tag{21}$$

15

α	Type	$f_t\ [MPa]$	$a_{n1}\ [mm^{-1}]$	$a_{n2}\ [mm^{-1}]$	$b_{n2}\ [-]$	$G_f^I[N/mm]$
0^0	Avg.	3.02	48.6	0.26	0.12	0.121
0^0	Stdev.	0.13	5.1	0.13	0.02	0.017
15^0	Avg.	2.93	60.7	0.13	0.10	0.102
15^0	Stdev.	0.06	8.0	0.05	0.05	0.046
30^0	Avg.	2.79	44.7	0.40	0.08	0.077
30^0	Stdev.	0.15	17.4	0.24	0.02	0.020

Table 3: Mode 1 bilinear parameters along with their standard deviation obtained in the inverse analysis according to step 1. The average estimate is based on three experiments for each mixed mode angle.

where Q_n and Q_t are vectors containing experimental values from Mode I and Mode II contributions. The values $\hat{Q}_n$ and $\hat{Q}_t$ denote vectors with values based on the estimated parameters. An example of an approximated bilinear stress-crack opening relationship relationship for an experiment performed with a mixed mode angle $\alpha = 30^0$ and its correlation to the experiment in Mode I and II are shown in Figure 11.
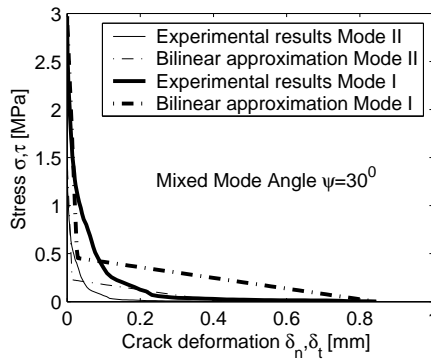
Figure 11: Example on experimental data from a test with $\alpha = 30^0$ and the approximation of two bilinear curves in Mode I and II.

The preliminary results from the inverse analysis Step 1 are summarized in Tables 3 and 4. As mentioned earlier, for each angle α a total number of three experiments have been carried out. In Table 3 the average results from the inverse analysis along with the standard deviations are given.

5.2   Inverse Analysis Step 2

After retrieving a total number of 15 bilinear relationships the final step is to couple the curves in the $\sigma - \tau$ and $\delta_n - \delta_t$ spaces. This is also carried out using an inverse analysis

16

α	Type	τ_t [MPa]	a$_{t1}$ [mm^{-1}]	a$_{t2}$ [mm^{-1}]	b$_{t2}$ [$-$]	G$_f^{II}$[N/mm]
15^0	Avg.	0.95	235	0.86	0.11	0.017
15^0	Stdev.	0.09	30	0.72	0.02	0.020
30^0	Avg.	1.41	90	0.79	0.12	0.115
30^0	Stdev.	0.06	35	0.50	0.03	0.007

Table 4: Mode 2 bilinear parameters along with their standard deviation obtained in the inverse analysis according to step 1. The average estimate is based on three experiments for each mixed mode angle.

procedure based on a numerical optimization routine. Since the experimental data consist of bilinear curves, the kink points on the curves have to be coupled. A total number of four values have to be determined, two stress and crack opening kink points, according to the expressions shown in (22) to (25).

$$\min_{(\sigma_1^{max}, \tau_1^{max})} \Sigma(Q_{s1} - \hat{Q_{s1}})^2 \tag{22}$$

$$\min_{(\sigma_2^{max}, \tau_2^{max})} \Sigma(Q_{s2} - \hat{Q_{s2}})^2 \tag{23}$$

$$\min_{(\delta_{n1}^{max}, \delta_{t1}^{max})} \Sigma(Q_{w1} - \hat{Q_{w1}})^2 \tag{24}$$

$$\min_{(\delta_{n2}^{max}, \delta_{t2}^{max})} \Sigma(Q_{w2} - \hat{Q_{w2}})^2 \tag{25}$$

Here Q_{s1} is a vector containing kink points according to the bilinear relationships found in the previous inverse analysis step. Each optimizing step is fitted using the criterion in Equation (11). The exponents have been fixed such that $m = n = 2$, which is an assumption. It might be possible to obtain different fits, using different exponents, however, the limited experimental data does not justify an optimization of these exponents. A further assumption is the bilinear shape of the pure Mode I and II uniaxial curves, whereas a different shape might be able to improve the fit. The only unknown parameters which have to be estimated are the kink points of the pure Mode I and II stress-crack normal/tangential opening curves. A full set of constitutive parameters consist of 8 variables, where two are found in each of the four sub steps, using the expressions 22 to 25

Coupling of the stress kink points can be viewed in Figures 12(a) and (b), using the inverse analysis procedure from expressions (22)-(25). Coupling of the two crack opening kink points are shown in Figures 13(a) and (b), which are found using optimizing expressions (24)-(25).

As seen from the figures, the coupling relationship is capable of linking the different kink points obtained from the bilinear curves. However, a large amount of scatter is observed in the coupling of the first crack opening kink point, cf. Figure 13(a). The scale between the different graphs, has to be considered when comparing the curves.
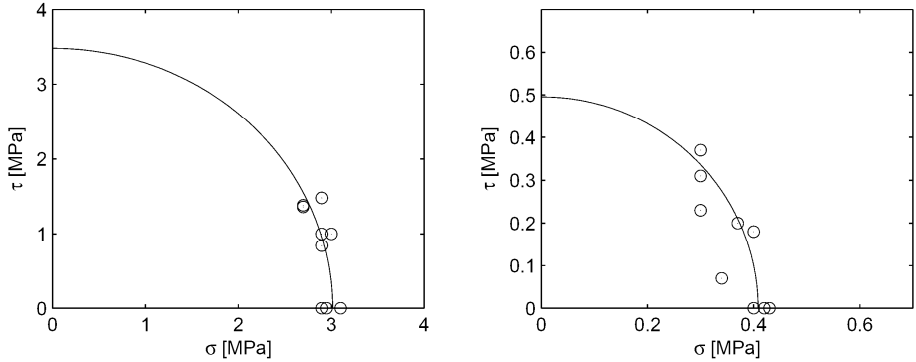
Figure 12: (a) Plot of coupling peak stress, $(\sigma_1^{max}, \tau_1^{max})$ (b)Plot of coupling kink point stress, $(\sigma_2^{max}, \tau_2^{max})$.

The final results and outcome of Step 2 in the inverse analysis is the pure Mode I and II uniaxial stress-crack opening curves. These are obtained straight forward by converting the kink points into the convention specified in Figure 4. The results for the bilinear parameters are shown in Table 5.

	σ_f, τ_f [MPa]	a_{n1}, a_{t1} [mm^{-1}]	a_{n2}, a_{t2} [mm^{-1}]	b_{n2}, b_{t2}	G_f^I, G_f^{II} [n/mm]
Mode I	3.01	59	0.28	0.13	0.12
Mode II	3.48	44	0.20	0.15	0.24

Table 5: Pure Mode I and II uniaxial parameters obtained in the inverse analysis, according to Figure 4.

As seen from Table 5 the fracture energy of the pure Mode II relationship is approximately twice as large as the pure Mode I curve. However, the results from using this experimental approach have to be considered carefully. It should be noted that no experimental data exist for high mixed mode angle and all data here are extrapolated from experiments with small mixed mode angles. This is one of the draw backs using a uniaxial set-up as shown in this paper. The problem is that in order to test large mixed mode angles a high inclination angle is needed hence a long specimen. As already discussed earlier, to perform stable test on brittle materials the length of the specimen is an important parameter. To test a very slender specimen might not be possible due to the low stiffness that it posses. More ideally, a biaxial testing machine would be preferable for obtaining data for large mixed mode angles. This is recommended for further research. The present results and method should together reflect the method of inverse analysis and the procedure to obtain constitutive parameters for the nonlinear mixed mode model.

18
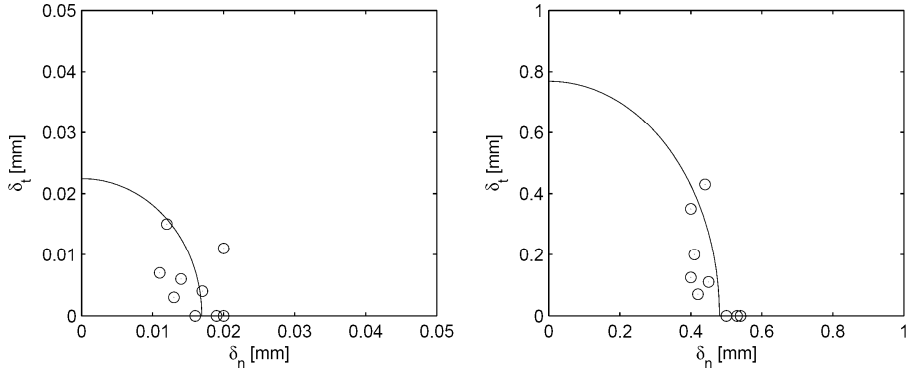
Figure 13: (a) Plot of coupling crack openings kink point 1, $(\delta_{n1}^{max}, \delta_{t1}^{max})$ (b) Plot of coupling crack openings kink point 2, $(\delta_{n2}^{max}, \delta_{t2}^{max})$.

6   Conclusions

A nonlinear mixed mode model first presented by Wernersson (1994) might be applicable for the modelling a steel-concrete interface exposed to mixed mode loading. It might be important to capture the physical path dependency behavior observed in experiments on cementitious interfaces, in numerical models of steel-concrete interfaces. Path dependency is taken into account for the mixed mode model presented, and is illustrated via a case study. An experimental set-up with the aim to characterize the constitutive parameters of a steel-concrete interface exposed to mixed mode loading has been presented. The set-up is simple and only gives an initial idea of the constitutive parameters of a steel-concrete interface but more sophisticated methods are needed to obtained improved results. The problem is to establish high mixed mode angles in this simple uniaxial configuration, which require long specimens that would have very low stiffness causing unstable testing. Ideally mixed mode tests could be performed in a biaxial testing machine recording normal and shear loading under different mixed mode angles. Test data has only been obtained for small mixed mode angles, however, the inverse analysis can extrapolate data for Mode II dominated fracture behaviour. The extrapolation is based on a two step inverse analysis, which is based on experimental data from experiments under different mixed mode angles.

References

ASTM C192-96 (1996), 'Standard practice for making and curing concrete test specimens in the laboratory', *American Society of Testing Standards (ASTM), West Conshohocken, Pennsylvania* .

Carpenteri, A. & Swartz, S. (1991), *Fracture Mechanics Test Methods for Concrete, Chapmann and Hall*, Chapmann and Hall, chapter 3, pp. 129–197.

Cervenka, J., Kishen, J. M. C. & Saouma, A. E. (1998), 'Mixed mode fracture of cemetitous bimaterial interfaces; part ii: Numerical simulation', *Engineering Fracture Mechanics* **60**(1), 95–107.

Gustafsson, P. (1985), Fracture mechanics studies of non yielding materials like concrete, Technical report, Report TVBM-1007, Division of Building Materials, Lund Institute of Technology.

He, M., Cao, H. & Evans, A. (1990), 'Mixed-mode fracture: The four point shear specimen', *Acta Metal. Mater.* **38**, 839–846.

Hillerborg, A. (1989), 'Stability problems in fracture mechanics testing', *Fracture of concrete and rock: recent developments* pp. 369–378.

Hillerborg, A., Modéer, M. & Petersson, P. (1976), 'Analysis of crack formation and crack growth in concrete by means of fracture mechanics and finite elements', *Cem. Concr. Res.* **6**(6), 773–782.

Lourenço, P. B. & Rots, J. G. (1997), 'Multisurface interface model for analysis of masonry structures', *Journal of Engineering Mechanics* **123**(7), 660–668.

Needleman, A. (1987), 'A continuum model for void nucleation by inclusion debonding', *Journal of Applied Mechanics* **29**, 525–531.

Olesen, J. F. (2001), 'Fictitious crack propagation in fiber-reinforced concrete beams', *Journal of Engineering Mechanics* **127**(3), 272–280.

Østergaard, L. (2003), Early-Age Fracture Mechanics and Cracking of Concrete. Experiments and Modelling, PhD thesis, Department of Civil Engineering, Technical University of Denmark, Lyngby, Denmark.

Peterson, P. (1981), Crack growth and development of fracture zones in plain concrete and similar materials, Technical report, Report TVBM-1006, Division of Building Materials, Lund Institute of Technology.

RILEM TC-108 (1996), *Interfacial Transition Zone in Concrete*, RILEM Report 11, Chapman and Hall.

Walter, R., Østergaard, L., Olesen, J. F. & Stang, H. (2005), 'Wedge splitting test for a steel-concrete interface', *Journal of Engineering Fracture Mechanics* **72**(17), 2565–2583.

Wernersson, H. (1994), 'Fracture characterization of wood adhesive joints', *Report TVSM-1006, Lund University, Division of Structural Mechanics* .

Wu, E. (1967), 'Application of fracture mechanics to anisotropic plates', *ASME Journal of Applied Mechanics* **34**, 967–974.

Notation

α	interface angle on mixed mode specimen
δ	mixed mode displacement
δ_n	normal crack opening
δ_t	tangential crack opening
$\delta_{measured}$	measured deformation
δ_{nk}^{max}	kink point on the pure Mode II uniaxial stress-crack normal opening curve
δ_{tk}^{max}	kink point on the pure Mode II uniaxial stress-crack tangential opening curve
$\hat{Q}_i$	vector containing experimental data
ψ	mixed mode angle
ψ_k	phase angle of stress intensity factors
σ	normal stress
σ_f	peak normal stress on pure Mode I uniaxial stress-crack normal opening curve
σ_k^{max}	kink point on the pure Mode I uniaxial stress-crack normal opening curve
τ	shear stress
τ_f	peak shear stress on pure Mode II uniaxial stress-crack tangential opening curve
τ_k^{max}	kink point on the pure Mode II uniaxial stress-crack tangential opening curve
a_{n1}	slope of pure Mode I uniaxial stress-crack normal opening curve
a_{n2}	slope of pure Mode I uniaxial stress-crack normal opening curve
A_s	area of fracture zone
a_{t1}	slope of pure Mode II uniaxial stress-crack tangential opening curve
a_{t2}	slope of pure Mode II uniaxial stress-crack tangential opening curve
b_{n2}	parameter of pure Mode I uniaxial stress-crack tangential opening curve
b_{t2}	parameter of pure Mode II uniaxial stress-crack tangential opening curve
D_{ij}	stiffness components for interface description
G_f	fracture energy
G_f^{II}	pure Mode II fracture energy
G_f^I	pure Mode I fracture energy

I	moment of inertia of fracture zone
K_{II}	Mode II stress intensity factor
K_I	Mode I stress intensity factor
K_i	initial flexibility of specimen
K_s	stiffness of set-up outside the fracture process zone
m	exponent to couple Mode I and II
n	exponent to couple Mode I and II
Q_i	vector containing estimated data
w	Mode I crack opening

Paper II

Wedge Splitting Test for a Steel-Concrete Interface

Wedge Splitting Test for a Steel-Concrete Interface

Rasmus Walter*, Lennart Østergaard, John F. Olesen & Henrik Stang
Department of Civil Engineering Technical University of Denmark DK-2800 Kgs.
Lyngby, Denmark, e-mail: rw@byg.dtu.dk

Abstract

This paper presents a test method designated for the determination of the stress-crack opening relationship of a steel-concrete interface. The method is based on the well known Wedge Splitting Test (WST), and it is illustrated how to obtain the stress-crack opening relationship through an inverse analysis. This inversion method utilizes the cracked hinge model, modified such that it describes the problem at hand. In this paper, pure concrete and steel-concrete composite specimens are tested and compared. It turns out that interfacial cracking of a bimaterial specimen usually behaves as one of the parent materials, in this case concrete. The stress-crack opening relationship of both the concrete and bimaterial specimens are obtained through the proposed inverse analysis. The results show, that interfacial cracking is dominated by the so-called wall-effect and its behavior can be described as quasi brittle. However, due to the wall-effect, interfacial cracking is more brittle than for the pure concrete.

Keywords Nonlinear fracture mechanics, steel-concrete interface, inverse analysis, bimaterial WST specimen.

1 Introduction

In composite structures and materials, the weakest part is often the interface between different materials. So, naturally, a lot of attention has been paid to the understanding of the characteristics of bimaterial interfaces. In the present study a steel-concrete interface is the focus and is defined as the region of the concrete mortar near the boundary between the two materials. Experimental experience shows that interfacial cracking of a steel-concrete interface usually occurs at a certain distance from the physical boundary. Physically, the interfacial transition zone between concrete and steel has a finite thickness on the micro scale, which is related to the penetration of the cement paste into the rough steel surface, cf. (RILEM TC-108 1996). In the present study interfacial cracking is defined as taking place close to or inside the interfacial transition zone. This zone is dominated by the presence of cement paste and lack of aggregates caused by the wall-effect.
The first model describing an interfacial crack between two dissimilar materials was developed by Williams (1959). Later, test set-ups to measure the fracture resistance of

bimaterial interfaces using linear elastic fracture mechanics concepts have been developed, i.e. the notched four-point bending beam specimen presented by Charalambides et al. (1989). Soares & Tang (1998) proposed a set-up to characterize the linear elastic fracture mechanical properties of a rock/mortar interface using a test which they call: The Bimaterial Brazilian Specimen. Since the introduction of the nonlinear fracture mechanics based fictitious crack model by Hillerborg et al. (1976), papers have been published utilizing this theory. Test specimens have been proposed to measure the stress-crack opening relationship of a cement-based interface. Wang & Maji (1995) investigated a rock/mortar interface and proposed a hinged uniaxial tension set-up to determine the stress-crack opening relationship. The stress-crack opening relationship was described by a single linear relationship. Verification was carried out comparing experiments on bimaterial interfaces using the so-called Compact Tension specimen with FE simulations using constitutive input obtained from the uniaxial tension tests. Recently, ? and Chandra Kishen & Saouma (2004) used the WST to evaluate the mode I fracture energy of limestone-concrete interfaces. Both studies included comparison between full concrete and limestone specimens, and as expected, in both cases, a more brittle behavior was observed in the bimaterial tests.

This paper proposes a test set-up to determine the fracture properties of a steel-concrete interface using a specimen where one half is steel while the other half is concrete. The applied set-up is similar to the well-known WST originally proposed by Linsbauer & Tschegg (1986). This new test method, is designated for the characterization of the mode I crack propagation taking place near the steel-concrete interface. It is hypothesized that this property may be described using the stress-crack opening relationship originally defined by Hillerborg et al. (1976). The most straight forward test to determine the stress-crack opening relationship would be the uniaxial test since no inverse analysis is necessary. However this test is rather demanding with respect to laboratory equipment and staff experience. This gives reasons for using the WST which stores little elastic energy during testing, thus resulting in a stable experiment, and is well suited for inverse analysis, see e.g. Østergaard (2003).

The need for this interfacial material description arises from an ongoing research project with focus on the application of strengthening steel bridge decks using a cement-based overlay. The goal is to cast a cement-based overlay on top of the steel bridge deck in order to form a top composite slab. Hence the fracture properties of a steel-concrete interface is of great interest, see, e.g., Walter et al. (2004).

2   The Bimaterial WST Specimen

The proposed test method uses the shape of the well-known wedge splitting specimen as described by e.g. Brühwiler & Wittmann (1990). This specimen is characterized by a groove and a starter notch, and the idea is to replace half of the specimen with a steel block, cf. Figure 1(a). The specimen is placed on a linear support. Two steel loading devices equipped with roller bearings are placed on top of the specimen. A wedge shaped

steel profile is placed between the bearings. Moving the actuator of the testing machine results in a splitting force P_{sp} acting between the two parts of the specimen, cf. Figure 1(b).
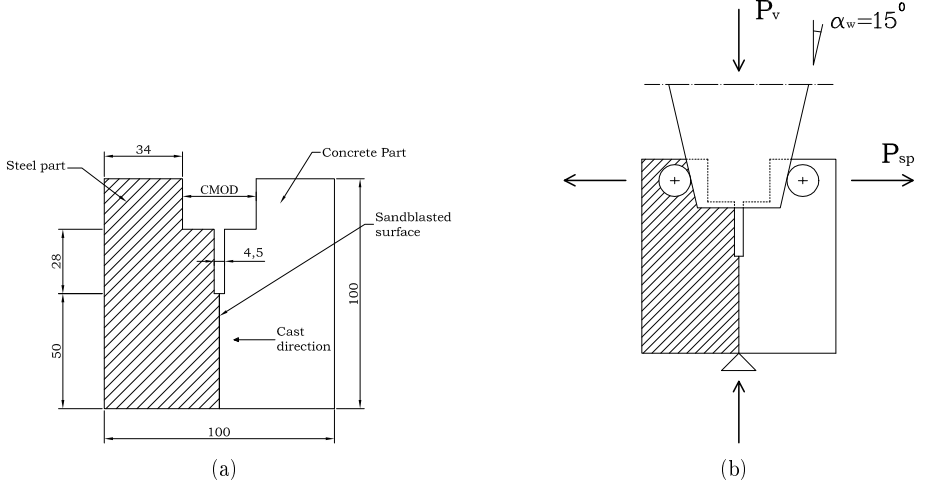

Figure 1: (a) Geometry of the tested bimaterial WST specimen. The hatched part represents a steel block (b) Load configuration

During the test, the load in the vertical direction P_v and the Crack Mouth Opening Displacement (CMOD) are recorded. For stable experiments closed loop control with CMOD as the control parameter is applied. Frictional forces of the bearing are not taken into consideration since the contribution will be less than 2% Rossi et al. (1991). The relation between the horizontal force and the splitting force is calculated using:

$$P_{sp} = \frac{P_v}{2tan(\alpha_w)} \tag{1}$$

In the current paper, an angle of $\alpha_w = 15^0$ is applied.

It is furthermore assumed, that all cracking is pure mode I. However, since the bimaterial WST specimen consist of two materials with different elastic moduli the interface is in fact not a plane of symmetry. Chandra Kishen & Saouma (2004) analyzed the assumption of pure mode I cracking in a bimaterial WST specimen. Their approach was to measure the stress intensity factors used in Linear Elastic Fracture Mechanics (LEFM) theory. In their investigation the fracture toughness of a limestone concrete interface was measured to $K_{1c} = 0.28MPa\sqrt{m}$ and $K_{2c} = 0.01MPa\sqrt{m}$. They conclude that the mode II fracture toughness is relatively low.

In the present study, the assumption of pure mode I cracking is analyzed using the commercial finite element package (DIANA 2003). The connection between steel and concrete is modelled using standard interface elements with a thickness of zero. Steel and concrete are both modelled assuming pure elastic behavior with an elastic modulus of 210GPa and

30GPa, respectively. The applied mesh is shown in Figure 2(a) and is found be to precise through a convergence analysis.
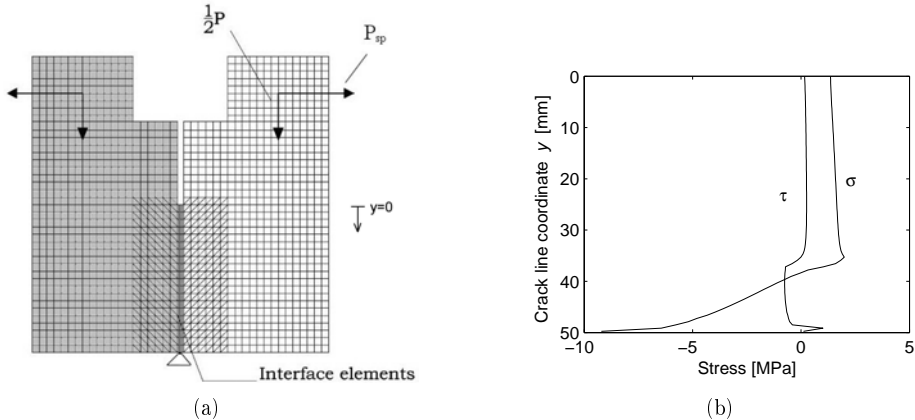

<div align="center">(a)   (b)</div>

Figure 2: (a) Applied mesh in the FE analysis to investigate the amount of pure mode I energy consumed using a bimaterial WST specimen. (b) Stress distribution at peak load for normal stress, σ, and shear stress, τ.

All nonlinear behavior is assumed to take place at the interface. The constitutive law of the interface employs a mixed mode model implemented in the commercial finite element package using user-supplied subroutines. The model is based on an coupling of the uniaxial $\sigma - \delta_n$ relationship and $\tau - \delta_s$ relationship. Consider a two dimensional configuration, where the interface element relates the stresses acting on the interface to the relative displacements, i.e. crack opening and crack sliding. The crack deformation in opening mode is denoted δ_n, while sliding mode is denoted by δ_s. Their relation to the normal, σ, and shear, τ, stress is given by:

$$\left[\begin{array}{c} \sigma \\ \tau \end{array} \right] = \left[\begin{array}{cc} D_{11} & D_{12} \\ D_{21} & D_{22} \end{array} \right] \left[\begin{array}{c} \delta_n \\ \delta_s \end{array} \right] \tag{2}$$

In the cracked state a permanent coupling is present between the normal and shear deformation described through the stiffness components D_{ij}. Two bilinear curves in pure mode I and mode II deformation are given as input. The model utilizes the following criterion to describe the state of deformation for every point on the curves:

$$\left(\frac{\delta_n}{\delta_n^{max}} \right)^2 + \left(\frac{\delta_s}{\delta_s^{max}} \right)^2 = 1.0 \tag{3}$$

where δ_n^{max} and δ_s^{max} is the maximum crack deformation in normal and sliding mode given in the two bilinear curves, respectively. For further details on the model see Walter et al. (2005) or Wernersson (1994).

The amount of fracture energy consumed in mode I, G_f^I, and mode II, G_f^{II}, along the steel concrete interface for every node can be calculated using the following formulas

$$G_f^I = \int_\Gamma \sigma(\delta_n)d\delta_n \qquad G_f^{II} = \int_\Gamma \tau(\delta_s)d\delta_s \qquad (4)$$

To investigate the amount of mode I and II energy which is consumed, three numerical simulations are investigated. In each case the mode I fracture energy of the bilinear curve is set to 0.1N/mm, whereas the bilinear curve in mode II is varied according to: $G_f^{II} \in [0.05; 0.1; 0.2]$N/mm. The maximum normal and shear stress is set to 2MPa in all three cases. Figure 2(b) shows the normal and shear stress distribution along the interface of the WST specimen at peak load. For each numerical simulation the amount of mode I and II energy consumed are calculated using equation 4. In every case the mode I energy consumed accounts for 99.5% of the total amount of energy consumed. Thus, when $E_s/E_c=7$ the pure mode I cracking assumption will produce a maximum error of 0.5%.
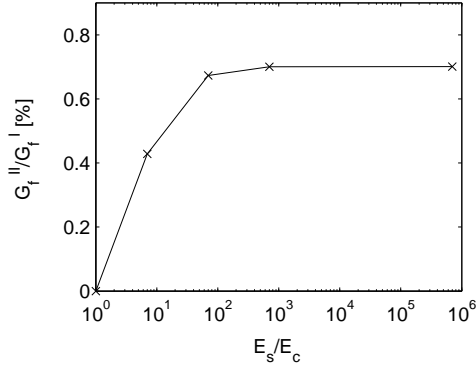
Figure 3: The ratio of consumed energy G_f^{II}/G_f^I in percent, according to formula (4), versus the elastic moduli ratio E_s/E_c.

Further, an additional investigation, varying the ratio of the two elastic moduli are carried out to determine the amount of mode II energy consumed for different E_s/E_c ratios. The elastic modulus E_c is kept constant at 30GPa, whereas E_s is varied according to the following ratios: $E_s/E_c \in [1; 7; 70; 700; 700000]$. The results are shown in Figure 3 as the ratio of consumed energy G_f^{II}/G_f^I in percent versus the elastic moduli ratio E_s/E_c on a logarithmic scale. As observed the amount of mode II energy consumed grows for increasing elastic moduli ratio. However, at some point a threshold is observed.

3 The Bimaterial Cracked Hinge Model

The cracked hinge model may be employed to obtain the stress-crack opening relationship using experimental WST results. However, since the outcome of the WST is a global load-deflection curve rather than the stress-crack opening relationship directly, the latter has to be determined by an inverse analysis. Here, the advantage of the cracked hinge model is that it yields closed-form analytical solutions, which can be implemented in a simple program written for the purpose of inverse analysis. The idea of a cracked hinge was originally developed by Ulfkjær et al. (1995) and further developed by Pedersen (1996), Stang & Olesen (1998), Stang & Olesen (2000), and Olesen (2001). Furthermore, the proposed method has proven to be robust and accurate for normal concrete, see Østergaard (2003).

The basic idea of the cracked hinge is to model the nonlinear behavior, in this case interfacial cracking, between two rigid boundaries. Inside the boundaries, independent horizontal spring elements are given a full elastic and nonlinear description, while the modelling outside the hinge is conducted using classical elastic theory. The specific hinge width of the steel and concrete parts are given as $s_s/2$ and $s_c/2$, respectively, while the sum is equal the total band width s, cf. Figure 4. The constitutive behavior of the steel and concrete parts are modelled using elastic moduli of E_s and E_c, respectively. In the cracked state the nonlinear behavior of the interface is described through a stress-crack opening relationship:

$$\sigma = \begin{cases} E_s\epsilon & \text{Steel part} \\ E_c\epsilon & \text{concrete part} \\ \sigma_w(w) = g(w)f_t & \text{Interface in cracked state} \end{cases} \tag{5}$$

The stress-crack opening relationship is approximated by a bilinear softening curve, see Equation (6) and Figure 5.

$$g(w) = b_i - a_i w = \begin{cases} b_1 - a_1 w & 0 \le w < w_1 \\ b_2 - a_2 w & w_1 \le w \le w_2 \end{cases} \tag{6}$$

where $b_1 = 1$; while the limit w_1 is given by the intersection of the two line segments. The intersection of the second line segment and the abscissa is denoted w_2:

$$w_1 = \frac{1-b_2}{a_1-a_2} \quad , \quad w_2 = \frac{b_2}{a_2} \tag{7}$$

The deformation of the hinge is described through the angular deformation $\varphi = \varphi_s + \varphi_c$, cf. Figure 4. The mean value of the curvature for each part of the hinge can be expressed as

$$\kappa_s^* = 2\frac{\varphi_s}{s_s}; \quad \kappa_c^* = 2\frac{\varphi_c}{s_c} \tag{8}$$

The distribution of the longitudinal strains at the depth y can be expressed by the mean curvature
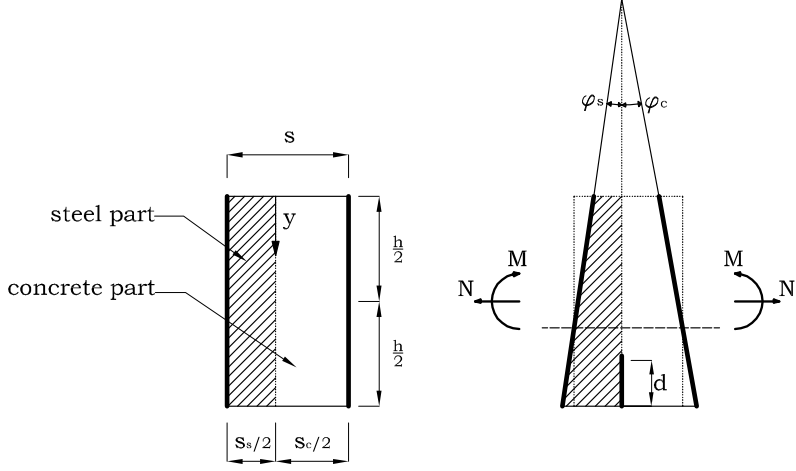
Figure 4: Geometry, loading and deformation of the bimaterial hinge element
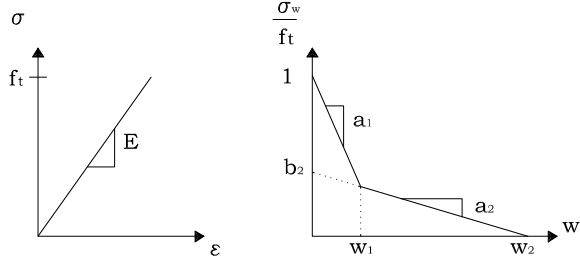
Figure 5: Definition of parameters of the bilinear stress-crack opening relationship

$$\epsilon_s = (y - y_0)\kappa_s^*; \qquad \epsilon_c = (y - y_0)\kappa_c^* \tag{9}$$

In the case where the strip has cracked, the deformation $u(y)$, can be obtained as the sum of the elastic deformation and the crack opening w.

$$u(y) = \frac{s_s}{2}\frac{\sigma_w}{E_s} + \frac{s_c}{2}\frac{\sigma_w}{E_c} + w \tag{10}$$

By combining equations (9) and (10), we may write

$$\sigma_w = \left((y - y_0)(\varphi_s + \varphi_c) - w\right)2\left(\frac{s_s}{E_s} + \frac{s_c}{E_c}\right)^{-1} \tag{11}$$

This solution can easily be implemented in the original mono-material solution by Olesen (2001), (briefly sketched in the Appendix). The ratio between the bimaterial elastic modulus, E^*, and the total band width is identified as

$$\frac{E^*}{s} = 2\left(\frac{s_s}{E_s} + \frac{s_c}{E_c}\right)^{-1} \tag{12}$$

The original solution is presented in terms of normalized properties, where the only modification lies in the third term.

$$\mu = \frac{6}{f_t h^2 t}M, \quad \rho = \frac{1}{f_t ht}N, \quad \theta = \frac{hE^*}{sf_t}\varphi, \quad \alpha = \frac{d}{h} \tag{13}$$

For any given value of the total angular deformation φ, the bending moment M and the external force N can be calculated. Since the crack propagation takes place in different stages, the solution is divided into four phases. Phase 0 represents the elastic state, followed by three cracked phases. These three phases represent softening: Linear, bilinear, and bilinear with stress-free tail. The solution is given in Olesen (2001).

Figure 6, shows the geometry and implementation of the cracked hinge in the WST specimen. As seen, the hinge is placed up-side down. It is noted that the load line (the center point of the roller bearings) and the level where CMOD is measured do not coincide. The distance from the bottom of the specimen to the load line is denoted d_2, where as the vertical distance to the CMOD line is denoted b, cf. Figure 6.
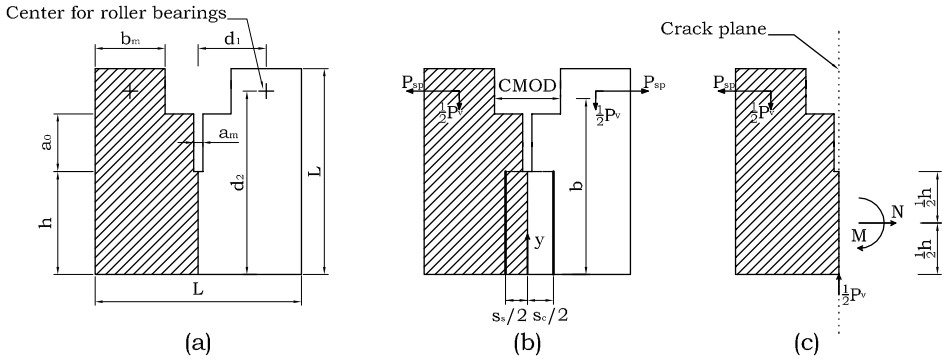
Figure 6: (a) Geometry and loading of the bimaterial WST specimen, (b) application of the hinge element to the bimaterial WST specimen, (c) loading.

Moving the wedge vertically downwards creates a force acting on the specimen. This force can be split into two forces acting at the center point of the roller bearing on each side of the specimen. The total load on the specimen consists of a vertical and a horizontal force, P_v and P_{sp} respectively. The self weight of the specimen is ignored since the influence can be neglected, see, e.g., Østergaard (2003).

The moment M and the normal force N acting at the cracking plane can be calculated using equilibrium. From Figure 6(c) it is seen that the moment and normal force is given by

$$N = P_{sp} \qquad (14)$$

$$M = P_{sp}\left(d_2 - \frac{h}{2}\right) + P_{sp}d_1 tan(\alpha_w) \qquad (15)$$

The CMOD, depends on three different contributions. The elastic deformation of the specimen causes an opening of CMOD, denoted δ_e. Second, a contribution δ_{COD} denotes the crack opening of the specimen. Finally, a contribution δ_g has to be taken into account since the line where CMOD is measured in the experiment is located differently than the actual crack mouth. Thus, CMOD is given by:

$$CMOD = \delta_e + \delta_{COD} + \delta_g \qquad (16)$$

Having a wedge splitting specimen consisting of one material, δ_e can be determined using handbooks on stress analysis, e.g. Tada et al. (1985). However, since the specimen differs in geometry and consist of two materials having different elastic moduli, the approximation formulaes by Tada et al. (1985) are not applicable. Using these formulas will produce an error on the determination of E_c of approximately 20%. For higher precision δ_e may simply be determined using a FE model of the adopted WST-geometry. This approach has been used here. Thus, the elastic contribution to the CMOD, δ_e, is calculated according to the following formula

$$\delta_e = \frac{1}{2}\frac{P_{sp}}{t}\nu_2\left(\frac{1}{E_s} + \frac{1}{E_c}\right) \qquad (17)$$

where t is the thickness of the specimen, and the term ν_2 is determined from a linear elastic FE analysis.
Opening of the crack mouth caused by the presence of the crack has been derived by Olesen (2001):

$$\delta_{COD} = \frac{sf_t}{E^*}\frac{1 - b_i + 2\alpha\theta}{1 - \beta i}, \qquad \beta_i = \frac{f_t a_i s}{E^*} \quad i \in [1,2] \qquad (18)$$

where the terms β_i and b_i must be chosen according to one of the three cracking phases. The third and final term δ_g, which is due to a geometrical amplification since there is a certain distance, $b - h$, from the crack mouth, located at h, to the line where CMOD is measured, located at b. The contribution can be found from

$$\delta_g = 2(b - h)\left(\frac{\delta_{COD}}{2\alpha h} - \frac{sf_t}{hE^*}\frac{\theta_{0-I}}{1 - \beta_1}\right) \qquad (19)$$

where θ_{0-I} represents the normalized angular deformation of the hinge at initiation of the crack. For further explanation see Østergaard (2003).

4   Inverse Analysis

Methods for the extraction of the constitutive properties of the cracked region of quasi-brittle materials has been investigated since Hillerborg et al. (1976) proposed the fictitious crack model in 1976. The methods have been analytically as well as numerically based and usually applied to pure concrete, employing the three point bending specimen. A successful approach was reported by Wittmann et al. (1987) in which a simple finite element based method proved applicable for the three point bending specimen. The output was a bilinear stress-crack opening curve. Another strategy presented by Kitsutaka (1997) yields a multi-linear curve based on an incremental approach linking specific parts of the load-displacement curve to specific parts of the stress-crack opening displacement curve. Lately, the proposed methods of inverse analysis tend to be more and more complex. Strategies based on evolutionary algorithms have been proposed Villmann et al. (2004), while also the Extended Kalman Filter procedure (EKF) has been applied by Bolzon et al. (2002). While complex methods may be justified for complex problems, inverse analysis of pure mode I cracking of concrete, assuming validity of the fictitious crack model, is in fact a simple problem and should be treated as such.

A simple approach to the inverse analysis of the concrete-steel interface is application of the semi-analytical hinge model proposed by Olesen (2001), utilizing e.g. the familiar simplex optimization algorithm. A method based on the above techniques applied to pure concrete employing the WST was proven to be fast and reliable in (Østergaard 2003). As will be shown in the present paper, this is also the case for the concrete-steel interfacial problem. The method proposed generally yields the solution to the inverse problem in a matter of minutes rather than hours or days for the more complex methods or FE-methods.

Equations (1)-(18) form the basis for interpretation and inverse analysis of the WST. The interpretation proceeds by balancing the internal moment and normal force with the external ones. The idea in the inverse analysis is to use a stepwise algorithm, where the optimization problem is solved in steps corresponding to the different phases of crack propagation. First, the optimization is conducted in the elastic phase with the modulus of elasticity of the concrete part as the only free parameter, and only considering the observations belonging to the elastic phase. This first part, named Step I, see Equation 20, will result in a fast and reliable determination of the modulus of elasticity. It is important to realize that the initial guess on the tensile strength will determine how many observations to include in the optimization. But with reasonable initial guesses and by globally re-running the optimization process (including all steps) this is a minor problem, since the global iterations will converge at the true phase change point. Having determined an estimate for the modulus of elasticity, the next step is to formulate an optimization strategy for the cracked phases. It turns out that the best strategy is to separate the problem into two, such that f_t and a_1 are determined first (Step II), while a_2 and b_2 are determined subsequently (Step III). This is due to results showing that local minima may be avoided using this approach. Note in this context that many methods

for inverse analysis are prone to finding local minima, see e.g. Ulfkjær & Brincker (1993), Villmann et al. (2004) and Bolzon et al. (2002). With the proposed method, local minima are entirely avoided. In contrast to Step I, all observations must be included in the optimization for Step II and III. If only observations belonging to the actual phase (e.g. phase I) were considered, a spurious solution may be found. This solution represents the minimum where the constitutive parameters have been selected such that no observation belongs to the considered phase.

Note that it is not possible in the cracked stages to determine both the bimaterial modulus of elasticity, E^* and the bimaterial hinge width s from Equation 12. However, this is no problem since only the ratio E^*/s enters the calculations, see Olesen (2001). Thus, assuming that the hinge width parameters s_c and s_s are known from an initial FEM-calibration, E_c is known from the initial optimization of the first slope of the load-CMOD curve, and that the steel modulus of elasticity is known a priori, the E^*/s-ratio may be calculated. This result is used for the determination of the constitutive parameters of the crack.

Utilizing all observations in the cracked phases, and using the mean square of differences between observations and predictions as an error norm, the optimization problem reads:

Step I - Determination of E$_c$

$$\min_{E} \ \frac{1}{N_{max}^0} \sum_{0}^{N_{max}^0} \left(P_{sp} - \hat{P}_{sp} \right)^2 \tag{20}$$

$$\text{subject to} \quad E > 0$$

Step II - Determination of f_t and a_1

$$\min_{(f_t, a_1)} \ \frac{1}{N_{max}} \sum_{0}^{N_{max}} \left(P_{sp} - \hat{P}_{sp} \right)^2 \tag{21}$$

$$\text{subject to} \quad f_t > 0$$

Step III - Determination of a_2 and b_2

$$\min_{(a_2, b_2)} \ \frac{1}{N_{max}} \sum_{0}^{N_{max}} \left(P_{sp} - \hat{P}_{sp} \right)^2 \tag{22}$$

where N_{max}^0 and N_{max} represent the last observation belonging to phase 0 and the total number of observations, respectively. The optimization is restricted such that only physical meaningful solutions are found ($E_c > 0$, $f_t > 0$ etc.). More details concerning the inverse analysis and the validation with regard to finite element analysis may be found in Østergaard (2003). The existence of local minima has been investigated by a large number of start guesses of the constitutive parameters and the results are clear: All starting guesses will eventually result in a convergence at the global minimum.

Table 1: Results from inverse analysis with 12 different materials together with the optimal choices of s_c and s_s. The number given on each place in the middle part of the table refers to the input value of the relevant constitutive parameter, while the number in parenthesis is the error on the determination of this value using the method of inverse analysis utilizing the s-parameters given to the right.

Material	f_t [MPa]	a_1 [mm^{-1}]	a_2 [mm^{-1}]	b_2 [-]	E_c [GPa]	E_s [GPa]	$\frac{s_c}{h}$	$\frac{s_s}{h}$
1	2 (8%)	10 (3%)	0.2 (-5%)	0.1 (-7%)	30 (-2%)	210	1.04	0.08
2	2 (2)	20 (-3)	0.2 (-7)	0.1 (-4)	30 (-2)	210	0.74	0.2
3	2 (4)	30 (-2)	0.2 (0)	0.1 (-1)	30 (-2)	210	0.86	0.25
4	2 (5)	40 (0)	0.2 (5)	0.1 (1)	30 (-3)	210	0.98	0.15
5	2 (3)	20 (-2)	0.6 (0)	0.1 (-4)	30 (-3)	210	0.8	0.2
6	2 (3)	20 (-2)	1.2 (2)	0.1 (-6)	30 (-3)	210	0.74	0.21
7	2 (4)	20 (-3)	0.2 (-1)	0.25 (-1)	30 (-2)	210	0.84	0.2
8	2 (4)	20 (-4)	0.2 (0)	0.4 (-1)	30 (-2)	210	0.9	0.18
9	2 (2)	20 (-22)	0.2 (1)	0.7 (1)	30 (-3)	210	0.83	0.18
10	2 (2)	20 (-3)	0.2 (-9)	0.1 (-6)	40 (-3)	210	0.77	0.19
11	2 (2)	20 (-3)	0.2 (-2)	0.1 (-2)	30 (-5)	60	1.22	0.11
12	2 (3)	20 (-3)	0.2 (-5)	0.1 (-4)	30 (-3)	120	0.94	0.17

The cracked hinge model is dependent on the width of the hinge in both the steel and the concrete parts. Thus, initially, a calibration is conducted in order to identify the most suitable values of these width parameters. This is done using a finite element model of the WST from which load-CMOD curves are generated for a number of different stress-crack opening curves. The selected values of the stress-crack opening profile and the error on the determination of these parameters through an inverse analysis using the optimal width parameters are given in Table 1. The optimal s-parameters have been determined by an optimization in which the the squared sum of differences between the predicted parameters and the input parameters has been minimized:

$$\min_{(s_c, s_s)} \sum \left(\left(\frac{\hat{f}_t - f_t}{f_t} \right)^2 + \left(\frac{\hat{a}_1 - a_1}{a_1} \right)^2 + ... + \left(\frac{\hat{E}_c - E_c}{E_c} \right)^2 \right) \qquad (23)$$

12

where $(\hat{f}_t, \hat{a}_1, \hat{a}_2, \hat{b}_2, \hat{E}_c)$ are the output values from the usual inverse analysis, see Equations 20-22, for the actual values of (s_c, s_s), while $(f_t, a_1, a_2, b_2, E_c)$ are the true values which have been entered into the finite element code to generate the load-CMOD curve.

The performance of the method of inverse analysis is striking. Only a few results produce errors above 5% while the majority of the results are within a error margin of 4% or better. It is not surprising since the hinge and the FE-models are quite similar. Disregarded effects in the hinge model are the stress concentration at the tip of the pre-sawn/cast notch and the shear stiffness of the material. The latter is not very important due the vanishing shear stresses (the problem is virtually symmetric), while the disregarded stress concentration results in an insignificant change of the curve at the load level of first crack (the crack initiates earlier in the FE-model, but this is almost invisible on the load-CMOD curve).

It is also encouraging that the s-values of the hinge are practically constant. The average values and the standard deviation, based on the results given in Table 1 are $(s_c, s_s) = (0.89 \pm 0.18, 0.14 \pm 0.05)$. This makes it possible to determine the width parameters once for all thereby making the method practically applicable. The actual results using constant s-values for the present materials are given in Table 2. Here it is noted that a few results are significantly less precisely determined, but also that the majority of results are still determined with a high precision (i.e. an error in the range of 5% or better).

Table 2: Results from inverse analysis with 11 different materials calculated using constant values of s_c and s_s. The number given on each place in the middle part of the table refers to the input value of the relevant constitutive parameter, while the number in parenthesis is the error on the determination of this value using the method of inverse analysis utilizing the s-parameters given to the right.

Material	f_t [MPa]	a_1 [mm^{-1}]	a_2 [mm^{-1}]	b_2 [-]	E_c [GPa]	E_s [GPa]	$\frac{s_c}{h}$	$\frac{s_s}{h}$
1	2 (6%)	10 (1%)	0.2 (-11%)	0.1 (-9%)	30 (-3%)	210	0.89	0.14
2	2 (5)	20 (0)	0.2 (-8)	0.1 (-6)	30 (-3)	210	0.89	0.14
3	2 (4)	30 (-1)	0.2 (0)	0.1 (-2)	30 (-3)	210	0.89	0.14
4	2 (3)	40 (-2)	0.2 (6)	0.1 (2)	30 (-2)	210	0.89	0.14
5	2 (5)	20 (0)	0.6 (5)	0.1 (-2)	30 (-3)	210	0.89	0.14
6	2 (5)	20 (0)	1.2 (61)	0.1 (39)	30 (-3)	210	0.89	0.14
7	2 (5)	20 (-1)	0.2 (-1)	0.25 (-2)	30 (-3)	210	0.89	0.14
8	2 (4)	20 (-4)	0.2 (0)	0.4 (-1)	30 (-3)	210	0.89	0.14
9	2 (3)	20 (-20)	0.2 (0)	0.7 (0)	30 (-2)	210	0.89	0.14
10	2 (4)	20 (-1)	0.2 (-9)	0.1 (-7)	40 (-4)	210	0.89	0.14
11	2 (-7)	20 (-15)	0.2 (-27)	0.1 (-12)	30 (-7)	60	0.89	0.14
12	2 (1)	20 (-6)	0.2 (-15)	0.1 (-8)	30 (-5)	120	0.89	0.14

13

It is important to realize that the results obtained by the method of inverse analysis are based on the entire load-CMOD curves, i.e. from onset of loading until the specimen has been fully separated. If the tails of the load-CMOD curves are omitted, the errors on the determination of the constitutive parameters will increase significantly. This is demonstrated in Figure 7, where the FEM generated P-CMOD curve has been truncated at different values of CMOD - and the inverse analysis subsequently has been conducted on the remaining curve. The parameter b_2 has been selected since it only enters the equations after the crack profile has turned into a bilinear function - thus a determination of this parameter (likewise a_2) requires more P-CMOD curve to be known than e.g. the tensile strength, f_t, or in particular modulus of elasticity, E_c, does. As Figure 7 shows, the determination of b_2 by the method of inverse analysis is spurious as long as the P-CMOD curve is truncated before the second point of transition. However, only a few data points after this transition point are necessary to make the algorithm come up with a reasonable result, but the quality of the result continues to improve each time a new portion of the P-CMOD curve is included. It is therefore recommended to obtain as much of the P-CMOD curve as possible in order to increase the accuracy of the results. Note also that where a total CMOD of 4 mm seems sufficient for material no. 8, this will not be the case for e.g. material no. 9 where the high value of b_2 results in a far more ductile response of the material. It is more relevant to require that for example the experiment is continued until the load is less than 0.5% of the peak load.
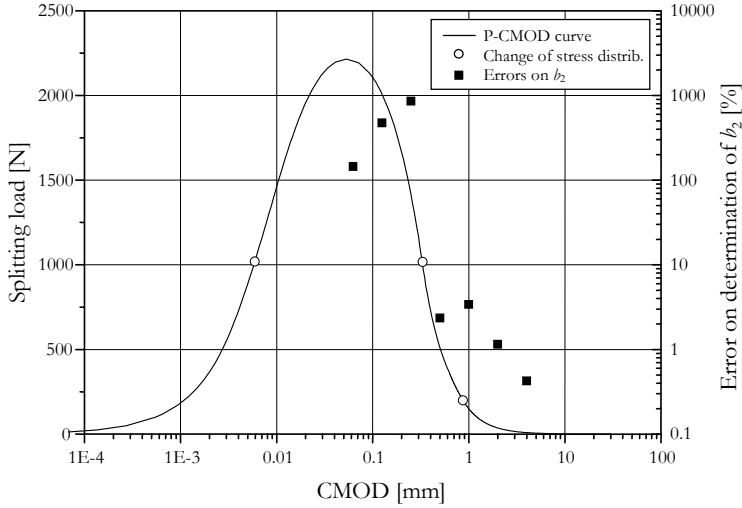
Figure 7: Load-CMOD curve for material no. 8 as generated by FEM. The hollow circles mark the transition points where, respectively, the crack initiates, changes from linear to bilinear stress distribution, and changes from bilinear to bilinear stress distribution with a stress free tail. The solid squares mark the error on the determination of b_2, given that the FEM-curve is truncated corresponding to the x-coordinate of the square.

5   Experimental Results

The use of the WST to determine the fracture properties of a steel-concrete interface using the inverse analysis described in the previous section is illustrated. Full concrete and bimaterial WST specimens are tested and their fracture properties are compared.

The concrete used in this study was composed of cement, coarse aggregates 16mm maximum grain size, fine aggregates, water and various admixtures, such as, fly ash, silica fume and plasticizer to improve the fresh properties of the mixture. The mix design is given in Table 3.

The mix is optimized for self-compacting properties and does therefore not need mechanical vibration after casting. This is believed to optimize the steel-concrete bond, see e.g. (Schiessl & Zilch 2001). In the case of the bimaterial WST specimens, the steel surface was sandblasted prior to casting to improve the bond and minimize the risk of defects. The test program consists of 12 test specimens in total, six concrete and six concrete-steel specimens. Specimens where cast in two batches with 3 of each type per batch.

Sample results of the WST experiments are given in Figure 8, where the splitting force P_{sp} versus CMOD is plotted. The Figure also compares results on both the full concrete and bimaterial WST specimens.

In the case of bimaterial WST specimens, cracking took place close to the physical bound-

ary between the steel and concrete block. This behavior indicates that the actual boundary is stronger than the cement paste itself. In each bimaterial test, patches of cement paste was left on the steel block. Figure 9 shows an actual picture of a bimaterial specimen after testing. The left part of the WST specimen is the steel block. It is clearly seen that some cement paste is still bonded to the steel block.

Table 3: Mix design

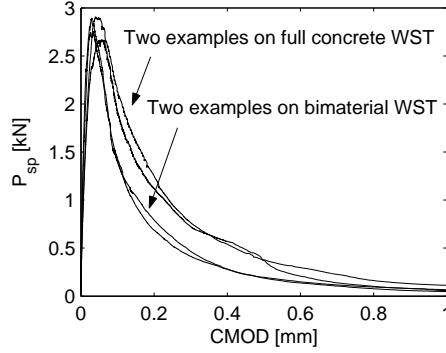| Mix	kg/m^3
Cement (Portland, CEM I 52.5)	245
Fly ash	94.5
Silica fume	10.5
Water	142.9
Air entraining agent	0.4
Plasticizer	4.2
Sand, 00-04 mm	752.6
Aggregates, 04-08 mm	450.6
Aggregates, 08-16 mm	594.0

Figure 8: Example on experimental data shown as the splitting load P_{sp} vs. $CMOD$
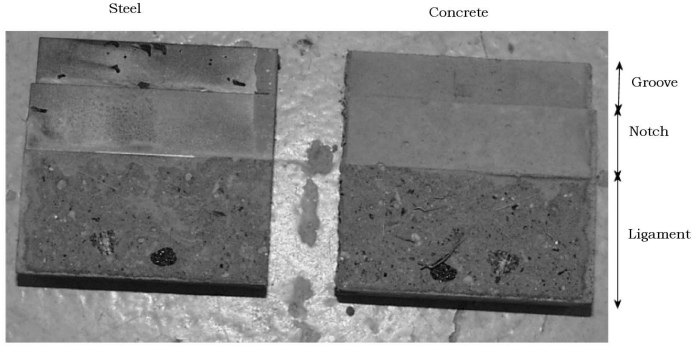
Figure 9: Actual picture of a bimaterial WST specimen after testing. The left part is the steel block.

5.1 Results from Inverse Analysis

The results of the inverse analysis on the bimaterial WST specimens are shown in Table 4 while the results from the tests on the full concrete specimens are shown in Table 5. The inverse analysis of the full concrete specimens are performed according to the method described in Østergaard (2003). Note that for two tests in batch no. 1 bearing failure occurred and no results are available.

Table 4: Results from inverse analysis on the steel-concrete WST specimens. *Note failure of bearing.

Batch	f_t [MPa]	a_1 [mm^{-1}]	a_2 [mm^{-1}]	b_2 [-]	E_s [GPa]	G_f [J/mm^2]
1	3.1	21	1.5	0.26	33	0.12
1	2.9	20	1.7	0.31	33	0.12
1*	-	-	-	-	-	-
Mean 1	3.0	20.5	1.6	0.29	33	0.12
2	2.3	21	1.4	0.26	29	0.088
2	1.8	15	2.7	0.38	26	0.076
2	2.1	22	3.3	0.40	35	0.071
Mean 2	2.1	19	2.5	0.35	30	0.078

In general, experimental results obtained in the present study are satisfactory. As a general result the bimaterial WST specimens produced a lower fracture energy in comparison with the full concrete specimen. Same observations have been made by Chandra Kishen & Saouma (2004) using the WST. They observed that limestone-concrete specimens exhibited a lower fracture energy than comparable full concrete specimens. Regarding the

Table 5: Results from inverse analysis on full concrete WST specimens. *Note failure of bearing.

Batch	f_t [MPa]	a_1 [mm^{-1}]	a_2 [mm^{-1}]	b_2 [-]	E_s [GPa]	G_f [J/mm^2]
1	3.0	15	1.5	0.35	31	0.17
1	3.1	13	1.7	0.38	36	0.18
1*	-	-	-	-	-	-
Mean 1	3.1	14	1.6	0.36	34	0.17
2	3.6	16	4.2	0.62	21	0.19
2	3.4	15	3.0	0.46	23	0.16
2	3.6	11	0.8	0.20	24	0.21
Mean 2	3.6	14	2.7	0.42	23	0.19

results in Tables 4 and 5, it should be noted that there exist some scatter between the two batches. No direct evidence exist in order to fully understand the difference but some indications regarding the behavior of the mix design might explain the difference. By comparing the results of the tests on the concrete specimens it is noted that the tensile strength f_t is higher in batch no. 2 than in batch no. 1. The opposite is the case with the bimaterial tests. A poor bond, due to possible shrinkage, at the edge of the bimaterial specimens might be the explanation. This is further supported by the visual inspection of the bimaterial specimens after testing, which revealed clear signs of shrinkage on the bimaterial specimens in batch no. 2.

5.2 Discussion

The results from the bimaterial and concrete specimens can be viewed in a normalized stress versus crack opening diagram. Figure 10 shows, for each specimen type, the average stress-crack opening relationship for batch no. 1 and batch no. 2, respectively.
It is seen that for each batch a consistent pattern is observed. The bimaterial tests exhibits a higher slope in the first part of the stress-crack opening relationship, denoted a_1, cf. Figure 5. In general, the shape of the $\sigma - w$ curve is influenced by the size of aggregates and the matrix/aggragate bond. When a crack propagates through the concrete the fracture strength of the individual parts, matrix/aggregates and their bond, determines if the crack propagates through the aggregate, the matrix or through a combination of both. In the case of a poor cement paste or a poor matrix/aggregate bond, aggregate pull out is often observed. This behavior leads to a long tail of the $\sigma - w$ curve. The present mix design, Table 3, consist of a mix with optimized bonding properties and as a result the cracking has lead to aggregate breakage. As observed in Figure 10 the bimaterial specimens show higher stress drop in the beginning of the $\sigma - w$ curve. This is due to the wall-effect, which is present in the region close to the steel-concrete boundary. Due to the wall-effect, crack propagation in the bimaterial specimens takes place in the matrix whereas in the full concrete specimens cracking takes place in a combination of aggragates/matrix.
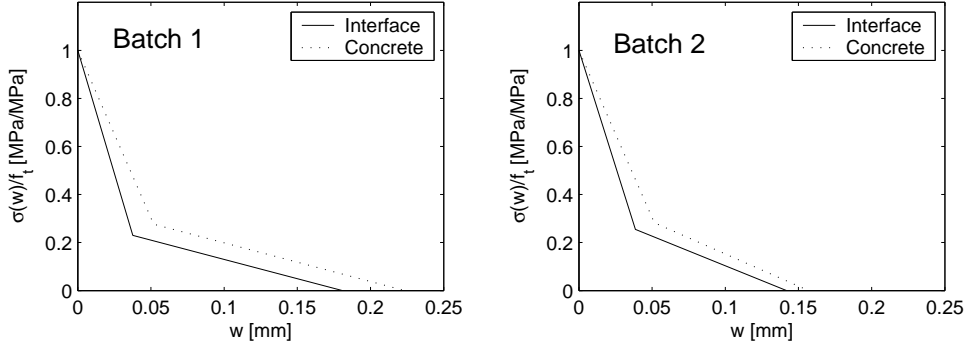
18

Figure 10: Stress-crack opening relationship for (a) batch no. 1 and (b) batch no. 2 determined using the inverse analysis

The higher stress drop in the beginning of the stress-crack opening relationship might be due to the fact that the matrix might be more brittle compared to that of aggregates. The wall-effect and the two different crack paths for concrete and bimaterial specimens are illustrated in Figure 11. As illustrated, close to the steel block a crack will mainly propagate in the matrix. On the contrary, path 2, consist of a combination of matrix and aggregates as observed in the full concrete WST specimens.
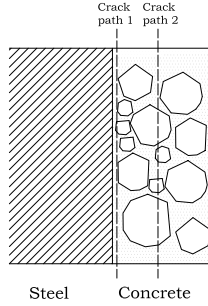

Figure 11: Schematic illustration of the wall-effect. A crack path (Path 1) close to a steel wall might be dominated by matrix crack propagation where as in the case of crack propagation in the concrete material (path 2) crack propagation takes place in combination of aggregates and matrix.

6   Conclusions

A test set-up combined with a fast and simple inverse analysis to determine the fracture properties of a bimaterial interface has been presented. Using the well known WST specimen as the basis set-up, a stable test has been established. The bimaterial cracked hinge model has proven applicable in this connection.

It is concluded that the optimization strategy is always able to find the global minimum for the FEM curves analyzed in this study. Two important issues are the width of the hinge and the amount of data recorded in the experiment. Using FEM, an optimum hinge width ratio was estimated for each of the 12 different theoretical materials analyzed. Applying the average hinge width ratio, the majority of the results show an acceptable error. Finally, the study shows the effect of varying the amount of recorded data, which concludes the significance of recording data throughout the entire experiment, from the very start to almost zero load.

The proposed set-up and inverse analysis has been employed to a test program aimed at determining the steel-concrete interface properties. The experimental set-up and the method of inverse analysis could well be applied for the investigation of other interface problems, e.g. mortar/rock, etc.

The experimental program consisted of full concrete and steel-concrete specimens. It can be concluded from the tests that interfacial cracking is influenced by the wall effect. The bimaterial specimens show a steeper slope in the beginning of the $\sigma - w$ relationship due to the more brittle behavior of the matrix compared to that of the aggregates used in this study.

References

Bolzon, G., Fedele, R. & Maier, G. (2002), 'Parameter identification of a cohesive crack model by kalman filter', *Computer Methods in Applied Mechanics and Engineering* **191**(25–26), 2847–2871.

Brühwiler, E. & Wittmann, F. H. (1990), 'The wedge splitting test, a method of performing stable fracture mechanics tests', *Engineering Fracture Mechanics* **35**, 117–126.

Chandra Kishen, J. M. & Saouma, V. E. (2004), 'Fracture of rock-concrete interfaces: Laboratory tests and applications', *ACI Structural Journal* **101**(3), 325–331.

Charalambides, P. G., Lund, J., Evans, A. G. & McMeeking, R. M. (1989), 'A test specimen for determining the fracture resistance of bimaterial interfaces', *Journal of Applied Mechanics* **56**, 77–82.

DIANA (2003), *DIANA User's Manual – Release 8.1*, june edn, TNO Building and Construction Research, P.O. Box 49, 2600 AA Delft, The Netherlands.

Hillerborg, A., Modéer, M. & Petersson, P. (1976), 'Analysis of crack formation and crack growth in concrete by means of fracture mechanics and finite elements', *Cem. Concr. Res.* **6**(6), 773–782.

Kitsutaka, Y. (1997), 'Fracture parameters by polylinear tension-softening analysis', *Journal of Engineering Mechanics* **123**(5), 444–450.

Linsbauer, H. N. & Tschegg, E. K. (1986), 'Fracture energy determination of concrete with cube shaped specimens (in german)', *Zement und Beton* **31**, 38–40.

Olesen, J. F. (2001), 'Fictitious crack propagation in fiber-reinforced concrete beams', *Journal of Engineering Mechanics* **127**(3), 272–280.

Østergaard, L. (2003), Early-Age Fracture Mechanics and Cracking of Concrete. Experiments and Modelling, PhD thesis, Department of Civil Engineering, Technical University of Denmark, Lyngby, Denmark.

Pedersen, C. (1996), New production processes, materials, and calculation techniques for fiber reinforced concrete pipes, PhD thesis, Department of Structural Engineering and Materials, Technical University of Denmark, Lyngby, Denmark.

RILEM TC-108 (1996), *Interfacial Transition Zone in Concrete*, RILEM Report 11, Chapman and Hall.

Rossi, P., Brühwiler, E., Chhuy, S., Jenq, Y.-S. & Shah, S. P. (1991), Fracture properties of concrete as determined by means of wedge splitting tests and tapered double cantilever beam tests, *in* S. Shah & A. Carpinteri, eds, 'Fracture Mechanics Test Methods for Concrete', Chapmann & Hall, chapter 2, pp. 87–128.

Schiessl, A. & Zilch, K. (2001), 'The effect of the modified composition of SCC on shear and bond behavior', *Proceedings of the Second International Symposium on self-Compacting Concrete, Tokyo* pp. 501–506.

Soares, B. J. & Tang, T. (1998), 'Bimaterial brazilian specimen for determining interfacial fracture toughness', *Journal of Engineering Fracture Mechanics* **59**(1), 51–71.

Stang, H. & Olesen, J. F. (1998), On the interpretation of bending tests on frc materials, *in* 'FRAMCOS-3', Vol. I, Aedificatio Publishers, Freiburg, Germany, pp. 511–520.

Stang, H. & Olesen, J. F. (2000), A fracture mechanics-based design approach to frc, *in* '5th RILEM Symp. on Fiber-Reinforced Concrete', BEFIB.

Tada, H., Paris, P. & Irwin, G. (1985), *The stress analysis of cracks handbook*, Paris Productions Incorporated, 226 Woodbourne DR., St. Louis, Missouri, USA.

Ulfkjær, J. P. & Brincker, R. (1993), Indirect determination of the σ-w relation of HSC through three-point bending, *in* 'Fracture and Damage of Concrete and Rock - FCDR-2', E & FN Spon, pp. 135–144.

Ulfkjær, J., Krenk, S. & Brincker, R. (1995), 'Analytical model for fictitious crack propagation in concrete beams', *Journal of Engineering Mechanics* **121**(1), 7–15.

Villmann, B., Villmann, T. & Slowik, V. (2004), Determination of softening curves by backward analyses of experiments and optimization using an evolutionary algorithm, *in* V. C. Li, C. K. Y. Leung, K. J. Willam & S. L. Billington, eds, 'Proceedings of the Fifth International Conference on Fracture Mechanics of Concrete and Concrete Structures/Vail, Colorado/USA/12-16 April', Vol. 1, Ia-FraMCoS, Ia-FraMCoS, pp. 439–446.

Walter, R., Gimsing, N. & Stang, H. (2004), 'Composite steel-concrete orthotropic bridge deck', *10th Nordic Steel Construction Conference, Copenhagen, Denmark, pp.519-530* .

Walter, R., Olesen, J. F. & Stang, H. (2005), 'Interfacial mixed mode model', *In: The 11th International Conference on Fracture, Turin, Italy* .

Wang, J. & Maji, A. K. (1995), Experimental studies and modeling of the concrete/rock interface, *in* B. O. & W. M., eds, 'Interface Fracture and Bond', ACI SP-156, pp. 45–68.

Wernersson, H. (1994), 'Fracture characterization of wood adhesive joints', *Report TVSM-1006, Lund University, Division of Structural Mechanics* .

Williams, M. L. (1959), 'The stress around a fault or crack in dissimilar media', *Bulletin of the Seismological Society of America* **49**(**2**), 199–204.

Wittmann, F. H., Roelfstra, P. E., Mihashi, H., Huang, Y.-Y. & Zhang, X.-H. (1987), 'Influence of age of loading, water-cement ratio and rate of loading on fracture energy of concrete', *Materials and Structures* **20**, 103–110.

7 Appendix

Considering the solution of the cracked hinge model, this appendix gives a short description of the original solution by Olesen (2001). Analysis of the hinge element makes it possible to determine the external normal force N and bending moment M for any given value of the angular hinge deformation φ, as shown for the bimaterial specimen in Figure 4. The problem is solved in four phases, one for each state of crack propagation. Phase 0 represents the elastic state, where no crack has formed, while phases I, II and III represent different stages of propagation (linear, bilinear and bilinear with stress-free tail). The solution is presented in terms of normalized properties, where the following normalizations are used:

$$\beta_1 = \frac{f_t a_1 s}{E}, \qquad \beta_2 = \frac{f_t a_2 s}{E}, \qquad c = \frac{(1 - b_2)(1 - \beta_1)}{\beta_2 - \beta_1} \tag{24}$$

$$\mu = \frac{6M}{f_t h^2 t}, \qquad \rho = \frac{N}{f_t h t}, \qquad \theta = \frac{hE\varphi}{s f_t}, \qquad \alpha = \frac{d}{h} \qquad (25)$$

The hinge solution is expressed in terms of the normalized crack depth α and the normalized moment μ as functions of the normalized hinge deformation θ and the normalized normal force ρ:

Elastic phase: $0 \leq \theta \leq 1 - \rho$

$$\alpha = 0 \qquad (26)$$
$$\mu = \theta \qquad (27)$$

Phase I: $1 - \rho < \theta \leq \theta_{\text{I-II}}$:

$$\alpha = 1 - \beta_1 - \sqrt{(1-\beta_1)\left(\frac{1-\rho}{\theta} - \beta_1\right)} \qquad (28)$$

$$\mu = 4\left(1 - 3\alpha + 3\alpha^2 - \frac{\alpha^3}{1-\beta_1}\right)\theta + (6\alpha - 3)(1 - \rho) \qquad (29)$$

Phase II: $\theta_{\text{I-II}} < \theta \leq \theta_{\text{II-III}}$:

$$\alpha = 1 - \beta_2 - \frac{1-b_2}{2\theta} - \sqrt{(1-\beta_2)\left(\frac{(1-b_2)^2}{4\theta^2(\beta_1 - \beta_2)} - \beta_2 + \frac{b_2 - \rho}{\theta}\right)} \qquad (30)$$

$$\mu = 4\left(1 - 3\alpha + 3\alpha^2 - \frac{\alpha^3}{1-\beta_2}\right)\theta + (6\alpha - 3)(1 - \rho)$$
$$- \frac{(1-b_2)\left(3\alpha^2 - \left(\frac{c}{2\theta}\right)^2\right)}{1 - \beta_2} \qquad (31)$$

Phase III: $\theta_{\text{II-III}} < \theta$:

$$\alpha = 1 - \frac{1}{2\theta}\left(1 + \sqrt{\frac{(1-b_2)^2}{\beta_1 - \beta_2} + \frac{b_2^2}{\beta_2} - 4\rho\theta}\right) \qquad (32)$$

$$\mu = 4\left(1 - 3\alpha + 3\alpha^2 - \alpha^3\right)\theta + (6\alpha - 3)(1 - \rho) - 3\alpha^2$$
$$+ \frac{1}{4\theta^2}\left(1 - \frac{b_2}{\beta_2}\right)\left(1 - \frac{b_2}{\beta_2} + c\right)\left(1 + \frac{\beta_1 c}{1 - \beta_1}\right) + \left(\frac{c}{2\theta}\right)^2 \qquad (33)$$

23

In terms of θ the points of transitions between phases are given as follows

$$\theta_{0-I} = 1 - \rho \tag{34}$$

$$\theta_{I-II} = \frac{1}{2}\left(1 - \rho - c + \sqrt{(1 - \rho - c)^2 + \frac{c^2}{\beta_1 - 1}}\right) \tag{35}$$

$$\theta_{II-III} = \frac{1}{2}\left(\rho(\beta_2 - 1) + \frac{b_2}{\beta_2} + \sqrt{\rho^2(\beta_2 - 1)^2 + 2\rho(\beta_2 - 1)\frac{b_2}{\beta_2} + \frac{(1 - b_2)^2}{\beta_1 - \beta_2} + \frac{b_2^2}{\beta_2}}\right) \tag{36}$$

The crack mouth opening displacement CMOD is given by:

$$\text{CMOD} = \frac{s f_t}{E} \frac{1 - b_i + 2\alpha\theta}{1 - \beta_i} \tag{37}$$

where:

$$(b_i, \beta_i) = \left\{ \begin{array}{ll} (1, \beta_1) & \text{in Phase I} \\ (b_2, \beta_2) & \text{in Phase II} \\ (0, 0) & \text{in Phase III} \end{array} \right. \tag{38}$$

Notation

α	normalized depth of fictitious crack
α_w	angle of wedge
$\beta_1, \beta_2, \zeta_1, \zeta_2$	normalized fracture parameters
$\delta_e, \delta_g, \delta_{COD}$	contributions to CMOD
δ_n	normal crack deformation

δ_s	crack sliding deformation
ϵ	strain
ϵ_c, ϵ_s	strain of concrete and steel part
κ	curvature
κ_c^*, κ_s^*	mean curvature of concrete and steel part
μ	normalized cross sectional moment
ρ	normalized cross sectional normal force
σ, σ_w	normal stress
τ	shear stress
θ	normalized hinge rotation
θ_{0-I}	point of transition between phase 0 and I
θ_{I-II}	point of transition between phase I and II
θ_{II-III}	point of transition between phase II and III
φ	angular deformation
φ_c, φ_s	angular deformation of concrete and steel part
a_0, a_m	coordinates for the notch
a_1, a_2, b_1, b_2	parameters in the bilinear stress-crack opening relationship
b	distance to line of CMOD-measurement
b_m	width of top specimen
c	constant
d	depth of crack
d_1, d_2	coordinates for the load point
D_{ij}	stiffness components for interface description
E^*	bimaterial elastic modulus
E_c	elastic modulus of concrete
E_s	elastic modulus of steel
f_t	tensile strength
$g(w)$	normalized function describing shape of stress-crack opening relationship
G_f	fracture energy
G_f^I	pure mode I energy
G_f^{II}	pure mode II energy
h	height of hinge and ligament

K_{1c}	mode I stress intensity factor
K_{2c}	mode II stress intensity factor
L	side length of WST-cube
M	cross sectional moment
N	cross sectional normal force
N_{max}	number of experimental observations
P_v	vertical load
P_{sp}	split load
s	total hinge width
s_c, s_s	hinge width - concrete and steel part
t	thickness of specimen
u	horizontal displacement of load point
w	crack opening
w_1, w_2	crack opening limits in the bilinear stress-crack opening relationship
y	coordinate along crack direction
y_0	depth of neutral axis

Paper III

Cement-Based Overlay in Negative Bending - Experimental and FEM Studies

Cement-Based Overlay in Negative Bending - Experimental and FEM Studies

Rasmus Walter*, John F. Olesen*, Victor Li** & Henrik Stang*

*Department of Civil Engineering, Technical University of Denmark, DK-2800 Kgs. Lyngby, Denmark, e-mail: rw@byg.dtu.dk

**Department of Civil and Environmental Engineering, The University of Michigan, Ann Arbor, MI, 48109-2125, USA

Abstract

A new type of composite bridge deck is currently under research. The concept is to achieve composite action by the adhesion between a thin layer of cement-based material cast on a steel plate. Of special concern is the performance of the composite deck in negative bending. Based on experiments and a nonlinear 2D finite element model a study has been conducted in relation to vertical cracking of the overlay and interfacial cracking (debonding) between the overlay and steel plate. Three types of cement-based composites, Fiber Reinforced Concrete (FRC), Fiber Reinforced Densit® (FRD) and Engineered Cementitious Composite (ECC) have been tested as overlay material and compared. Finally, the paper shows modeling of the test set-up applying the different materials. The modeling is carried out using nonlinear fracture mechanics and the Finite Element Method (FEM). A good correlation between experimental and numerical results is obtained. The study shows, both numerically and experimentally, that debonding is related to macro cracking of the overlay.

Keywords Composite beam, cracking, debonding, overlay, FEM, Fibre reinforced concrete.

1   Introduction

A large number of steel bridge decks, in particular steel orthotropic bridge decks, suffer significantly from increased traffic intensity and higher wheel loads. Stress concentrations and large amplitudes of stresses caused by traffic give rise to fatigue problems in welded joints and surfacing, see, e.g., Kolstein & Wardenier (1998), (1999). When improving the fatigue behavior of a bridge deck, one strategy is to reduce the stress range in the fatigue sensitive details. Traditional road pavement may contribute to dispersion of concentrated

wheel loads, however, traditional asphaltic layers are characterized by viscoelastic behavior and are strongly temperature dependent, thus their contribution to distribution of concentrated loads might be insufficient. A promising solution might be to stiffen the structure by casting a cement-based overlay to form a top composite plate. A typical stiffening solution consists of a 40-60 mm layer of fiber reinforced cement-based material bonded to the steel plate see, e.g., Walter et al. (2004). Whereas conventional composite constructions achieve composite action by mechanical fasteners, the idea here is to achieve composite action only through adhesion. The adhesion between the cement-based overlay and steel is enhanced by sand blasting of the steel plate, creating a clean surface and minimizing the risk of defects. For this particular system, debonding of the overlay is of special interest since the composite strength is closely related to a fully bonded structure. The debonding mechanism is significantly influenced by vertical cracking of the overlay. During flexural cracking of the overlay, the distribution of shear and normal stresses along the steel-concrete interface changes dramatically from that of the elastic phase. In the fracture process zone of an interfacial crack, high stress concentrations develop in a plane perpendicular to the crack and consequently lead to debonding.

Debonding is a well-known problem from repair of existing structures by thin cement-based overlays, see, e.g., Granju (2001), (1996). It is shown that cracking of the overlay induces high interfacial tensile stresses leading to debonding between the two materials. Once initiated, the interfacial crack will propagate in a mixed mode characterized by tensile and shear stresses along the interface. The use of fibers in the overlay might be beneficial in order to increase the vertical crack resistance and consequently reduce the risk of debonding. This study aims at investigating the hypothesis that debonding is closely related to cracking of the overlay.

Focus of this study is on a small structural element, a composite beam, exposed to three point bending. The structural performance governed by the composite action is investigated. In a design situation applying an overlay to stiffen a steel deck, one would be concerned about several factors. Different kinds of loading might have an impact on the strength and durability of a stiffening overlay. In particular, mechanical/environmental loading and shrinkage of the overlay would need to be taken into account when designing a stiffening overlay. Environmental loading such as temperature gradients and shrinkage of the overlay is not considered in this study. Until now, experimental tests on composite beams with overlay materials have been performed, although mostly with the overlay on the compressive side of the beams and with focus on concrete-concrete bonds. Silfwerbrand (1984) investigated test specimens (concrete overlay on concrete beams) exposed to three point bending with focus on interface bonding agents and failure modes. The significance of the present study is to test the structural performance of different fiber reinforced composites bonded to steel.

To analyze the experiments, numerical modeling of the test set-up is carried out. Furthermore, the effect of matrix toughness and the fiber bridging effect on debonding will be analyzed. Three fiber reinforced cement-based overlays are tested and modeled numerically. Ordinary Fiber Reinforced Concrete (FRC), Fiber Reinforced Densit® (FRD) and an Engineered Cementitious Composite material (ECC) are all tested and modeled.

The modeling work, carried out using FEM, adopts the so-called Fictitious Crack Model (FCM) for the tension softening behavior of the overlay materials developed by Hillerborg et al. (1976). The advantage of the model is the simplicity and the good correlation between theory and experimental tests. The two types of cracking - vertically through the overlay and interface debonding between steel and overlay - will be described by the FCM. For small crack openings, an interfacial fracture between steel and concrete shows the ability to transfer stresses across the crack. The experiments are modeled in a two-dimensional nonlinear finite element model to simulate the overlay cracking and debonding. Input for the modeling work is determined independently using uniaxial tension tests.

2   Research Significance

This study contributes to ongoing research projects concerning the improvement of fatigue life of traditional orthotropic steel bridge decks. The present work is concerned with the performance of three different types of fiber reinforced cementitious composites applied as a stiffening overlay to steel bridge decks. The work is based on experimental as well as numerical studies, and it contributes to the understanding of the composite action of different types of fiber based cementitious overlays on steel plates, with emphasis on fracture processes in the overlay.

3   Experimental Procedures

3.1   Materials and Specimen Preparation

The well-known advantage of fiber reinforced concrete is its ability to sustain major deformation after the first crack is formed. The fibers will typically remain unbroken after crack initiation and the fibers that cross a crack will resist further opening. Depending on the crack bridging effect, fiber reinforced composites can show different failure modes. If the average fiber bridging effect is increasing during crack initiation and propagation, multiple cracks can form. This behavior is also known as strain hardening. On the other hand, if the fibers cannot carry more load after the formation of the first crack, then further deformation is governed by opening of a single crack. This behavior is called tension softening. In the following, composite beams comprising materials with tension softening and strain hardening behavior are examined. Two materials, classified as tension softening materials, are tested: Fiber Reinforced Concrete (FRC) and Fiber Reinforced Densit® (FRD). A material known as Engineered Cementitious Composite (ECC) is also tested and can be characterized as a strain hardening material, see, e.g., Li (2002).

The ECC material contains 2% by volume poly-vinyl-alcohol (PVA) fibers, with a length of 8 mm, in random orientation along with standard mortar matrix components, cement, fine aggregate (0.3 mm maximum grain size), water, and various admixtures to improve the fresh properties of the mixture, cf. Table 1. The ECC material exhibits strain-

Cement [kg/m^3]	Water [kg/m^3]	Super Plasticizer [kg/m^3]	Fly ash [kg/m^3]	Sand 0.1-0.3 mm [kg/m^3]	PVA fibers l_f=8 mm [kg/m^3]
583	298	17.5	700	467	26

Table 1: Mix design for ECC

Cement [kg/m^3]	Water [kg/m^3]	Fly ash [kg/m^3]	Silica Fume [kg/m^3]	Super Plasticizer [kg/m^3]	Aggr. 0-4 mm [kg/m^3]	Aggr. 4-8 mm [kg/m^3]	Aggr. 8-16 mm [kg/m^3]	Steel fibers l_f=30 mm [kg/m^3]
245	140	94.5	10.5	2.8	753.9	452.9	570.3	78

Table 2: Mix design for FRC

hardening behavior in tension. This behavior is achieved through a micro-mechanic design approach, (Li 2002). The FRC material used in this study was composed of cement, coarse aggregates (16 mm maximum grain size), fine aggregates, admixtures, and water. A fiber volume of 1% hooked-end steel fibers, with a length of 30 mm, was applied, cf. Table 2 for mix design. The FRD material contains a maximum grain size of 2 mm, 2% by volume steel fiber, with a length of 8 mm, and Densit® binder, type Joint-Cast, cf. Table 3 for mix design. All the materials used in this study exhibit self-compacting properties and no mechanical vibration is needed during casting. It is believed that this feature is of great importance to achieve a good bond between the overlay and underlying steel plate. Vibration might cause water to separate from the mix and create a weak interface between the fresh mix and steel plate. All the steel plates were prepared by an initial sand blasting followed by casting of the cement-based layer within 24 hours. Sand blasting technique is adopted to ensure a clean surface with a minimum risk of adhesion defects.

Densit®Binder Type: Jointcast [kg/m^3]	Water [kg/m^3]	Aggregates 0-2 mm [kg/m^3]	Steel fibers l_f=8 mm [kg/m^3]
1057	210	1300	157

Table 3: Mix design for FRD

3.2   Experimental Set-up

The present study is limited to monotonic mechanical loading. Applying mechanical load to the composite system might introduce cracking of the overlay and would be of interest in a design situation. Crack formation in the overlay and associated debonding under negative bending is of particular concern. Hence, a test set-up is used, simulating a part of a stiffening overlay cast on a steel bridge deck, loaded in negative bending. A composite beam, turned up-side down, subjected to three-point bending is used as the primary test set-up. The composite beam consists of a steel plate and a thin cement-based layer. Additionally, in a design situation concerning durability, crack spacing and

crack width is of significance. Thus, when testing the ECC composite beams, emphasis is also put on observation of crack spacing, crack width, and debonding between the steel plate and overlay. Crack width during loading is monitored using a microscope (Olympus OVM1000N) with a magnification of 200 times. A single crack is selected and measured throughout the experiment. Testing of the composite beam is performed in closed-loop control, using the stroke of the crosshead as the controlling parameter. The set-up is depicted in Figure 1.
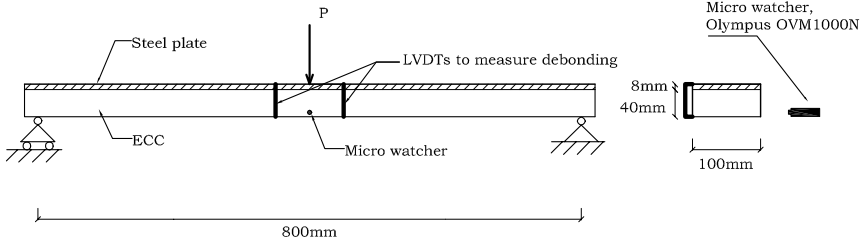
Figure 1: Experimental set-up for ECC composite beams, the crack width of overlay cracks are monitored and debonding is measured. The test set-up simulates a part of a stiffening overlay cast on a steel bridge deck loaded in negative bending.

Debonding between the steel plate and ECC is measured using two LVDTs, termed Omega-gages, mounted on either side, 50 mm from the load point. The Omega-gages are attached with one end to the steel plate and the other to the ECC layer. They measure any elastic deformation between the two end points and additionally capture any steel-ECC interfacial cracking.
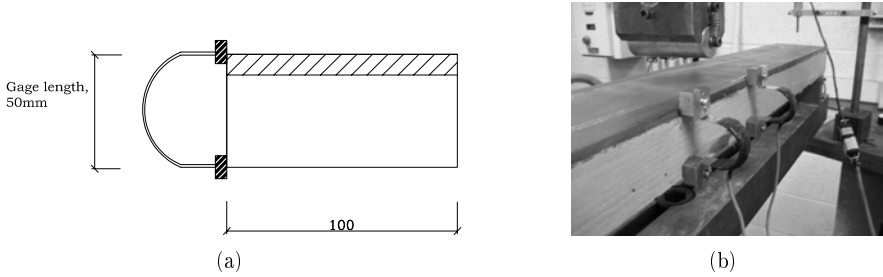

Figure 2: (a) Placing of Omega-gages, beam viewed from end. (b) Actual picture of Omega-gages on beam

The steel-FRC and steel-FRD composite beams formed one discrete crack in the overlay at midspan, where the negative bending moment attains its maximum. Since the crack hardly forms exactly at midspan, acknowledged through a series of pilot tests, a notch is applied in order to record the crack opening during loading. The notch with a depth of

1/8 of the beam height is sawn prior to testing, which consequently will lower the peak load but is of no significance in the present study. A clip gage is mounted on the bottom face of the beam, across the notch, measuring the crack opening displacement (COD) of the vertical overlay crack. To ensure stable crack growth throughout the experiment, this signal is used as the controlling parameter in the closed-loop control of the experiment. Furthermore, attention is put on interfacial debonding and the opening of the overlay crack (COD). Again, to detect and measure possible debonding, two Omega-gages are mounted on either side, 50 mm from the load point to record interfacial cracking, as depicted in Figure 2. The set-up for steel-FRC and steel-FRD beams is depicted in Figure 3.
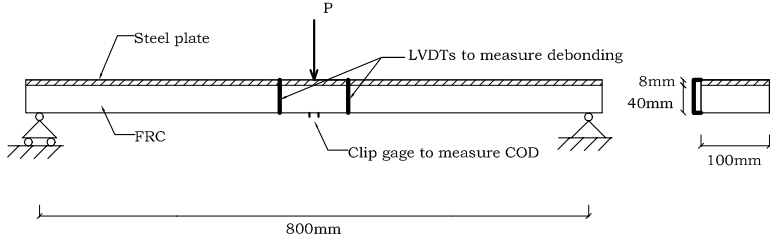

Figure 3: Experimental set-up for FRD and FRC composite beams. Since a single crack is formed at midspan a clip gauge is placed to measure the crack opening displacement (COD). The test set-up simulates a part of a stiffening overlay cast on a steel bridge deck loaded in negative bending.

3.3 Uniaxial Testing of Materials in Tension

To determine the tension properties of the materials tested, uniaxial tension tests have been performed. Two different test set-ups were used. The principle of testing a tension-softening material compared to a strain hardening material differs slightly. For the tension softening materials FRC and FRD, a cylindrical specimen with a height of 300 mm and diameter of 150 mm, was used, according to RILEM (2001). To capture the stress-crack opening relationship a notch is sawn in the middle. Further details on the set-up can be found in Østergaard (2003).

In the experiment a deformation u is measured across the specimen, in this specific case a gage length of 40 mm is used. In order to transform the deformation measurement u to the crack opening w a method is used according to formula (1).

$$w = u_{avg}(\sigma) - u_{avg}(\sigma_{max}) + \frac{\sigma_{max} - \sigma}{K_i} \tag{1}$$

where K_i is the initial slope of the curve and u_{avg} is the average signal recorded across the gage length. Figure 4 shows the principle of transforming the deformation signal recorded to a crack opening.
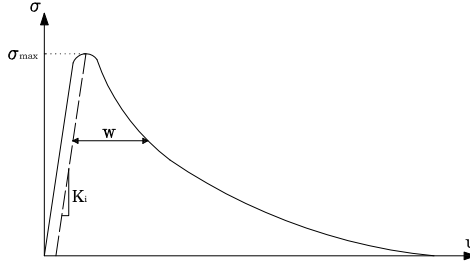
Figure 4: Transformation of the deformation u measured in the experiment to the crack-opening measurement w, cf. Formula 1

In the case of a strain hardening material, multiple cracks are expected, and the elongation of the material can be interpreted as strain. The principle of the test set-up can be found in Li et al. (2002). In this study, only the strain hardening phase is of interest and when a macro crack develops the uniaxial test is stopped.

For the steel used in the test set-ups, the elastic modulus is approximately 210 GPa with a yield stress of 310 MPa (manufacturer's data). These values are important in the ECC composite beam tests as the steel will reach its yield stress, as will be shown in the following.

4   Experimental Results

4.1   Results from Uniaxial Tests

To explain the results in the composite beam tests, the three materials and their properties in tension have been characterized using uniaxial tension tests. Results from the tension softening materials, FRC and FRD are given in Figure 5(a) and ECC is shown in Figure 5(b).

Note that in the case of tension softening materials, the results are given as load versus crack opening and in the ECC case, the result is given as load versus strain. A total of three specimens for each individual material have been tested. The standard deviation is given in the Figure symbolized with error bars. Comparing the two tension softening materials, it can be seen that FRD exhibits a higher first cracking strength than that of FRC. After peak stress, FRD drops significantly more than FRC, mainly due to its more brittle matrix. The difference in matrix strength and brittleness is mainly due to different water cement ratios, FRD has a w/c-ratio around 0.2 whereas the w/c-ratio for FRC lies around 0.5. After crack development, the effect of fibers transferring stresses across the crack is revealed as a plateau in the stress-CMOD curve after a crack opening of approximately 0.025 mm. The ultimate crack opening for FRD and FRC are 4 and 2 mm, respectively. The ECC material shows a strain hardening behavior and as seen from the Figure, it exhibits an ultimate strain capacity of around 2-3%. At this ultimate stage,
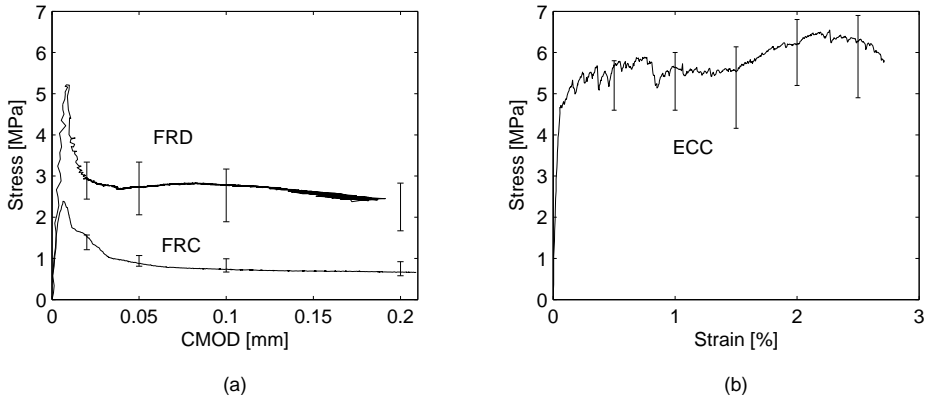
Figure 5: Results from uniaxial tension testing. (a) Materials FRC and FRD shown as stress versus crack mouth opening relationship (CMOD) (b) Strain hardening material ECC shown as stress vs. strain.

a crack will localize and the behavior can then be described in a stress-crack opening relationship.

4.2 Results from Composite Beam Tests

The failure mode of the ECC composite beam is characterized by formation of multiple cracks along the beam, whereas in the case of FRD and FRC composite beams, a single crack forms at midspan. During the experiment, attention has been paid to the flexural crack growth. In the ECC case, the crack width was observed during the experiment and for the FRD and FRC beams, the crack opening displacement (COD) for the single crack at midspan was measured. In Figure 6(a), load versus COD is plotted for FRD and FRC beams along with the standard deviation represented by error bars. Figure 6(b) shows the load-deflection diagram of the ECC composite beam along with the crack width represented by a second y-axis.

The difference in scaling of the two y-axes representing the load in Figures 6 (a) and (b), should be noted when comparing the two results. It is seen from Figures 6 (a) and (b), that cracking of ECC and FRD initiates around the same load, approximately 2000 N, whereas in the case of FRC, a lower cracking strength is observed. Comparing FRD and FRC, it is observed that in both cases, a plateau is present for a certain load value. FRD has a higher fracture energy, hence a higher plateau. On the contrary, for the ECC composite beam, an increase of the load is observed for increased deflection until some point where failure occurs. For the ECC beam, two failure modes are possible: (i) localization of a crack and (ii) reaching of the yield strain in the steel plate. Numerical studies, see later in this paper, show that even for small strain capacities of the ECC, less than 1%, in this
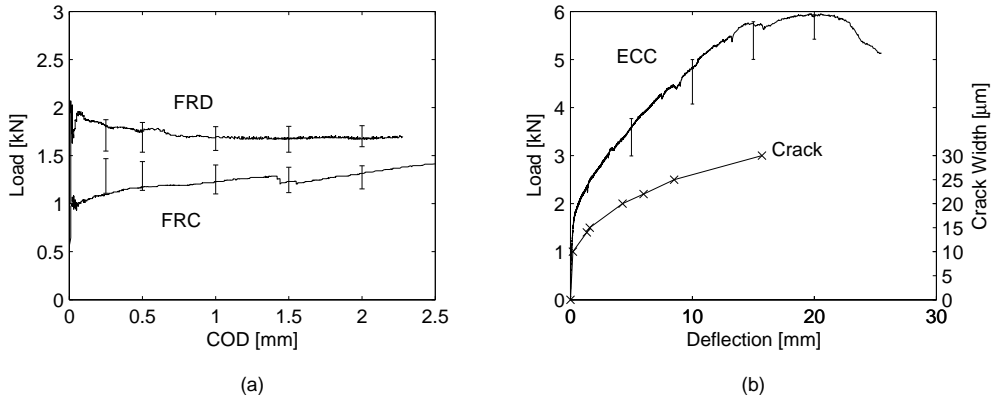
8

Figure 6: Experimental results from composite beam tests (a) for layer using tension softening materials FRC and FRD presented in a load versus COD diagram. (b) for layer using a strain hardening material ECC in a load versus deflection diagram with a second y-axis showing associated crack width. Note the different scaling on the y-axis representing the load.

specific test set-up, yielding of the steel plate is the main cause of failure. Yielding of the steel plate will subsequently cause crack localization in the ECC. In this study, yielding of the steel plate is the governing failure mode and is taken into account.

Figure 6(b) shows the crack width of the first crack of the ECC plotted versus the deflection. The first few cracks form at a low load level and as the beam is monitored during the whole experiment, one crack is selected and monitored until complete failure of the beam. It is seen that the crack width remains in the range of 10-30 micron.

Debonding of the overlay, measured using Omega-gages, is shown for the FRC, FRD and ECC composite beams in Figure 7. The significant relation between an overlay macro-crack and debonding is clearly illustrated in Figure 7 and supports the hypothesis, see, e.g., Granju (2001), (1996), that debonding is closely related to defects in the overlay. The FRC and FRD composite beams develop a macro-crack at an early stage compared to that of ECC and debonding is observed for a deflection around 2 mm. In contrast, the ECC-steel interface remains intact even for large deformations. It is clearly observed that the ECC composite beam exhibits a more ductile behavior when exposed to negative bending.

Actual pictures of the composite beam specimens are shown in Figure 8 (a)-(b). In the first picture a FRD specimen is shown. A single macro crack is observed along with formation of interfacial debonding. In the other case, having an ECC composite beam, multiple cracks are formed and debonding happens when a crack localizes. Formation of multiple cracks in the composite beam is marked and clearly seen in the picture.
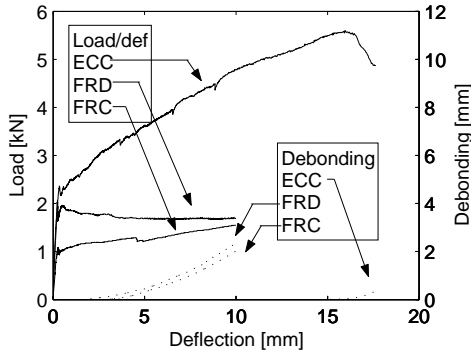
9

Figure 7: Results from three representative tests of composite beams with FRD, FRC and ECC overlay materials. Results are plotted in a load versus displacement diagram with a second y-axis showing the corresponding debonding.

5   Numerical Modelling

The experiments described in the previous sections are analyzed using FEM. The aim of the finite element analysis is to extend the interpretation of the results and observations obtained in the tests to gain a better understanding of the behavior of the present composite beams. The FE model should be able to simulate the composite beams in a realistic way. Phenomena such as cracking of the overlay and bond between the overlay and steel plate have to be taken into account. For the ECC composite beam, yielding of the steel plate also needs to be taken into consideration. The present nonlinear finite-element analysis was carried out with DIANA (2003).

5.1   Finite Element Model

The model consists of a steel plate and an overlay either of FRC, FRD or ECC. The composite beam is modeled as a plane structure and only two dimensions are considered. As the beam is loaded, cracking can occur in the overlay and at the interface between the overlay and steel plate. The constitutive modeling of the overlay depends on whether the overlay material is tension softening or strain hardening. In the case of tension-softening materials, FRC and FRD, cracking is treated as a discrete process and cracking of the overlay, located at the notch, takes place at midspan. Midspan cracking is modeled using standard interface elements available in the software package DIANA (2003). In the case of a strain-hardening material, multiple cracking of the overlay occurs and standard shell elements are used, applying cracking in a smeared manner. Finally, the interfacial cracking between the overlay and steel plate is in all cases treated as a discrete process using standard interface elements. The modeling concept and the applied mesh are given

10
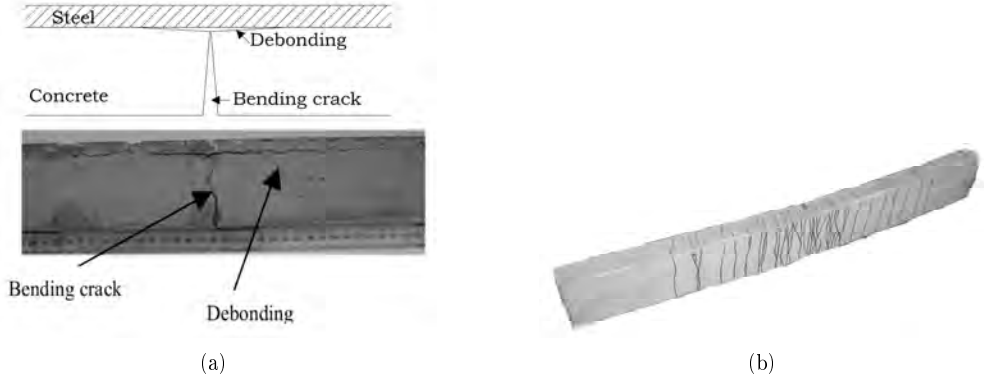
(a)   (b)

Figure 8: (a) Top: Illustration of discrete fracture process with bending crack and associated debonding. Bottom: Composite beam specimen (FRD) after testing, a bending macro crack and resulting debonding is observed. (b) ECC specimen, multiple cracks are observed. All cracks are marked.

in Figure 9. The quality of the mesh has been verified in a convergence analysis checking the invariability of the curve shapes. Based on this investigation, the mesh is found to be adequate.
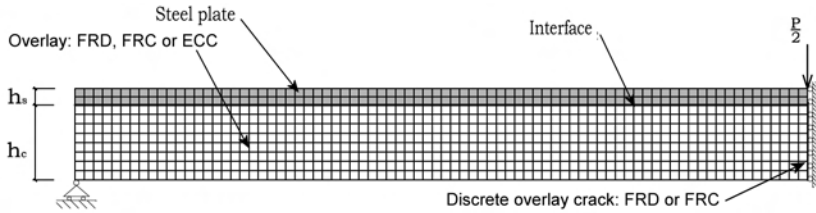

Figure 9: Half beam mesh used in FEM calculation of the experimental set-up. The thick line represents the interface between the overlay and steel plate. In the case of FRC and FRD a discrete crack is modeled at midspan also using interface elements.

5.2   Modelling of Steel

An elastic-plastic model, with the von Mises yield criterion, associated flow rule, and isotropic strain hardening, was used to describe the constitutive behavior of the steel, see DIANA (2003). A stress-strain relation with an elastic modulus of 210 GPa, a yield stress of 310 MPa, and an ultimate stress of 510 MPa was used in the FE analysis. Poisson's ratio in the elastic part was set to 0.3.

11

5.3   Modelling of Interface

To simulate the interface between the overlay and underlying steel plate, a model based on fracture mechanics is used. The steel/overlay debonding phenomenon is often considered a discrete process and modeled as taking place at the bimaterial interface. As debonding takes place in a mixed mode, represented by normal and shear stresses, a mixed mode interface model is applied. The mixed mode model takes into account gradual softening of shear and normal stresses for normal and sliding crack propagation. The normal stress in Mode I is denoted σ and crack opening normal to the interface is denoted δ_n. Similarly, Mode II fracture is described by the shear stress, τ, and the crack sliding deformation, δ_t. The constitutive law of the mixed mode model is based on a coupling of the uniaxial $\sigma - \delta_n$ relationship and $\tau - \delta_t$ relationship, corresponding to Mode I and II fracture, respectively. Consider a two dimensional configuration, where the stresses acting on the interface are related to the relative displacements, i.e., crack opening and crack sliding. The relation is given by:

$$
\begin{bmatrix} \dot{\sigma} \\ \dot{\tau} \end{bmatrix} = \begin{bmatrix} D_{11} & D_{12} \\ D_{21} & D_{22} \end{bmatrix} \begin{bmatrix} \dot{\delta_n} \\ \dot{\delta_t} \end{bmatrix} \tag{2}
$$

In the cracked state the coupling between the normal and shear deformation is described through the stiffness components D_{ij}. Two bilinear curves in pure Mode I and II deformation is given as input. The model utilizes the following criterion to describe the state of deformation for every point on the bilinear curves:

$$
\left(\frac{\sigma}{\sigma^{max}} \right)^m + \left(\frac{\tau}{\tau^{max}} \right)^n = 1.0 \tag{3}
$$

where σ^{max} and τ^{max} are the maximum cracking stresses, according to the two bilinear uniaxial curves defined in pure Mode I and II. For further details on the model, see (Walter, Olesen & Stang 2005), (Walter & Olesen 2005). The model is applied as a user-supplied subroutine and implemented in the commercial FE software package. The parameters used in this study are not obtained directly but are based on experimental work (Walter & Olesen 2005). As a conservative value, a fracture energy of 0.1 N/mm was used as pure Mode I and II fracture energy and was applied in all numerical simulations. The role of the interfacial fracture parameters has been studied (Walter et al. 2003). It shows that for the specific set-up used, interfacial crack propagation is highly dominated by Mode I cracking. Furthermore, previous studies have been performed in order to analyze the interfacial bond. An interfacial crack propagates, for the materials used in this study, in the overlay close to the steel plate. Hence, the constitutive behavior can be treated as the overlay matrix without fibers. When using this approach, the wall effect has to be considered, as big aggregates are rarely present close to the steel plate, see, e.g., (Walter, Østergaard, Olesen & Stang 2005), for experimental studies on the interfacial bond.

5.4 Constitutive Modelling of ECC

Modeling of the ECC overlay is carried out using a crack band model. This is a modification of the so-called fictitious crack model by Hillerborg et al. (1976), further developed by Bažant & Oh (1983). The material is modeled in three phases, cf. Figure 10. For small deformations - the first phase - the material is assumed to behave linear elastically, with an elastic modulus denoted by E. Second phase is the strain-hardening phase, described by a stress-strain relationship. In this phase, the total strain of the material consists of two strain parts, an elastic strain ϵ_e and a cracking strain ϵ_{cr}, according to the following formula

$$\epsilon_{tot} = \epsilon_e + \epsilon_{cr} \tag{4}$$

At some point, the tensile capacity is exhausted, due to the fact that fiber bridging of a certain crack has reached its load carrying capacity, and softening takes place. At this point, the material moves from a stress-strain stage into a stress-crack opening stage. Similar constitutive modeling of ECC has been carried out by Kabele (2001).
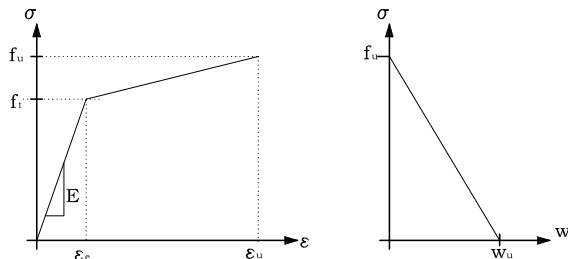

Figure 10: Constitutive modeling of ECC. The material is described in three phases: a linear elastic range, a strain hardening range and a linear stress-crack opening relationship.

5.5 Constitutive Modelling of FRC and FRD

Modeling of the FRC composite beam is carried out considering a single crack in the overlay, modeled using interface elements. A large amount of work has been carried out modeling FRC and it turns out that a bilinear stress-crack opening relationship provides reasonable results, see, e.g., Olesen (2001). The constitutive description of the FRC material consists of two parts: a linear elastic and a bilinear tension softening part, cf. Figure 11.

The two parts of the bilinear stress-crack opening relationship are conceptually associated with the matrix cracking and the fiber bridging, respectively. The two line segments have a slope of a_1 and a_2, respectively and can be expressed by the following formula:
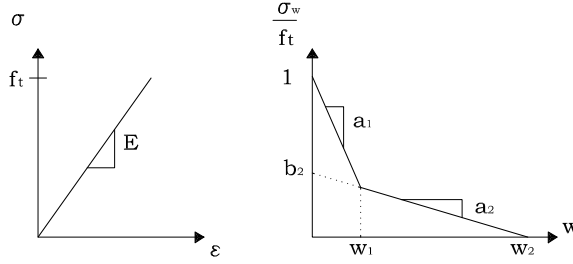
Figure 11: Definition of parameters of a bilinear stress-crack opening relationship, used in the constitutive modeling of FRC and FRD.

$$\frac{\sigma(w)}{f_t} = b_i - a_i w = \begin{cases} b_1 - a_1 w, & 0 \le w < w_1 \\ b_2 - a_2 w, & w_1 \le w \le w_2 \end{cases} \tag{5}$$

where b_1=1; and where the limits w_1 and w_2 are given by the two line segments, and the intersection of the second line segment and the abscissa, respectively.

5.6 Parameters from Uniaxial Tests

Using the simple interpretation described in the previous sections, the uniaxial tension test yields directly the stress-crack opening relationship (Eq. 5) for the specific material. Approximation of the experimental result to a bilinear curve is optimized using numerical tools like Matlab®. The best fit is obtained by first locking the tensile strength f_t and the ultimate crack opening w_2. Next step is then to calculate the two slopes a_1 and a_2 using an optimizing routine.

An example, comparison of the bilinear approximation to the experimental recorded, for a representative FRC specimen, is shown in Figure 12.

From Table 4, the parameters for FRC and FRD are given according to the bilinear stress-crack opening relationship as shown in Figure 11. The results are given as an average and the standard deviation from three tests of each material.

	FRC Average	FRC STD	FRD Average	FRD STD
f_t [MPa]	2.30	0.16	4.8	0.35
a_1 [mm^{-1}]	26.7	3.20	64	24.1
a_2 [mm^{-1}]	0.47	0.13	0.37	0.24
b_2 [-]	0.35	0.05	0.46	0.16

Table 4: Parameters for the bilinear stress-crack opening relationship obtained from the uniaxial tension test for materials FRC and FRD.
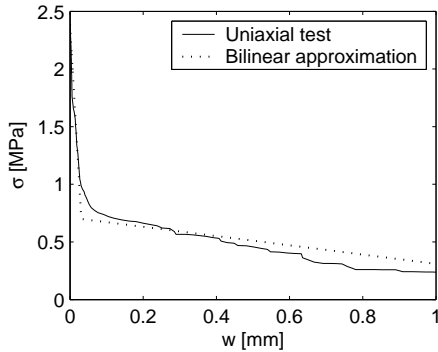
Figure 12: Comparison of the uniaxial experimental measurements, for a FRC specimen, and the bilinear approximation.

From the uniaxial test of the ECC specimens, the interpretation for constitutive model parameters is straight forward. The measurements from the test give the stress-strain curve directly and the stress-crack opening phase is not considered. Table 5 shows the average tensile strength f_t, ultimate strain ϵ_u, and ultimate stress f_u. The results are given as an average based on three experiments along with their standard deviation.

	ECC Average	ECC STD
f_t [MPa]	4.2	0.37
ϵ_u [%]	1.9	0.71
f_u [MPa]	5.3	0.9

Table 5: Parameters obtained from the uniaxial tension test of ECC, according to Figure 10.

6   Model Verification

To verify the FE modeling, the numerical results are compared with experimental results. Fitting the results can be a long and often slow process depending on the accessible computational power. The ultimate test is when the constitutive parameters from the uniaxial tests produce a good correlation between numerical and experimental results. However, as already shown some scatter is present for the results obtained in the uniaxial tension tests and might not produce a perfect correlation. In order to illustrate this phenomenon and to verify the numerical modeling work, two numerical curves are compared to the experimental results. One curve shows the numerical result using the average parameters

obtained in the uniaxial tension tests compared to the composite beam tests for FRC and FRD, cf. Figure 13 (a) and (b), respectively.
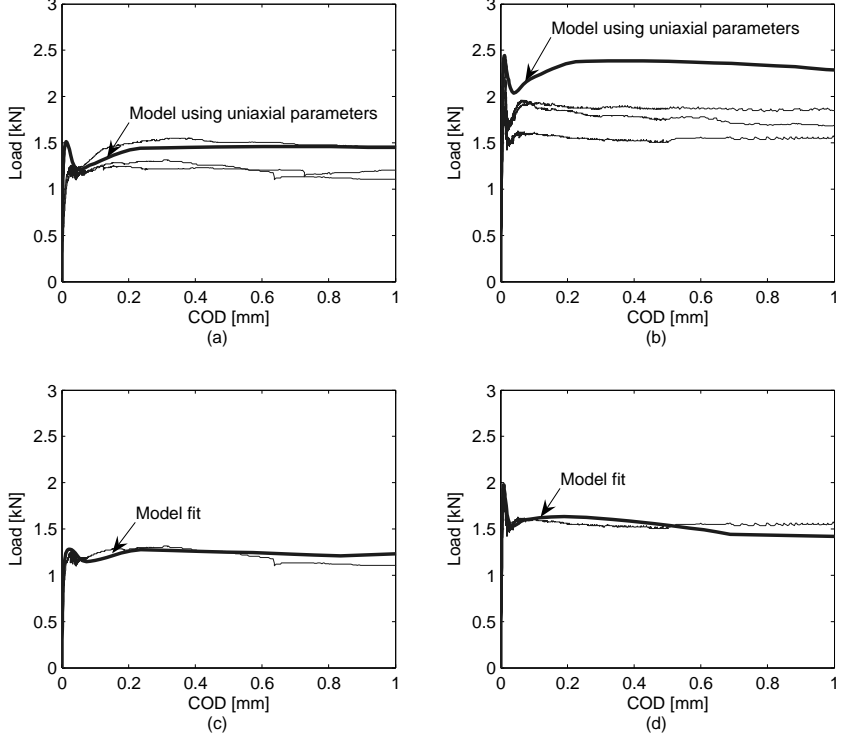

Figure 13: Comparison between experimental and numerical results. (a) and (b) show numerical result using average stress-crack opening parameters from uniaxial tension tests compared to FRC and FRD composite beam tests, respectively. (c) and (d) show best fit using trial and error and experimental results, from a representative FRC and FRD composite beam test, respectively.

The thick solid line in Figure 13 (a) and (b) are obtained by using the average constitutive parameters from the uniaxial tension tests as the model input. Some differences are observed when comparing the composite beam experiment to numerical results using uniaxial test parameters. In this case, for the two examples in Figure 13 (a) and (b), using uniaxial parameters produces a result characterized by higher fracture energy, observed by a higher threshold. The only explanation for this phenomenon is the general scatter

observed in the uniaxial tests, however, the results and the verification of the model are acceptable. Furthermore, Figures 13 (c) and (d), show an example of curve fitting. Curve fitting has been carried out using trial and error. Only one, representative, experiment is studied, which is a strong limitation of this study. It has not been the purpose to fit all the curves but to show the principle of comparing numerical and experimental results.

Furthermore, the following conclusions can be drawn from the numerical solutions. It is confirmed that the normal stresses perpendicular to the interface, for an un-cracked specimen in the set-up considered, are compressive and not critical to the bond. When a vertical macro-crack forms and propagates in the overlay, it will cause a critical change in the interfacial normal stresses, changing them from compression to tension. For any further deformation of the beam, debonding of the overlay takes place in a combination of shear and normal tensile stresses. A parametric study using this model has been carried out, see Walter et al. (2003). This study shows that the fracture energy of the interface has little influence on the global composite beam response. Moreover, as observed in the experiments, debonding is closely related to the formation of a macro crack in the overlay. In the case of a discrete cracking process, debonding will always occur when an overlay macro crack has reached an opening in the range of 0.1 - 0.2 mm.

In Table 6, the bilinear stress-crack opening parameters used in the comparison of numerical results and experiments are given. For each tension softening material, FRC and FRD, the average parameter and their standard deviation from the uniaxial tests along with the parameters from the fitted curve are given.

	FRC Average	FRC STD	FRC BEAM FIT	FRD Average	FRD STD	FRD BEAM FIT
f_t [MPa]	2.3	0.16	1.5	4.8	0.35	3.2
a_1 [mm^{-1}]	26.7	3.2	15.0	64.0	24.1	84.0
a_2 [mm^{-1}]	0.47	0.13	0.57	0.37	0.24	0.50
b_2 [-]	0.35	0.05	0.41	0.46	0.16	0.42

Table 6: Comparison between average stress-crack opening parameters obtained from the uniaxial tension test of FRC, FRD along with the standard deviation (STD) and the ones obtained fitting a curve from the composite beam test

Verification of the numerical model using a strain hardening material, ECC, is carried out in the same manner as for FRC and FRD. A comparison is made between the average parameters obtained in the uniaxial tension tests, a representative composite beam experiment, and a fitted curve. Again, the fitted curve is obtained using the trail and error method. The curves are compared and plotted, cf. Figure 14.

The point where the steel plate starts to yield, was not measured in the experiment. The yielding point is extracted from the numerical results and shown along with the point where a crack localizes in the overlay. In present case, the uniaxial parameters produce a result of a 'weaker' composite beam. By the term 'weak' is meant that the steel plate starts to yield at a lower load level and a crack localizes at a lower load level than in the case of the fitted result. The values from the fitted curve are compared with the ones
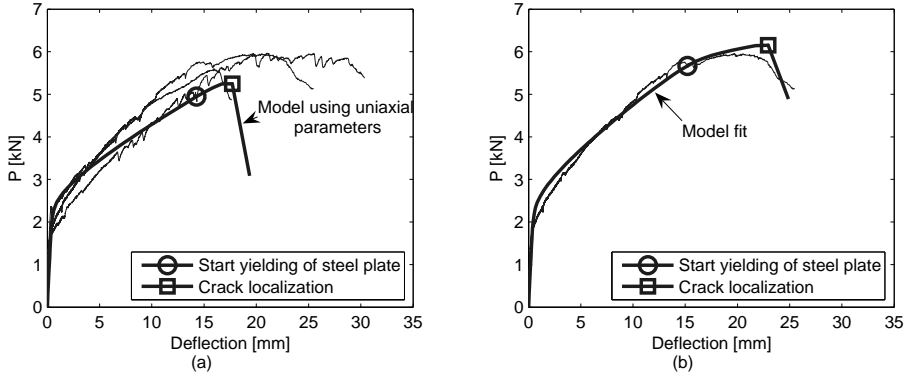
Figure 14: Comparison between experimental and numerical results. (a) Numerical result using average parameters from uniaxial tension test. (b) Best fit using trial and error on an experimental result from a representative ECC composite beam test.

obtained in the uniaxial tension test of ECC, cf. Table 7. Again, taking the scatter into account, verification of the model is acceptable.

	ECC Average	ECC STD	ECC BEAM FIT
f_t [MPa]	4.2	0.37	4.3
ϵ_u [%]	1.9	0.71	2.3
f_u [MPa]	5.3	0.9	6.2

Table 7: Comparison between average uniaxial parameters, cf. Figure 10, obtained from the uniaxial tension test of ECC along with the standard deviation (STD) and the ones obtained fitting curves from composite beam tests

7 Conclusions

A proposed system to stiffen a steel plate with a fiber reinforced cement-based overlay has been investigated with respect to composite beam elements. To study the composite behavior of the cement-based overlay and underlying steel plate, a specific three point bending set-up has been used to simulate the very top part of a bridge deck exposed to negative bending. Only monotonic mechanical loading has been considered. Two classes of materials have been investigated: tension softening and strain hardening materials. Finally, numerical modeling of the test set-up has been performed using the Finite Element Method (FEM). Based on this work, the following conclusions can be drawn.

- Overall, this study supports the hypothesis that debonding of an overlay is related to defects in the overlay. Of major concern in the present stiffening system would be the initiation of a bending crack, i.e., in negative bending.

- The two tension-softening materials tested, Fiber Reinforced Concrete (FRC) and Fiber Reinforced Densit® (FRD) exhibit an overall good structural performance in the test set-up considered. A reasonable scatter in the experiments was observed. Less scatter is present in the case of FRC compared to FRD. As expected a lower load capacity was observed in the case of FRC.

- For the overlay with strain hardening material, ECC, multiple cracking in the overlay prevented steel/ECC debonding in the ultimate limit state. Furthermore, tight crack width below 30 micron favorable from a durability viewpoint was observed.

- A good correlation between experimental and numerical results was obtained. However, to get a perfect fit uniaxial parameters have to be modified in a fitting procedure. In this study, fitting was performed using trial and error producing, in most cases, a slight difference between material parameters from the uniaxial tension tests and the ones from curve fitting.

The conclusions concerning structural performance, (limited to monotonic mechanical loading using small beam elements), can be drawn for three different fiber reinforced materials in an overlay system with the aim to stiffen a steel deck. To give a full recommendation for these materials, broader considerations regarding topics such as: shrinkage, environmental loading and fatigue have to be included in further research.

8   Acknowledgements

References

Bažant, Z. P. & Oh, B. H. (1983), 'Crack band theory for fracture of concrete', *Materials and Structures* **16**, 155–157.

DIANA (2003), *DIANA User's Manual – Release 8.1*, june edn, TNO Building and Construction Research, P.O. Box 49, 2600 AA Delft, The Netherlands.

Granju, J. (2001), 'Debonding of thin cement-based overlays', *Journal of Materials in Civil Engineering* **13**(2), 114–120.

Granju, J. L. (1996), 'Thin bonded overlays: About the role of fiber reinforcement on the limitation of their debonding', *Adv. Cement Based Mat* **4**(1), 21–27.

Hillerborg, A., Modéer, M. & Petersson, P. (1976), 'Analysis of crack formation and crack growth in concrete by means of fracture mechanics and finite elements', *Cem. Concr. Res.* **6**(6), 773–782.

Kabele, P. (2001), Assessment of structural performance of engineered cementitious composites by computer simulation., Ctu reports no. 4, vol. 5, Czech Technical University.

Kolstein, M. H. & Wardenier, J. (1998), A new type of fatigue failures in steel orthotropic bridge decks, *in* 'Proceedings of the fifth Pacific Structural Conference, Korea', pp. 483–488.

Kolstein, M. H. & Wardenier, J. (1999), Laboratory tests of the deckplate weld at the intersection of the through and the crossbeam of steel orthotropic bridge decks, *in* 'Proceedings of the Eurosteel', pp. 411–414.

Li, V. (2002), 'Advances in ECC research', *ACI Special Publication on Concrete: Material Science to Applications* **SP 206**(23), 463–472.

Li, V., Wu, C., Wang, S., Ogawa, A. & Saito, T. (2002), 'Interface tailoring for strain-hardening PVA-ECC', *ACI Materials Journal* **99**(5), 373–400.

Olesen, J. F. (2001), 'Fictitious crack propagation in fiber-reinforced concrete beams', *Journal of Engineering Mechanics* **127**(3), 272–280.

Østergaard, L. (2003), Early-Age Fracture Mechanics and Cracking of Concrete. Experiments and Modelling, PhD thesis, Department of Civil Engineering, Technical University of Denmark, Lyngby, Denmark.

RILEM (2001), 'Test and design methods for steel fiber reinforced concrete. recommendations for uniaxial tension test', *Materials and Structures* **34**(3–6). Prepared by RILEM-Committee-TDF-162, Chairlady L. Vandewalle.

Silfwerbrand, J. (1984), 'Composite action between partially chipped concrete bridge deck and overlay', *Bulletin No. 142, Dept. of Structural Mechanics and Engineering, Royal Institute of Technology, Stockholm, Sweden (in swedish)* p. 149.

Walter, R., Gimsing, N. & Stang, H. (2004), 'Composite steel-concrete orthotropic bridge deck', *10th Nordic Steel Construction Conference, Copenhagen, Denmark, pp.519-530* .

Walter, R. & Olesen, J. F. (2005), 'Cohesive mixed mode fracture modelling and experiments', *Paper submitted to: Journal of Engineering Fracture Mechanics* .

Walter, R., Olesen, J. F. & Stang, H. (2005), 'Interfacial mixed mode model', *In: The 11th International Conference on Fracture, Turin, Italy* .

Walter, R., Østergaard, L., Olesen, J. F. & Stang, H. (2005), 'Wedge splitting test for a steel-concrete interface', *Journal of Engineering Fracture Mechanics* **72**(17), 2565–2583.

Walter, R., Stang, H., Olesen, J. F. & Gimsing, N. J. (2003), 'Debonding of FRC composite bridge deck overlay', *Brittle Matrix Composites BMC7, Warsaw, Poland, pp. 191-200* .

Paper IV

Experimental Investigation of Fatigue in a Steel-Concrete Interface

Experimental Investigation of Fatigue in a Steel-Concrete Interface

R. Walter, B. H. Jansen, M. R. Østergaard & J. F. Olesen

Department of Civil Engineering Technical University of Denmark DK-2800 Kgs.
Lyngby, Denmark, e-mail: rw@byg.dtu.dk

Abstract

A new type of composite bridge deck is currently under research. The concept is to achieve composite action by the adhesion between a thin layer of fiber reinforced concrete and a steel plate. Of special concern is the fatigue strength of the bond between the concrete and steel plate. In this paper, emphasis is put on the steel-concrete interface and how it performs under cyclic loading. A series of tests have been carried out on composite beams made by casting a layer of self-compacting concrete directly onto the sandblasted surface of a steel plate. A four point bending set-up was used, subjected to static as well as cyclic loading. A good performance of the steel-concrete interface under cyclic loading was observed. Furthermore, in order to analyze the stress/deformation situation in the interface, numerical modeling of the test set-up using the finite element method is carried out. This analysis mainly show that the fatigue threshold load corresponds to the static load level at which interfacial cracks are initiated in the numerical model.

Keywords FRC, fatigue, fracture mechanics, steel-concrete interface.

1   Introduction

A typical orthotropic steel bridge deck in Europe consists of a 12 mm steel plate with supporting ribs welded to the bottom face. This type of bridge deck suffers significantly from increasing traffic loads, particularly from heavy trucks. The increased traffic intensity and higher wheel loads results in fatigue cracks in both welded structures and surfacing. Therefore the development of an entirely new concept of deck systems is of interest. Increasing the local stiffness of a typical orthotropic steel deck, using a cement-based overlay to form a composite plate, is the subject of an ongoing research project. Even casting a thin layer increases the local stiffness significantly and might be beneficial in a fatigue situation. It is hoped, that the concept under development can either be applied to retrofitting or in the design of new bridge decks.

To achieve high local stiffness, the steel deck must act compositely with the cement-based overlay. Since the overlay is treated as an integral part of the structural deck system, the

1

strength of the steel-concrete interface is of major importance. Emphasis in this case is put on the interface, especially, how it performs under cyclic loading.

A typical deck according to the proposed system consists of a 40-60 mm layer of Self-Compacting Steel Fiber Reinforced Concrete, (SCSFRC), bonded to an 8-14 mm steel plate (Walter, Stang, Gimsing & Olesen 2003). Whereas conventional composite constructions achieve composite action by mechanical fasteners, the idea here is to achieve composite action only through adhesion. The adhesion between concrete and steel is enhanced by sandblasting of the steel plate. The major concern is how the interface between the concrete overlay and steel plate performs under cyclic loading.

To illustrate stiffness effects under the influence of a thin overlay on a steel plate, an example taken from Wolchuk (2002) is used. A composite section consisting of an overlay fully bonded to a steel part is examined through a linear static analysis, cf. Figure 1(a). A bending moment with a magnitude of 4000 Nmm/mm is applied to the composite section and illustrates the bending moment, which might be critical to the welding of the longitudinal ribs in an orthotropic steel deck. The geometry is defined by an overlay height h_c and a steel height h_s. The maximum stress for a given bending moment is observed for varying thickness of the overlay, cf. Figure 1(b), where σ_c and σ_s are the maximum stresses at the edges of the overlay and steel plate, respectively.
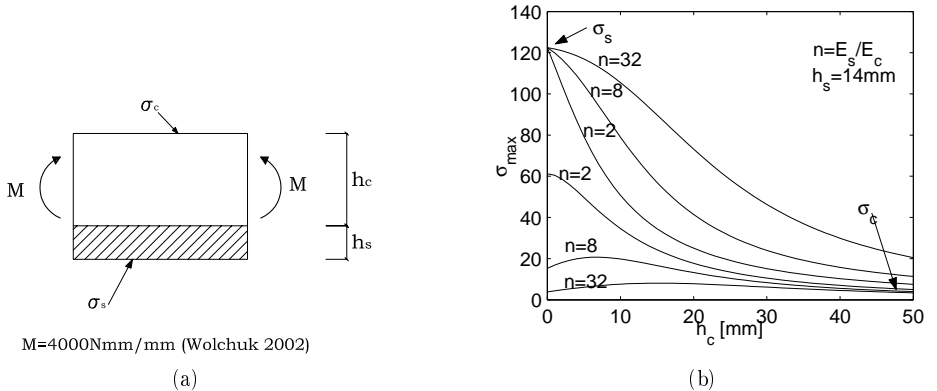

Figure 1: Failure modes. (a): Notched composite beam, beside the interfacial cracking a number of cracks in the bulk material is observed. (b): Stress reduction: (— σ_s , $\cdots$ σ_c), due to overlay contribution to the deck plate rigidity for different heights h_c, in the case of three different elastic ratios denoted n.

Stress reduction in the steel deck is desirable because it substantially enhances fatigue safety. However, a fatigue problem may arise at the steel-concrete interface. This will be discussed in the present paper as it is the main topic of the project behind it (Jansen & Østergaard 2003).

2   Experimental Set-Up

A number of composite beams where prepared for the experiments. In order to ensure bond between the two materials, the steel plates where sand blasted before casting. Two types of steel plates where used in the tests: a plain flat steel plate and a checker steel plate. The motivation for using a checker steel plate is that the macroscopic roughness may play a role in the overall composite performance. The composite beams were tested in four point bending to investigate the behavior of the steel-concrete interface subjected to static and cyclic loading. The set-up is shown in Figure 2.
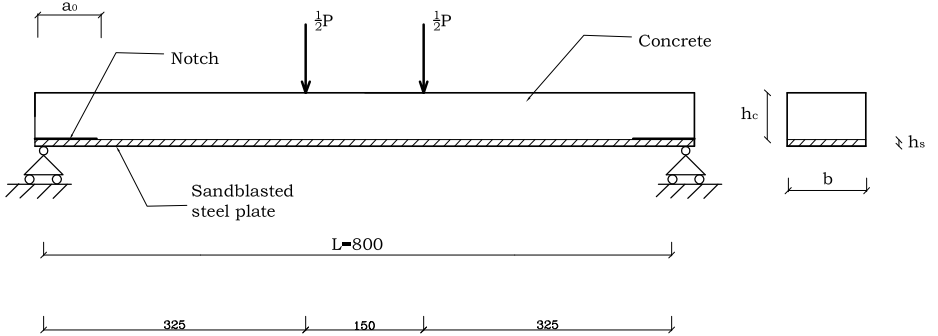

Figure 2: Test set-up, two types of steel plates where used: flat and checker, both sandblasted. The steel plate thickness is denoted h_s, concrete height h_c and a possible notch length a_0.

Loading the composite beam in four point bending creates a zone of constant shear at the steel-concrete interface between the support and the load point. It is expected that the shearing zone will be critical to the steel-concrete interface. In some experiments an interfacial notch (created by preventing adhesion) of length a_0 measured from the beam-end, was applied. Since large compressive stresses perpendicular to the interface exist close to the support, the interface here is more likely to sustain large shear forces, whereas an interface notch at the beam-end will eliminate this effect. The interfacial shear stresses will peak at the end of the notch, which makes it possible to observe crack propagation in the interface during the experiment.

3   Material Properties

Specimens were cast from four different batches, using the same recipe. The mix used in the experiment is given in Table 1. Emphasis was made on making the steel fiber reinforced concrete self-compacting in order to have the mix spread evenly and to create a uniform bond between the concrete and the sandblasted steel surface.

Mix	kg/m
Cement (RAPID)	245
Fly ash	94.5
Silica fume	10.5
Water	142.9
Air entraining agent	0.4
Plasticizer	4.2
Sand, 00-04 mm	752.6
Aggregates, 04-08 mm	450.6
Aggregates, 08-16 mm	594.0
Fibers, l=30mm,D=0.5mm	78

Table 1: Mix design

One percent of hooked end steel fibers were used with a diameter of 0.5 mm and a length of 30 mm. Workability and compressive strength of all batches were similar. For each batch, three cylinders were cast. The average ultimate strength for all batches was f_c=44.6 MPa with a standard deviation of 2.7 MPa.

4   Experimental Results

Both static and cyclic tests on the composite beams have been carried out. In the static tests, the maximum interfacial shear stress and the fracture behavior are of interest. During the cyclic tests emphasis is put on the maximum number of cycles prior to failure.

4.1   Static tests

To measure the slip of the steel-concrete interface during loading of the composite beam, a special end-slip measurement arrangement is applied. A clip gauge was mounted between two small extending rods, which had been glued onto the specimen, one on the steel plate and another on the concrete, cf. Figure 3.
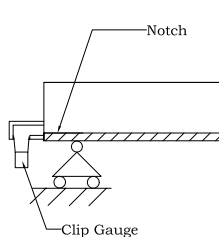

Figure 3: Mounting of clip gauge to measure end-slip

Batch No.	Steel plate	h_c [mm]	h_s [mm]	τ_c [MPa]
1	Flat	62	10	3.09±0.24
1	Checker	62	8	3.19±0.15
2	Flat	62	10	3.30±0.13
2	Checker	62	8	3.29±0.10
3+4	Flat	70	8	3.04±0.02
3+4	Checker	70	8	3.07±0.13

Table 2: Results of static tests for each batch using flat and checker steel plates, all beams un-notched.

To illustrate the effect of an interfacial notch, two static examples are analyzed using the end-slip measurement. The load vs. end-slip diagram showed in Figure 4 reveals that a notched beam gives more information on the crack propagation during the test that of an un-notched beam. This information is essential to the comparison and validation of the numerical model and is discussed further, in the latter. A number of static experiments using the four point bending set-up were carried out to determine the maximum load of each batch. This has been repeated for each type of steel plate and the results are given in Table (2).
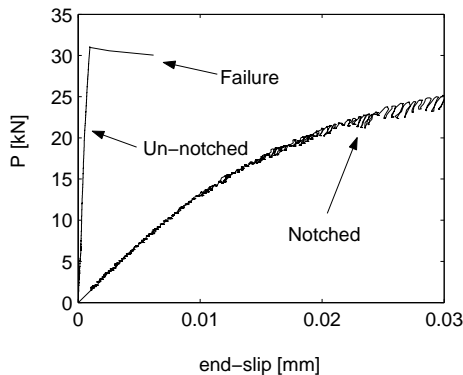

Figure 4: Load end-slip curves of a typical composite beam in static load using an un-notched and notched configuration.

Global failure is associated with debonding of the interface. Since the composite beam geometry is not the same for each experiment, the maximum linear static shear stress acting at the steel-concrete interface is calculated using the maximum load at global failure. The maximum shear stress was calculated using the classic shear formula for beams, see e.g. Gere & Timoshenko (1999), assuming a fully bonded steel-concrete interface. This maximum shear stress at failure is denoted τ_f and is shown for each batch in Table 2.

4.2   Fatigue Tests

The experimental results related to cyclic loading involve 14 specimens, 6 with a flat steel plate and 8 with a checker steel plate. During the fatigue tests, a cyclic load was applied between two values P_{max} and P_{min} in the shape of a sinusoidal wave and at a frequency of 5 Hz. Results from the cyclic tests are given for each beam in Table 3. For each type of plate, an additional two tests were carried out applying an interface notch with a length of a_0=40 mm. The results for each series of flat and checker steel plates are presented graphically in Figures 5 (a) and (b), where the ratio τ_{max}/τ_f is plotted against $\log(N_f)$, τ_{max} being the maximum shear stress at the interface and N_f the number of cycles at failure. A fatigue threshold value for τ_{max}/τ_f of approximately 65% is observed for the un-notched beams. The notched beams exhibit a lower threshold value.

Beam	h_c [MPa]	h_s [MPa]	τ_{max}/τ_f	$\log(n_f)$
FU1	62	10	0.64±0.04	*6.91
FU2	70	8	0.65±0.01	6.89
FU3	62	10	0.69±0.05	6.05
FU4	70	8	0.70±0.01	5.06
FN1	62	10	0.65±0.03	6.47
FN2	62	10	0.70±0.03	3.23
CU1	62	8	0.59±0.03	*7.00
CU2	70	8	0.68±0.01	*6.88
CU3	70	8	0.69±0.03	*6.18
CU4	62	8	0.69±0.03	5.26
CU5	70	8	0.75±0.03	3.90
CU6	62	8	0.78±0.04	3.41
CN1	62	8	0.66±0.02	6.56
CN2	62	8	0.60±0.02	6.44

*Test stopped before failure

Table 3: Results of cyclic tests. FU: (Flat steel plate un-notched); FN: (flat steel plate notched); CU: (Checker steel plate un-notched); CN: (Checker steel plate notched).

5   Numerical Modeling

To study the behavior of the test set-up a numerical model is used. A two dimensional configuration of the composite beam is considered. The set-up is modeled as a half beam, using a commercial finite element program package (DIANA 2003). The half beam is modeled assuming a nonlinear behavior in the overlay and the interface. The steel plate is modeled as a linear elastic material. The steel-concrete interface is modeled using so-called interface elements. The interface elements have a thickness of zero and are placed between the steel and concrete and relate the forces acting on the interface to the relative
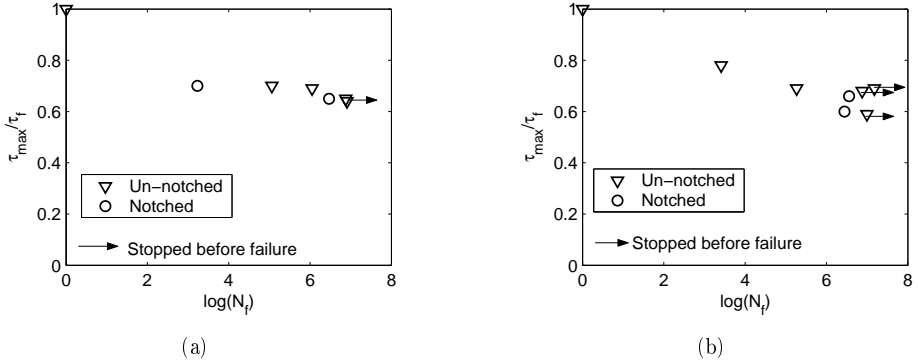
Figure 5: (a) Results from tests of composite beams with a flat steel plate. The arrow symbolize that the test were stopped before failure. (b) Results from tests of composite beams with a checker steel plate. The arrow symbolize that the test were stopped before failure.

displacement of the two sides of the interface. All elements representing the overlay are of quadratic shape having a size of 3.5x3.5 mm^2.

5.1 Material Characterization

As the composite beam is loaded, fracture can occur in the overlay and/or in the steel-concrete interface. This requires two types of fracture modeling approaches, one for the overlay and a second for the interface.

Cracking of the overlay is modeled using the smeared cracking approach. A bilinear (σ-w) relation is used with constant shear retention. The stress-crack opening relationship is given by

$$\frac{\sigma(w)}{f_t} = b_i - a_i w = \left\{ \begin{array}{ll} b_1 - a_1 w, & 0 \leq w < w \\ b_2 - a_2 w, & w_1 \leq w \leq w_1 \end{array} \right. \tag{1}$$

where b_1=1; and the limit w_1 is given by the intersection of the two line segments and w_2 correspond to the intersection between the second line and the abscissa. The material parameters used for the concrete are taken from Sigurdsson (2003), who measured the fracture mechanical properties of the same type of steel fiber reinforced concrete as used in these experiments (Table 1). The parameters in equation (1) used in the analysis were: f_t=4.0 MPa, a_1=10 mm^{-1}, a_2=0.12 mm^{-1}, b_2=0.9.

The interfacial fracture is modeled using a composite interface model originally developed by Lourenço & Rots (1997), and implemented in DIANA. The interfacial failure criterion is of a Mohr-Coulomb type, and able to describe failure in either shear, tension or mixed mode. The governing parameters are cohesion, tensile strength and friction angle φ, as well as the fracture energy for pure (Mode I and II), assuming exponential softening of

the cohesion and tensile strength. For further details see either Lourenço & Rots (1997) or Walter, Stang, Olesen & Gimsing (2003).

The steel is modeled as a linear elastic material with the following engineering constants: $E_s = 210$ GPa, $\nu=0.3$. The elements modeling the overlay and steel plate are 8-node isoparametric plane stress elements.

5.2 Crack Propagation

To illustrate the interfacial crack behavior, with and without a notch, a numerical example is studied. Figure 6 shows how the interfacial crack propagates. For a given load P the figure illustrates where cracking occurs along the beam axis as defined in Figure 7. In the case of an interfacial notch, cracking starts at the tip of the notch at a relatively low load value and propagate towards the load point. In the case of an un-notched composite beam, interfacial cracking initiates somewhere in between the support and load, and the crack propagates towards the support and load point, resulting in a more dramatic global failure.
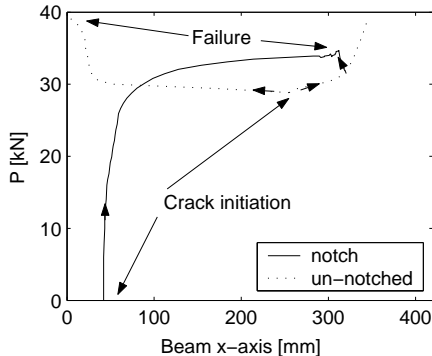

Figure 6: Crack propagation along the interface, calculated using FEM. Crack propagation is plotted for a given position on the x-axis according to Figure (7) versus the load for a notched and un-notched beam.

The significant differences between the two cases are: where the interface crack initiates and how it propagates. Running an experiment without a notch is somewhat less useful for the study of the interfacial crack propagation. However, when applying a notch, the crack initiates at the notch tip close to the support and propagates towards the load point. This is suitable for closed-loop testing using the end-slip as the controlling parameter. Photos of sample beams, with and without a notch, are shown after failure in Figure 8. It reveals that the notched beam has cracks running from the interface into the overlay, whereas the un-notched beam has only one dominant interface crack.
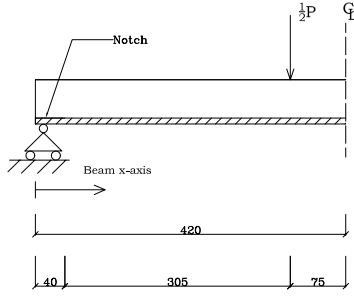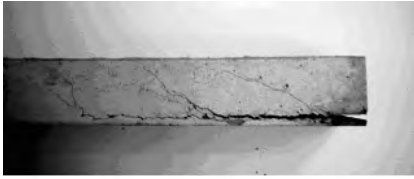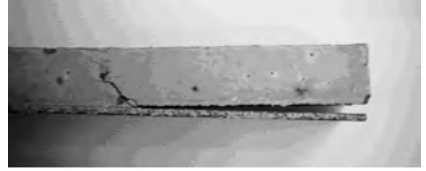
Figure 7: Definition of beam x-axis, position of support and load.

(a)   (b)

Figure 8: Failure modes. (a): Notched composite beam, beside the interfacial cracking a number of cracks in the bulk material is observed. (b): Un-notched composite beam after failure, a dominant interface crack is observed.

5.3   Model Predictions and Experimental Results

Two characteristic experimental results using flat and checker steel plates, each with an interfacial notch, are compared to the FE-model. The comparison is carried out in a load vs. end-slip diagram. Two examples in which FE-calculations are fitted to experimental results are shown in Figures 9 (a) and (b). The material data for the steel-concrete interface are obtained by such fitting and the following interfacial parameters (tensile strength, cohesion, friction angle and pure Mode I+II fracture energies) were found: f_t=4.0 MPa; c=3.0 MPa; $\tan(\varphi)$=0.7; G_f^I =0.2 N/mm; G_f^{II}=2.6 N/mm for the checker steel plate, (Figure (11)) and f_t=4.0 MPa; c=3.1 MPa; $\tan(\varphi)$=0.7; G_f^I=0.2 N/mm; G_f^{II}=2.6 N/mm for the flat steel plate, (Figure 9 (a)). It is noticed that the numerical modeling captures the nonlinear behavior of the experiment.

According to the numerical model, interfacial cracking initiates at the interface for an un-notched beam at approximately 65% of the maximum static load (Figure 6). Comparing this with the results of the cyclic tests, it is seen, that this corresponds to the fatigue threshold value.
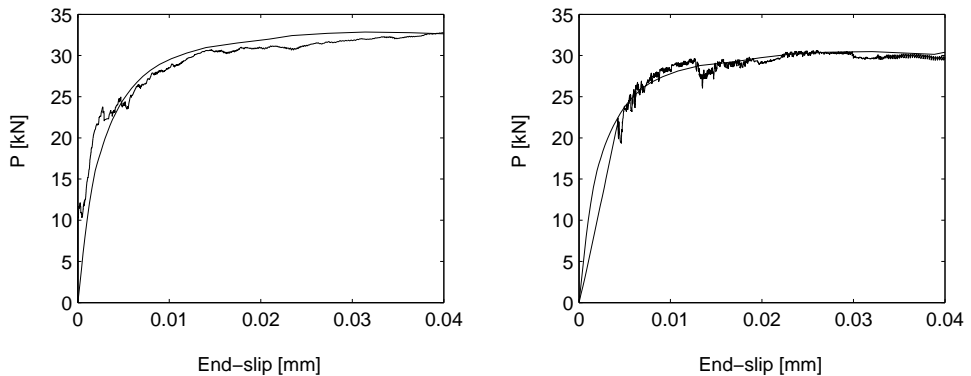
9

Figure 9: (a): Fitting of FE-calculations to experiments for a checker steel plate. (b): Fitting of FE-calculations to experiments for a flat steel plate.

6 Conclusions

A test set-up using a composite beam consisting of a cement-based overlay cast upon a sandblasted steel plate has been investigated experimentally under static as well as cyclic loading. A checker and a flat steel plate were used in the experiments. The different steel plates did not reveal any significant differences in static or fatigue strength. A modified version of the test set-up was used, introducing an interfacial notch between the concrete and the steel plate near the support. This set-up has proven suitable for studying the interfacial crack propagation during loading. A number of different specimens were used in the study of a composite beam exposed to cyclic loading. A primary result is that the steel-concrete interface shows a good fatigue resistance, as a fatigue threshold level was observed around 65% of the static failure load for the un-notched beams.

Numerical modeling was carried out using FEM. The model has been validated, using the notched beam set-up. The modeling helped reveal the different fracturing behavior of the notched and un-notched composite beams. Finally, the numerical modeling confirms that cracking at the interface occurs at a load level of approximately 65% of the static failure load for an un-notched beam, which corresponds well to the observed fatigue threshold load. As expected, the notched beams have a lower threshold in fatigue, since interfacial cracking is initiated at a lower load.

References

DIANA (2003), *DIANA User's Manual – Release 8.1*, june edn, TNO Building and Construction Research, P.O. Box 49, 2600 AA Delft, The Netherlands.

Gere, J. & Timoshenko, S. (1999), *Mechanics of Materials*, Stanley Thomes, Fourth SI edition.

Jansen, B. J. & Østergaard, R. M. (2003), Cracking and fatigue of the interface in composite bridge decks, Master's thesis, Department of Civil Engineering, Technical University of Denmark, Lyngby Denmark.

Lourenço, P. B. & Rots, J. G. (1997), 'Multisurface interface model for analysis of masonry structures', *Journal of Engineering Mechanics* **123**(7), 660–668.

Sigurdsson, S. (2003), Composite bridge decks of sfrc/steel, Master's thesis, Department of Civil Engineering, Technical University of Denmark, Lyngby.

Walter, R., Stang, H., Gimsing, N. J. & Olesen, J. F. (2003), 'High performance composite bridge decks using scsfrc', *The Fourth International Workshop on High Performance Fiber Reinforced Cement Composites, Ann Arbor, Michigan* pp. 495–504.

Walter, R., Stang, H., Olesen, J. F. & Gimsing, N. J. (2003), 'Debonding of FRC composite bridge deck overlay', *Brittle Matrix Composites BMC7, Warsaw, Poland, pp. 191-200* .

Wolchuk, R. (2002), 'Structural behaviour of surfacing on steel orthotropic decks and considerations for practical design', *Structural Engineering International* **2**, 124–129.

Paper V

Debonding of FRC Composite Bridge Deck Overlay
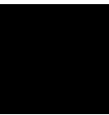
Debonding of FRC Composite Bridge Deck Overlay

Rasmus Walter, Henrik Stang, John F. Olesen, Niels J. Gimsing
Department of Civil Engineering Technical University of Denmark DK-2800 Kgs. Lyngby, Denmark, e-mail: rw@byg.dtu.dk

Abstract

A new type of composite bridge deck is currently under research. The concept is to achieve composite action by the adhesion between a thin layer of fiber reinforced concrete cast on a steel plate. Of special concern is the strength of the bond between the concrete and steel plate in the case of vertical cracking of the overlay. Based on a nonlinear 2D finite element model a theoretical parameter study has been conducted in relation to debonding of a concrete overlay. Discrete crack theory was used to model vertical cracking of the overlay and interfacial cracking (debonding) between the steel plate and concrete. Two parameter studies were made. One concerns the fracture energy of the overlay and steel-concrete interface. These results show that the composite performance is dependent primarily on fracture energy of the concrete overlay, and less on the fracture energy of the steel-concrete interface. In the other, the mixed mode behaviour of the steel-concrete interface is studied in relation to the interfacial failure criterion.

Keywords Debonding, FRC, fracture mechanics, steel-concrete interface.

1 Introduction

A large number of steel bridge decks suffer significantly from increased traffic intensity and higher wheel loads. This results in fatigue cracks in both welded structures and surfacing. Development of an entirely new concept of deck systems is of interest. A typical deck according to this system consists of a 40-60 mm layer of Self-Compacting Steel Fiber Reinforced Concrete, (SCSFRC), bonded to an 8 mm steel plate (Walter et al. 2003). Whereas conventional composite constructions achieve composite action by mechanical fasteners, the idea here is to achieve composite action only through adhesion. The adhesion between concrete and steel is enhanced by sand blasting of the steel plate. Since a controlling factor of the composite strength is related to the vertical cracking of the overlay, the composite plate subjected to a negative bending moment is of interest. During flexural cracking of the overlay, the distribution of shear and normal stresses along the steel-concrete interface changes dramatically from that of the elastic phase. In the fracture process zone of a discrete crack, high stress concentrations develop in a plane perpendicular to the crack direction due to the presence of the steel plate that opposes

the opening of the flexural crack. The debonding problem is known from the repairing of existing structures by thin cement-based overlays, see e.g. Granju (1996) or Granju (2001). They show that cracking of the overlay induces high interfacial tensile stresses leading to debonding between the two materials. Once initiated, the interfacial crack will propagate in a mixed mode characterized by tensile and shear stresses along the interface. The aim of this paper is to study the behaviour of the interface between concrete and steel with a fracture mechanical approach. In this study the so-called fictitious crack model (FCM) developed by Hillerborg et al. (1976) will be applied. The advantage of the model is the simplicity and the good correlation between theory and experimental tests. The basic idea of the FCM is a relationship between the stress and the crack opening. This relationship describes the stresses transferred across the crack. This method has also been applied to fiber reinforced concrete, see e.g. Olesen (2001). The two types of cracking - vertically through the overlay and interface debonding between steel and concrete - will be described by the FCM. For small crack openings, an interfacial fracture between steel and concrete shows the ability to transfer stress across the crack. This phenomenon is called 'interlocking' and its significance in a debonding process is described in Granju (2001). The 'interlocking' effect is synonymous with the FCM. The main focus of the present paper is the presentation of a two-dimensional nonlinear finite element model to simulate the debonding process discussed above. Furthermore, the model is used to carry out two theoretical parameter studies in order to illustrate the influence of debonding on the overall behaviour.

2 Numerical Modelling

The problem of a vertical crack penetrating a concrete layer bonded to a steel plate and the subsequent debonding is studied in a three point bending set-up according to Figure 1. The modelling is carried out as a two dimensional composite beam model, consisting of a concrete layer bonded to a thin steel plate. The vertical cracking zone in the composite beam under the applied load P corresponds to the zone near a midspan support in a bridge structure. Note that the composite beam is turned upside down for convenience.
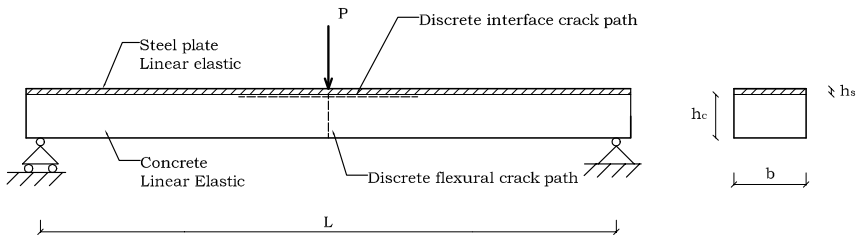

Figure 1: Experimental set-up: Simulating a negative bending moment in a bridge deck

The vertical concrete cracking is modelled using standard interface elements as imple-

mented in the applied software Package DIANA (2003). The interfacial mixed mode fracture is modelled using a composite interface model originally developed by Lourenço & Rots (1997), also implemented in DIANA. The mixed mode behaviour and the significance of constitutive material parameters are investigated through two parameter studies. Firstly, the influence of a tough concrete overlay and different fracture energies of the steel-concrete interface are investigated. Then, a parameter study is carried out concerning the failure criterion for the steel-concrete interface.

2.1 Material Characterisation

Considering the concrete-steel interface, the state of stress is described through normal and shear stresses. In many cases the failure surface of the stress state in a steel-concrete interface is well described through a Mohr-Coulomb criterion. The failure criterion in the applied constitutive model, consist of two surfaces, denoted f_1 and f_2, representing shear and tension failure respectively, cf. Figure 2.
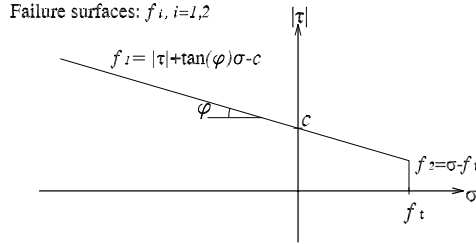

Figure 2: Failure surfaces f_1 and f_2, defined by the cohesion c, slope $\tan(\varphi)$, and the tensile strength f_t.

Nonlinear softening of the interface is characterized by degradation of the tensile stress f_t and the cohesion c. The nonlinear softening of the tensile stress and cohesion is assumed to behave according to the following law

$$c(s) = c_0 exp\left(-\frac{c_0}{G_f^{II}}s \right) \quad ; \quad f_t(w) = f_{to} exp\left(-\frac{f_{t0}}{G_f^{I}}w \right) \tag{1}$$

where c_0 and f_{t0} are initial values of the cohesion and tensile strength, and represent the fracture energy of MODE I and II respectively, s and w represent the slip and opening after crack initiation. The nonlinear exponential behaviour given in Equations 1(a-b), originates from experiments on mortar/brick interfaces by der Pluijm (1992).

At the intersection between the failure surfaces f_1 and f_2, cf. Figure 2, a permanent coupling between tension and shear failure is present. The softening of the two surfaces f_1 and f_2 are coupled assuming isotropic softening, meaning that the percentage of softening on the cohesion is assumed to be the same on the tensile strength. This is explained

3

in further details in Lourenço et al. (1998). Furthermore, for simplicity, all calculations are carried out assuming associated plasticity: $\tan(\varphi)=\tan(\psi)$, where ψ is the dilatation angle.

Cracking of the overlay is assumed to propagate at midspan $0.5L$, using discrete crack theory. Nonlinear effects of the bulk material are not considered in this case. The stress-crack opening relationship of concrete can in many cases be modelled using a bilinear curve (Olesen 2001). In the present study a bilinear curve is applied according to equation (2).

$$\frac{\sigma(w)}{f_t} = b_i - a_i w = \left\{ \begin{array}{ll} b_1 - a_1 w, & 0 \leq w < w \\ b_2 - a_2 w, & w_1 \leq w \leq w_1 \end{array} \right. \tag{2}$$

where $b_1=1$; and the limit w_1 are given by the intersection of the two line segments and w_2 correspond to the intersection by the second line and the abscissa.

The steel and concrete outside the crack paths is modelled as a linear elastic materials with the engineering constants $E_s = 210$ GPa, $\nu_s=0.3$, $E_c = 30$ GPa and $\nu_c=0.15$. The elements representing the bulk material are 8-node isoparametric plane stress elements or triangular for mesh refining, cf. Figure 3 for the applied mesh.

The two crack paths - the vertical and interface crack - are modelled using so-called interface elements, available in the applied FEM-package (DIANA 2003). A two dimensional configuration is considered, where the interface element relates the forces acting on the interface to the relative displacement of the two sides of the interface. In the present case, the interface element is described by a traction vector and a vector which represents the relative displacements. In the elastic regime the relationship between traction and relative displacement is given by:

$$\left[\begin{array}{c} t_w \\ t_s \end{array} \right] = \left[\begin{array}{cc} k_w & 0 \\ 0 & k_s \end{array} \right] \left[\begin{array}{c} u_w \\ u_s \end{array} \right] \tag{3}$$

with k_w and k_s assigned large penalty values to model initial continuous geometry. The interface elements have a thickness of zero and are placed between the steel and concrete and at midspan to represent a possible vertical crack, cf. Figure 3.
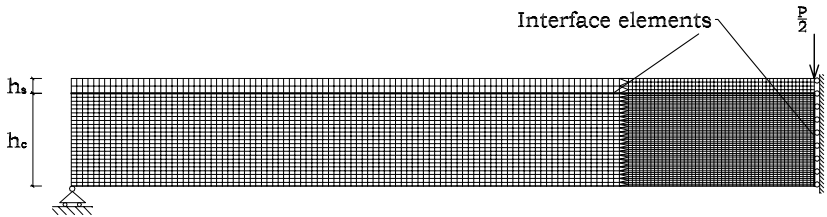

Figure 3: Half beam mesh used in FEM calculations, the two thick lines represent interface elements.

2.2 Study of Debond Mechanism

Consider a load P acting on a composite beam as shown in Figure 1. The load causes a 'negative bending moment', characterised by tensile stresses in the concrete layer. This will eventually, at some stage, lead to cracking of the concrete. The vertical crack propagates through the concrete overlay, but at some stage it is opposed by the steel plate. The opposition of the steel plate will lead to an increase of normal stress in a plane perpendicular to the vertical crack tip, i.e. in the plane of the steel concrete interface. The horizontal stress intensity is likely to introduce cracking, along the 'weakest link' - which in this case is assumed to be the interface between steel and concrete.

The initiation of an interfacial crack is illustrated through a case study. A composite beam is studied given the geometry: L=800 mm, h_c=50 mm, h_s=8 mm, b=100 mm and a vertical crack described through Equation (2) given the values: f_t=3 MPa, a_1=10 mm^{-1}, a_2=0.1 mm^{-1}, b_2=0.5.

The distribution of interface stresses is illustrated for different openings of the vertical crack. The opening of the vertical crack, called the crack mouth opening displacement (CMOD), is calculated at midspan, cf. Figure 4-a. For an opening of 0 and 0.03 mm the stress distribution is shown as a function of the x-coordinate normalised with the concrete height h_c, cf. Figure 4-b. The x-coordinate is measured from midspan.

(a)   (b)
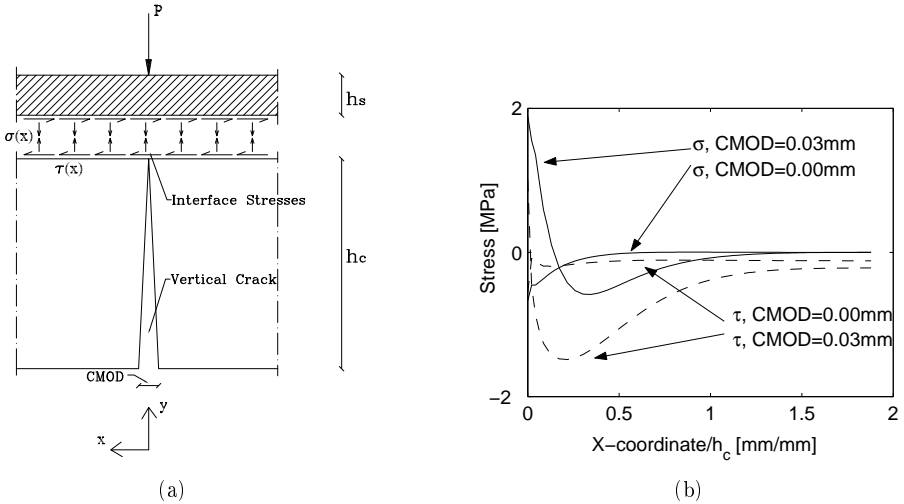
Figure 4: Stress distribution along the interface for a CMOD value of zero and 0.03mm (a) Interfacial forces and configuration (b) Stress distribution along the interface versus the x-coordinate normalised with the concrete height h_c. Dashed lines represent shear stress τ and solid line represent the normal stress σ.

It is observed that for an uncracked concrete overlay (CMOD=0 mm), the normal interface stresses are governed by compression. As the crack is initiated and further opened, the

5

normal stresses changes from compression to tension, in many cases critical to the bond between steel and concrete. Further the shear stresses are significantly increased.

3 Parametric Study I - Fracture Energy

The purpose of this parametric study is to simulate the global behaviour of the set-up given in Figure 1 for different fracture energies of the overlay and steel-concrete interface. The different simulations performed are grouped into 3 different groups denoted A-C. Simulation A1 is the reference case, and each of the other groups involves simulations where parameters have been changed in relation to this case. The different groups of simulations are:

A. Variation of the bilinear $\sigma - w$ relation of the vertical crack as defined in Equation (2)

B. Variation of Mode I energy for the steel-concrete interface. The nonlinear softening of the interface in Mode I is defined in Equation (1-a)

C. Variation of Mode II energy for the steel-concrete interface. The nonlinear softening of the interface in Mode II is defined in Equation (1-b)

The different groups of simulations and their parameter values are summarized in Table 1.

Name	Changing Parameter and values
A1	Reference
A2	$0.2b_2$
A3	$1.8b_2$
B1	$0.5G_f^I$
B2	$2.0G_f^I$
C1	$0.5G_f^{II}$
C2	$2.0G_f^{II}$

Table 1: The Parameter variation of b_2-value of the vertical crack and Mode I+II fracture energies of steel-concrete interface.

The first case (A) concerns the significance of the toughness of the vertical crack. The vertical crack is characterised by a bilinear crack-opening relationship according to equation (2). The b_2-value may be taken as a measure of the amount of fiber used in the material, where a high b_2-value corresponds to high fiber content. Finally, the significance of different Mode I and II energies of the steel-concrete interface is studied through cases B-C. In the reference case, A1, the following numerical values of the geometry parameters were used, cf. Figure 1: L=800 mm, h_s=8 mm, h_c=50 mm, b=100 mm. The numerical values

used for the material parameters in the bilinear $\sigma - w$ relation of the vertical crack were: f_t=3 MPa a_1=10 mm^1, a_2=0.1 mm^1, b_2=0.5. The numerical values of the steel-concrete interface were, f_t=2 MPa , c=3 MPa , $\tan(\varphi)$=0.5, $G_f^I = G_f^{II} = 0.1$ N/mm.

Changing the toughness of the vertical crack leads to a change in global behaviour. This is presented in Figure 5 (a), showing the maximum moment versus the opening of the vertical crack. It is observed that changing the b_2-value of the vertical crack affects the global ductility significantly.

The relation between the interface crack length and CMOD is shown in Figure 5 (b). Here it is shown that the toughness of the vertical crack has little influence on the relation between the interface crack length and the opening of the vertical crack.

Changing Mode I and II energy for the interface has a larger effect on the cracklength-CMOD relation than the ductility of the vertical crack. This is illustrated in Figure 6 (b). Furthermore, a higher interfacial Mode I energy, has an influence on the Moment-CMOD relationship, cf. Figure 6(a). Comparing cases B and C shows that - for these material properties - the energy consumed at the interface primarily consist of Mode I energy.
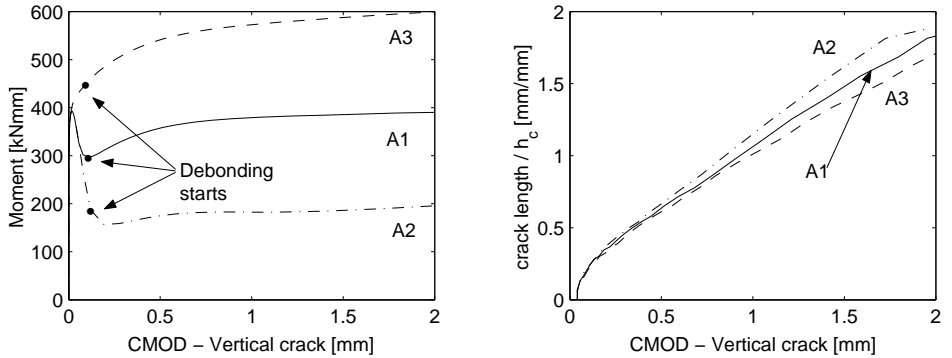

Figure 5: Graphical representation of three hypothetical cases: —A1, -.-. A2, - - - A3. (a) The bending moment $M = PL/4$ versus the crack opening of the vertical crack - CMOD, (b) The interface crack length normalised with respect to the concrete height h_c versus CMOD.
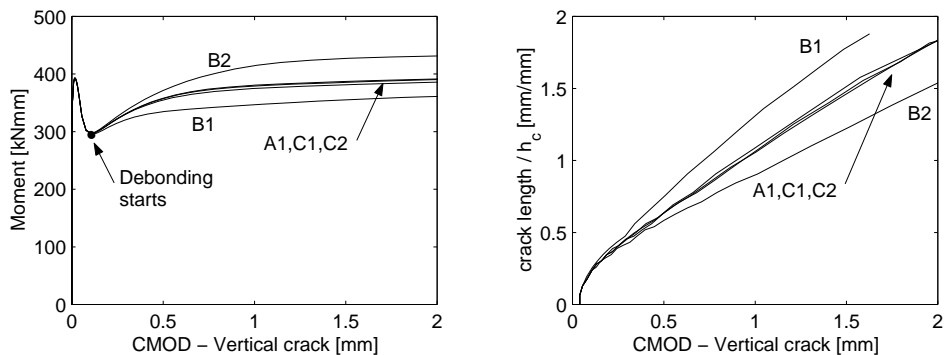
Figure 6: Graphical representation of five hypothetical cases cf. Table 1. (a) The bending moment $M = PL/4$ versus the crack opening of the vertical crack - CMOD, (b) The interface crack length normalised with respect to the concrete height h_c versus CMOD.

4 Parametric Study II - Failure Surface

In order to study the degree of mixed mode propagation a second parameter study is carried out. Same reference case as in previous section A1 is considered. One group of simulations, denoted D, is performed. This group involves a variation of the slope of failure surface f_1, cf. Figure 2. The parameter values are summarized in Table 2.

Name	Changing Parameter and value
A1	Reference
D1	$2\tan(\varphi)$
D2	$3\tan(\varphi)$

Table 2: Parameter variation of slope of failure surface f_1, $\tan(\varphi)$ as defined in Figure 2.

For constant cohesion c a change in the slope $\tan(\varphi)$ of f_1, will change the position of the corner of the failure criterion. Mixed shear and tension failure takes place in the corner when f_1 and f_2 intersects, and is of special interest, since the steel-concrete interface crack propagates in a mixed mode.

The stress distribution during crack propagation is shown in Figure 7. Results for the cases A1 and D1 for a vertical crack opening of CMOD=0.5 mm are shown. The interface crack has propagated a length of around (x-coordinate/h_c) ≈ 1. The peak of tensile normal stresses represents the interfacial crack tip.

The corner values for cases A1 and D1 differ due to a different slope of surface f1. As the crack propagates along the interface, it will try to transfer maximum normal- and shear stress across the interfacial crack. Dominated by Mode I fracture, the stress state in the

8

fracture process zone will tend to stay in the corner of failure surfaces f_1 and f_2, cf. Figure 2. Considering the cases A1 and D1, the corner of normal and shear failure before crack initiation is given by: A1($\sigma_{corner},\tau_{corner}$)=(2 MPa,2 MPa), D1($\sigma_{corner},\tau_{corner}$)=(2 MPa,1 MPa). As the corner values are different, a different stress distribution along the steel-concrete interface is observed. For an opening of the vertical crack (CMOD=0.5mm), the distribution of shear-normal stresses at the crack tip and along the fracture process zone is different. The crack tip is characterised by a peak of normal stress.
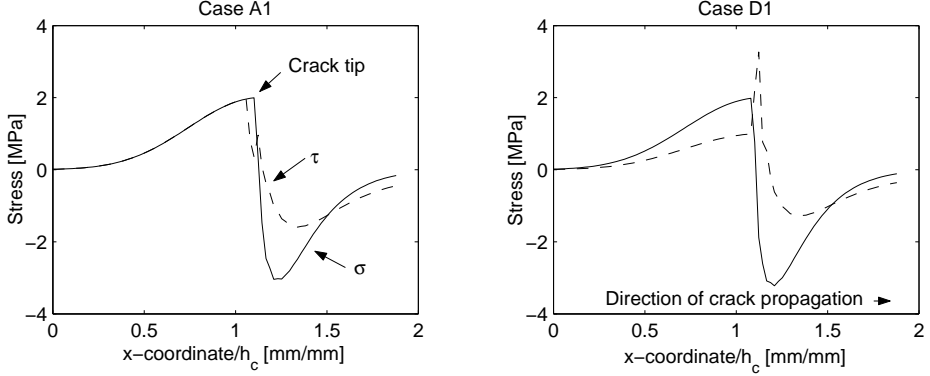

Figure 7: Stress distribution along the interface for cases D1 and A1 for a crack opening of CMOD=0.5mm. The two line types represent the normal and shear stresses acting at the interface between steel and concrete: — σ, - - - τ

It turns out that the mixed mode state at the crack tip varies during crack propagation. In order to illustrate varying mixed mode state during crack propagation, the mixed mode state is defined by:

$$\beta = arctan\left(\frac{s}{w}\right) \qquad (4)$$

where s and w relates to the crack opening of the interface. The relative deformation s is the cracking deformation related to Mode II fracture and w is the Mode I opening. A failure in pure opening mode (Mode I) corresponds to $s = 0 \Rightarrow \beta = 0^0$ and pure shear crack propagation correspond to $w = 0 \Rightarrow \beta = 90^0$. The angle β is plotted versus the crack tip position in order to illustrate the changing mixed mode state during crack propagation of the interface, cf. Figure 8. The curves of Figure 8 are given in terms of the mixed mode angle β, as defined by equation (4) versus the crack tip position. The value of β is calculated at the normal stress peak. The Figure illustrates the three cases A1, D1 and D2, each possessing different slopes of failure surface f_1. All cases considered start out close to Mode I fracture. As the crack tip propagates along the steel-concrete interface, cases D1 and D2 increase in Mode II fracture. Case D2 corresponds to a situation where failure surface f_1 intersect the σ-axis and propagates almost in pure Mode II.
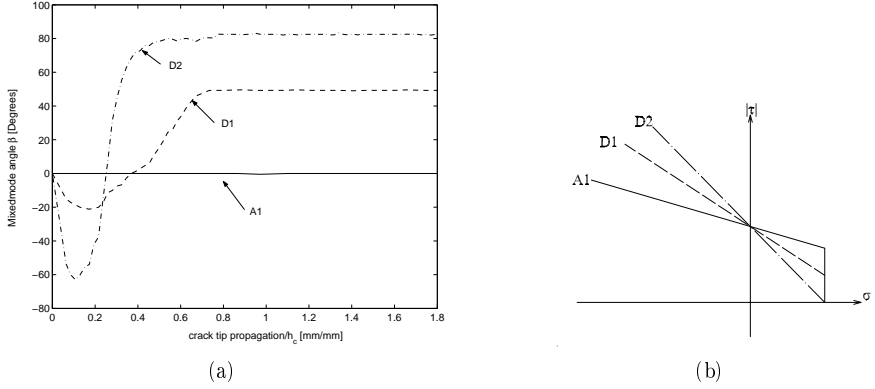
9

(a)   (b)

Figure 8: (a) Mixed mode angle β as defined in Equation (4) versus interface crack tip position normalised with the concrete height h_c for three hypothetical cases: —A1, - - - D1, -.-. D2. The mixed mode angle is calculated at the peak of normal stress, (b) Schematic representation of the three failure surfaces considered.

5   Conclusion

A model to investigate the debonding process of a concrete overlay cast on a steel plate has been developed. Based on discrete crack theory, the model describes the situation where a vertical crack propagates through the concrete overlay and causes debonding between the steel-concrete interface. The interfacial mixed mode fracture has been modelled using a composite interface model taking into account nonlinear softening of the interface.

The debonding process in the case of a negative bending moment has been investigated through two parameter studies. Firstly, the effect of a ductile concrete overlay has been investigated and the results show how it influences the global performance. However, a ductile concrete overlay has little effect on the relation between the interfacial crack length and the opening of the vertical crack CMOD. Secondly, Mode I energy of the steel-concrete interface has in the case considered, larger effect on global ductility than Mode II energy. Furthermore, interfacial Mode I energy has a significant influence on the Moment-CMOD relationship.

A second parameter study has been carried out in order to study the stress distribution along the interface. The stress distribution during crack propagation has been investigated for different shapes of the failure criterion. It can be concluded that the crack initiates in a mixed mode, where the stress distribution along the steel-concrete is dependent on the intersection between the shear and normal stress failure surfaces. Dependent on the failure criterion, the stress state along the interfacial process zone tends to stay in the corner between shear and tension failure. The mixed mode state changes through crack propagation of the interface.

From a practical point of view the model carried out attempts to illustrate the role of the different parameters, which might be considered in a design situation. In addition to the

significance of high fracture energy of the overlay in the debonding situation considered, this study shows the difference in behaviour for different Mode I and II energies of the steel-concrete interface.

References

der Pluijm, R. V. (1992), 'Material properties and its components under tension and shear', *Proceeding of 6th Can. Masonry Symp. Saskaton Canada* .

DIANA (2003), *DIANA User's Manual – Release 8.1*, june edn, TNO Building and Construction Research, P.O. Box 49, 2600 AA Delft, The Netherlands.

Granju, J. (2001), 'Debonding of thin cement-based overlays', *Journal of Materials in Civil Engineering* **13**(2), 114–120.

Granju, J. L. (1996), 'Thin bonded overlays: About the role of fiber reinforcement on the limitation of their debonding', *Adv. Cement Based Mat* **4**(1), 21–27.

Hillerborg, A., Modéer, M. & Petersson, P. (1976), 'Analysis of crack formation and crack growth in concrete by means of fracture mechanics and finite elements', *Cem. Concr. Res.* **6**(6), 773–782.

Lourenço, P. B. & Rots, J. G. (1997), 'Multisurface interface model for analysis of masonry structures', *Journal of Engineering Mechanics* **123**(7), 660–668.

Lourenço, P. B., Rots, J. G. & Blaauwendraad, J. (1998), 'Continuum model for masonry: Parameter estimation and validation', *Journal of Structural Engineering* **124**(7), 642–652.

Olesen, J. F. (2001), 'Fictitious crack propagation in fiber-reinforced concrete beams', *Journal of Engineering Mechanics* **127**(3), 272–280.

Walter, R., Stang, H., Gimsing, N. J. & Olesen, J. F. (2003), 'High performance composite bridge decks using scsfrc', *The Fourth International Workshop on High Performance Fiber Reinforced Cement Composites, Ann Arbor, Michigan* pp. 495–504.

Paper VI

Method for Determination of Tensile Properties of ECC
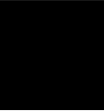
Method for Determination of Tensile Properties of Engineered Cementitious Composites (ECC)

Lennart Østergaard, Rasmus Walter and John F. Olesen
Department of Civil Engineering Technical University of Denmark DK-2800 Kgs. Lyngby, Denmark.

Abstract

Today, ECC has been developed to a stage where the material is being used in field testing and limited full scale constructed facilities. However, the lack of reliable, practical, standardized test methods for determination of the strain hardening properties of the material constitutes a significant obstacle for day-to-day structural engineering design and material quality control during construction execution. In practice a simple and robust test method is required on a construction site. The uniaxial tension test (UTT) is regarded too complicated to serve as such. Instead, the widely adopted four point bending test (FPBT) may be used for this purpose, provided that an appropriate interpretation of the test data is available. The present paper presents a contribution in this direction. Sectional analysis of ECC beams in the strain-hardening stage is used in a parametric analysis aimed at revealing the fine details of correlation uniqueness between the tensile stress-strain (σ-ε) curve parameters of an ECC and its FPBT load-deflection diagram. Further, an inverse analysis designated for the determination of the strain hardening properties is described. Finally, experimental results based on FPBT test results are presented.

Keywords: ECC, FPBT, inverse analysis, hinge model, strain hardening, tensile properties

1. Introduction

Over the past decade, a new class of civil engineering materials has been developed, often referred to as High Performance Fiber Reinforced Cementitious Composites (HPFRCC). A subclass is the Engineered Cementitious Composites (ECC), which are *engineered* by detailed design of the microstructure in order to obtain extraordinary toughness and ductility. The fundamental difference between ECC and a conventional Fiber Reinforced Concrete (FRC) is its behavior in tension. For FRC, fracture localization occurs immediately after the first crack is formed. In the case of ECC, propagation of the initial crack will be prevented by the fiber bridging, causing a second matrix crack to form elsewhere. This results in non-localized multiple cracking, also known as macroscopic pseudo strain hardening behavior. ECCs have presented new alternatives in the design of civil structures. Due to their high ductility they are well suited in the design of structures exposed

to cyclic loading, e.g. bridge slabs and retrofit of walls subject to seismic loading. A comprehensive summary of the state of the art and present applications are given in Li (2003).

The aforementioned paper, Li (2003), points out that despite an increasingly complete material database is being established for the properties of ECC under various mechanical loading, there is still a need to develop standardized test methods, particularly for the fundamental uniaxial tensile σ-ε curve. Such a method could greatly ease comparisons between different ECC materials which, today, relies on the complicated UTT. Also in practice a simple and robust test method is required for on-site quality control and for material suppliers. Formulation of a simple standardized test is one of the objectives of a technical committee recently established under the auspices of RILEM (RILEM TC HFC).

Today, most characterization of the σ-ε relationship of ECC is carried out using the UTT as shown in Li et al. (2002). However, the UTT is generally regarded as too demanding with respect to laboratory equipment and staff expertise. First of all, the testing machine needs to be closed-loop controlled and sufficiently stiff. Furthermore, no notch can be introduced into the specimen, and thus, the experiment is particularly sensitive to stress concentrations occurring at the fixation points of the specimen. Also the specimen dimensions must be observed carefully, since shrinkage or unprecise form filling may lead to stress variations throughout the specimen, and thus, premature crack localization.

A simpler alternative to the UTT is the FPBT. This setup utilizes that the moment is constant between the loading points, which allows for strain hardening in the material and subsequent, determination of the σ-ε relationship by inverse analysis of the load-deflection response. Furthermore, the FPBT is already widely adopted in the user community of cementitious materials (Stang & Li 2004), while inverse analysis has recently been attempted (Kanakubo et al. 2003).

This paper explores the possibility of employing the FPBT for determination of the σ-ε relationship of ECC. Sectional analysis of ECC beams in the strain-hardening stage is used in a parametric analysis aimed at revealing the correlation uniqueness between the tensile σ-ε curve of an ECC and its FPBT load-deflection diagram. Further, an inverse analysis designated for the determination of the σ-ε relationship is described. The complete method is demonstrated through the analysis of experimental FPBT results.

2. Modelling of ECC

The pseudo-strain hardening properties of ECC in tension are often described using a bilinear σ-ε relationship since this assumption captures the main characteristics of the material behavior. This also holds true for the compressive properties, see e.g. Maalej & Li (1994) or Kabele & Horii (1997). Also the possibility of crushing of the ECC in the compressive region was modelled in Maalej & Li (1994). These constitutive conditions are all included in the present model and illustrated in Figure 1.
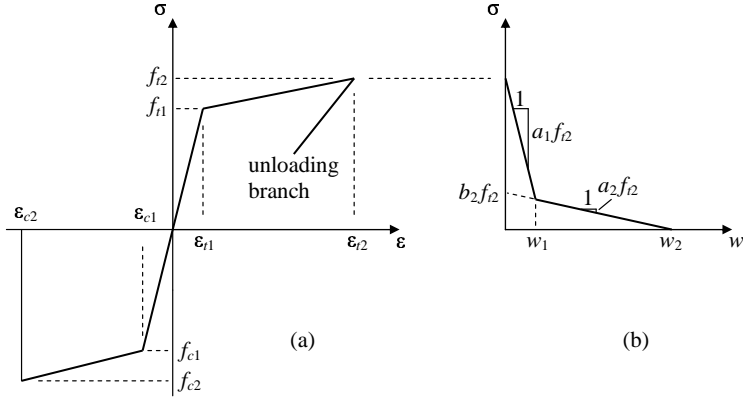
Figure 1: Assumed constitutive relationships for ECC: bilinear in tension and compression prior to crack localization (a), while a bilinear σ-w relationship after crack localization is assumed (b).

However, also the localization and softening of ECC is important when a FPBT is considered since it may influence the pre-peak response significantly. In fact, up to 50% of the pre-peak response may be associated with localization. This is due to the ductile behavior of the ECC which influences the σ-w relationship, making it very tough. This is illustrated in Kabele & Horii (1997), where the softening was described using a linear curve from peak stress to zero stress with $w_2 = L_f/2$, where w_2 is the crack opening for which the stress transfer is equal to zero, and L_f is the fiber length. The typical length of the fibers in ECC is 8-12 mm.

Thus, the present model includes the influence of the σ-w relationship, however, using the bilinear approximation shown in Figure 1. Consideration of this part of the material behavior will make it possible to determine the influence of the localization on the FPBT response.

3. The Hinge Model

The modelling will follow the nonlinear hinge concept described in Olesen (2001). The hinge is illustrated in Figure 2a. The propagating crack is modelled within the element boundaries as a layer of independent spring elements. These spring elements are formed by incremental horizontal strips, and are attached at each end to a rigid boundary. Each boundary may rotate and translate such that it may be joined with an uncracked beam modelled according to the classical beam theory. Figure 2b shows the stress distribution in the hinge when both crushing and localization with stress free tail has developed. Based on this distribution, the entire hinge behavior from unset of loading to failure may be described. It proves convenient to introduce the mean values of the curvature and the distribution of longitudinal strains, κ^* and ε^*, respectively:
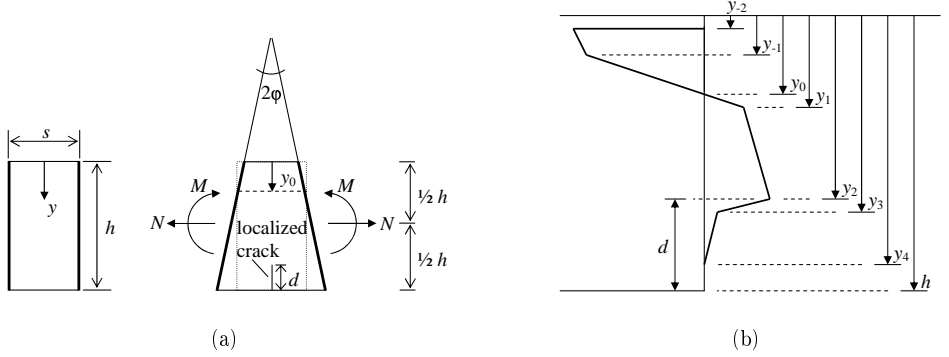
Figure 2: Geometry, loading and deformation of the hinge element (a) and stress distribution in the hinge element when crushing and localization of the crack has developed (b)

$$\kappa^* = 2\frac{\varphi}{s}; \qquad \varepsilon^* = 2(y - y_0)\kappa^* \tag{1}$$

The deformation of an incremental strip is given by $u(y) = s\varepsilon^*(y)$ where s is the width of the hinge. Thus, given the material parameters in Figure 1, the depths y_{-2}, y_{-1}, y_1 and y_2 may be determined:

$$y_{-2} = y_0 - \varepsilon_{c2}\frac{s}{2\varphi} \ , \quad y_{-1} = y_0 - \varepsilon_{c1}\frac{s}{2\varphi} \ , \quad y_1 = y_0 + \varepsilon_{t1}\frac{s}{2\varphi} \ , \quad y_2 = y_0 + \varepsilon_{t2}\frac{s}{2\varphi} \tag{2}$$

The total deformation, $u(y)$, in the cracked stages may be determined as the sum of the elastic deformation, the opening of the crack and the elastic unloading due to the stress drop caused by the localization:

$$u(y) = \varepsilon_{t2}s + w(y) - \frac{f_{t2} - \sigma_w(y)}{E_{ul}}s = \bar{\varepsilon}s + w(y) + \frac{\sigma_w(y)}{E_{ul}}s \tag{3}$$

Here, the crack opening in the cracked incremental strip in the depth y, $w(y)$, has been introduced. The associated crack bridging stress, $\sigma_w(w(y))$ is given by $\sigma_w(w(y)) = f_{t2}(b_i - a_i w(y))$, $i = 1, 2$ where $b_i = (1, b_2)$, see Figure 1, and where a_1 and a_2 are the first and second slopes of the normalized σ-w relationship, respectively. The unloading is assumed elastic and the stiffness is denoted E_{ul} while $\bar{\varepsilon}$ is the unrecovered strain after complete unloading:

$$\bar{\varepsilon} = \varepsilon_{t2} - \frac{f_{t2}}{E_{ul}} \tag{4}$$

Combining Equations 1 and 3 results in an expression for the crack stress at depth y:

4

$$\sigma_w(w(y)) = (2(y - y_0)\varphi - \bar{\varepsilon}s - w(y)) \frac{E_{ul}}{s} \tag{5}$$

Utilizing the bilinear σ-w relationship assumption, an expression for the crack opening, $w(y)$, and the stress, $\sigma(y)$, may be derived:

$$w(y) = \frac{2(y - y_0)\varphi - \bar{\varepsilon}s - \zeta_i}{1 - \beta_i} \quad, \quad \sigma(y) = \frac{\zeta_i - 2(y - y_0)\varphi\beta_i + \bar{\varepsilon}s\beta_i}{1 - \beta_i} \frac{E_{ul}}{s} \tag{6}$$

where the dimensionless parameters β_i and ζ_i are defined by:

$$\beta_i = \frac{f_{t2}a_i s}{E_{ul}} \quad, \quad \zeta_i = \frac{f_{t2}b_i s}{E_{ul}} \quad, \quad i \in [1, 2] \tag{7}$$

The depths y_3 and y_4 may be determined from Equation 6 by solving $w_1 = w(y_3)$ and $w_2 = w(y_4)$:

$$y_{i+2} = y_0 + \frac{1}{2\varphi}(\zeta_i + \bar{\varepsilon}s + (1 - \beta_i)w_i) \quad, \quad i \in [1, 2] \tag{8}$$

The complete stress distribution may now be established for any given rotation of the hinge, φ, and thus, the normal force, N and the moment, M may be derived. This is done by piecewise numerical integration in the range $y \in [0, h]$ using the phase change parameters y_i, $i \in [-2, -1, .., 4]$. The calculations proceed by incrementing the hinge rotation, φ, and subsequently determining first the depth of the neutral axis and then the hinge moment M.

4. Implementation of the hinge model in the FPBT

Figure 3a shows the FPBT. The clear span of the beam is L_t, while the distance from the ends to the loading points is L_c. The constant moment span is denoted by L_m. The deflection at midpoint of the beam is measured with reference to the loading points. Since the moment is constant in the middle part of the beam, this part may be modelled with incremental hinge elements, all undergoing the same rotation. Prior to localization of the crack in the hinge, the hinge rotation and the midpoint deflection will be governed by the initial elastic part and the strain hardening part of the $\sigma - \varepsilon$ curve. These contributions are both non-local and may be termed the non-localized rotation, φ_{nl}, and the non-localized deflection, u_{nl}. This is the situation in the upper part of Figure 3a. However, after the peak moment, M_p, is reached, a structural localization will take place, i.e. the cracks will continue to open at one or two locations, while the cracks in the remaining parts of the beam will close. One possible mechanism in this situation is shown in the lower part of Figure 3a, while others may be constructed by superposition of similar mechanisms. After the structural localization, the total rotation of the hinge and the midpoint deflection will include a localized part, φ_l and u_l. Modelling of the unloading requires that a certain unloading branch is defined. Figure 3b shows the assumed unloading branch for the closing hinges with a common focus point with the coordinates (φ_{fp}, M_{fp}). The opening

hinges will determine the moment capacity of the beam since here the material continues to degrade. The midpoint deflection, u_{nl}, and the load, P, prior to the structural localization are readily obtained as:

$$u_{nl} = \frac{1}{8}\kappa L_m^2 = \frac{1}{4}\frac{\varphi_{nl}}{s}L_m^2 \quad , \quad P = \frac{4M}{L_t - L_m} \tag{9}$$

After the structural localization has occurred, the total hinge rotation is given by: $\varphi_{tot} = \varphi_{nl} + \varphi_l$. For a given total hinge rotation and calculated moment, $M(\varphi_{tot})$, these contributions may be determined as:

$$\varphi_{nl} = \varphi_p - (\varphi_p - \varphi_{fp})\left(\frac{M_p - M}{M_p - M_{fp}}\right) \quad , \quad \varphi_l = \varphi_{tot} - \varphi_{nl} \tag{10}$$

where M_p is the peak moment and φ_p the correspoinding rotation. The localized deformation, u_l, is determined from the actual localization mechanism. For the situation shown in the lower part of Figure 3a, the result is:

$$u_l(\varphi_l) = \frac{1}{2}\left(L_a - L_c\right)\varphi_l \quad \text{for} \quad L_a \le L_b \tag{11}$$

The total deflection in the case where structural localization has taken place is readily obtained as the sum of Equations 9 and 11. Note, that other localization mechanisms may be modelled by superposing the mechanism in Figure 3 using different localization points.
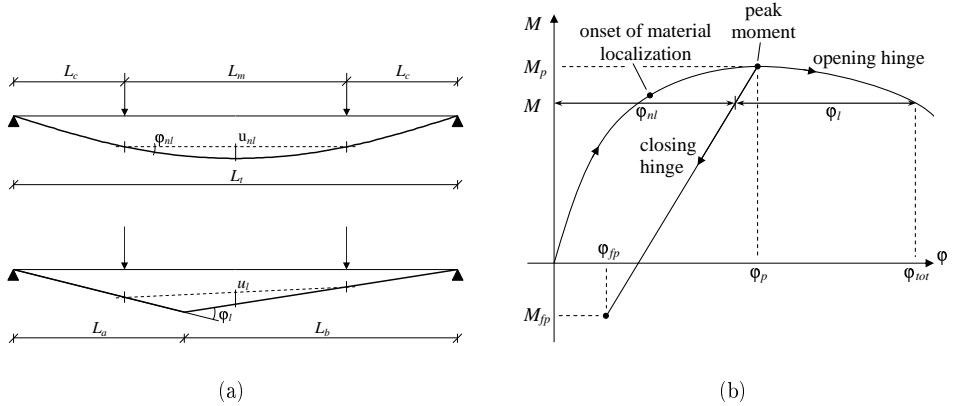

(a)   (b)

Figure 3: Deformations of the FPBT during loading. Initially, no structural localization is present, while later, a structural localization occurs (a). Schematic moment-rotation curve for the non-linear hinge showing the incorporation of a simple elastic unloading criterion (b).
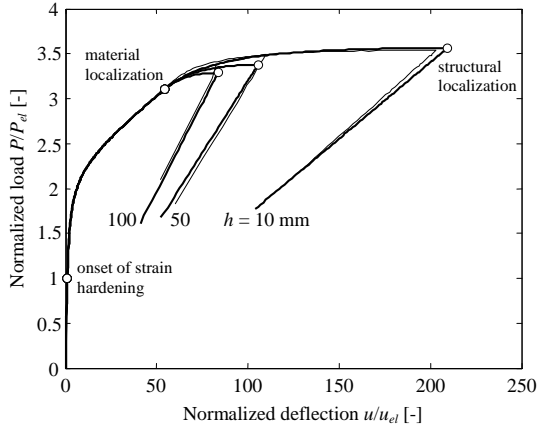
Figure 4: FEM results (thin lines) compared with the hinge model results (thick lines) (a) for a FPBT for three different beam heights with s/h=0.9. The white circles mark the transition points of the hinge model.

5. FEM calibration of the FPBT model

The hinge model introduces the hinge width parameter, s, which needs to be determined through an FEM calibration. Investigations on normal concrete and FRC applying the hinge model on the Three Point Bending Test (TPBT) indicate that s may be selected roughly as $h/2$ for all material choices and beam geometries, see e.g. Østergaard (2003). However, for the FPBT it appears that the FEM results are approximated most precisely using s/h=0.9. Figure 4 shows a comparison between the hinge model and the FEM results for different beam heights. The remaining parameters for the beams are: L_t=500 mm, L_m=250 mm and thickness t=100 mm. The material parameters have been selected as: f_{t1}=4 MPa, f_{t2}=6 MPa, $E_{t1}=E_{c1}$=22000 MPa, E_{t2}=100 MPa and a_1=0.0833 mm^{-1}, where E_{c1}, E_{t1} and E_{t2} denotes the slopes of the σ-ε relationships. Compressive softening and crushing has been disregarded in this comparison by selecting large values of f_{c1} and f_{c2}. The σ-w relationship has been approximated with a linear curve by selecting small values of a_2 and b_2 while the calculation of a_1 is based on the assumption that $w_2 = L_f/2$, $L_f = 12$ mm. The strain capacity of the material is approximately 2% ($\varepsilon_{t2} \approx 0.02$). The structural localization of the FEM model occurs symmetrically around the midsection at both loading points (Figure 3a with $L_a = L_c$ superposed with the same situation mirrored). This is due to a small stress concentration at those points caused by the concentrated loading. The choice of s in Figure 4 is made based on an attempt to fit the point of structural localization for all beam heights. The curves in Figure 4 are normalized with regard regard to the elastic deflection, u_{el}, and load, P_{el}, which may be calculated using Equations 2 and 9.

The FEM and hinge model curves show a high degree of correlation. Prior to the material localization, where only the tensile strain hardening accounts for the non-linearity of the load-deflection response, the results are essentially identical. However, after the material localization is initiated, the hinge model results become dependent on s, but with the optimal choice of s, the differences are still limited.

6. Inverse analysis

Methods for the extraction of the strain hardening properties of ECC is the subject of only one paper in the literature (Kanakubo et al. 2003). However, this paper does not include the effect of localization of the crack. Using the hinge model described in the previous sections, localization is included, and a precise result is obtained by simply using the squared sum of differences between the experimental result and the model result as object function:

$$\min_{(f_{t1}, f_{t2}, E_{t1}, E_{t2})} \sum_{i=1}^{N} \left(\frac{\hat{P}_i - P_i}{P_i} \right)^2 \tag{12}$$

in which $\hat{P}_i$ is the load obtained by the hinge model for a certain deflection, u_i, while P_i denotes the experimentally obtained load for the same deflection. The data points on the graph must be equidistantly spaced on the curve in order to give each part the same weight in the calculations. Note that the compressive properties are not included in the optimization since they may be determined initially by a simple compression test. Also knowledge of the σ-w relationship is unimportant - in fact it turns out, in comparison with FEM results that the strain hardening properties may be determined without knowing this relationship.

Table 1: Results from inverse analysis with different beam heights, h [mm], together with an analysis on the sensitivity of the selection of a_1 [mm^{-1}] and s [mm]. The strain hardening material parameters were selected to $f_{t1} = 4\ MPa$, $f_{t2} = 6\ MPa$, $E_{t1} = 22\ GPa$ and $E_{t2} = 100\ MPa$. The numbers in the table represent the error on the determination of the material parameters in percent

h	10	40	50	60	100	50	50	50
s	1	1	1	1	1	1	45	90
a_1	0.0833	0.0833	0.0833	0.0833	0.0833	2.6656	0.0833	0.0833
E_{t1}	− 1.2 %	+1.1 %	+2.3 %	+4.4 %	+29.7 %	+2.3 %	+2.3 %	+2.3 %
E_{t2}	+9.3 %	− 0.8 %	+1.0 %	+2.1 %	+8.0 %	− 0.6 %	− 1.4 %	− 4.0 %
f_{t1}	− 1.1 %	− 0.1 %	− 0.5 %	− 0.9 %	− 4.2 %	− 0.4 %	− 0.3 %	− 0.1 %
f_{t2}	− 1.7 %	− 0.2 %	− 0.8 %	− 1.1 %	− 1.9 %	+1.4 %	+2.4 %	+5.4 %

This is shown in Table 1 where various FEM results have been subject to the method of inverse analysis. The correlation between the results is remarkably good. If moderate

h/L_m values are selected the inverse analysis is very precise - only extremely thin beams, $h = 10$ mm, or very thick beams, $h = 100$ mm give less fine results. This is particular seen for the thick beam where E_{t1} is determined with an error of 30%. Note that the selection of s is unimportant - small as well as high values of s give good results, which shows that a close fit of the point of structural localization is not important. It is also interesting to notice that the strain hardening properties can be determined regardless of the fact that a part of the total deflection of the beam is caused by crack localization. However, note that this is only true if the material localization point is predicted accurately. Finally, as demonstrated in Table 1, even if a_1 is selected as 32 times larger than the value used in the FEM model, accurate results are obtained.

7. Experimental results

The method for extraction of the σ-ε relationship of ECC has been tested on an ECC mix with the mix proportions given in Table 2. In total 9 beams were cast with varying beam heights, $h = 40, 50$ and 60 mm. The remaining beam dimensions were $L_m = 250$ mm, $t = 100$ mm and $L_t = 500$ mm. The casting direction was perpendicular to the beam height in order to avoid any material variations throughout the beam height. The beams were cast in wooden water-tight molds and stored in the concrete lab for the first 24 hours, covered with plastic. Then, they were water cured until the testing began at an age of 7 days.

Table 2: Mix design. The cement type was CEM I 52.5. FA is fly ash, while SP is super plasticizer

Mix	Cement	Sand	Quarts	FA (milled)	FA	Water	SP	Fibers
kg/m^3	581	232	233	209	489	315	8	26

The FPBT setup was designed such that both supports and loading points could rotate independently around two axes: a horizontal axis parallel to the beam and a horizontal axis perpendicular to the beam. Furthermore, each loading point could move vertically independently of each other. This system ensures that no redundant forces were acting on the beam.

The results from the experiments are shown in Figure 5a. As expected, there is some scatter, which usually is the case for ECC. Figure 5b shows a comparison between one experimental curve and the corresponding output from the inverse analysis. The correlation is convincing and it demonstrates the ability of the model to capture real ECC behavior. The average output from the different beam heights are shown in Table 3. It is evident that all beams height gives the same result, which is rather promising for the method since this excludes the possibility of structural influence on the material parameters determined.
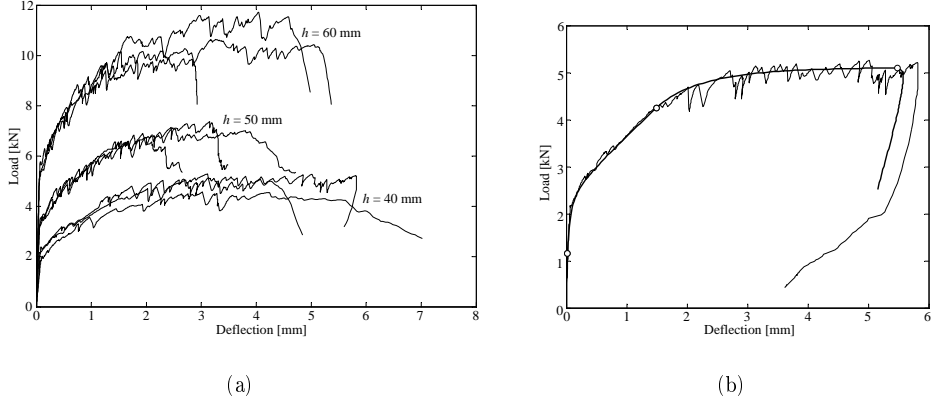
Figure 5: Experimental results (a), and a comparison between one experimental curve and the outcome of the inverse analysis (b), ($h = 40$ mm, $s/h = 0.9$, unloading according to Figure 3a with $L_a = L_c + 20$ mm)

Table 3: Experimental results obtained through the inverse analysis. The result for each beam height represent the average of three experiments. The latter column gives the average and standard deviation for all nine beams.

h [mm]	40	50	60	Average	Std. dev.
E_{t1} [GPa]	34	33	34	33	7
E_{t2} [GPa]	0.30	0.20	0.21	0.24	0.06
f_{t1} [MPa]	2.5	2.5	2.6	2.6	0.2
f_{t2} [MPa]	4.3	4.0	4.1	4.1	0.3
ε_{t1} [$\mu\varepsilon$]	84	77	80	80	18
ε_{t2} [%]	0.6	0.8	0.7	0.7	0.1

8. Conclusions

This paper presents a new method for interpretation of the load-deflection response of the ECC FPBT setup, by incorporating crushing, the bilinear compressive and tensile σ-ε relationships and the bilinear σ-w relationship of the ECC material. The method proves very accurate when compared with FEM results.

It has been demonstrated that localization of the crack occurs prior to the peak load, and thus, only a part of the total deflection of an ECC beam may be attributed to the strain hardening response.

However, a method proposed for inverse analysis proves able to distinguish between the strain hardening and the crack localization parts of the deflection, thus enabling extrac-

tion of the strain hardening properties. Compared with FEM, this method gives very precise results. The method also performs well in comparison with experiments. However, complementary UTT experiments are needed in order to finally validate the model.

9. Acknowledgements

References

Kabele, P. & Horii, H. (1997), 'Analytical model for fracture behaviour of pseudo strain-hardening cementitious composites', *Concrete Lib. of JSCE* **29**, 105–120.

Kanakubo, T., Shimizu, T., Katagiri, K., Kandra, M., Fukuyama, T. & Rokugo, K. (2003), Evaluation of tensile properties for DFRCC - results of round robin test by JCI technical commitee, *in* 'Proc. JCI Symp. on DFRCC (in Japanese)', pp. 101–111.

Li, V. (2003), 'On engineering cementitious composites (ECC)', *Journal of Advances Concrete Technology* **1**(3), 215–230.

Li, V., Wu, C., Wang, S., Ogawa, A. & Saito, T. (2002), 'Interface tailoring for strain-hardening PVA-ECC', *ACI Materials Journal* **99**(5), 373–400.

Maalej, M. & Li, V. C. (1994), 'Flexural/tensile strength ration in engineered cementitious composites', *ACSE Journal of Materials in Civil Engineering* **6**(4), 513–528.

Olesen, J. F. (2001), 'Fictitious crack propagation in fiber-reinforced concrete beams', *Journal of Engineering Mechanics* **127**(3), 272–280.

Østergaard, L. (2003), Early-Age Fracture Mechanics and Cracking of Concrete. Experiments and Modelling, PhD thesis, Department of Civil Engineering, Technical University of Denmark, Lyngby, Denmark.

Stang, H. & Li, V. C. (2004), Classification of fiber reinforced cementitious materials for structural applications, *in* 'BEFIB', RILEM, pp. 197–218.

Paper VII

Analysis of Steel Bridge Deck Stiffened with Cement-Based Overlay

Paper submitted to ASCE - Journal of Bridge Engineering
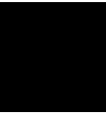
Analysis of Steel Bridge Deck Stiffened with Cement-Based Overlay

Rasmus Walter*, John F. Olesen*, Henrik Stang*, & Tina Vejrum**

*Department of Civil Engineering Technical University of Denmark DK-2800 Kgs. Lyngby, Denmark, e-mail: rw@byg.dtu.dk

**COWI A/S Consultant Engineers, Parallelvej 2, DK-2800 Kgs. Lyngby, Denmark

Abstract

Over the past years, with increasing traffic volumes and higher wheel loads, fatigue damage in steel parts of typical orthotropic steel bridge decks, has been experienced on heavily trafficked routes. A demand exists to find a durable system to increase the fatigue safety of orthotropic steel bridge decks. A solution might be to enhance the stiffness of the traditional orthotropic bridge deck by using a cement-based overlay. In this paper, an orthotropic steel bridge deck stiffened with a cement-based overlay is analyzed. The analysis is based on nonlinear fracture mechanics, and utilize the finite element method. The stiffness of the steel deck reinforced with an overlay depends highly on the composite action. The composite action is closely related to cracking of the overlay and interfacial cracking between the overlay and underlying steel plate (debonding). As an example, a real size structure, the Farø Bridges located in Denmark, are analyzed. The steel box girders of the Farø Bridges spans 80 meters, and have a depth of 3.5 m, and a width of 19.5 m. The focus of the present study is the top part of the steel box girders, which is constructed as an orthotropic deck plate. Numerous factors can influence the cracking behavior of the cement-based overlay system. Both mechanical and environmental loading have to be considered and effects such as shrinkage, temperature gradients and traffic loading are taken into account. The performance of four overlay materials are investigated in terms of crack widths. Furthermore, the analysis shows that debonding is initiated for a certain crack width in the overlay. The load level where cracking and debonding is initiated depends on the stress-crack opening relationship of the material.

Keywords Orthotropic bridge deck, cement-based overlay, FEM, fibre reinforced concrete, nonlinear fracture mechanics.

1 Introduction

Orthotropic steel bridge decks are widely used for large and medium span bridges. Compared to composite girder structures in long-span structures, the advantage of orthotropic steel decks is the considerably reduced dead load. The success of orthotropic bridge decks

may be due to its high strength to weight ratio (Dowling 1968). However, compared to a rigid concrete bridge deck, a steel deck plate is subjected to considerable local deformations caused by the wheel loads on the deck. Over the years, it has been acknowledged that the record of durability on heavily trafficked routes has not been satisfactory. Fatigue damage, especially in welds and steel plates have been observed, (Kolstein & Wardenier 1997), (Kolstein & Wardenier 1998). Repairs, particularly to highway surfacing, have been necessary on many important bridges within the last 20 years or less, see e.g. Smith & Bright (2003).

With the aim to analyze the fatigue problem in details, the mechanical behavior of orthotropic steel bridge decks has been the subject of numerous research projects over the recent years. The surfacing, and its contribution to stress reduction has, been investigated by several authors. The characteristic properties of two basic surfacing categories, bitumenous and polymeric materials, have been analyzed by Wolchuk (2002). The study shows, that for a high elastic moduli of the surfacing material, the stress range in the critical fatigue parts of the steel deck is reduced considerably. However, traditional surfacing materials are generally viscoelastic or plastic and behave elastically at low temperatures only. Experiments carried out by Jong et al. (2004) performed on orthotropic bridge decks with different surfacing materials at different temperatures, show that the stress range compared to a deck without surfacing is reduced by a factor of 1 to 6.

A promising solution might be to use a cement-based overlay to reduce the stress range in the fatigue sensitive steel parts of an orthotropic bridge deck. This approach has already been investigated by several authors, see e.g. Battista & Pfeil (2000) or Braam et al. (2003). In practice, the first pilot test applying a cement-based overlay to an orthotropic steel bridge deck has already been carried out. A replacement of a 60 m^2 area of the bascule part on the Van Breinenoord Bridge in Rotterdam, The Netherlands has been carried out, cf. Buitelaar (2002) or Jong & Kolstein (2004). Here it is concluded that stresses in fatigue sensitive details, compared to a traditional orthotropic steel bridge deck, are reduced from 128 MPa to 28 MPa. The economical investment for placing the overlay is equal to the cost of a traditional bituminous wearing course of melted asphalt.

The present analysis investigates the performance of an orthotropic steel bridge deck with a cement-based overlay applied with the aim of reducing the stress range. As the composite action between the overlay and underlying steel deck is closely related to cracking, overlay cracking and debonding is the main focus of this study. Based on nonlinear fracture mechanics, modeling of cracks is carried out using the so-called Fictitious Crack Model (FCM) first presented by Hillerborg et al. (1976). The advantage of the FCM is its simplicity and good correlation with experiments.

Environmental and mechanical loading such as traffic, early age shrinkage and temperature gradients, are all significant factors which can initiate cracking. High concentrated wheel loads cause considerable local deformations of the deck. Since the overlay is bonded to the deck, local deformation caused be wheel loads produces large tensile stresses in the overlay and increases the risk of cracking. To overcome the problem of high tensile stresses in the overlay, the application of high performance concrete might be effective. However, when applying modern high performance concretes, cracking sensitivity is dramatically

increased in early ages as well as in the hardened stage. Since these concretes have low water to cement ratios and often include silica fume, autogenous deformations are increased (Jensen & Hansen 2001). Thus, an analysis of the stress history of the overlay in early ages might be important. Another important aspect, concerns the influences of temperature gradients between the overlay and steel plate. Since the overlay is restrained from moving due to its bond to the steel deck, cooling of the bridge deck produces high tensile stresses in the cement-based overlay. The above considerations all point towards applying ductile fiber reinforced concrete as overlay material.

Based on nonlinear fracture mechanics, this paper aims to analyze an orthotropic bridge deck stiffened with a cement-based overlay. Load effects such as mechanical and environmental loadings are considered. The aim of the study is to describe a method, which is capable of analyzing the cement-based overlay system by means of cracking behavior. Crack widths and patterns are important factors in the estimation of the durability and hence the service life of a given structural system.

2   The Farø Bridges

The present analysis is carried out on the Farø Bridges, which is a part of the Sjælland-Falster connection located in Denmark. The Farø Bridges were built between 1980 and 1985 and carries the "South Motorway" leading from Copenhagen to the European continent over waterways between the two islands Sjælland and Falster, with a small island, Farø, in the middle. The two bridges are called the Sjælland-Farø Bridge and the Farø-Falster Bridge, cf. Figure 1 for a picture of the two bridges. For detailed information, see e.g. The Danish Ministry of Transportation (1987).

Figure 1: The Farø Bridges.

Fatigue problems have not yet been experienced in the orthotropic steel deck of the Farø

Bridges. The traffic intensity on the bridges is shown in Figure 2 for the period from 1990 to 2004. The traffic intensity on the Farø Bridges can be considered low compared to other bridges which have experienced fatigue damage in orthotropic bridge deck, cf. (Jong et al. 2004).
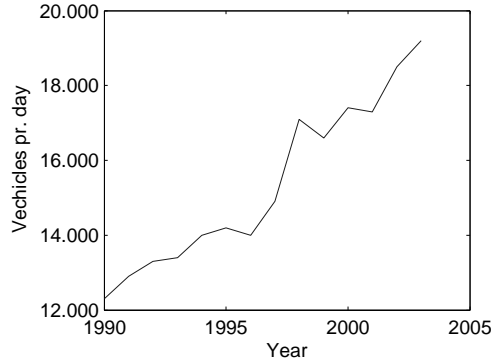

Figure 2: Traffic intensity on the Farø Bridges, source: (Danish Ministry of Transportation, *www.vd.dk*).

The two Farø Bridges are almost the same total length, approximately 1600 and 1700 m, respectively, and are only separated by the small island Farø. The statical main system of the Sjælland-Falster Bridge consist of 18 spans each 80 meters long apart from the two end spans which are 78 meters long, cf. Figure 3. The southern bridge, the Farø-Falster Bridge, has a cable stayed part with a span of 290 m. Figure 4, shows the statical main system of the Farø-Falster Bridge.

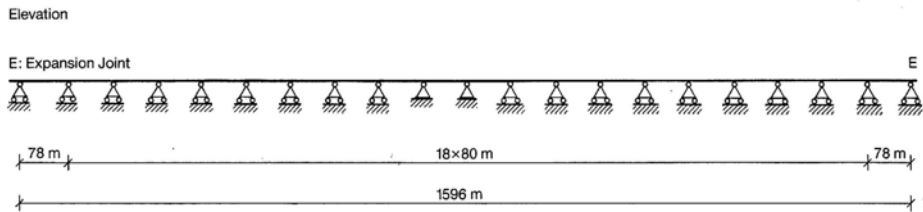Figure 3: Statical main system, the Sjælland-Farø Bridge.

The approach spans of the Sjælland-Farø Bridge and the Farø-Falster Bridge all have a span of 80 m. The approach spans are the focus of the present study, and thus the cable stayed part is not considered. The steel box girder designs for the two bridges are similar. The steel box girder is designed as a closed box with a trapezoidal cross-section and an
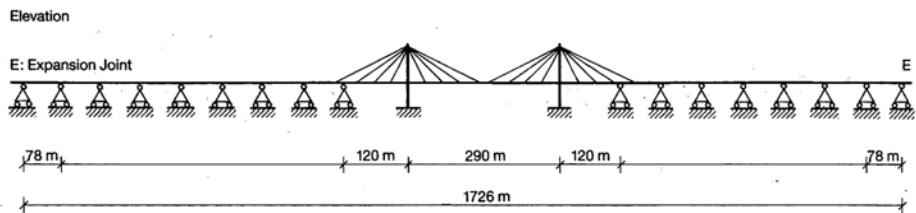
4

Figure 4: Statical main system, the Farø-Falster Bridge.

all-welded orthotropic roadway deck, with a structural depth of 3.5 m. Traffic is placed in two lanes in each direction and the steel girder has a total width of 19.6 m, cf. Figure 5 for a cross-sectional view.
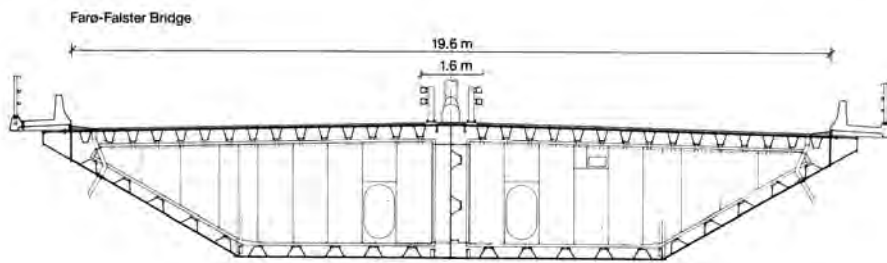

Figure 5: Cross-sectional view of the steel girder of the Farø Bridges.

The bridge deck is designed as an orthotropic 12 mm deck plate provided with longitudinal trapezoidal ribs of 6 mm plate thickness. The ribs are 300 mm high and placed at 620 mm centres. The orthotropic deck is supported on transverse bulkheads at every 4 meters. Figure 6 displays the structural lay-out of the box girder.

2.1 Cement-Based Overlay System

A way to increase the local stiffness of the top orthotropic bridge deck in the steel girder might be to combine a thin cement-based overlay with the steel plate. It is suggested in this system to achieve composite action through adhesion and leaving out mechanical shear connectors. The motivation for leaving out shear connectors is mainly based on two reasons: (i) using shear connectors creates undesirable local peak stresses, and (ii) a system with small shear connectors in large numbers will be costly with regard to labor. Furthermore, shear connectors are only activated for large differential deformations off the two materials.

A number of small scale tests have been performed to investigate the fracture mechanical
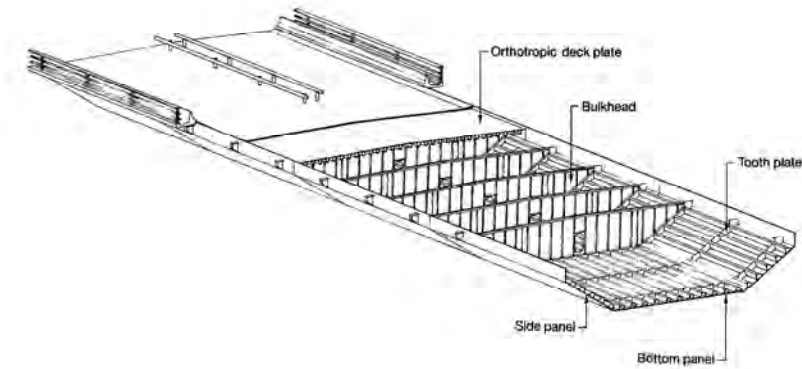
Figure 6: Box girder, structural principle. Bulkheads every 4 m.

behavior of a cement-based overlay bonded to a steel plate, cf. Walter et al. (2005). Small scale tests give an initial idea of bond properties. The steel plate is sand blasted prior to casting of the overlay to ensure a good bond. Furthermore, sand blasting leaves a clean micro-rough surface and thereby the risk of bond defects is minimized. Based on experience from small scale tests, it is believed that the use of an overlay with self-compacting properties might create a good and sound bond. Vibration of the overlay might cause water to separate from the mix, which might result in a weak interface. Similar conclusions have been drawn by Schiessl & Zilch (2001). So far, laboratory tests on bond between steel plates and self-compacting concrete have shown surprisingly good results. The experimental steel-concrete interface studies conclude that it is possible to achieve a steel-concrete bond, which possesses fracture energy close to that of concrete.

In the proposed overlay system, a typical deck consists of a 40-60 mm thick cement-based overlay bonded to the steel plate by self adhesion. An example of the proposed overlay system, with a cement-based overlay having a thickness of 50 mm is shown in Figure 7 along with the traditional steel deck.

Obviously, a disadvantage of the overlay system would be increased dead load. An increase in the dead load might, at some point, require stronger members elsewhere in the structural system. In order to keep the increase in dead load at a minimum an optimization of the wearing course would be necessary. In traditional orthotropic steel bridge decks, the surfacing consists of a wearing course (30 mm) and an underlying intermediate layer (25 mm), cf. The Danish Ministry of Transportation (1987). The steel plate is of crucial importance to secure the structural system and is protected by the intermediate layer in the original system. Since a 50 mm thick cement-based overlay may give enough protection to the underlying steel plate, it could well be possible to replace the intermediate layer by a cement-based layer. Leaving out the intermediate layer and using a system with the cement-based overlay and an asphaltic layer on top, may be sufficient to keep the dead load at a minimum. The two surfacing systems are shown in Figure 8.

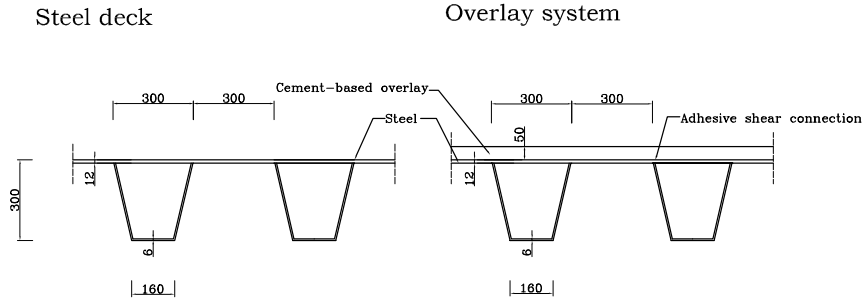Steel deck   Overlay system

Figure 7: (a) Typical steel system, with a center span of 300 mm between the supporting ribs and a 12 mm steel plate. (b) Cement-based overlay system with a 50 mm thick cement-based overlay.
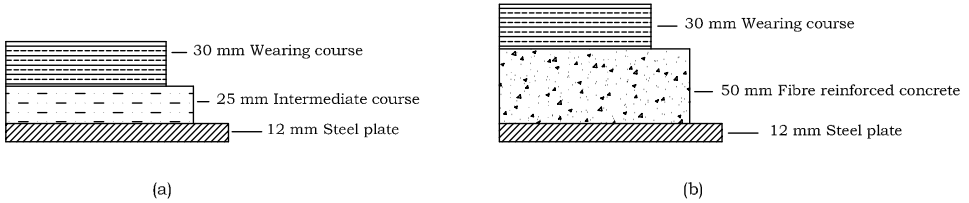

Figure 8: (a) Detail showing typical surfacing for an orthotropic steel bridge deck (b) Proposed system using a steel plate and a layer of cement-based material acting as a composite and a 30 mm wearing course on top.

The wearing course and intermediate layer in the typical steel deck system have a total weight of approximately 1.21 kN/m^2. In the proposed system, the intermediate layer is left out and replaced by the cement-based overlay. The total sum of weights in the proposed system is 1.76 kN/m^2. Thus, the overlay system increases the dead load of the deck by approximately 0.55 kN/m^2. Compared to the average dead load of the box girder on the Farø Bridges which is 8.6 kN/m^2, the cement-based overlay system increases the dead load by 6.5 %.

3   Modeling

The performance of the overlay system is studied based on nonlinear fracture mechanics. Numerical calculations are performed using finite elements. The orthotropic bridge deck of the 80 meter long approach spans of the Farø-Falster Bridge and the similar spans of the Sjælland-Farø Bridge are analyzed. The cable stayed part is not analyzed in the present study. The analysis of the overlay system is carried out by considering a local model of

7

3.9 meters times 8 meters. Exterior effects from traffic and dead load are considered in the modeling.

3.1 Loading and Boundary Conditions

3.1.1 Exterior effects

Three types of mechanical loading are considered, dead load, distributed traffic load and concentrated tandem loading. When considering a local model, exterior effects from loading are taken into account. Emphasis is put on the situation where the cement-based overlay is exposed to maximum tension, which is considered to be the most critical situation with regards to the overlay. The overlay is exposed to maximum tension where the negative bending moment will attain its maximum. The exterior forces on the local model can be found using simplified two-dimensional beam models as shown in Figure 9.

Lane	UDL [kN/m^2]	Tandem [kN/m^2]	Width [m]
1	6.0	300	3
2	1.7	200	3
3	1.7	100	3
4	1.7	0	3

(a)

Lane	UDL [kN/m^2]	Tandem [kN/m^2]	Width [m]
1	6	300	1.95

(b)
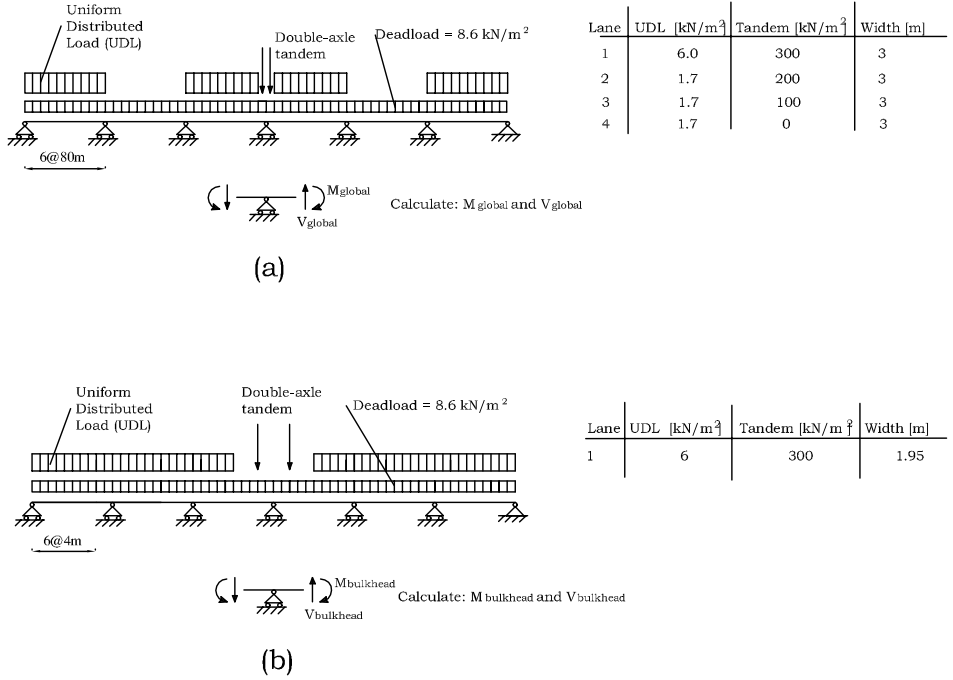
Figure 9: (a) Global model to calculate exterior effects on the local model from traffic and dead load. A bending moment M_{global} and shear force V_{global} are found. A total number of 6 spans are taken into account and 4 traffic lanes are used. (b) Model to calculate exterior forces, $M_{bulkhead}$ and $V_{bulkhead}$, caused by bulkheads placed at every 4 meters. A total number of 6 spans of 4 meters and one traffic lane is taken into account.

8

The exterior forces from traffic and dead load on the bridge can be divided into two groups as shown in Figure 9 (a) and (b). A global bending moment M_{global} and shear force V_{global} are found by placing uniform distributed traffic and dead load on the bridge, cf. Figure 9(a). A statical main system of 6 spans, each having a span of 80 meters is used to find the global forces caused by traffic and dead load along the bridge. A bending moment $M_{bulkhead}$ and shear force $V_{bulkhead}$ caused by bending locally in the orthotropic deck due to the bulkheads placed every 4 meters, are also taken into account, cf. Figure 9(b). The exterior forces at the bulkhead are found by considering a statical system of 6 spans of 4 meters each. Forces found from the two dimensional beam models are then later applied to the local three dimensional model.

3.1.2 Load

Traffic load, denoted Uniform Distributed Load (UDL), and tandem load are chosen in accordance to ENV 1991-3 (1991). In the global bridge model, cf. Figure 9(a), a total number of four lanes are considered, where each lane has a width of 3 m. Three lanes have an uniform distributed traffic load of 1.7 kN/m^2, and one lane has a traffic load of 6 kN/m^2. The average dead load of the steel girder, including bridge equipment, has been calculated to 8.6 kN/m^2, cf. (The Danish Ministry of Transportation 1987). The tandem system applied consists of three double-axle tandems with the following load values: 100, 200 and 300 kN.
Exterior effects caused by the bulkheads at every 4 meters, cf. Figure 9(b), are found by considering 6 spans of 4 meters each. Both the uniformly distributed load and a tandem system are taken into account. In this case the width of 3 meters (the width of one single lane) is used. From each of the two cases in Figure 9(a)-(b) a bending moment and a shear force is found.

3.1.3 Local Model

The local three-dimensional model is a part of the orthotropic deck, as well as part of the bulkhead. The local orthotropic deck part considered has a height of 1.5 m, a width of 3.9 meters and a length of 8 m, cf. Figure 10(a). Dead load, uniform distributed load and the double-axle tandem system are applied as loads. Placement of the double-axle tandem is shown in Figure 10(a). As illustrated, the tandem pressure is applied over an area of 0.4 x 0.4 m^2. Due to symmetry, the actual modeling is reduced to a quarter of the section considered, cf. Figure 10(b). The exterior effects found previously are applied to the model as boundary conditions.
The boundary conditions of the model are shown in Figure 11. As observed in the figure, the UDL and one quarter of the double-axle tandem are applied as loads to the model. One end of the orthotropic deck, opposite the bulkhead, is modeled as a rigid plane. Exterior effects, found from Figure 9(a)-(b), are applied to the rigid plane.
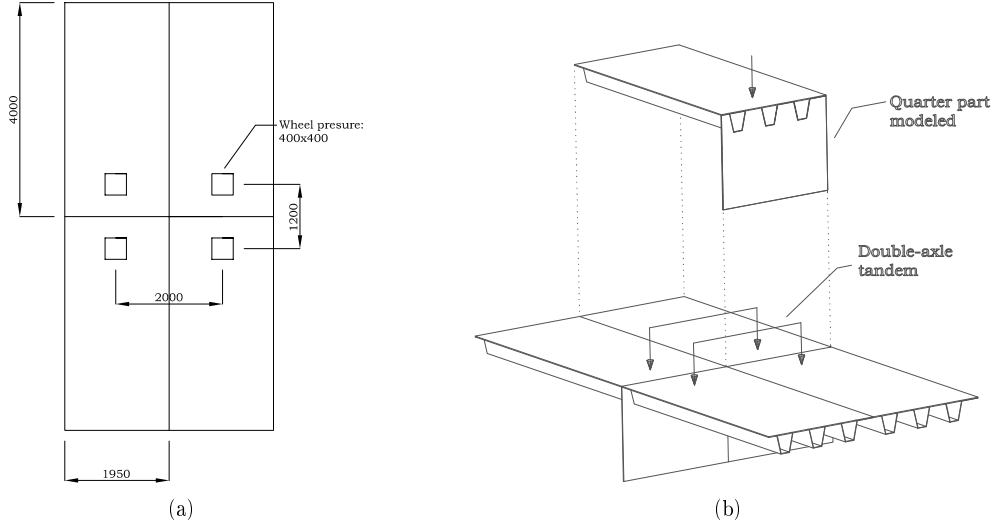
Figure 10: Figure showing part of bridge deck that is modeled using FE. (a) Detailed drawing showing measurements and showing placing of wheel loads. (b) Due to symmetry only one quarter is modeled (Note all measurements are in millimeters).
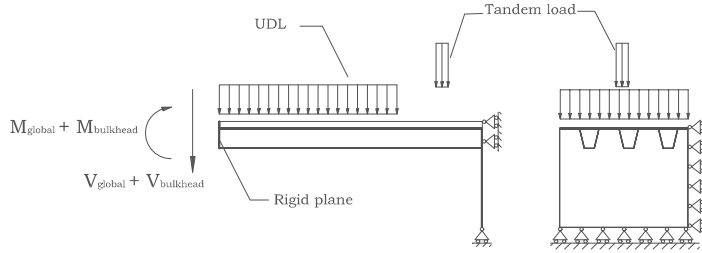

Figure 11: Boundary conditions of bridge deck model. The exterior bending moments and shear forces are applied to a rigid plane.

3.2 Finite Element Modeling

A three dimensional Finite Element (FE) model using solid elements has been established. A commercial finite element software package, (DIANA 2003), has been applied. Modeling of the steel and cement-based overlay has been utilized using standard 20-node solid elements. The connection between the overlay and underlying steel deck has been modeled using an 8-node interface element available in DIANA (2003), together with a user-supplied constitutive model as described in Section 3.5. The applied element mesh is shown in Figure 12.
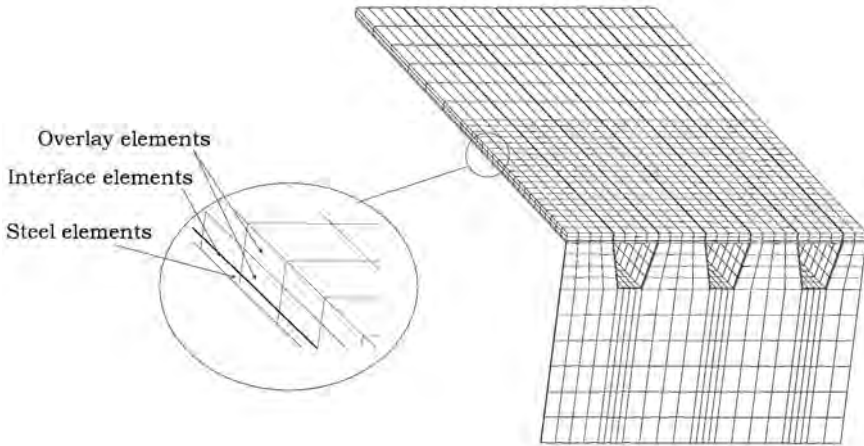
Figure 12: Applied finite element mesh of the deck part. To model steel and overlay a solid 20-node element is used. The connection between the overlay and steel plate is modeled using a 8-node interface element.

The density of the mesh has been verified using a convergence test comparing the deformation mode and stresses. The mesh shown in Figure 12, has shown to be adequate. In total the FE model of the bridge deck consists of 4108 elements.

3.3 Steel

According to The Danish Ministry of Transportation (1987), the main structural elements have been designed in a high yield steel quality, grade St. 52-3 N, with a yield stress of 360 MPa and a ultimate tensile strength of 550 MPa.
Engineering constants of the steel used in the modeling work are an elastic modulus of 210 GPa and a poisson ratio of 0.3. It is assumed, that the steel stresses in the present analysis are kept below its yield value. Furthermore, buckling of steel parts is not taken into consideration.

3.4 Overlay Material

The well-known advantage of fibre reinforced concrete is its ability to carry load after the first crack is formed. The fibres will typically stay unbroken after the first crack is formed and the fibres, that cross a crack, will resist further opening. Depending on the crack bridging effect, fibre reinforced composites can show different failure modes (Li & Leung 1992). If the average fibre bridging effect is increasing during crack initiation and propagation, then multiple cracks can form. This behavior is also known as *strain hardening*. On the other hand, if the fibres cannot carry more load after the formation of the first crack, further deformation is governed by opening of a single crack. This behavior is called *tension softening*. In the following, both overlays of tension softening and strain hardening materials are analyzed using the FE model.

3.4.1 Constitutive Modeling of Tension Softening Materials

The tension softening behavior can be modeled, conceptually, by modeling a localized crack. A simple mechanical description of the localized crack in concrete was suggested by Hillerborg et al. (1976), known as the *Fictitious Crack Model* (FCM). A comprehensive overview of the use of nonlinear fracture mechanics for concrete structures using modeling concepts for tension softening materials is given in Karihaloo (1995).

The required constitutive input for modeling a tension softening material is the so-called stress-crack opening relationship. This relationship, expresses the amount of crack opening w as a function of the stress across the crack σ. It turns out that a bilinear shape, as shown in Figure 13, correlates well to experimental data.

Figure 13: Constitutive modeling of a tension softening material. The material is described in two phases: a linear elastic range, and a bilinear stress-crack opening relationship.

The stress-crack opening relationship in Figure 13 is shown normalized with respect to the uniaxial tensile strength f_t. The bilinear shape is described by two line segments, having the negative slopes a_1 and a_2, respectively. The intersection between the second line segment and the y-axis is denoted b_2, which is a dimensionless parameter.

Application of the FCM in a FE formulation is rather straight forward. Modeling of the crack can be carried out either by the use of standard interface elements or in a continuous formulation. The continuous formulation, also known as the smeared crack approach, was formulated for concrete by Bažant & Oh (1983). In contrast to the modeling of discrete cracks by using interface elements, the smeared crack approach smears out localized deformation over a characteristic length. The FE formulation is described in terms of strains instead of relative displacements.

Experimental studies investigating the behavior of tension softening materials in composite action with steel have been carried out in Walter et al. (2004). The studies included two tension softening materials, the which constitutive parameters of which were obtained using a uniaxial test set-up similar to RILEM (2001). The uniaxial tests were used to obtain the stress-crack opening relationship in the bilinear form shown in Figure 13. The tension softening materials tested were Fibre Reinforced Concrete (FRC) and Fibre Reinforced Densit®(FRD). The average constitutive parameters obtained in the uniaxial tests for the two tension softening materials are listed in Table 1. Additionally, typical softening parameters for plain normal strength concrete are used for comparison.

Material	f_t [MPa]	a_1 [mm^{-1}]	a_2 [mm^{-1}]	b_2 [-]	G_f [N/mm]
FRC	2.3	27	0.50	0.35	0.30
FRD	4.8	64	0.57	0.46	0.90
Concrete	2.0	50	1.0	0.1	0.03

Table 1: Constitutive parameters of three tension softening materials analyzed as overlay material. Parameters are based on values from Walter et al. (2004).

In addition to the bilinear stress-crack opening parameters, the fracture energy G_f is shown in Table 1. As observed, the fibre reinforced materials, FRC and FRD, are characterized by a much higher fracture energy than plain concrete due to their fibre contents. The FRC material in the experiments contained 1 %, 30 mm long, hooked end steel fibers with a diameter of 0.5 mm, and the FRD material contained 2 % straight steel fibers with a length of 6 mm and a diameter of 0.16 mm.

3.4.2 Constitutive Modeling of Strain Hardening Materials

The constitutive behavior of a strain-hardening material can be divided into three phases: (i) a linear elastic phase, (ii) a multiple cracking phase, and (iii) a localization phase. The behavior is illustrated in Figure 14.

The second phase, the multiple cracking phase, can be described in a stress vs. strain relationship, with an ultimate tensile strength f_u at the strain ϵ_u. The third and final part is described in a stress-crack opening relationship, with an ultimate crack opening denoted w_u.

A strain hardening material denoted Engineered Cementitious Composite (ECC) has also been analyzed experimentally in Walter et al. (2004). The fracture behavior of ECC were
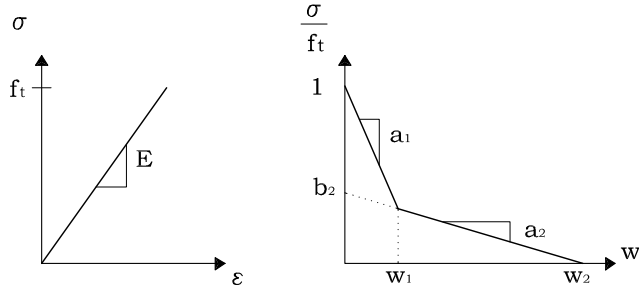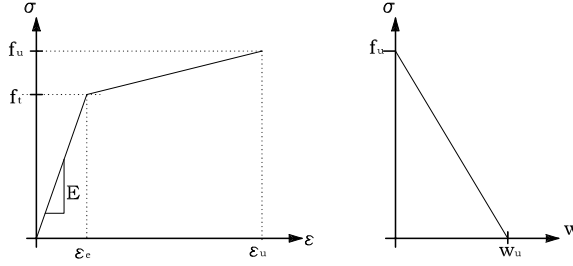
Figure 14: Constitutive modeling of a strain hardening material. The material is described in three phases: a linear elastic phase, a strain hardening phase, and a localization phase.

characterized using a uniaxial test set-up according to Li et al. (2002). The notation for the constitutive parameters is in accordance with Figure 14. The average parameters obtained in the tests are shown in Table 2.

Material	f_t [MPa]	f_u [MPa]	ϵ_u [%]	w_u [mm]
ECC	4.2	5.3	1.9	4*

Table 2: Constitutive parameters of a strain hardening material ECC (*Note this value is an assumption). Parameters are based on values from Walter et al. (2004).

As all ready mentioned the ECC material exhibits strain hardening properties when subjected to tension. The material has been engineered through a micro mechanical design approach, see e.g. Li (2002). The material tested contained 2 % by volume poly-vinyl-alcohol (PVA) fibers, with a fibre length of 8 mm.

3.5 Overlay-Steel Interface

The overlay-steel interface behavior is based on localized cracking and modeled using standard three-dimensional interface elements. An applied constitutive mixed mode model has been implemented in DIANA (2003), using user-supplied subroutines. The model is based, conceptually, on the fictitious crack model by Hillerborg et al. (1976). However, the model by Hillerborg only includes normal cracking (Mode I cracking) and does not take into account the influence of shear (Mode II cracking). The current model is an expansion of the FCM in three dimensions, based on a model by Wernersson (1994) and later in the three-dimensional case by Serrano (2000).

The interface is assumed to have a thickness of zero, so the stresses that should be taken into account are the normal stress and two in-plane shear stresses. Prior to cracking, linear elastic behavior is assumed, whereas after cracking, the model describes the cracking behavior as decreasing stress for increasing normal and tangential crack opening. The

three stress components are, in the pure Mode I or II case, described as stress vs. crack opening in either normal or tangential direction. These three curves are coupled in the three dimensional space, so that the corresponding stiffness and stress values can be obtained for any state of mixed mode cracking.

The normal stress component (σ) and the two shear stress components (τ_x and τ_y) are shown in Figure 15 along with their crack opening displacement components (δ_n, δ_{tx}, and δ_{ty}).
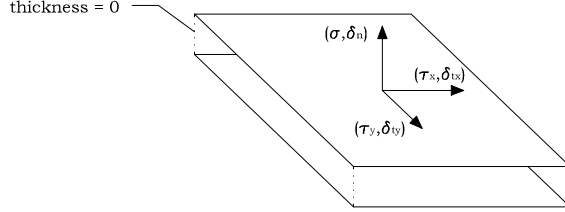

Figure 15: Three dimensional interface configuration. The interface is described by one normal stress and two shear stress components.

The relation between the gradients of the six components is described through the following formula:

$$\begin{bmatrix} \dot{\sigma} \\ \dot{\tau}_x \\ \dot{\tau}_y \end{bmatrix} = \begin{bmatrix} D_{11} & D_{12} & D_{13} \\ D_{21} & D_{22} & D_{23} \\ D_{31} & D_{32} & D_{33} \end{bmatrix} \begin{bmatrix} \dot{\delta_n} \\ \dot{\delta_{tx}} \\ \dot{\delta_{ty}} \end{bmatrix} \tag{1}$$

where the D_{ij} components describe the relation between the gradients of stress and crack deformation. If the current state is elastic, the response is linear and uncoupled, hence, the off-diagonal terms of D_{ij} are equal to zero. The diagonal elements are, in the elastic stage, assigned large values to model initial continuous geometry.

The interface behavior after peak load is obtained through the construction of a three-dimensional stress-crack deformation relation. The construction is based on an assumption regarding the coupling of stress and crack deformations in three dimensions. The coefficients in Equation 1 can then be derived by differentiation. Furthermore, a general assumption in the present study is isotropy in the shear plane, so that $D_{22} = D_{33}$, $D_{32} = D_{23}$, $D_{21} = D_{31}$, and $D_{12} = D_{13}$.

A mixed mode state can be defined using two mixed mode angles ϕ_{xy} and ϕ_{tn}:

$$\phi_{xy} = arctan\frac{\delta_{tx}}{\delta_{ty}} \tag{2}$$

$$\phi_{tn} = arctan\frac{\delta_t}{\delta_n} \tag{3}$$

where

15

$$\delta_t = \sqrt{\delta_{tx}^2 + \delta_{ty}^2} \tag{4}$$

The coupling is based on the two bilinear curves in pure Mode I and II, cf. Figure 16.
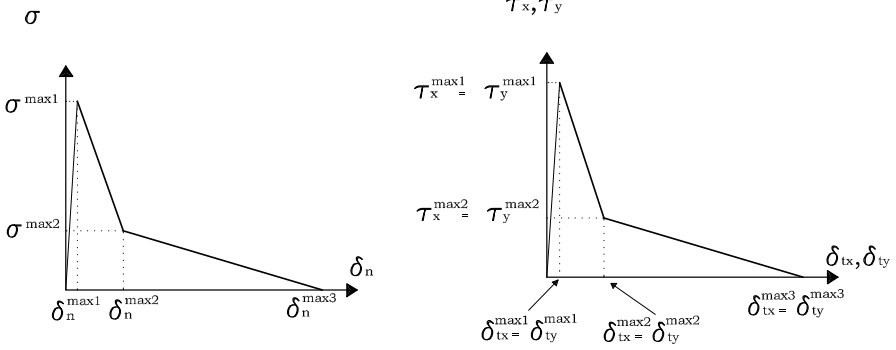

Figure 16: Bilinear stress-crack curves in pure Mode I and II. Until peak stress the curves are uncoupled, and the slopes are assigned large values to model continuous geometry.

The kink points of the pure Mode I and II curves are coupled with the kink points for the current mixed mode state, by assuming the following criteria:

$$\left(\frac{\delta_n^k}{\delta_n^{max\ k}} \right)^p + \left(\frac{\delta_{tx}^k}{\delta_{tx}^{max^k}} \right)^n + \left(\frac{\delta_{ty}^k}{\delta_{ty}^{max\ k}} \right)^m = 1.0 \tag{5}$$

where $\delta_n^{max\ k}$, $\delta_{tx}^{max\ k}$ and $\delta_{ty}^{max\ k}$ denote a kink point (defined by index k) on either the pure Mode I or II curve. The terms δ_n^k, δ_{tx}^k and δ_{ty}^k denote a kink point on the current crack deformation curve for a given mixed mode state. The powers p, n and m are material constants, and are in the present study assumed to be:

$$p = n = m = 2 \tag{6}$$

Finally, the kink point relationship between crack deformations and stresses, in the pure Mode I or II case and the mixed mode case, are assumed to be:

$$\sigma^k = \delta_n^k \frac{\sigma^{max\ k}}{\delta_n^{max\ k}} \tag{7}$$

$$\tau_{tx}^k = \delta_{tx}^k \frac{\tau_{tx}^{max\ k}}{\delta_{tx}^{max\ k}} \tag{8}$$

$$\tau_{ty}^k = \delta_{ty}^k \frac{\tau_{ty}^{max\ k}}{\delta_{ty}^{max\ k}} \tag{9}$$

16

The coupling can then be found using equations (5) and (7)-(9). Every kink point on the pure Mode I and II curves are linked in the three-dimensional space, so that the current stress state can be found via linear interpolation. The required input is the two bilinear curves along with the powers p, n and m. The required bilinear curves are the pure Mode I curve (σ-δ_n), and the bilinear pure Mode II curve, which are the same in the x and y direction, so that the pure τ_x-δ_{tx} and τ_y-δ_{ty} curves are given the same input due to isotropy in the plane. After the three dimensional stress versus crack deformation relationships have been constructed as described above, the D_{ij} terms in Equation (1) can be found by differentiation.

The input of the pure Mode I and II curves are in the current study based on experimental work carried out on concrete-steel interfaces. It has been shown in a previous study, (Walter et al. 2005), that interfacial fracture properties are close to those measured for the concrete itself. The so-called *wall effect* has to be taken into account, since big aggregates are not present close to the steel plate where the interfacial fracture occurs. Experimental studies have been carried out to characterize a concrete-steel interface exposed to mixed mode loading, see e.g. Walter & Olesen (2005). The notation for the pure Mode I and II curves is given in Figure 16.

The constitutive properties applied are the same for all the materials analyzed in the present study, and are listed in Table 3. This is an assumption and limitation of the present study, since it would be more correct to measure the fracture properties of each individual material, FRC, FRD and ECC. The constitutive parameters applied in the study are based on experimental work on a steel-concrete interface, close to what could be measured for cement-based materials since fibres are not likely to influence the overlay-steel interface cracking. Numerical studies, analyzing the role of fracture toughness of the interface and how debonding influences the global response, has already been carried out, see e.g. Walter et al. (2003). The conclusion is that the fracture energy of the steel-concrete interface plays a minor role and debonding is initiated for a crack mouth opening of approximately 0.03 to 0.1 mm.

Mode I n-direction	σ^{max1} [MPa]	σ^{max2} [MPa]	δ_n^{max2} [mm]	δ_n^{max3} [mm]	G_f [n/mm]
	3.0	0.4	0.02	0.5	0.12
Mode II tx-direction	τ_x^{max1} [MPa]	τ_x^{max2} [MPa]	δ_{tx}^{max2} [mm]	δ_{tx}^{max3} [mm]	G_f [n/mm]
	3.5	0.5	0.02	0.77	0.23
Mode II ty-direction	τ_y^{max1} [MPa]	τ_y^{max2} [MPa]	δ_{ty}^{max2} [mm]	δ_{ty}^{max3} [mm]	G_f [n/mm]
	3.5	0.5	0.02	0.77	0.23

Table 3: Pure Mode I and II parameters (Figure 16) based on values from Walter & Olesen (2005), used as constitutive interface parameters. Note that δ_n^{max1} and $\delta_{ty}^{max1}=\delta_{tx}^{max1}$ are assigned a small value for numerical reasons.

4   Results and Discussion

The first study is based on linear elasticity and nonlinear effects such as overlay cracking and debonding are not considered in this part. The linear elastic study is carried out to give a simple estimate on how much the overlay contributes to stress reduction in the fatigue sensitive steel parts, when exposed to traffic load. Later in the present section an estimation of crack width and debonding based on nonlinear fracture mechanics is given. The estimation is given in terms of crack width and debonding. The nonlinear study takes into account mechanical loading along with temperature gradients between the overlay and steel structure. Finally, early-age shrinkage is modeled and discussed. Fatigue and service life is not part of the present study, however, the aspects of cyclic loading are discussed later with regards to further developments.

4.1   Linear Elastic Studies

One of the problems causing fatigue in traditional orthotropic steel bridge decks, is lack of transverse bending stiffness. Lack of transverse bending stiffness and the contribution to bending stiffness from the cement-based overlay can well be illustrated in a linear elastic study. Consider a double-axle tandem with an axle load of 260 kN placed as shown previously in Figure 10, together with global traffic as outlined in Figure 9(a)-(b). The geometry of the Farø Bridges is used in the analysis and the part modeled is shown in Figure 10. Placing a double-axle tandem on the structure creates a transverse bending moment, and initiates large stresses in the welded joint between the steel plate and rib. This is illustrated in Figure 17, showing a deformation plot of the finite element model.

| (a) | (b) |

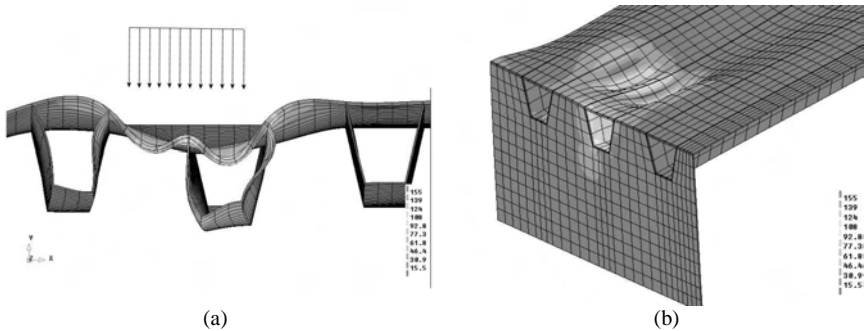Figure 17: Deformation plots from linear elastic FE calculations. (a) Wheel load causing transverse bending. (b) Three dimensional view of deformation caused by wheel load.

The position of the wheel load is shown on the deformation plot, cf. Figure 17. As observed, the wheel load causes considerable transverse bending. Parametric studies assuming linear elasticity, using finite element calculations, have been carried out. Through

a parametric study, the influences of: (i) different steel plate thicknesses, and (ii) different overlay thicknesses on a deck with a steel plate thickness of 12 mm, are investigated. In this study, full composite action is assumed, and no debonding or cracking of the overlay is modeled. The maximum von Mises stress in the intersection between the steel plate and the rib is in focus. The results from the linear elastic study are presented in Figure 18.
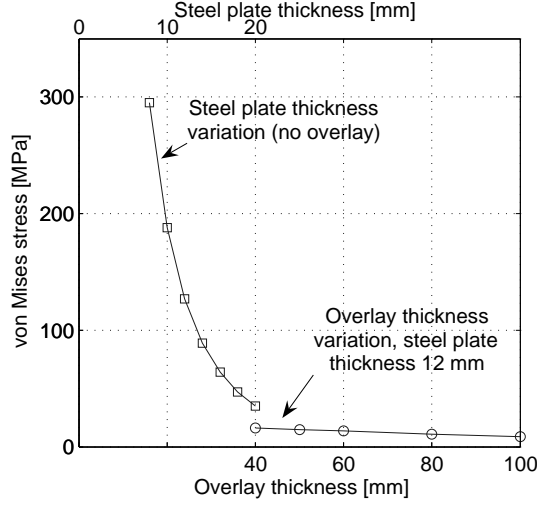

Figure 18: Result of linear elastic studies for traffic and an axle load of 260 kN. The left most line represents the von Mises stress of different steel plate thicknesses without an overlay. The other line represents results from a steel plate of 12 mm and different overlay thicknesses.

The graph shows the maximum von Mises stress in the intersection between the steel plate and rib for different orthotropic deck geometries. The first parametric study investigates a pure orthotropic steel deck without any overlay. In this study, the geometry of the Farø Bridges is applied, and the only modification to the original design is the thickness of the top steel plate which is the variable of the first parametric study. As seen in Figure 18, the von Mises stresses have been calculated for steel plate thicknesses of 8, 12, 14, 16, 18, and 20 mm. In the second parametric study, von Mises stresses have been calculated in the similar intersection, where the only modification to the original design is the application of an overlay.

The results from Figure 18 show a reduction in the von Mises stress for increasing steel plate thickness. The von Mises stress is around 300 MPa when having a steel plate thickness of 8 mm and around 25 MPa when having a steel plate thickness of 20 mm. However, comparing the stress levels for that of a pure steel deck to the overlay case, it is observed that even applying a thin overlay results in a significant reduction of the von

Mises stresses. Comparing the original steel design with a steel plate of 12 mm, with systems reinforced with overlay thicknesses of 40 mm and 100 mm, a stress reduction factor of 8 to 15, respectively, is achieved. The linear elastic study suggests that even a small overlay thickness leads to a significant stress reduction, since changing the overlay height from 40 mm to 100 mm, only reduces the stress from 16 MPa to 9 MPa.

Stress reductions, due to an increased stiffness by the overlay, in the weld between the rib and steel plate, have also been investigated by other authors. These investigations have been carried out through linear elastic studies and experiments. Numerical simulations on an orthotropic steel bridge deck has been reported by Buitelaar et al. (2004). This study shows a stress reduction factor of 21 in the steel plate near the rib. A paper by Jong & Kolstein (2004), reports strain measurements on the Caland Bridge in Rotterdam, The Netherlands, prior to and after upgrading the deck with a cement-based overlay. Four weeks prior the repair work, strain gauges at various locations collected data for 4 weeks. After casting of a 50 mm thick overlay, the strain gauges collected additional data for 5 weeks. For strain signals caused by heavy vehicles, at the steel plate close to the rib, stress reduction factors were measured in the range of 5.9 to 7.7.

4.2   Cracking Behavior of Overlay due to Traffic Load

Cracking of the overlay and debonding might be of major concern when applying a cement-based overlay to an orthotropic steel bridge deck. The aim of the nonlinear study is to investigate the factors that play a role in overlay cracking, and to give an estimate of the crack width and initiation of debonding. Some of the main goals in a design situation might be to minimize crack widths and to keep the solution economically feasible.

In this section, the four cement-based materials presented previously: Concrete, FRC, FRD, and ECC, are analyzed. The analysis concerns cracking pattern and crack widths due to mechanical loading. The development of cracks in the overlay for fixed traffic load and increasing axle load has been investigated utilizing finite elements. The investigation is carried out considering concrete (cf. Table 1 for constitutive parameters) as overlay material. The development of cracks for various stages of axle loads is illustrated in Figure 19(a)-(d).

As observed in the figure, the first cracks develop in the area on top of the bulk head, denoted localized crack area no. 1, cf. Figure19(a). Even for a small axle load of approximately 52 kN, the maximum tensile stress in the concrete overlay reaches a value of 2 MPa. When further loading is applied, the maximum crack width is increased and further cracks develop. At some point, in this case for an axle load of approximately 286 kN, cracks develop in the direction of the bridge axis. Cracking of the overlay in the direction of the bridge axis is denoted crack area no. 2, cf. Figure 19(d).

The maximum crack width for fixed traffic load, and variable tandem load, is shown in a load vs. crack width diagram, cf. Figure 20.

The figure illustrates the axle load as a function of the maximum crack width, for the four materials considered: Concrete, FRC, FRD and ECC. In the case of ECC, the results are presented as load vs. strain. In the load range considered, the maximum crack width is

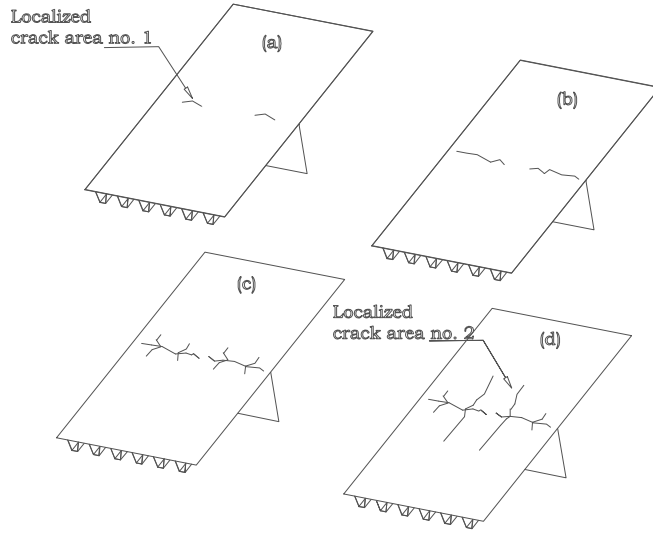Figure 19: Crack patterns of the overlay (concrete) for traffic and an axle load of: (a) 50 kN, (b) 180 kN, (c) 260 kN, and (d) 290 kN.
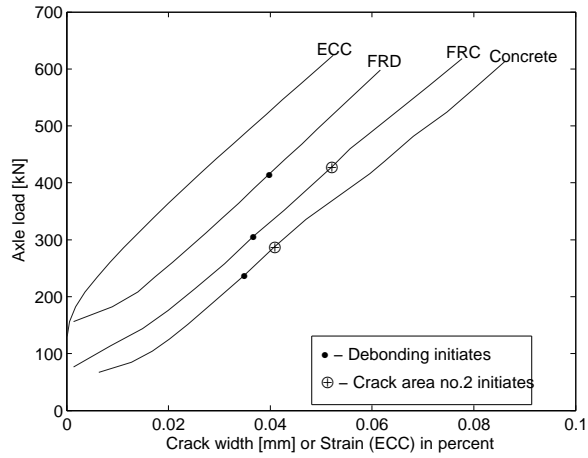

Figure 20: Numerical results of three overlay materials for fixed traffic load and variable axle loading. The results are presented in a load vs. crack width diagram for concrete, FRC and FRD. In the case of ECC material the results are presented as load vs. strain in percent.

always located in crack area no. 1 as defined in Figure 19(a). In addition to the value of the crack width, initiation of cracking in crack area no. 2 (as defined in Figure 19(d)) is marked. In the load range considered, cracking only initiates in concrete and FRC in crack area no. 2. In the case of tension softening materials, increasing crack width will at some point lead to debonding. Debonding is initiated for a certain crack width which is also marked in Figure 20. It is noted that debonding is initiated at approximately the same crack width for the materials: Concrete, FRC and FRD.

4.3   Temperature Gradients

A temperature gradient between the overlay and underlying steel plate may give rise to tensile stresses in the overlay. Since the overlay is restrained from moving due to its bond to the steel plate, temperature gradients might play a significant role on the cracking behavior of the overlay system. Temperature gradients have to be taken into account in order to estimate the maximum crack width of the overlay. Of special concern is cooling of the bridge deck (bottom warmer than top). Since the overlay is restrained from moving, cooling of the bridge deck results in a situation with tensile stresses in the overlay. For this study, temperature gradients and thermal expansion coefficients have been chosen according to ENV 1991-2-5:1997 (1997). Thus, a thermal expansion coefficient of $10 \cdot 10^{-6}/^0$C has been applied to the overlay. For a composite structure with a slab height of 0.2 m, the temperature difference in a cooling situation depends on the surface thickness. It ranges from 5.9 ^{0}C (for unsurfaced) to 1.6 ^{0}C (200 mm surface). In the present analysis a parametric study is carried out lowering the temperature of the overlay to study cracking behavior. The applied temperature difference and distribution applied are shown in Figure 21.
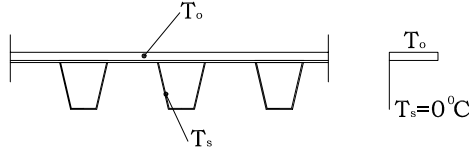

Figure 21: Temperature distribution in bridge deck.

The temperature in the steel part, T_s, is always set to zero degrees. The temperature difference is expressed by:

$$\Delta T = T_s - T_o \tag{10}$$

where

$$T_s \equiv 0^0 C \tag{11}$$

The cracking behavior of the overlay is studied for a temperature difference ΔT of: 0 ^{0}C, 2.5 ^{0}C, 5 ^{0}C, 7.5 ^{0}C, and 10 ^{0}C. The analysis is carried out by, first, setting the temperature in the steel part, T_s, to zero degrees and changing the temperature in the overlay. After applying the temperature, fixed traffic loads are applied, and finally the tandem load is increased stepwise.
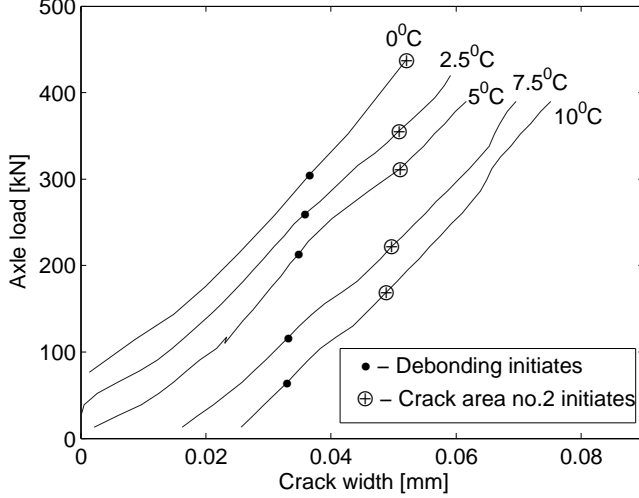

Figure 22: Axle load vs. crack width for a temperatures gradient of $\Delta T = 0$ ^{0}C, 2.5 ^{0}C, 5 ^{0}C, 7.5 ^{0}C, and 10 ^{0}C between the FRC overlay (lowest temperature) and the steel deck (highest temperature).

The result of the analysis for a FRC overlay is plotted in an axle load vs. crack width diagram for different temperature differences in Figure 22. As the temperature difference increases, the value of axle load that initiates cracking is lowered. For temperature differences larger than 5 ^{0}C, cracking is initiated by the temperature loading itself. Moreover, the load levels where debonding and cracking in the direction of the bridge axis initiates are also lowered. The analysis shows that temperature differences between the overlay and steel plate influences the cracking behavior considerably and should be taken into account in a design situation. It should also be noted, that the wavy shaped curves in Figure 22 are due to numerical uncertainties and could be improved by decreasing the element size.

4.4   Early Age Shrinkage

Immediately after casting of the cement-based overlay, the cement starts to hydrate. As a consequence of hydration, the material experiences a macroscopic volume reduction

known as autogenous shrinkage. Autogenous shrinkage can be quite significant in high performance concretes due to their low water to binder ratio (w/b ratio). Autogenous shrinkage plays an important role for water-cement ratios below 0.40-0.45 (Jensen & Hansen 2001). The magnitude of autogenous shrinkage has been measured, on cement paste, of more than 1000 micro strains after a few weeks of hardening, (Jensen & Hansen 2001). Since the overlay is restrained from moving, due to its bond with the steel plate, shrinkage may cause cracking and early age performance has to be taken into account. Proper curing conditions should be established, since poor curing conditions may cause additional shrinkage, known as drying shrinkage. In the following, autogenous shrinkage is the main focus, as this is hard to avoid, when using high performance concretes.

In this section, a short introduction to the applied modeling framework will be given, with the aim to analyze the shrinkage behavior and risk of cracking at early ages. Given a shrinkage history, it is the aim of the study to give an estimate of the risk of cracking and the stress level in the overlay at a given time. Creep of the overlay is a significant factor at early age and has to be taken into account.

4.4.1   Shrinkage Function

An expression for the autogenous shrinkage over time, based on experimental data, has been proposed by the Japanese Concrete Institute (Tazawa et al. 2000). Shrinkage as a function of time can be found by the following expression:

$$\epsilon_{shrinkage}(t) = [\gamma \epsilon_{inf}(w/b)\beta(t)]10^{-6} \tag{12}$$

where γ is a coefficient to describe the effect of cement type (γ=1 for ordinary Portland Cement), $\epsilon_{inf}(w/b)$ is the ultimate autogenous shrinkage. The ultimate autogenous shrinkage is a function of the water-binder ratio w/b, and can be found from $\epsilon_{inf}(w/b) = 3070exp(-7.2(w/b))$. The development of shrinkage over time is described by $\beta(t)$ in the following form:

$$\beta(t) = [1 - exp(-a(t - t_0)^b)] \tag{13}$$

where t_0 is the initial setting time. The two remaining variables a and b are constants.

4.4.2   Modeling of Creep

As discussed earlier, autogenous shrinkage in the overlay causes tensile stresses in the overlay. Moreover, when applying a constant stress over time in a cement-based material, relaxation of the material needs to be taken into account. As the cement-based material is exposed to a constant stress over time, the stresses will decline with time. This behavior can be described by viscoelasticity and various models can be applied to describe the viscoelastic behavior of cement-based materials. In this study, a Kelvin chain is applied, for modeling of shrinkage and creep. Bažant (1988) gives a full detailed review of creep modeling in cement-based materials. For clarity of the modeling and to make the paper self-contained, a short introduction is given to the applied model. The Kelvin chain model

is based on a unique compliance function $J(t, t')$, which predicts the time dependent deformations as function of time of load application t' and the duration of load $(t - t')$. The compliance function is expressed as:

$$J(t, t') = \frac{1}{E_0(t')} + \frac{1}{E_1(t')}H_1(t, t') + \frac{1}{E_2(t')}H_2(t, t') + ... + \frac{1}{E_n(t')}H_n(t, t') \qquad (14)$$

where t is time, $E_0(t, t')$ is the instantaneous elastic deformation, for the load applied at an age of t'. The function $H_n(t, t')$ is given by:

$$H_n(t, t') = 1 - exp\left(\frac{t' - t}{\tau_n}\right) \qquad (15)$$

where τ_n is the so-called retardation time of chain unit n. The link between the retardation time and the viscosity of the dashpot η_n, is given by:

$$\tau_n = \frac{\eta_n}{E_n} \qquad (16)$$

The development of the modulus of elasticity over time, as included in Equation (14), can be expressed by the following function:

$$E(t) = A_1[1 - e^{-(t/\tau_1)^{n_1}}] + A_2[1 - e^{-(t/\tau_2)^{n_2}}] \qquad (17)$$

where n_i is a dimensionless factor related to geometry of the problem.
Experimental creep properties obtained by Østergaard (2003) are applied in this study. He conducted experiments at $t' = 1$, 3 and 5 days. The fit to experimental values have been obtained by using a 4 chain unit, cf. Figure 23.
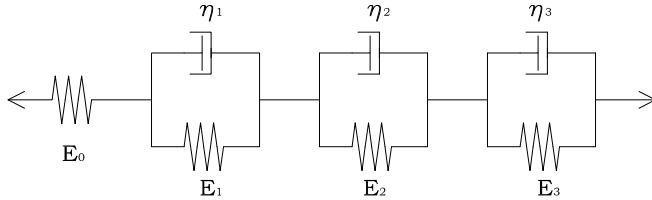
Figure 23: Kelvin chain used in the analysis, composed 4 Kelvin units in serial connection.

The Kelvin Chain consists of 4 units, all of them with a spring, and three units have a dashpot. The spring values, according to Equation (17), are listed in Table 4. The dashpot parameters to the three units are given in Table 5.

4.4.3 FE Modeling of Shrinkage and Creep

Viscoelasticity of cement-based materials can be modeled using finite elements. In the present study modeling is carried out using a Kelvin chain, which is implemented in

	E_0	E_1	E_2	E_3
A_1 [GPa]	43.4	180	280	360
τ_1 [hours]	23.9	5	50	500
n_1 [-]	2.19	1	1	1
A_2 [GPa]	20.0	-	-	-
τ_2 [hours]	100	-	-	-
n_2 [-]	4	-	-	-

Table 4: Fitting parameters of the springs in the applied Kelvin Chain

	H_1	H_2	H_3
τ_n [hours]	50	5	500

Table 5: Fitting parameters of the three dashpots in the applied Kelvin Chain

DIANA (2003). To illustrate an overlay cast on a steel plate a small example is analyzed. An infinity long specimen is considered, with a thickness of 50 mm, bonded to a steel plate, exposed to shrinkage over time. The investigation aims at calculating the stresses as a function of time. Since the modulus of elasticity and creep properties develop over time, the material is given the creep properties shown previously. The infinity long specimen is analyzed through a parametric study. The specimen is given four different shrinkage histories using Equation (12). As an example, a water binder ration is chosen to 0.45, an ordinary Portland Cement ($\gamma = 1$), and a constant b value (b=1). The constant a is varied according to: $a = 0.3, 0.5, 0.7, 0.9$.
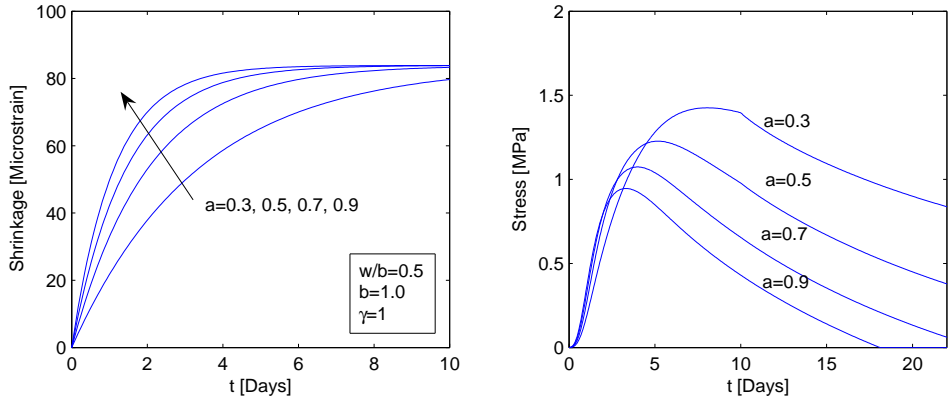

Figure 24: (a) Shrinkage over time using Equation (12). (b) Stresses in overlay for different shrinkage histories.

The results of the analysis, varying the shrinkage history, are shown in Figure 24. Figure 24(a), shows the four different shrinkage histories, computed varying the constant a in formula (12). As observed, in all the cases, the curves all end at the same ultimate shrinkage value. However, a low value of the constant a, produces a more slow approach to the ultimate shrinkage value. The corresponding responses of the stress level in the specimen are shown in Figure 24(b). As seen, the four cases produce quite different responses. In the case of a low value of the constant a, the maximum stress level becomes quite large compared to the other cases. Moreover, the rate of stress drop is slower over time, which is caused by the fact that relaxation of a cement-based material is largest in the first few hours after casting. Since the magnitude of relaxation is large at this stage, it is ideal to have autogenous shrinkage developing here.

In relation to the present overlay application, the development of the tensile stresses and the risk of cracking have to be taken into account. Too large shrinkage values at early ages might exceed the tensile strength and thereby cause cracking. Another aspect is the stress level when the bridge is opened for traffic. A considerable stress level may have to be considered along with traffic and temperature load in order to give an estimate of the overlay performance. In a given design situation, different shrinkage levels should be applied to the overlay together with traffic and temperature loading.

5   Further Investigations

Cyclic loading has not been analyzed in the present study, but should be a part of a full assessment of the cement-based overlay system. The maximum crack width will increase for a certain number of cycles, which has not been taken into account. At present, a number of fracture mechanical studies on the fatigue behavior of cement-based materials have been carried out, see e.g. Matsumoto & Li (1999) or Zhang et al. (2001). In order to estimate the service life of the overlay system, the influence of load cycles should be implemented in the constitutive models applied.

6   Conclusions

One of the main causes of fatigue in orthotropic steel bridge decks is their lack of stiffness. In a linear elastic study using finite elements it has been shown, that applying a cement-based overlay results in a significant and in many cases sufficient reduction of stresses in the fatigue sensitive steel regions.

The cement-based overlay system for stiffening a traditional orthotropic steel bridge deck has been analyzed applying nonlinear fracture mechanics. The investigation concerns the orthotropic bridge deck of the steel box girders of the approach spans of the Farø Bridges, Denmark. The focus is on the situation with maximum negative bending (tension in the overlay), since this situation is believed to be critical to the overlay. Performance of the overlay might be closely related to cracking and debonding. Cracking behavior of the overlay system has been analyzed for four different materials. The materials investigated

are: plain concrete, Fibre Reinforced Concrete (FRC), Fibre Reinforced Densit®(FRD), and Engineered Cementitious Composite (ECC). Concrete, FRC and FRD can be classified as tension softening materials, whereas ECC is characterized as a strain hardening material.

Cracking and eventually debonding is initiated due to mechanical and environmental loading. Mechanical loading (traffic) and environmental loading such as early age shrinkage and temperature gradients have been analyzed. A double axle tandem system placed across the bulkhead initiates cracking of the overlay due to large tensile stresses. At some point (for a certain crack width in the overlay) debonding is initiated and develops perpendicular and away from the bulkhead. When comparing the performance of the different tension softening materials, debonding is initiated at approximately the same crack mouth opening in the overlay. Debonding is not initiated for the strain hardening material analyzed, ECC. Further loading of the tandem system initiates cracking perpendicular to the bridge axis. In the load range considered, cracking perpendicular to the bridge axis is only initiated for the tension softening materials. The analysis shows that applying a cement-based material that exhibits multiple cracking is desirable due to the fact that debonding can be avoided in the load range considered.

Temperature gradients might have a significant influence on the performance of the cement-based overlay system. Cooling of the overlay (bottom warmer than top), produces tensile stresses in the overlay since it is restrained from moving because of its bond to the steel deck. For different temperature gradients and tandem load the performance of the overlay system is shown in terms of crack width. Again, debonding is initiated across the bulkhead for a certain crack mouth opening.

Finally, it is demonstrated how early age shrinkage can be taken into account. After casting of the overlay, high tension stresses develop in the overlay due to macroscopic volume changes. In the worst case, cracking might be initiated due to early age shrinkage, or high tensile stresses may be present when the bridge is opened for traffic.

References

Battista, R. & Pfeil, M. (2000), Stranghening fatigue cracked orthotropic decks with composite layers, *in* 'Annual Technical Sesseion, and Meetin, Structural Stability Research Council', pp. 376–389.

Bažant, Z. P. (1988), *Mathematical Modeling of Creep and Shrinkage of Concrete*, UK: John Wiley.

Bažant, Z. P. & Oh, B. H. (1983), 'Crack band theory for fracture of concrete', *Materials and Structures* **16**, 155–157.

Braam, C. R., Buitelaar, P. & Kaptaijn, N. (2003), Reinforced high performance concrete overlay system for steel bridges, *in* 'In the 5th International CROW-Workshop on Fundamental Modelling of the Design and Performance of Concrete Pavements, Istanbul, Turkey'.

Buitelaar, P. (2002), Ultra thin heavy reinforced high performance concrete overlays, *in* '6th International Symposium on Utilization of High Strength / High Performance Concrete, Leipzig, Germany', pp. 1577–1590.

Buitelaar, P., Braam, R. & Kaptijn, N. (2004), Reinforced hig performance concrete overlay system for rehabilitation and strengthening of orthotropic steel bridge decks, *in* 'Orthotropic Bridge Conference, Sacremento, USA', ASCE, pp. 384–401.

DIANA (2003), *DIANA User's Manual – Release 8.1*, june edn, TNO Building and Construction Research, P.O. Box 49, 2600 AA Delft, The Netherlands.

Dowling, P. J. (1968), The Behaviour of Stiffened Plate Bridge Deck under Wheel Loading, PhD thesis, Imperial College London.

ENV 1991-2-5:1997 (1997), *Eurocode 1 - Actions on Structures - Part 1-5: General Actions - Thermal Actions*, European Commitee for Standardisation.

ENV 1991-3 (1991), *Eurocode 1 - Basis of Design and Actions on Structures, Part 3: Traffic Loads on Bridges*, European Commitee for Standardisation.

Hillerborg, A., Modéer, M. & Petersson, P. (1976), 'Analysis of crack formation and crack growth in concrete by means of fracture mechanics and finite elements', *Cem. Concr. Res.* **6**(6), 773–782.

Jensen, O. M. & Hansen, P. F. (2001), 'Autogenous shrinkage and RH-change in perspective', *Cement and Concrete Research* **31**(12), 567–575.

Jong, F. B. P. & Kolstein, M. H. (2004), Strenghening a bridge deck with high performance concrete, *in* 'Orthotropic Bridge Conference, Sacremento, USA', ASCE, pp. 328–347.

Jong, F. B. P., Kolstein, M. H. & Bijlaard, F. S. K. (2004), Strain measurement tests at orthotropic steel bridge decks with a heavy vehicle simulator, *in* 'Prooceddings of the 10th Nordic Steel Construction Conference, Copenhagen, Denmark', pp. 401–412.

Karihaloo, B. L. (1995), *Fracture Mechanics and Structural Concrete*, Concrete Design and Construction Series, Longman Scientific and Technical, Harlow, Essex, England.

Kolstein, M. H. & Wardenier, J. (1997), 'Stress reduction due to surfacing on orthotropic steel decks', *IABSE Workshop, IABSE Reports, Vol. 76, Zurich, Lausanne* .

Kolstein, M. H. & Wardenier, J. (1998), A new type of fatigue failures in steel orthotropic bridge decks, *in* 'Proceedings of the fifth Pacific Structural Conference, Korea', pp. 483–488.

Li, V. (2002), 'Advances in ECC research', *ACI Special Publication on Concrete: Material Science to Applications* **SP 206**(23), 463–472.

Li, V. C. & Leung, C. K. Y. (1992), 'Steady-state and multiple cracking of short random fiber composites', *Journal of Engineering Mechanics* **118**(11), 2246–2264.

Li, V., Wu, C., Wang, S., Ogawa, A. & Saito, T. (2002), 'Interface tailoring for strain-hardening PVA-ECC', *ACI Materials Journal* **99**(5), 373–400.

Matsumoto, T. & Li, V. C. (1999), 'Fatigue life analysis of fiber reinforced concrete with a fracture mechanics based model', *Cement and Concrete Composites* **21**(4), 249–261.

Østergaard, L. (2003), Early-Age Fracture Mechanics and Cracking of Concrete. Experiments and Modelling, PhD thesis, Department of Civil Engineering, Technical University of Denmark, Lyngby, Denmark.

RILEM (2001), 'Test and design methods for steel fiber reinforced concrete. recommendations for uniaxial tension test', *Materials and Structures* **34**(3–6). Prepared by RILEM-Committee-TDF-162, Chairlady L. Vandewalle.

Schiessl, A. & Zilch, K. (2001), 'The effect of the modified composition of SCC on shear and bond behavior', *Proceedings of the Second International Symposium on self-Compacting Concrete, Tokyo* pp. 501–506.

Serrano, E. (2000), 'Adhesive joints in timber engineering - modelling and testing of fracture properties', *Doctoral Thesis, Lund University, Division of Structural Mechanics* .

Smith, J. W. & Bright, S. (2003), Upgrading orthotropic bridge decks with fiber reinforced composites, *in* 'High Performance Materials in Bridges', pp. 463–472.

Tazawa, E., Sato, R., Sakai, E. & Miyazawa, S. (2000), Work of JCI commitee on autogenous shrinkage, *in* V. Baroghel-Bouny & P. C. Aitcin, eds, 'Shrinkage of Concrete, International RILEM Workshop', Vol. PRO 17.

The Danish Ministry of Transportation (1987), 'The superstructure of the farø bridges 1. design of the steel superstructure', *The Danish Ministry of Transportation, The Road Directorate, ISBN 87-7491-238-0* .

Walter, R. & Olesen, J. F. (2005), 'Cohesive mixed mode fracture modelling and experiments', *Paper submitted to: Journal of Engineering Fracture Mechanics* .

Walter, R., Olesen, J. F., Li, V. C. & Stang, H. (2004), 'Cement-based overlay in negative bending', *Paper submitted for publication (included in PhD Thesis by R. Walter)* .

Walter, R., Østergaard, L., Olesen, J. F. & Stang, H. (2005), 'Wedge splitting test for a steel-concrete interface', *Journal of Engineering Fracture Mechanics* **72**(17), 2565–2583.

Walter, R., Stang, H., Olesen, J. F. & Gimsing, N. J. (2003), 'Debonding of FRC composite bridge deck overlay', *Brittle Matrix Composites BMC7, Warsaw, Poland, pp. 191-200* .

Wernersson, H. (1994), 'Fracture characterization of wood adhesive joints', *Report TVSM-1006, Lund University, Division of Structural Mechanics* .

Wolchuk, R. (2002), 'Structural behaviour of surfacing on steel orthotropic decks and considerations for practical design', *Structural Engineering International* **2**, 124–129.

Zhang, J., Stang, H. & Li, V. C. (2001), 'Crack bridging model for fibre reinforced concrete under fatigue tension', *International Journal of Fatigue* **23**(8), 655–670.

Notation

$\beta(t)$	function to describe the development of shrinkage
δ_n	crack opening in normal plane
δ_{tx}	tangential crack opening in x-direction
δ_{ty}	tangential crack opening in y-direction
δ_t	resulting tangential crack opening in t-plane
ϵ_e	elastic strain limit for strain hardening material
$\epsilon_{inf}(w/b)$	ultimate autogenous shrinkage
$\epsilon_{shrinkage}$	shrinkage strain
ϵ_u	ultimate strain limit for strain hardening material
η	viscosity
γ	coefficient in shrinkage formulation
ϕ_{tn}	mixed mode angle in the t-n plane
ϕ_{xy}	mixed mode angle in the x-y plane
σ	normal stress
τ	retardation time
τ	shear stress
τ_x	shear stress in x-direction
τ_y	shear stress in y-direction
A	material constant
a	constant
a_1, a_2, b_1, b_2	parameters in the bilinear stress-crack opening relationship

b	constant
D_{ij}	stiffness components for interface description
E	modulus of elasticity
f_t	tensile strength
f_u	ultimate tensile strength
G_f	fracture energy
H	function
J	compliance
M	bending moment
n, m, p	material exponents
T	temperature
t	thickness of steel plate
t	time
t_0	initial setting time
V	shear force
w	crack opening
w_1, w_2	crack opening limits in the bilinear stress-crack opening relationship (overlay)
w_u	ultimate crack opening for strain hardening material

DTU